THÈSE POUR OBTENIR LE GRADE DE DOCTEUR DE L'UNIVERSITÉ DE MONTPELLIER

En Physique

École doctorale I2S

Unité de recherche UMR 5221

En partenariat international avec l'Université d'Aveiro, Portugal

Nano-objets multifonctionnels pour la nanothermomètrie en milieu biologique : Etude de propriétés physiques sous confinement.

Présentée par Imane El Moujarrad
Le 5 décembre 2023

Sous la direction de Jean-Louis Bantignies et Luís D. Carlos

Devant le jury composé de

Pr. Andrea PARMEGGIANI, Professeur, Université de Montpellier	Président de jury
Pr. Stéphane PAROLA, Professeur, Ecole Normale Supérieure de Lyon	Rapporteur
Dr. Xavier CATTOËN, Chargé de recherche, Institut Néel, Grenoble	Rapporteur
Pr. Carlos BRITES, Professeur, Université d'Aveiro	Examinateur
Pr. Luc VELLUTINI, Professeur, Université de Bordeaux	Examinateur
Pr. Jean-Louis BANTIGNIES, Professeur, Université de Montpellier	Directeur de thèse
Pr. Luís D. CARLOS, Professeur, Université d'Aveiro	Co-directeur de thèse
Dr. Michel WONG CHI MAN, Directeur de recherche, Institut Charles Gerhardt Montpellier	Co-encadrant
Dr. Rozenn LE PARC, Maître de conférences, Université de Montpellier	Co-encadrante

UNIVERSITÉ DE MONTPELLIER

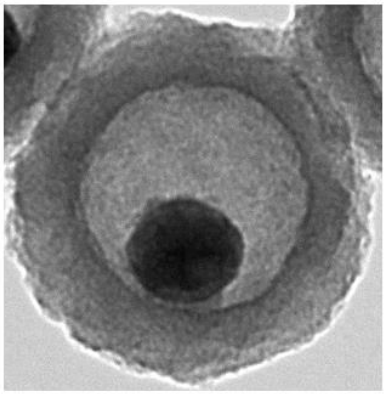

Nanoscale



Aveiro scale

Café Ria

Portuguese
traditional pavement

Remerciements

Me voici aujourd'hui au bout de mon travail de thèse, une expérience qui m'a enrichie tant sur le plan professionnel que personnel, et à travers laquelle j'ai pu mesurer mes capacités mais aussi mes limites. Arriver au bout de ce long parcours n'a pas été seulement une question de persévérance et obstination personnelle, mais aussi le fruit d'une collaboration avec deux excellentes équipes de recherche que j'ai eu le privilège d'intégrer : l'équipe NMAT du Laboratoire Charles Coulomb (L2C) et l'équipe Phantom-g de CICECO-Aveiro Institute of Materials. En effet, dans le cadre d'une cotutelle internationale, j'ai pu mener mes travaux de recherches au sein de deux universités : l'Université de Montpellier et l'Université d'Aveiro.

L'exercice des remerciements est donc pour moi un moment solennel, important mais ne pourra jamais exprimer assez ma profonde gratitude envers toutes les personnes que j'ai pu croiser durant ces trois ans.

Tout d'abord, je voudrais remercier tous les membres de mon jury de thèse, Prof. Stéphane PAROLA, Dr. Xavier CATTOËN, Prof. Luc VELUTTINI, Prof. Carlos BRITES, Prof. Andrea PARMEGGIANI, pour le temps accordé à la lecture, à la révision rigoureuse et bienveillante de mon manuscrit de thèse. Merci également pour les échanges fructueux qui ont débouché sur plusieurs questions ouvertes qui feront, sans doute, l'objet de nouveaux projets de recherche.

Je voudrais témoigner toute ma reconnaissance à mes deux directeurs de thèse Prof. Jean-Louis BANTIGNIES et Prof. Luís D. CARLOS.

Jean-Louis, merci infiniment pour ta rigueur scientifique, ta patience, ta ténacité, ton andragogie et ton soutien infaillible durant ces trois ans. Nos échanges souvent animés mais toujours riches d'enseignement ont beaucoup contribué à développer mon sens de la nuance.

Luís, merci de m'avoir accueillie au sein de ton équipe très compétente et de m'avoir accordé de ton temps précieux. Ta disponibilité à mon égard me fut d'une grande aide pour m'initier au domaine de la nanothermométrie et y développer mes connaissances. Muito Obgrigada !

Ce travail de thèse n'aurait pu aboutir sans mes encadrants que je remercie chaleureusement.

Dr. Michel WONG CHI MAN, un immense merci car sans toi ce travail n'aurait pas eu la même saveur, ton humour et ta joie de vivre ont été de véritables ressources pour moi. Je n'en oublie pas pour autant ta grande expertise en chimie (et en « couac »). Sache que je suis fière de faire partie du team des Wongchimettes.

Dr. Rozenn LE PARC, merci infiniment pour tes précieux conseils, ta bienveillance qui était pour moi une source de motivation et réconfort, je garde à l'esprit ton leitmotiv « Ne te bile pas ». Dr. Carole CARCEL et Dr. Magali GARY-BOBO, même si je n'ai pas eu l'occasion de travailler plus de temps avec vous, sachez que votre présence et votre gentillesse me furent d'un grand soutien.

Un travail de recherche ne serait rien sans les experts de techniques de caractérisations qui y ont contribué. Ma pensée va donc vers Dr. Guillaume TOQUER et Prof. Philippe TRENS, que serait l'Ecole Nationale de Chimie de Montpellier sans vous ?! Votre passion pour la recherche et votre convivialité ont rendu nos discussions scientifiques toujours vivantes et captivantes. Merci pour votre soutien et disponibilité !

Mes remerciements vont aussi vers Dr. Philippe DIEUDONNÉ et Dr. Christophe BLANC qui ont fait preuve d'une extrême gentillesse à mon égard, qui m'ont à chaque fois donné de leur temps et m'ont éclairée de leurs lumières. Je remercie également Said TAHIR, David MAURIN, Franck GODIARD et Erwan OLIVIERO pour leur contribution dans la caractérisation de mes matériaux, ainsi que Patrick HERMET pour ses valeureux apports théoriques.

Je tiens à remercier chaleureusement ma team « conférence », Prof. John R. BARTLETT, ce fut un immense privilège d'avoir fait ta connaissance et échangé avec toi, tout comme ce fut le cas pour Monique Deon et Mathilde Laird avec qui les conférences ont toujours été amusantes.

Merci à tous les chercheurs de l'équipe Nanomatériaux du L2C, Nicolas IZARD, Vincent JOURDAIN, Eric ANGLARET, François HENN, Adrien NOURY, Renaud METZ, Laurent ALVAREZ et Lucyna FIRLEJ, qui m'ont très bien accueilli parmi eux.

Merci à mes collègues de l'Université de Montpellier : Laure Bsawmaii, Clarisse Basset, Eira Anais, Luc Chavignon, ainsi que Domitille Baux, Abdallah Alayan, Hocine Merini et Said Pashayev qui ont soutenu avec succès leurs thèses dans la même période que moi et je les félicite par la même occasion pour cet accomplissement auquel nous aspirions tant ! Une attention spéciale à une de mes meilleures rencontres montpelliéraines, Clara Manesco, merci d'être ce que tu es.

Je n'oublie pas mes collègues de l'Université d'Aveiro, notamment Joana Martins qui m'a beaucoup aidé dans mes démarches administratives quand je suis arrivée au Portugal. Je remercie Fernando Maturi, Rodolfo Nunes, Sandra Correia et Miguel Rodriguez pour leurs collaborations. Un merci tout particulier à Sofia Zanella et ses chats pour leur belle compagnie.

L'accomplissement de cette thèse n'aurait pas pu être possible sans le soutien de mes proches, elle leur est spécialement dédiée.

À mes meilleurs amis de la vie, Nada et Bachir, pour leur sens de l'écoute, leur sagesse, finesse d'esprit et leur soutien inconditionnel. Je vous remercie du fond du cœur !

À mes parents qui m'ont tout donné et m'ont permis de tracer ma voie. Mama, je ne pourrais jamais te remercier assez pour tes sacrifices, merci d'être un exemple de femme puissante auquel je me réfère quotidiennement. Baba, merci d'être mon supporter n°1, ton soutien et ta confiance me poussent à donner le meilleur de moi-même. À mon petit frère Othmane, à mes tantes Touria, Rahma, Saida et Rachida, je vous aime. Cette thèse est dédiée à la mémoire de ma grand-mère Thamia Manar qui est décédée lors de ma troisième année. Repose en paix.

Abbreviations

Ln^{3+}	Trivalent lanthanide ions
RE	Rare earth
NPs	Nanoparticles
MOFs	Metal-organic frameworks
FND	Fluorescent nanodiamonds
QDs	Quantum dots
GFP	Green fluorescent protein
LIR	Luminescence Intensity Ratio
UCNP	UpConverting NanoParticle
$NaYF_4$	Sodium yttrium fluoride crystal
Er	Erbium
Yb	Ytterbium
Lu	Lutetium
Gd	Gadolinium
Nd	Neodymium
Tm	Thulium
Ho	Holmium
IR	Infrared
NIR	Near-infrared
MIR	Mid-infrared
FT-IR	Fourier-transform infrared spectroscopy
UV-vis	Ultraviolet-visible
SNR	Signal-to-noise ratio
P_D	Laser power density
2D	Two-dimensional
OP	Optical window
BW	Biological window
EPR	Enhanced Permeability and Retention
PDT	Photodynamic therapy
PMO	Periodic Mesoporous Organosilica
MSN	Mesoporous Silica Nanoparticles
HPMO	Hollow Periodic Mesoporous Organosilica
HMON	Hollow Mesoporous Organosilica Nanoparticles
HMSN	Hollow Mesoporous Silica Nanoparticles
TEOS	Tetraethyl orthosilicate
TMOS	Tetramethyl orthosilicate
ORMOSIL	Organically modified silicate
SiO_2	Silica
HT	Hard template
BTEB	1,4-**b**is (**t**ri**e**thoxysilyl)**b**enzene
BTSEENE	1,2-**b**is (**t**riethoxy**s**ilyl)**e**th**ene**
BTSE	1,2-**b**is (**t**riethoxy**s**ilyl)**e**thane
VTSE	Vinyltriethoxysilane
APTES	(3-Aminopropyl)triethoxysilane

CTAB	Cetyltrimethylammonium bromide
CTAC	Cetyltrimethylammonium chloride
SDA	Structure Directing Agent
CMC	Critical Micelle Concentration
TEM	Transmission Electron Microscopy
SEM	Scanning Electron Microscopy
HRTEM	High Resolution Transmission Electron Microscopy
BET	Brunauer-Emmett-Teller
N_2	Nitrogen
XRD	X-ray diffraction
SAXS	Small Angle X-ray Scattering
WAXS	Wide Angle X-ray Scattering
EDX	Energy-dispersive X-ray spectroscopy
HCl	Hydrochloric acid
HF	Hydrofluoric acid
NH_4OH	Ammonia
NH_4NO_3	Ammonium nitrate
EtOH	Ethanol
MeOH	Methanol
NaOH	Sodium hydroxide
Na_2CO_3	Sodium carbonate
PVP	Polyvinylpyrrolidone
PEI	Polyethylenimine
OA	Oleic Acid
OCD	Octadecene
$Ln(CF_3COO)_3$	Lanthanides trifluoroacetates
$LnCl_3$	Lanthanides chlorides
LnF_3	Lanthanides fluorides
NaF	Sodium fluoride
NaCl	Sodium chloride
NH_4F	Ammonium fluoride
Fe_2O_3	Iron oxide

TABLE OF CONTENTS

Introduction **1**

Chapter I. **10**

State of the art: Nanothermometry for biological applications **10**

1.1 Conventional thermometry 12

1.1.1 Etymology and history 12

1.1.2 Invention of thermometers 13

1.2 Thermometry at the nanoscale 14

1.2.1 Contact nanothermometry 15

1.2.2 Non-contact nanothermometry 16

1.2.3 Remote-detection nanothermometry using luminescence 17

1.3 Ratiometric nanothermometry using upconverting trivalent lanthanide ions 24

1.3.1 Ln^{3+} electronic structure and luminescence properties 25

1.3.2 Upconversion 28

1.3.3 The choice of luminescence intensity ratio (LIR) as a thermometric parameter 29

1.3.4 Nanothermometer performance 30

1.4 Ln^{3+}-doped crystal as a thermal probe 31

1.4.1 The choice of Ln^{3+} dopants 31

1.4.2 Crystal field effect 32

1.4.3 β-$NaYF_4$ host crystal 34

1.4.4 Tuning Ln^{3+}-doped materials up-converting performance 36

1.5 Intracellular temperature measurement: challenging issues and perspectives 38

1.5.1 Biological windows and accuracy of temperature measurement 38

1.5.2 Calibration 41

1.5.3 Biocompatibility 41

1.5.4 Heat transfer at the nanoscale 42

Chapter II. **45**

Hollow Periodic Mesoporous Organosilica Nanoparticles (HPMO NPs) as model functional nanoplatforms **45**

2.1 Introduction 47

2.2 Periodic Mesoporous Organosilica (PMO): Litterature review 48

2.2.1 Introduction to sol-gel 48

2.2.2 From inorganic to hybrid silica materials 55

2.2.3 Mesostructured organic-inorganic hybrid materials 57

2.2.4 From bulk to Periodic Mesoporous Organosilica (PMO) nanoparticles 63
2.2.5 Hollow Periodic Mesoporous Organo-silica Nanoparticles (HPMO-NPs) 64
2.3 Synthesis and study of a reference HPMO compound 68
2.3.1 Synthesis strategy of HPMO NPs 68
2.3.2 Silica hard template synthesis 69
2.3.3 PMO deposition 72
2.3.4 Formation of HPMO NPs 76
2.3.5 HPMO NPs synthesized in the absence of ethanol 87
2.4 Size tuning of Hollow Periodic Mesoporous Organo-silica Nanoparticles (HPMO-NPs) 90
2.4.1 Strategy of HPMO NPs size tuning 90
2.4.2 Size tuning of silica NPs (hard template) 91
2.4.3 Size-tuned phenylene-bridged (BTEB) HPMO NPs 92
2.5 HPMO NPs prepared using different bridged organosilanes 100
2.5.1 Single shell 100
2.5.2 Toward a double-shell nanoplatform 107
2.6 Experimental section 112
2.6.1 Synthesis of phenylene-bridged HPMO NPs with different sizes (HPMO BTEB) 112
2.6.2 Synthesis of HPMO NPs using different bridged organosilane precursors .. 113
2.6.3 Synthesis of the double shell HPMO NPs 113
2.7 Conclusion 114
Chapter III. 117
Encapsulation of $NaYF_4$: Er, Yb-based upconverting nanothermometers in a PMO shell 117
3.1 Introduction 119
3.2 Elaboration of $NaYF_4$: Er, Yb (UCNP) 121
3.2.1 Synthesis strategies 121
3.2.2 Phase, size and morphology tuning of β-$NaYF_4$: Er, Yb 125
3.2.3 Synthesis of β-$NaYF_4$: Er, Yb NPs 128
3.3 Encapsulation of $NaYF_4$: Er, Yb nanoparticles 138
3.3.1 Surface modification 138
3.3.2 UCNP silica coating 141
3.3.3 PMO shell deposition 144
3.4 Synthesis of multifunctional nanoplatforms through multilayered material engineering 146

3.4.1 1st coating of UCNP with silica layer (UCNP-S1@SiO_2) 149
3.4.2 Yolk/shell nanoplatforms synthesis (UCNP@void@PMO) 154
3.5 Conclusion 171
Chapter IV. 174
The nanothermometric performance of PMO-encapsulated $NaYF_4$: Er, Yb upconverting nanophosphors 174
4.1 Introduction 176
4.2 Luminescence properties of encapsulated $NaYF_4$: Er, Yb: Overview 179
4.2.1 Silica coating effect on the luminescence properties of $NaYF_4$: Er, Yb nanophosphor 179
4.2.2 Multifunctional nanoplatforms for remote nanothermometry 181
4.3 Assessing the nanothermometric performance of the encapsulated $NaYF_4$: Er, Yb nanocrystals 183
4.3.1 Methodology: Spectroscopy measurements 183
4.3.2 Methodology: Nanothermometric parameters determination 186
4.4 Results 195
4.4.1 Upconversion emission intensity 195
4.4.2 Luminescence lifetime 198
4.4.3 Thermometric parameters and performance 199
4.5 Discussion 214
4.5.1 Upconversion emission intensity: red-to-green ratio analysis 214
4.5.2 Effect of the amorphous silica layer: UCNP@SiO_2 nanoplatforms 216
4.5.3 Effect of the PMO-CTAB layer: UCNP@SiO_2@PMO-CTAB 216
4.5.4 Effect of CTAB removal from mesopores: UCNP@SiO_2@PMO 218
4.5.5 Effect of the void: UCNP@void@PMO 220
4.5.6 Nanothermometers performance 221
4.6 Conclusion 224
General conclusion 227
and perspectives 227
Appendix A 232
Appendix B 235
Analytical techniques 243
References 247

Introduction

The 20th century has witnessed the emergence of a new era in the field of material science distinguished by groundbreaking findings and innovative technologies. It is driven by a revolutionary approach, centered on the design of composite hybrid organic-inorganic materials with engineered properties, and multiple functionalities, intended to meet a broad spectrum of requirements in many scientific and industrial fields. The building blocks of this approach are the implementation of biomimetics, miniaturization of materials through nanotechnology and the deployment of soft chemistry for materials elaboration. This contributed in the initiation of numerous interdisciplinary collaborations within scientific communities.

The main focus of this work fits within this context, through the design of a multifunctional nanoplatform employed for nanothermometry and destined for a biological use. The interdisciplinary side of the project is emphasized throughout the different chapters of this manuscript, discussing the chemical elaboration of the nanoplatforms, as well as the fundamental study of structural and physical properties, all within the perspective of addressing the challenge of nanothermometry in biological environments (**Fig.1**).

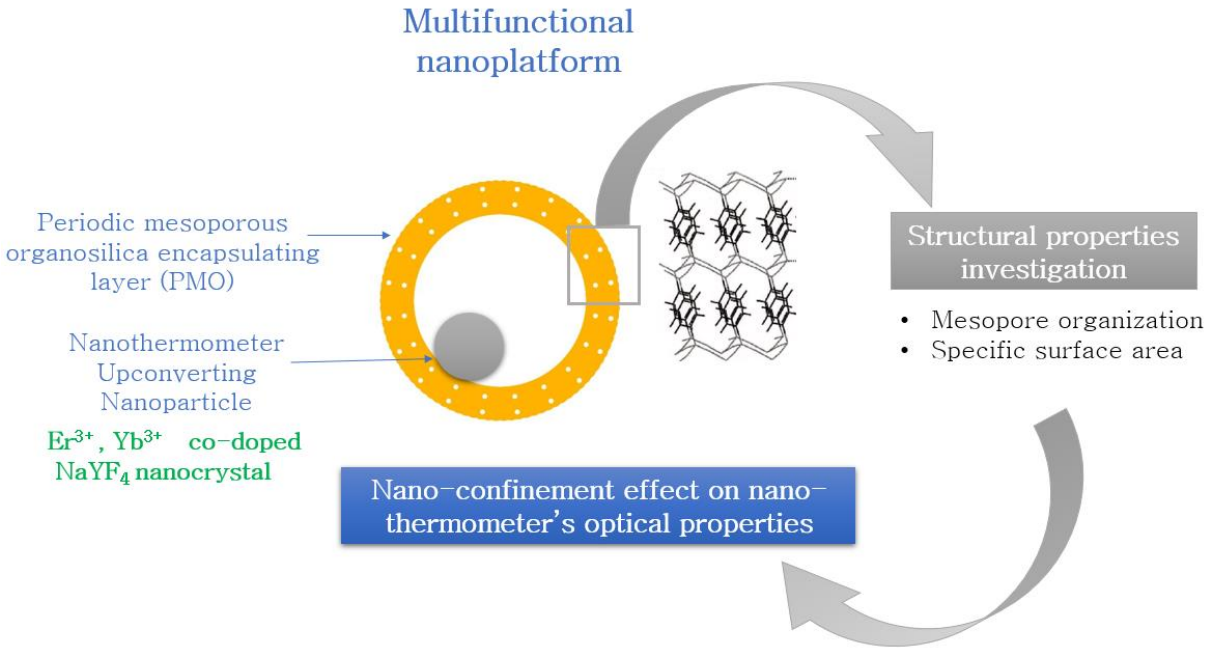

Figure.1 *Schematic summary of thesis work.*

Temperature is a fundamental parameter associated with every aspect of the natural world, as it is involved in mainly every physical, chemical, and biological process. The existence of

living organisms is temperature-dependent. Cells represent the headquarters of the overall biochemical reactions collectively referred to as cellular metabolism, which plays a pivotal role in various vital biological processes including cell division, enzyme activity and gene expression [1, 2]. These processes consume energy that originates from a series of endothermic and exothermic chemical reactions governed by the intracellular temperature that affects the dynamics of biomolecules [3]. An abnormal deviation from the standard core temperature (37 °C) typically reflects a pathological condition and has traditionally been referred to as "fever" throughout the ages. The increase in temperature is a natural response of the body to combat harmful stimuli, by activating the immune system. Another form of cellular temperature increment occurs due to localized heat generation in tumoral tissues, driven by the enhanced metabolic rate, fueling the rapid division and growth of cancer cells [4 - 6].

Understanding the mechanisms underlying the cell functions, as well as the identification and the targeting of malignant cells for therapeutic purposes, urged the development of contactless nanothermometry techniques enabling the quantification of cellular temperature variation. Most of these techniques surely surpass the conventional thermometers' performance but are still restricted by some drawbacks such as low sensitivity, low spatial resolution, superficial sensing, and limited monitoring wavelengths unsuiting tissue penetrability. They are also subject to systemic errors linked to the choice of the experimental approach and often do not fully meet the requirement of an accurate local thermosensing, mainly the capacity of non-invasive intracellular temperature mapping.

In this sphere, optically-based remote nanothermometry using luminescent probes with the ability to inoffensively penetrate the intracellular space, shows potential for a viable alternative, and has lately been explored in the nanothermometry community. The probes can be shaped in the form of nanoparticles and their surface can be functionalized in multiple ways in order to adhere to the biological environment and enter the cell via endocytosis.

Lanthanide-based nanothermometers are regarded as promising nanoprobes due to their excellent all-in-one advantages, including their versatility, originating from their characteristic 4f orbitals, and offering multiple possible electronic transitions that can cover the entire electromagnetic spectrum. The possibility of Ln^{3+} mixing by co- or multi-doping provides numerous options for ion-ion energy transfers responsible for Stokes/anti-Stokes shifts. In addition, the small gap between energy sub-levels (<2000 cm^{-1}) makes them thermally coupled,

meaning that the population distribution between these levels is temperature-dependent according to Boltzmann statistics. This provides an additional advantage, which is the possibility to monitor temperature changings based on the luminescence intensity ratio (LIR) of the two thermally coupled levels. This ratiometric spectroscopic approach is very worthwhile because the intensity ratio variation is only temperature-dependent, and thus prevents from errors induced by excitation fluctuation and the probe's local concentration. This makes the temperature-measurement method compatible with the calibration procedure, unlike the single transition emission intensity. Most of all, Ln^{3+} display temperature variation within the physiological temperature range.

In this thesis we propose to encapsulate such nanothermometers, not only to achieve biocompatibility but also to build a prospective nanoplatform for multifunctionalization. Within this context, organic-inorganic hybrid silica-based porous materials, known for their outstanding versatility and biocompatibility appear as the most qualified candidates. Periodic Mesoporous Organosilica (PMO) based materials are particularly attractive and popular for the molecular scale organization of organic moieties, and narrow-sized mesopores structuring.

The use of a PMO shell for encapsulation is used for many reasons (**Fig.2**):

- To confer biocompatibility to the nanoplatforms and reciprocally protecting the biological environment from UCNP cytotoxicity.
- To prevent the agglomeration of the nanoparticles leading to undesired luminescence quenching.
- The mesoporous structure can be used to load drugs or molecules for energy transfer.
- The versatility of the bridged silsesquioxane network allows for the grafting of molecules in various ways.

As the optical response of upconverting Ln^{3+}-based nanomaterials is highly sensitive to the local environment, the encapsulation step must be necessarily followed by a fundamental examination of the effect of PMO encapsulating material. For this work, $NaYF_4$: Er, Yb nanocrystal will serve as an UpConverting NanoParticle (UCNP), followed by the addition of an amorphous silica shell that promotes the deposition of a PMO layer. Our objective is to gain an insight on how the nanothermometric performance of the core UCNP is modified through different encapsulation configurations.

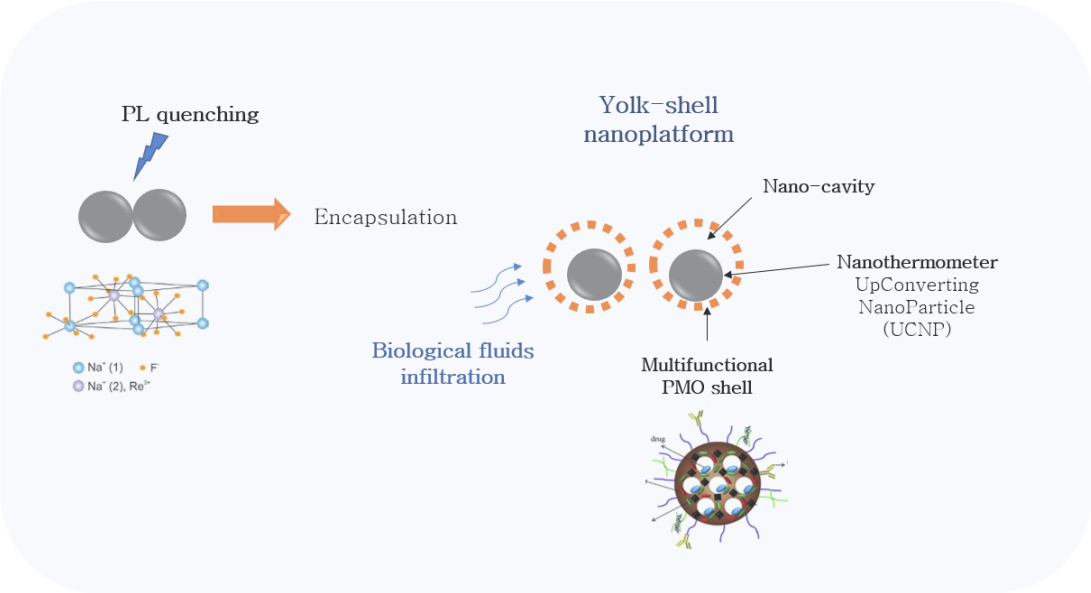

Figure.2 *Design strategy of multifunctional nanoplatforms for nanothermometry in biological environment.*

This manuscript is divided into four major chapters described below:

Chapter. I presents a state of art tracing the evolution of thermometry, starting from conventional methods to recent approaches developed for temperature sensing at the nanoscale. The characteristics of each approach and the materials crafted for its application are introduced and are subject to a comparative discussion, aiming to justify the methodology adopted for this work.

Chapter. II focuses on studying the structural properties of a hybrid silica shell. For this purpose, Hollow Periodic Mesoporous Organosilica NanoParticles (HPMO NPs) are synthesized using the hard template strategy. The main idea is to track the modification of the PMO mesostructure based on the size and chemical composition of HPMO NPs. First, the size tuning is performed while fixing the bridged organosilane precursor, in this case, phenylene-bridged organosilane (BTEB) is chosen. Second, the chemical composition of the mesoporous shell is tuned by the use of four kinds of precursors, while fixing the same size of NPs (**Fig.3**).

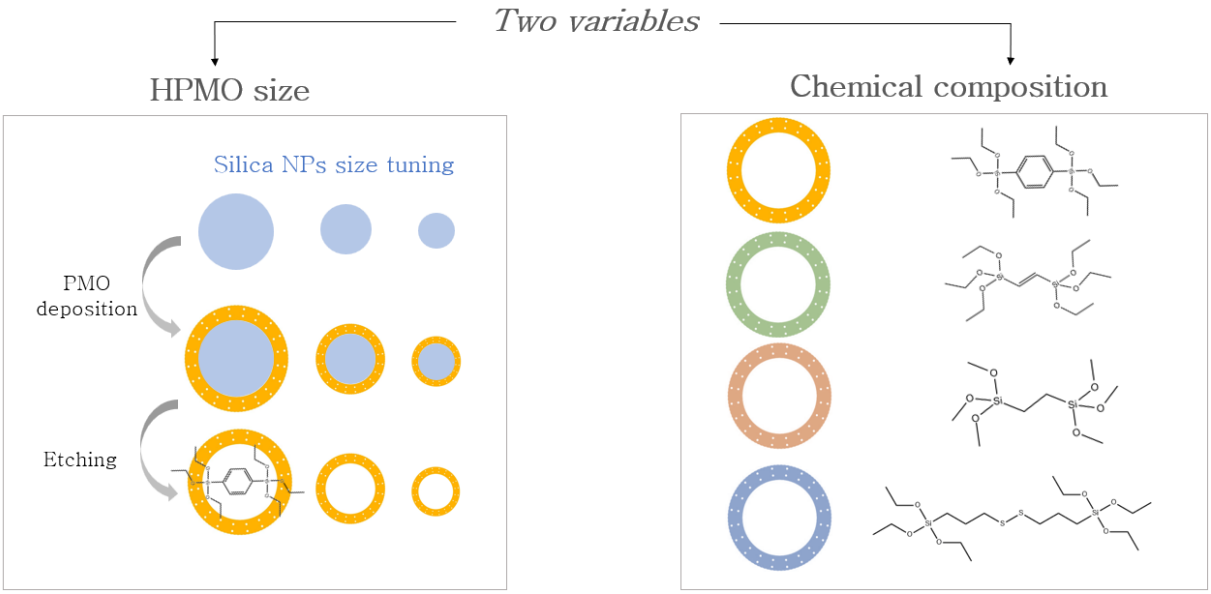

Figure.3 *HPMO NPs structural properties investigation by size and chemical composition variation.*

Mesopore size and structuring determined by these parameters are studied using X-ray diffraction, nitrogen physisorption analysis and infrared spectroscopy. Indeed, HPMO nanoplatforms are used as a model system to initially establish a fundamental comprehension on the structural properties of a PMO shell independently from the presence of a functional core. Since encapsulation of the nanothermometer (functional core) inside a PMO shell is performed through a sacrificial intermediate hard template strategy, the same used for HPMO (**Fig.4**), the synthesis challenges encountered to tailor the HPMO NPs size provides some insights on how uniform multifunctional NPs can be successfully achieved.

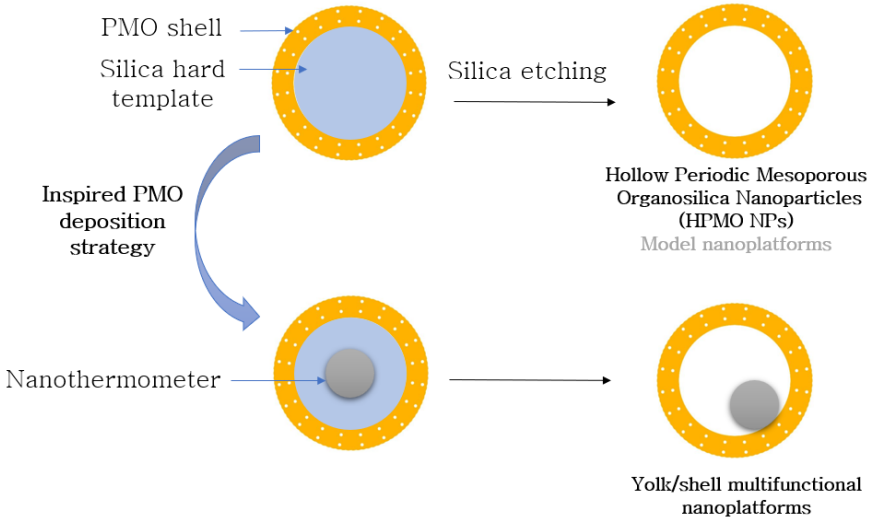

Figure.4 *HPMO NPs as model system to synthesize multifunctional nanoplatforms.*

In **Chapter. III**, the various routes to prepare UpConverting NanoParticles (UCNPs) used for nanothermometry are explored. The steps toward achieving pure hexagonal phase $NaYF_4$: Er, Yb, known for superior luminescence properties, are presented in detail. The challenges encountered for the PMO encapsulation are discussed, and a new synthetic strategy to achieve highly uniform and homogenous samples is suggested. The multi-step synthesis approach used to encapsulate UCNPs enables to preserve samples at each stage of the synthesis, and study them individually.

The purpose of **Chapter. IV** is to respond to the ultimate question of this thesis, which is how the performance of the UCNP is modified under confinement. These nanoplatforms are studied while being suspended in an aqueous environment and in a temperature range between 20 and 50° C, close to physiological conditions. Thermometric performances are assessed using the Luminescence Intensity Ratio (LIR) method (**Fig.5**), for all the nanoplatforms from the four synthesis steps in two series of samples having as a difference the thickness of the sacrificial silica layer between the nanothermometer and the PMO layer. This chapter also outlines the experimental approach, involving steady-state and time-resolved spectroscopic measurements, and elucidates the methodology employed for data processing to ensure accurate results.

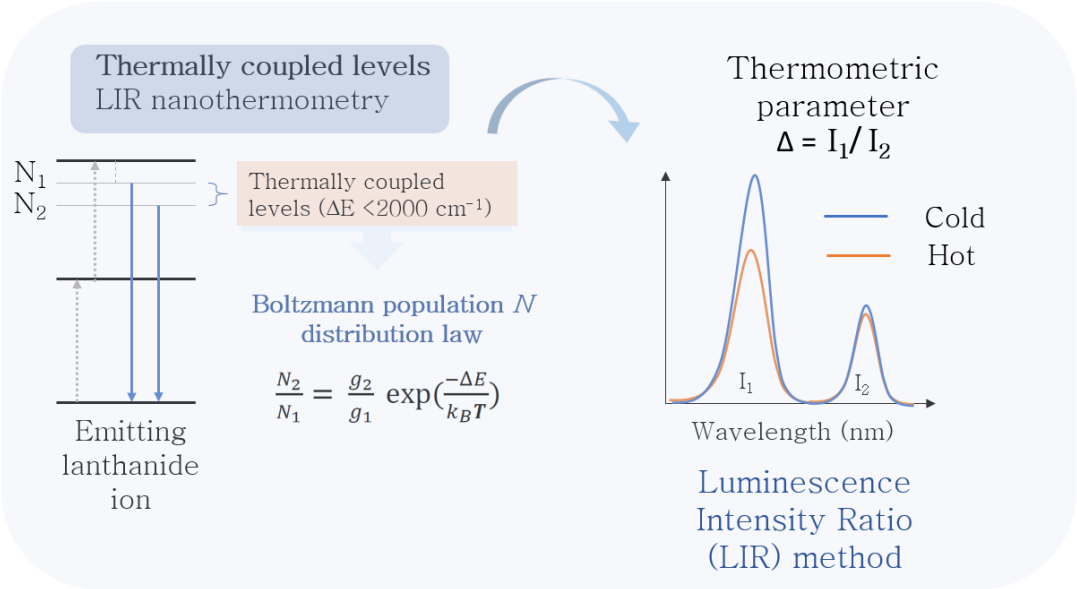

Figure.5 *Schematic representation of LIR method used for nanothermometry.*

Chapter I.

State of the art: Nanothermometry for biological applications

1.1 Conventional thermometry

1.1.1 Etymology and history

The origin of the word "temperature" comes from the Latin word "temperatura" which means “the quality of a substance of being in proportioned and moderated mixture”, it derives from the verb “temperar” which means “to mix, to moderate, to temper”. Based on this context, the word “temperature” was employed in humorism or humor theory, provided by the ancient Greek physician Hippocrates (c. 460 – c. 370 BC) and all the authors of the Hippocratic Corpus, by which they postulate that the human body is regulated by four major quality, heat, cold, moisture and dryness in analogy to the four elements: fire, water, earth and wind, and that these elements must remain in a harmonic coexistence within the body in order for it to stay in a good health. These elements were also assigned to the four vital body fluids called humors, hence the name of the theory. From another perspective, the word “temperament” is used to describe how these qualities are proportioned to construct a subject within a particular condition.

Back to then, the hot and cold qualities were only distinguished based on perception. Fever for instance used to be identified using tactile sensing. Galen (129 – c. AD 216), who substantially contributed to the humor theory, had that idea of conferring the temperature a value. He attempted to accomplish that in two ways: first, he defined a standard neutral temperature that he obtained by mixing two equal quantities of boiled and iced water, and second, he referred by the word “degree” to the level of how much the temperature of a substance can impact a patient. His approach was still not relevant enough for a precise temperature determination, because his referential standard temperature contains a lot of error, considering the thermodynamic evolution of the mixture within a short time, and the fact that his experiments were still based on perception and are qualitative rather than quantitative.

Although he failed to provide a physical meaning to temperature through measurable quantities, Galen’s ideas were a crucial start to a new paradigm of temperature measurement called thermometry, which was progressively developed and transitioned from several efforts like Al-Kindi’s and Haslerus to improve Galen’s “hot and cold degrees” model, into the conception of temperature measurements instrument called “thermometer” [7].

1.1.2 Invention of thermometers

Temperature is an essential physical quantity in almost all scientific fields, and though, the journey into its quantitative measurement was not that straightforward. Temperature is defined as an intrinsic property of the matter manifested by the total kinetic energy of its particles, which makes its direct measurement unrealizable. Therefore, the only way to make an accurate measurement is through another measurable physical quantity to which temperature is thermodynamically related, the volume of a gas or a liquid for example. The invention of the thermometer was the first step toward this purpose [7 - 10].

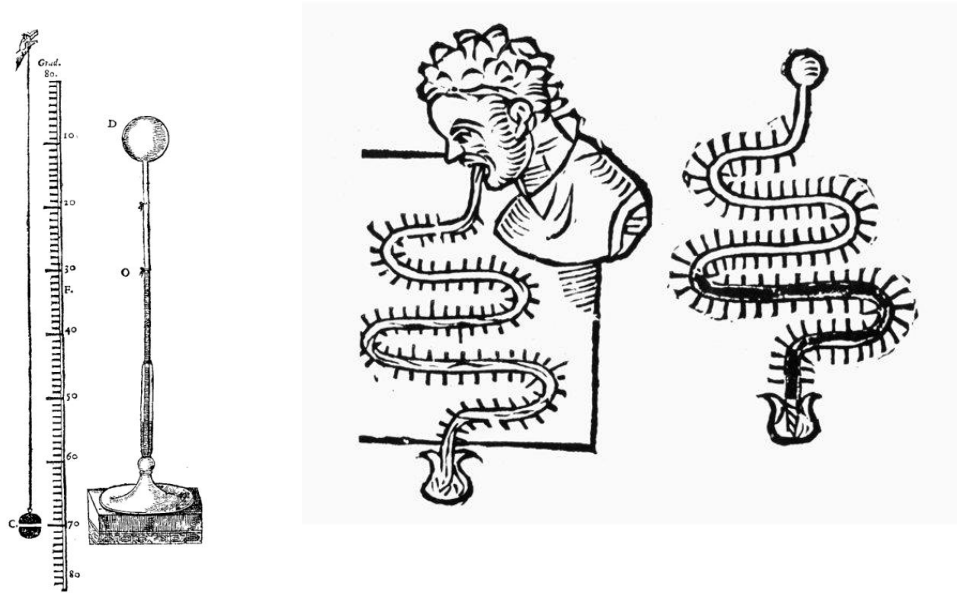

Figure I.1 *Santorio's alcohol thermoscope illustration.*

Early thermometers were named "thermoscopes" (**Fig I.1**) because they could only display the temperature changing by thermal dilatation of the air, and could not rigorously measure it. This was because these instruments had an open end and the system undergoes volume variation due to atmospheric pressure, which makes them function as barometers as well. The first air thermoscopes to be conceived were during the ancient times by Philo of Byzantium (ca. 280 BC – ca. 220 BC) and Hero of Alexandria (fl. 60 AD) who described the variation of water level in a tube due to the expansion of air. In 1610, Galileo invented the alcohol thermoscope using wine, which, despite being calibrated two years later by Santorio with the interest to measure patient's temperature, was still not considered as a thermometer because of the open system that would still bias the measured temperatures [7 - 10].

The first true thermometer was developed in 1654 by Ferdinand II de' Medici who came up with the idea to close the extremity of the alcohol thermoscope, in such a way as to avoid the impact of atmospheric pressure on temperature reading. Many modifications followed Ferdinand's II invention between the 17th and 18th centuries, mainly centered around choosing the optimal method to scale the thermometers. The most significant scalings, still in use up to the current time, are the Fahrenheit scale established in 1724 by Gabriel Fahrenheit who by the same opportunity replaced alcohol with mercury for more precise measurement, the Centigrade scale in 1749 by Andres Celsius and the Kelvin scale in 1848 by Lord Kelvin. The invention of the thermometer was highly beneficial and was certainly fundamental in many fields like medicine and climatology. However, its utilization is limited when it comes to applications that require high temperatures measurements, often encountered in industrial areas. Dilatation of liquids like alcohol and mercury can no longer be effective because of their low ebullition points compared to the measured temperatures [10].

In 1820, Thomas Seebeck fortuitously noticed that when he formed a junction between two different metallic wires with different temperatures, an electrical potential was generated due to the gradient of temperature. This effect, called "Seebeck effect", is the working principle of the thermoelectric thermometer, better known as the thermocouple. It's indeed a very convenient method for high-temperature sensing given the high resistance of metallic materials [10].

Modern thermometry has expanded to keep pace with the widespread use of electronics and digital technologies. As a result, sensors based on electrical resistance sensitivity to temperature variation, such as thermistors and resistance temperature detectors (RTDs), are developed and are subject to highly accurate calibrations. These sensors are used to build electronic devices for temperature sensing with high precision and quality, besides providing digital readings of temperature.

1.2 Thermometry at the nanoscale

Throughout the past decades, the exponential advancement of technology across a broad spectrum of industrial fields has generated a growing demand for scientific research. In 1959, Richard Feynman, through his famous quote *"There's plenty of room at the bottom",* invited to explore a whole new area of science and technology and considered the possibility of

controlling matter's properties at the nanoscale through atoms and molecules manipulation. In fact, nanotechnology has enormously revolutionized many fields such as energy, electronics, optics, and biomedicine through a variety of approaches involving the miniaturization of devices and the engineering of intrinsic features of materials, targeting novel physical properties. These properties have simultaneously implied the development of specific methods for their characterization, which must be adjusted to their distinct behavior at the nanoscale. As for most of the fields cited above, temperature represents a crucial information given the importance of tracking heat transfer and dissipation in some applications, or any chemical or biological process involving variation of temperature. In this scope, accurate temperature sensing necessitates a careful consideration to some prerequisites like high spatial resolution and good sensitivity to small temperature fluctuations, which conventional thermometers don't fulfill.

1.2.1 Contact nanothermometry

The first reflex to perform nano-thermometry is to miniaturize conventional contact thermometers. For instance, the thermocouple operating based on the Seebeck effect is downsized to a nanometric tip integrated into a scanning thermal microscope (SThM) (**Fig I.2.c**) [11, 12], which is limited by the fact that the measurement must be performed at the level of a solid surface. It can also be in the form of a micro-thermocouple, like it was used by M. S. Watanabe [13] to sense temperature inside a cell by introducing the probe directly inside of it (**Fig I.2.a**), but this technique can cause cell damage. Another example of thermometer miniaturization can be found in carbon nanotubes filled with gallium [14 - 16], and monitored with SEM, which mimics the traditional mercury thermometer. While this method sounds very attractive, it is not that straightforward to implement in many applications because it should be coupled with a microscopy (**Fig I.2.b**).

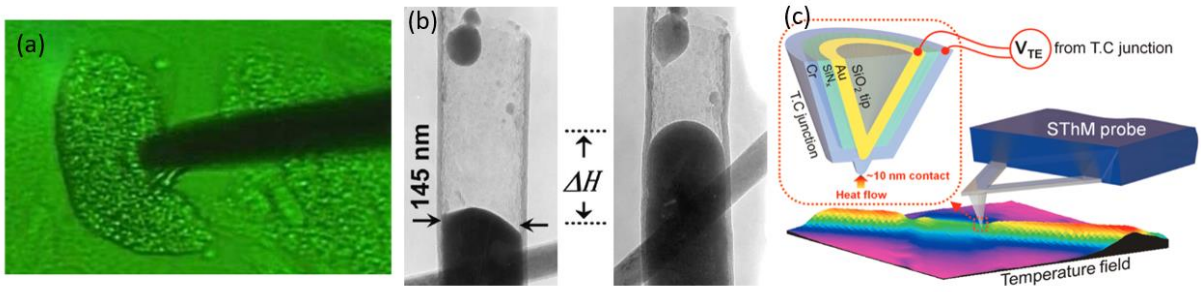

Figure I.2 *Examples of contact miniaturized thermometers.* ***a.*** *Micro-thermocouple [13].* ***b.*** *Ga-CNT [14].* ***c.*** *SThM [12].*

1.2.2 Non-contact nanothermometry

In the context of accurate sub-micrometric temperature measurements, contact thermometers offer very limited options that can hardly be adapted to a variety of nano-systems, as they require physical contact with the sample being measured [17]. In fact, contact thermometry is associated with three major issues. Firstly, it is often invasive, and secondly, it cannot probe the temperature of a fast-moving object. Lastly, the direct contact measurement between the sample and the sensor requires the establishment of a steady state equilibrium during heat transfer according to Fourier's heat law, which subsequently threatens to disturb the real temperature of the sample [18].

As an alternative, non-contact and remote detection thermometers based on the interaction of matter with light and the analysis of optical properties changes induced by temperature were developed. As an example, one can cite one of the most popular and expertly implemented examples of non-contact thermometers, the thermal camera, principally relying on the detection of temperature changes based on the electromagnetic radiation emission of the black body. The same principle is followed to develop infrared thermal microscopy for sub-micrometric temperature mapping that can reach a maximum spatial resolution of 5 µm for two-dimensional surfaces [19]. Raman spectroscopy based on the inelastic scattering of monochromatic light, is another non-contact temperature sensing technique that can provide a good spatial resolution (1 µm) and a three-dimensional measurement. The ratio of the Stokes and anti-Stokes signal is used for temperature measurement. However, the material should have a Raman signal, and the measurement usually requires a long acquisition time because of the weak signal [6, 19].

Non-contact nanothermometry involving thermoreflectance and interferometry techniques [6, 20], have both higher spatial and thermal resolution, however, knowledge of the reflectivity and refractive indexes of the material is a prerequisite. Near-field scanning optical microscopy (NSOM) in the other hand has demonstrated the best performance regarding spatial resolution (above 50 nm) because it operates at distances shorter than the diffraction limit [21], but again, the measurement is only superficial.

1.2.3 Remote-detection nanothermometry using luminescence

Non-contact thermometry was the first compelling approach to bridge the gap between conventional and nanoscale thermometry, but it remains insufficient when it comes to measuring temperature in depths and within complex structures such as cells. In fact, intracellular temperature sensing continues to be one of the most attractive technologies [22 - 24], that would unlock numerous research opportunities in the biomedical field, aiming to acquire deeper insights into some biological mechanism involving temperature changings or to detect malignant cells in the scope of theranostic applications [25, 26]. For this, nanoprobes in direct contact with the subject under examination were designed to remotely sense the local temperature. These nanoprobes are intrinsically characterized by luminescent properties that change in response to temperature variations. Indeed, over the last decade, considerable focus has been dedicated to exploring how luminescence can be utilized to measure temperature at the nanoscale level [27]. Various luminescent materials with temperature-dependent emissions like semiconductor quantum dots (QDs) [28], fluorescent proteins [29], and Ln^{3+} doped nanomaterials have the potential to serve as luminescent remote nanothermometers [30].

1.2.3.1 Luminescence

Luminescence emerges from a radiative light-matter interaction in which a material, holding luminescence properties, can emit light of a different wavelength than the excitation wavelength.

Fluorescence and phosphorescence are two types of radiative processes distinguished by the duration of emitted light. Fluorescence (10^{-9} to 10^{-7} s) occurs when the release of a photon involves an electron transition from an excited state singlet S_1 to a ground state singlet S_0 (10^{-9} to 10^{-7} s), whereas phosphorescence is induced by an electronic transition involving an excited state triplet T_1 and a ground state singlet S_0 characterized by a longer duration time than fluorescence (10^{-3} –10^{-2} s) [31].

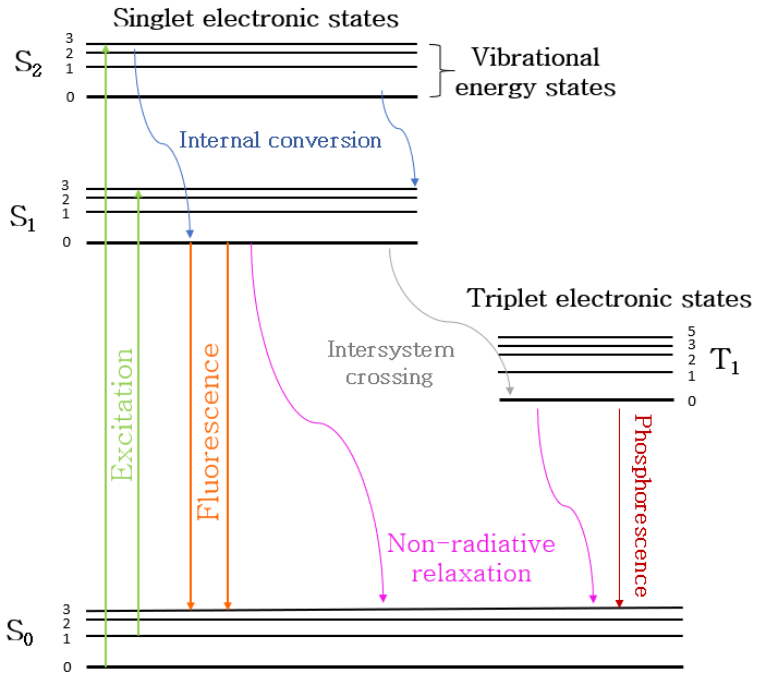

Figure I.3 *Perrin-Jablonski Diagram summarizing possible radiative and non-radiative processes.*

Phosphorescence is uncommon because it arises from a forbidden transition according to the selection rules, but can occur through intersystem crossing, particularly favored by certain materials (**Fig I.3**). The non-radiative transition is a very rapid process (10^{-14}–10^{-11} s) referring to a vibrational relaxation where the energy is released in the form of phonons, inducing heat generation. A radiative process can sometimes be supported by a non-radiative process to generate a photon emission at lower energy than photon absorption, with the difference in energy being referred to as Stokes-shift (**Fig I.4**). Inversely when the emitted photon has more energy than the absorbed photon by absorbing the energy of an already existent phonon, the difference in energy is called anti-Stokes shift. The latter can also manifest as a result of a photon upconversion process.

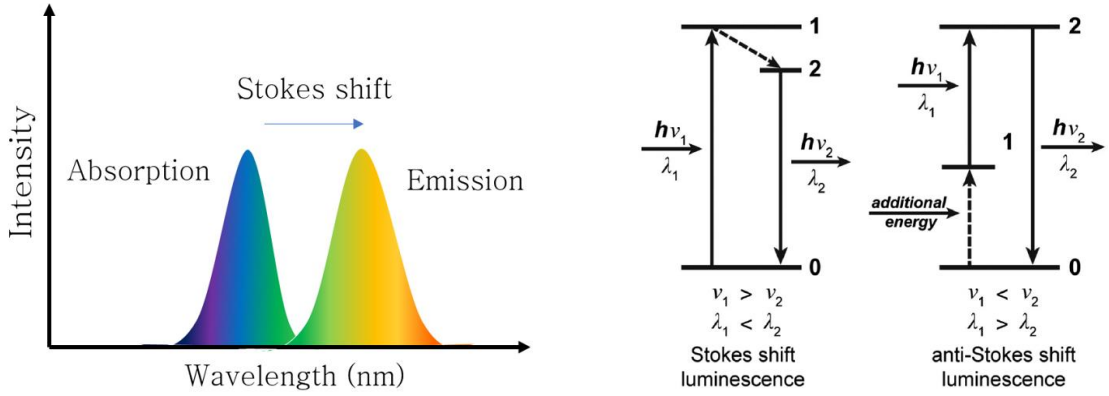

Figure I.4 *Stokes and anti-Stokes shifts [32].*

The quantum yield $\Phi(\lambda)$ characterizes the conversion efficiency of absorbed photons into emitted photons, which is related to the brightness B of a given material through its extinction coefficient ε with the following equation [33]:

$$B = \Phi(\lambda).\ \varepsilon \qquad (I.1)$$

Extinction coefficient ε is estimated from the Beer-Lambert law (I.2), where A is the absorbance, C_m is the molar concentration and l is the optical path and I_0 and I_1 are the intensities of the incident and transmitted light, respectively.

$$A = \varepsilon\, C_m\, l = -\log\left(\frac{I_1}{I_0}\right) \qquad (I.2)$$

The luminescence lifetime $\boldsymbol{\tau}$ refers to the average time the system stays in its excited state before decaying exponentially (I.3) [34].

$$I(t) = I_0\,.\,e^{-\frac{t}{\tau}} \qquad (I.3)$$

Luminescence quenching refers to the phenomenon where the emission efficiency, that can be assessed by the previous optical properties, is altered due to the presence of competing non-radiative processes activated through diverse pathways like:

- **High concentrations:** The use of luminescent molecules or ions in high concentrations may cause their aggregation which increases their proximity and favors their interactions leading to non-radiative losses by cross-relaxation for instance [35, 36]. The latter is caused by energy exchange between one emitting center in its excited state and another in its ground state, in a way that both transition to their intermediate state.

- **Energy transfer:** Energy transfer arising from the energy resonance between an electronic transition of the emitting center and the high-energy vibrations of solvent/ligand molecules containing -OH or -CH bonds (**Fig I.5**) [37].

- **Thermal quenching:** Non-radiative processes can be activated at high temperatures; the heat is converted into vibrations and the energy is lost in the form of phonons. The efficiency of light absorption and emission is therefore reduced.

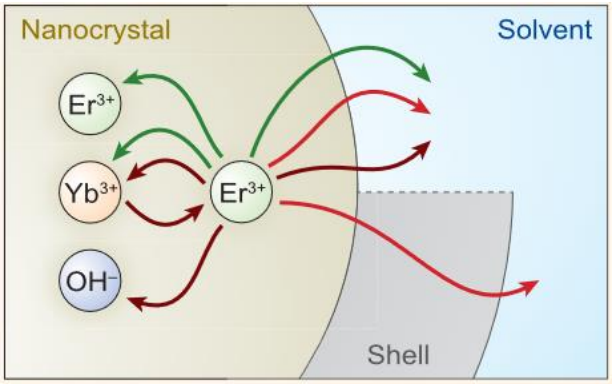

Figure I.5 *Schematic representation of some quenching pathways of Ln^{3+} doped materials, the arrows represent the different energy transfers processes that may occur between Ln^{3+} ions and the surrounding environment [37].*

1.2.3.2 Spectroscopic methods used for remote nanothermometry

Luminescence is a temperature-dependent process. The temperature readout can be performed using different spectroscopic parameters (**Fig I.6**) depending on the nature of the nanomaterials and the way their luminescence properties vary as a function of temperature and the excitation modes as well. These spectroscopic parameters can be categorized into two schemes: The time-resolved scheme, also known as lifetime nanothermometry, in which the thermometric information is expressed as a function of time, and where the excited state of a given emitting center is populated through a pulsed excitation mode, then depopulates following an exponential decay. The decay profiles are subsequently fitted to deduce the luminescence lifetime.

The steady-state scheme, in which the sample is continuously excited until reaching an equilibrium state and the thermometric information is based on the emission intensity. It is noteworthy that some nanomaterials can have the ability to be multiparametric [38], which means that temperature readout can be performed using more than one spectroscopic parameter, while some parameters are only exclusive to some specific emitting centers.

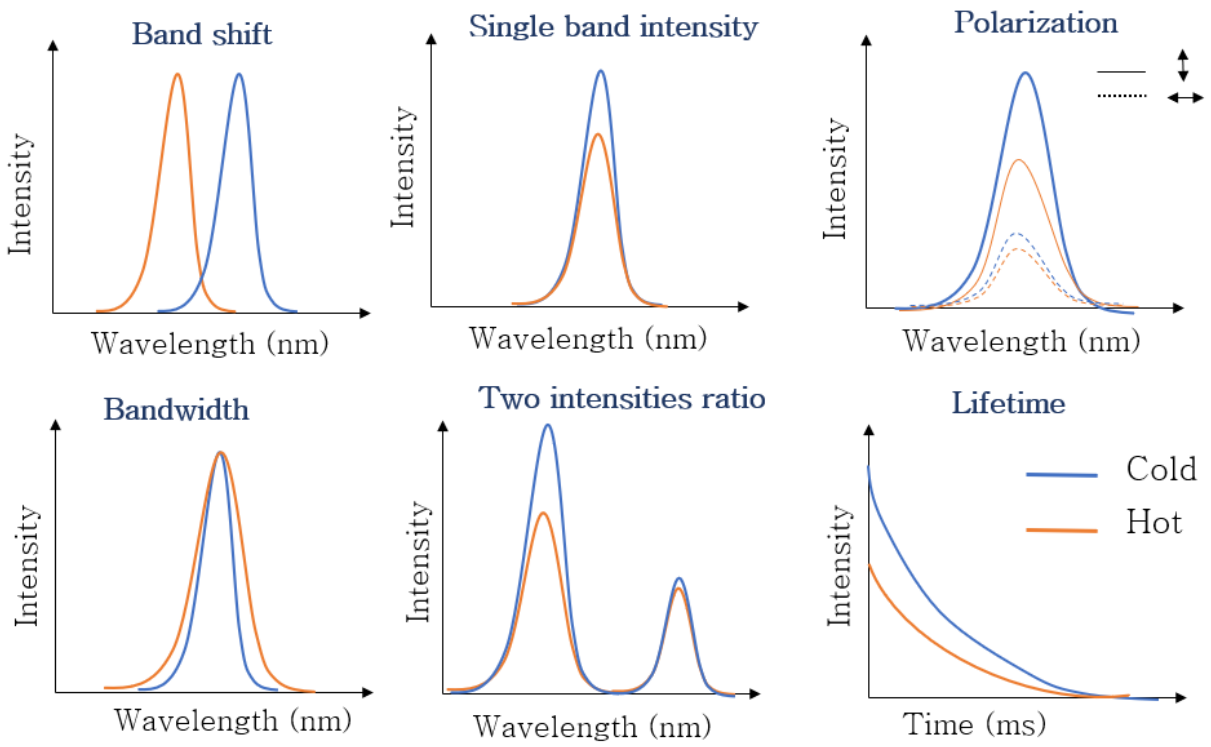

Figure I.6 *Schematic representation of the temperature effect on the optical properties of a luminescent probe using different spectroscopic methods.*

The spectral properties based on temperature changes can be studied with the following methods [17, 19]:

- **Intensity (single intensity) measurement:** The intensity of the emission spectrum is proportional to the number of emitted photons per second according to Boltzmann population distribution statistics depending on temperature. Temperature is also responsible for different quenching mechanisms like the non-radiative relaxation processes induced by thermal activation. Thus, resulting in intensity decrease with the increase of temperature. The expression of this proportionality can be stated as follows, where g is the degeneracy of the energy level, h is Planck constant, v is the frequency, k_B is Boltzmann constant, A is the spontaneous emission rate and E is the energy level [6]:

$$I \propto g\ A\ h\ \nu \exp\left(\frac{-E}{k_B\, T}\right) \qquad \text{(I.4)}$$

- **Intensity ratio (two-intensities) measurement:** Or the band-shape that characterizes the relative intensity of the emission between two independent energy levels, but with emitting electronic states that are so close that they are thermally coupled (ΔE ranging between 200 and 2000 cm^{-1}). The determination of the thermometric parameter Δ using this approach is obtained by the ratio of the two transitions from $|2\rangle \rightarrow |0\rangle$ with the correspond intensity denoted I_2, and from $|1\rangle \rightarrow |0\rangle$ with the corresponding intensity denoted I_1, where $|1\rangle$ and $|2\rangle$ are the thermally coupled levels, and $|0\rangle$ is the common ground state [6].

  If we consider the Boltzmann equation describing the population distribution between two thermally coupled energy levels separated by k_BT, where g_1 and g_2 are degeneracies of the two levels:

$$\frac{N_2}{N_1} = \frac{g_2}{g_1} \exp\left(\frac{-\Delta E}{k_B \boldsymbol{T}}\right) \tag{I.5}$$

  Using the equations in (I.4) and (I.5), we obtain the expression of the thermometric parameter:

$$\Delta = \frac{I_1}{I_2} = \frac{g_1 A_1 h\nu_1}{g_2 A_2 h\nu_2} \exp\left(\frac{-\Delta E}{k_B \boldsymbol{T}}\right) = B\, exp\left(\frac{-\Delta E}{k_B \boldsymbol{T}}\right) \tag{I.6}$$

- **Bandwidth measurement:** The bandwidth of an emission is ruled by the interaction between the lattice phonon-ion, and results in a homogenous broadening of lines, strongly triggered by temperature increase and is marked by a symmetric profile and well-defined width. Whereas an inhomogeneous line broadening is particularly caused by the local environment of the emitting center and its degree of disorder [6]. The thermometric parameter W using bandwidth is calculated following the Henderson and Imbusche equation (I.7), where W_0 is the emission full width at half maximum (FWHM) at the zero-absolute temperature:

$$W = W_0 \sqrt{\coth\left(\frac{h\nu}{2k_B \boldsymbol{T}}\right)} \tag{I.7}$$

- **Spectral shift measurement:** The spectral position of a given transition is related to the energy gap between the electronic states involved in it. The lattice vibration caused by an increase in temperature can result in variation of these energy levels and thus the peak energy of the emitted light is shifted. The thermometric parameter using the spectral shift is calculated using McCumber and Sturge equation (I.8) that relates the band shift to Debye's temperature, where $\delta\upsilon_0$ is the band shift at the zero-absolute temperature, T_D is Debye's temperature, x is equal to $h\nu/k_BT$, and α is the phonon-ion coupling coefficient [39].

$$\delta\upsilon = \delta\upsilon_0 + \alpha \left(\frac{T}{T_D}\right)^4 \int_0^{\frac{T_D}{T}} \frac{x^3}{e^x - 1} \tag{I.8}$$

- **Polarization measurement:** The shape and intensity of emission can be modified based on the polarization state of the luminescent probe. The latter can be affected by the Brownian movement that modifies the dipole orientation of the particles, which is also conditioned by temperature. As a result, the luminescent body emits partially polarized light due to its movement as a response to a linear polarized excitation light. The thermometric parameter considered in this case is called "polarization anisotropy", denoted r (I.9), described as the ratio between the intensities of two possible polarization outputs: parallel $I_{/\!/}$ or perpendicular $I_{\perp}$ to the excitation polarization [40].

$$r = \frac{I_{\parallel} - I_{\perp}}{I_{\parallel} + 2\, I_{\perp}} \tag{I.9}$$

r can have a maximum value of 0.4 and is denoted r_0. This value is reduced as a result of polarization anisotropy increase, due to the Brownian movement that affects the luminescence lifetime denoted τ_L which can be compared to the rotational relaxation lifetime denoted τ_R that is proportional to the temperature T, viscosity of the solvent η, the hydrodynamic volume V, and the Boltzmann constant k_B, according to Debye-Stokes-Einstein equation:

$$\tau_R = \frac{V\,\eta}{k_B T} \tag{I.10}$$

r can be expressed as the following:

$$\frac{1}{r} = \frac{1}{r_0}\left(1 + \frac{\tau_L}{\tau_R}\right) \quad \text{(I.11)}$$

- **Lifetime measurement:** It corresponds to the time it takes for an emission intensity to exponentially decay after a pulsed laser excitation. The overall lifetime expression involves the contribution of the radiative decay τ_r and the non-radiative decay $\tau_{nr,}$ depending on the radiative W_r and non-radiative W_{nr} decay rates (I.12). Lifetime variation depends only on the non-radiative decay rate since it is the only one varying as a function of temperature. To determine the thermometric parameter, lifetime is expressed as a function of temperature *T*, the temperature-independent emission lifetime denoted $\tau_{0,}$ which corresponds to the lifetime at the zero-absolute temperature, and the pre-exponential factor *k* [6].

$$\tau = \frac{1}{W_r + W_{nr}(T)} = \frac{1}{\tau_0^{-1} + k\, e\left(\frac{-\Delta E}{k_B T}\right)} \quad \text{(I.12)}$$

1.3 Ratiometric nanothermometry using upconverting trivalent lanthanide ions

Nanothermometers of various types, such as quantum dots (QDs), polymers, fluorescent proteins, have found favor in different fields, each chosen for its distinctive characteristics that make them well-suited to specific applications. Considering the rising interest in intracellular temperature measurement, temperature sensing in such a highly complex environment appears to be very challenging and demands the fulfillment of a maximum of criteria for optimal measurements. In this framework, the use of trivalent lanthanide ions (Ln^{3+}), incorporated within a host matrix seems to be a very promising strategy and already attracted a considerable amount of attention in this field. In fact, besides their interesting optical properties characterized by large Stokes/anti-Stokes shifts, they are known to be a narrow band emitter covering the whole electromagnetic spectrum, and they can be used on a wide temperature range including the physiological one (20-50 °C). Ln^{3+}-based nanothermometers are also known to possess unique luminescence properties arising from their electronic structure characterized by shielded 4f orbitals. They also enable the utilization of the ratiometric nanothermometry method based on two close energy levels with a population distribution equilibrium ruled by Boltzmann law.

1.3.1 Ln^{3+} electronic structure and luminescence properties

Lanthanides are a family of 15 metallic elements that constitute the upper f-block of the periodic table starting from lanthanum (Z=57) to lutecium (Z=71). They have an electronic configuration *[Xe] $4f^n$ $5d^1$ $6s^2$* consisting of a closed shell similar to xenon's electronic configuration *$1s^2$ $2s^2$ $2p^6$ $3s^2$ $3p^6$ $3d^{10}$ $4s^2$ $4p^6$ $4d^{l0}$ $5s^2$ $5p^6$ ([Kr] $4d^{10}$ $5s^2$ $5p^6$)*, and an open shell *$4f^n$ $5d^1$ $6s^2$*, with *n* the number of electrons progressively filling the 4f orbitals from n=1 for cerium (Z= 58) to n=14 for lutecium. 4f orbitals are shielded from ligands by $5s^2$ $5p^6$ orbitals that are completely filled before 4f ones according to the Aufbau principle (**Fig I.7**). This explains why they are less likely to contribute in chemical bonding, as well as having optical properties that are independent from the chemical environment, hence their sharp spectral features. Lanthanides are generally found as trivalent cations (Ln^{3+}) in their most stable ionic form. The substitution occurs for two electrons from 6s, then one electron from 5d or 4f.

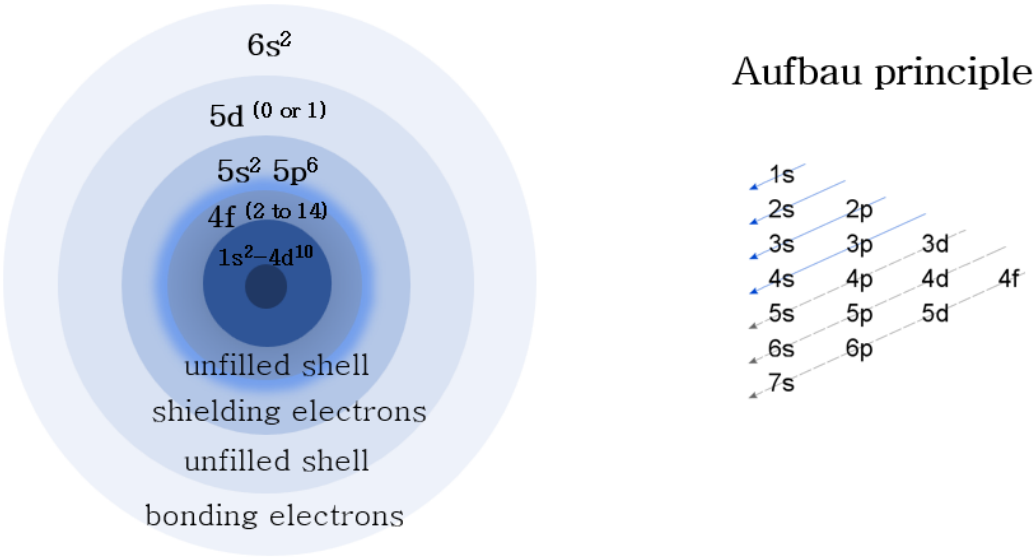

Figure I.7 *Schematic representation of the shielded 4f orbitals.*

The sharp spectral features of Ln^{3+} emerging from 4f-4f electronic transitions remained misunderstood for a long time, since electronic dipole transitions are known to be forbidden between states with even parity according to Laporte's selection rules. In 1937, Van Vleck [41] stated that the only way this transition could be possible, is through a distortion of the electronic motion of Ln^{3+} under the effect of a host crystal field, where the crystal, in this case, should be non-centrosymmetric. This is further true for transition metals categorized by the outer 3d unfilled and unshielded shell, coupled with the crystal lattice and is strongly sensitive to its

perturbations. Whereas for Ln^{3+}, the optically active electrons in 4f transitions are well protected by the outer shell. Consequently, Ln^{3+} almost behave like free ions even when being incorporated within a host matrix. The average energy of each energy level of Ln^{3+} is represented by the Hamiltonian of the free ion H_{FI} expressed as the following:

$$H_{FI} = H_0 + H_C + H_{SO} \qquad \text{(I.13)}$$

H_0 represents the Hamiltonian of configuration $4f^n$ and represents the sum of kinetic and potential energies of electrons in the field of the nucleus. H_C represent the Coulomb mutual repulsion between pairs of electrons creating different S (spin angular momentum) and L (orbital angular momentum) terms noted ^{2S+1}L resulting in the first degeneracy lifting of the $4f^n$ electronic state and splitting into $(2S+1)$ $(2L+1)$ levels. H_{SO} represents the spin-orbit interactions by coupling the S and the L, to form the total angular momentum J resulting in the second degeneracy lifting by splitting ^{2S+1}L into $^{2S+1}L_J$ terms with $2S+1$ level if $S<L$ or $2L+1$ level if $L<S$ (Russel-Saunders coupling).

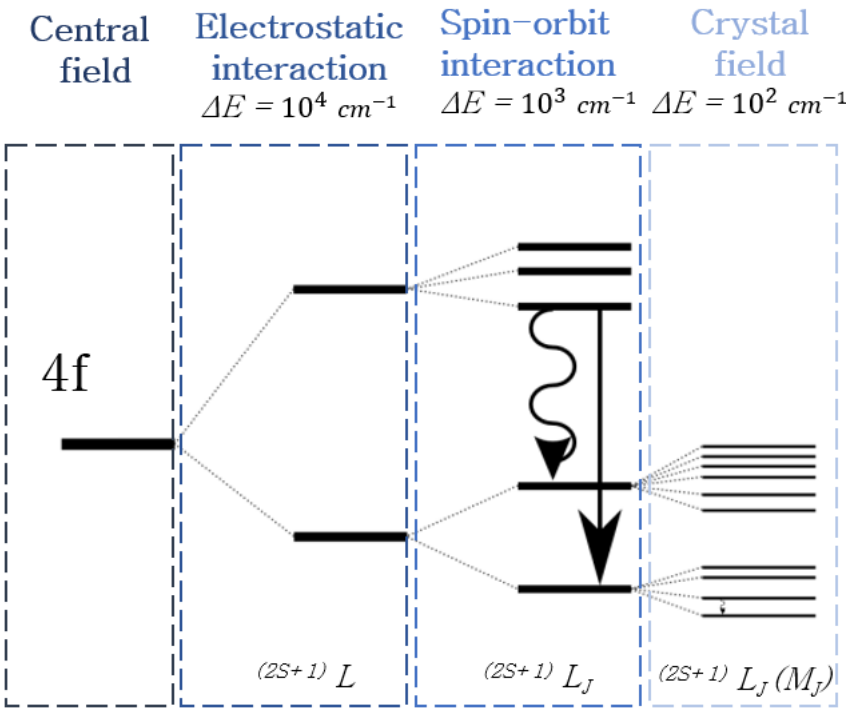

Figure I.8 *Ln^{3+} energy levels splitting.*

When Ln^{3+} are incorporated in a host matrix, the spherical symmetry of the Ln^{3+} ion is disturbed by the surrounding lattice ions, as the electrons of the former interact with electrons of the latter.

The overall disturbances from the crystal field are represented by the Hamiltonian field denoted H_{CF}. The total Hamiltonian can then be expressed by equation **I.14**.

$$H = H_{FI} + H_{CF} \quad \text{(I.14)}$$

Given the shielding effect of the 4f orbitals by the 5s,5p orbitals, 4f electrons are only weakly influenced by the crystal field, that generates a 3rd degeneracy breaking of the $^{(2S+1)}L_J$ energy levels and splits them into *2J+1* or *J+1/2* Stark sub-levels (Stark effect). However, as it occurs at an energy of 10 times less than the spin-orbit coupling energy, and 100 times less than the Coulomb electron repulsion energy ($H_0 > H_C > H_{SO} > H_{CF}$) (**Fig I.8)**, the energy levels of Ln^{3+} remain unchanged under the effect of the ion's local environment. This explains why each Ln^{3+} owns its finger print of energy levels, all identified by Dieke in 1968, using LaF_3 as a host crystal and summarized in what is known as "Dieke's diagram" [42] (**Fig I.9**). Appropriate combination of Ln^{3+} can be made to create upconversion or down-conversion processes, which offer new opportunities for extending either the excitation range or the emission range to the NIR [43, 44].

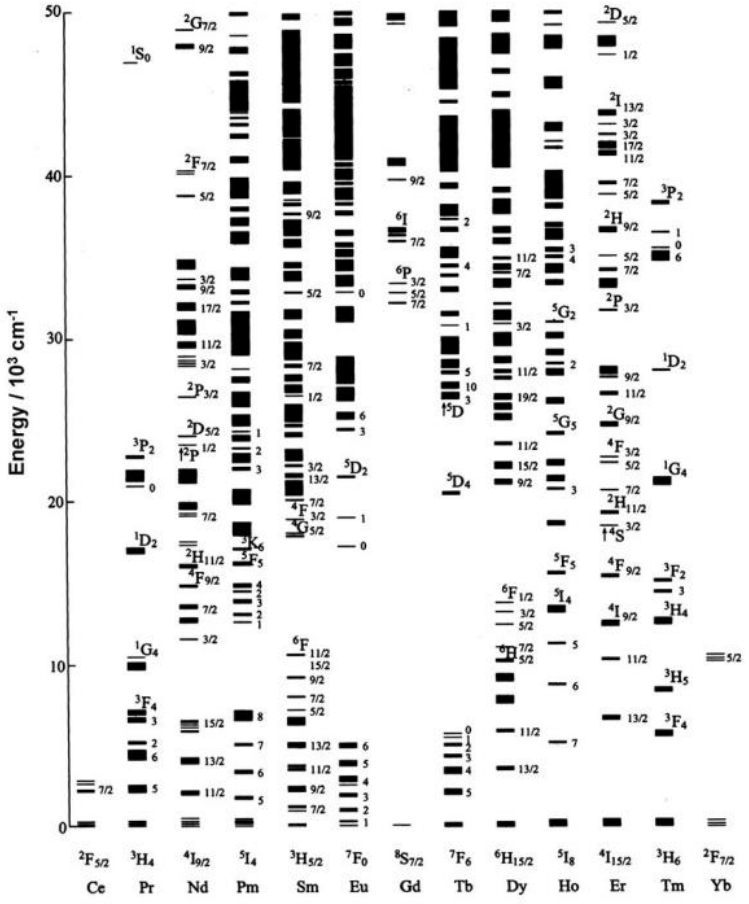

Figure I.9 *Dieke's diagram representing the energy levels of* Ln^{3+} *[44].*

1.3.2 Upconversion

Upconversion is the process by which a low photon energy excitation (long wavelengths like NIR) is converted to a high photon energy emission (short wavelengths UV-vis) (**Fig I.10**). It can be observed when using transition metals or actinides, but it is most likely encountered in lanthanides, given their unique spectral features, as well as their multiple active optical levels offering a wide emission range in the UV-visible and NIR, with lifetimes in the order of the milli- and the microsecond. Two different ions are usually selected to avoid mechanisms like cross-relaxation taking place in the presence of ions of the same sort. The first ion is termed "sensitizer", which, upon being excited through absorption from a ground state, it transfers its energy to a neighboring center termed "activator", which then can transition to either its ground state or an intermediate state, emitting light at a distinct wavelength. For that, the sensitizer and the activator must be selected among ions that have identical energy gaps for a resonant energy transfer. Sometimes, upconversion can still occur between ions with mismatched energy gaps, where the energy transfer is supported by a non-radiative process through the absorption or the emission of a phonon by the host material, thus counterbalancing the difference in energy gap as long as the energy gap is higher than 10^3 cm^{-1} [45]. The efficiency of upconversion can be affected either by quenching mechanisms due to the environment of the doped material (solvent/surface ligand), or by some competing processes like downshifting, where the optical transition in the activator ion is located at lower energy than the excitation energy.

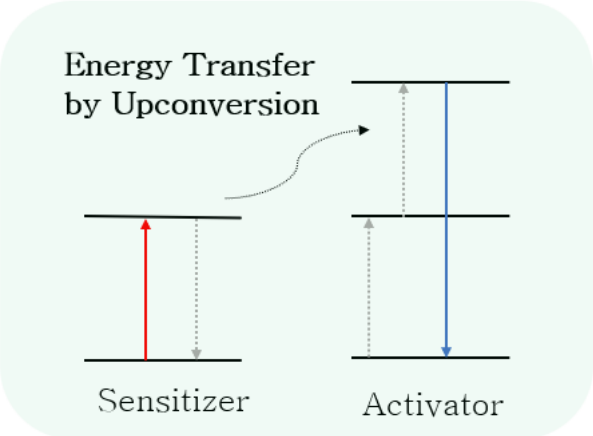

Figure I.10 *Scheme of upconversion mechanism involving a sensitizer and activator.*

1.3.3 The choice of luminescence intensity ratio (LIR) as a thermometric parameter

Temperature sensing using a remote nanothermometer is based on a calibration curve construction based on the variation of the thermometric parameter Δ corresponding to the ratio of thermally coupled intensities as a function of temperature. This method is sensitive to external operating parameters such as the excitation power, the luminescent probe concentration, the emission detection efficiency, etc. The variation of these parameters may cause considerable errors resulting in large temperature uncertainties, and the accurate comparison between different systems becomes a challenging task. For instance, lowering the excitation power density can have the same effect as increasing the temperature. That is because the emission intensity is proportional to n^{th} power of the excitation power density, with n the number of photons involved in the excitation (**I.15**) [45]. This implies that if the excitation power density decreases, the emission intensity also decreases. In contrast, when increasing the local temperature of the probe, the emission intensity decreases here as well because high temperature activates non-radiative processes (thermal quenching) that compete with radiative ones. In some cases, the peak position of a given transition can also be affected by the excitation power, depending on how many photons are involved in populating the excited state. When using SrF_2: Yb,Tm for instance, Tm^{3+} ion displays two overlapping emission bands at 769 nm ($^1G_4 \rightarrow {}^3H_5$ transition) and 795 nm ($^3H_4 \rightarrow {}^3H_6$ transition), based on whether a three-photon excitation process is generated or a two-photon one, thus exciting different energy levels [46]. This is why, when recording the spectral properties of the probe as a function of temperature, the excitation power density must be kept constant to avoid its impact. However, sometimes laser power density can still be subject to some mild fluctuations which would still have a considerable impact on the temperature uncertainty. This limitation is particularly encountered when relying on a single band intensity to perform nanothermometry.

$$I \propto P^n \tag{I.15}$$

Other examples of constraints may arise when using other spectroscopic methods, like polarization, where information on the viscosity of the probe's environment or the solvent is required. Lifetime, in the other hand, can be a very reliable method because it is based on a time-resolved scheme and is independent of the excitation power and the other parameters that

may bias temperature reading. Nevertheless, lifetime measurement also comes with some drawbacks, such as long acquisition time and the need to dispose of powerful instruments when it comes to recording very short decays. Moreover, the principle of recording lifetime makes it unsuitable to measure temperature for fast-moving objects, because the variation of temperature of the moving object might be situated in a time interval equal or shorter than the lifetime of the probe [18]. Methods like bandwidth are very difficult to implement because the variation of bandwidth as a function of temperature is complex, it is not always linear and requires high-resolution instruments to detect small variations [17]. To date, the most accurate spectroscopic method to adopt in order to overcome all these issues is the ratiometric luminescence nanothermometry based on two transitions, where the ratio variation between the two emissions is only linked to temperature changes, independently from all the setup conditions. Thermalization can occur either between two emission bands or between two Stark sub-levels in the same emission band [46, 47].

1.3.4 Nanothermometer performance

The evaluation of the nanothermometer performance relies on five characteristic parameters usually found in the literature to compare different kinds of probes: thermal sensitivity, temperature uncertainty, repeatability, reproducibility and spatiotemporal resolution [47]:

- **Thermal sensitivity:** It refers to the variation of the thermometric parameter Δ as a response to temperature variation. The absolute temperature sensitivity S_a is calculated as follows:

$$S_a = \frac{\delta \Delta}{\delta T} \tag{I.16}$$

  In order to use the thermal sensitivity as a benchmark for comparison between different nanothermometers using different spectroscopic principles, it is important to consider the relative sensitivity:

$$S_r = \frac{1}{\Delta} \frac{\delta \Delta}{\Delta T} = \frac{\Delta E}{k_B T^2} \tag{I.17}$$

- **Temperature uncertainty:** also known as the temperature resolution, can be considered as the most essential parameter to evaluate the reliability of a given probe. In the case of remote detection nanothermometry, using Ln^{3+} doped materials for instance, temperature uncertainty also depends on the experimental setup involving parameters like the signal detection quality, and the acquisition time, thus affecting the signal-to-noise ratio. $\delta\Delta/\Delta$ represents the relative uncertainty of the determination of the thermometric parameter Δ, which can be minimized by increasing the acquisition time, and by averaging a maximum of spectral data to decrease the errors in Δ calculations.

$$\delta T = \frac{1}{S_r}\frac{\delta\Delta}{\Delta} \tag{I.18}$$

- **Repeatability**: It indicates the reliability of the probe based on how much it is capable of reproducing the same results after a given number of tests under the same conditions. The repeatability R is verified by the following equation, where Δ_C is the mean of the thermometric parameter and Δ_i is the value of the thermometric parameter of each measurement:

$$R = 1 - \frac{\max|\Delta_c - \Delta_i|}{\Delta_c} \tag{I.19}$$

  The nuance between repeatability and reproducibility is based on the fact that for the latter, the measurement is carried out in different conditions than the initial ones.

- The spatial resolution δx and temporal δt are defined as the minimum distance and time interval between measurements that could enlarge the value of δT.

1.4 Ln^{3+}-doped crystal as a thermal probe

1.4.1 The choice of Ln^{3+} dopants

The design of an upconverting nanoprobe consists of doping a host crystal with optically active centers. It is important to combine the fitting sensitizer-activator pair of ions along with choosing the appropriate host lattice for optimal upconversion luminescence efficiency. The spectral properties can accordingly be tuned based on the selected Ln^{3+} and their concentration

in a given host lattice. In this perspective, Er^{3+}, Ho^{3+} and Tm^{3+} are the most commonly employed because they offer several 4f excited energy levels described as ladder-like arranged levels, unlike Ce^{3+}, Yb^{3+}, and Lu^{3+} that only have one excited energy level (**Fig I.9**). They also have large energy gaps, which minimizes the non-radiative transitions. In fact, the multi-phonon relaxation rate constant W_{nr} is inversely proportional to the energy gap between populated levels (I.20), where ΔE is the energy gap, β is an empirical constant of the host lattice and $\hbar\omega_{max}$ is its highest energy vibrational mode.

$$W_{nr} \propto \exp(-\beta \Delta E / \hbar\omega_{max}) \qquad \text{(I.20)}$$

The crystal doping with activators often does not exceed 2 % to avoid concentration quenching due to cross-relaxation between dopants of the same kind. Whereas sensitizers can be used with higher concentrations reaching 20 %, for a maximum energy absorption even at low excitation power density. Besides, the control over dopant concentrations is also crucial in terms of enhancing the upconversion probability, which can be also conditioned by the distance between the activator and sensitizer within a crystal lattice [36, 45].

Ions like Yb^{3+} and Nd^{3+} are often selected as sensitizers thanks to their large ground-state absorption cross-section that is higher than the activators'. Yb^{3+} in particular, have an absorption cross section of 1.2×10^{-20} cm^2 at 980 nm from the single transition $^2F_{7/2} \rightarrow {}^2F_{5/2,}$ which is higher compared to Er^{3+} using the same excitation wavelength (1.7×10^{-21} cm^2). This makes cooperative upconversion Yb-Er, more efficient than cumulative upconversion Er-Er. Yb-Er is considered the most popular sensitizer-activator upconversion pair for their high resonant energy transfer levels leading to a remarkable NIR-to-visible upconversion yield, with Er^{3+} offering two strong green emissions $^2H_{11/2} \rightarrow {}^4I_{15/2}$ and $^4S_{3/2} \rightarrow {}^4I_{15/2}$ from two thermally coupled levels, commonly utilized in LIR-based nanothermometry.

1.4.2 Crystal field effect

When Ln^{3+} are placed in a crystal, they undergo electron repulsion and nuclei attraction from the surrounding ions, the overall electric field is known as the crystal field effect. We mentioned before that the crystal field only weakly influences "the free ion" energy levels by destroying its spherical symmetry and breaking the *2J+1* degeneracy by splitting its levels into Stark sub-levels, thus allowing 4f-4f transitions (**Fig I.11**). The way the spherical symmetry of the free

ion is altered depends on its local point symmetry, which could be any of the thirty-two crystallographic symmetry groups belonging the four groups classified from the highest to the lowest symmetry groups [41]:

1. Cubic: O_h, O, T_d, T_h, T
2. Hexagonal: D_{6h}, D_6, C_{6v}, C_{6h}, C_6, D_{3h}, C_{3h}, D_{3d}, D_3, C_{3v}, S_6, C_3
3. Tetragonal: D_{4h}, D_4, C_{4v}, C_4, D_{2d}, S_4
4. Lower symmetry: D_{2h}, D_2, C_{2v}, C_{2h}, C_2, C_s, S_2, C_1

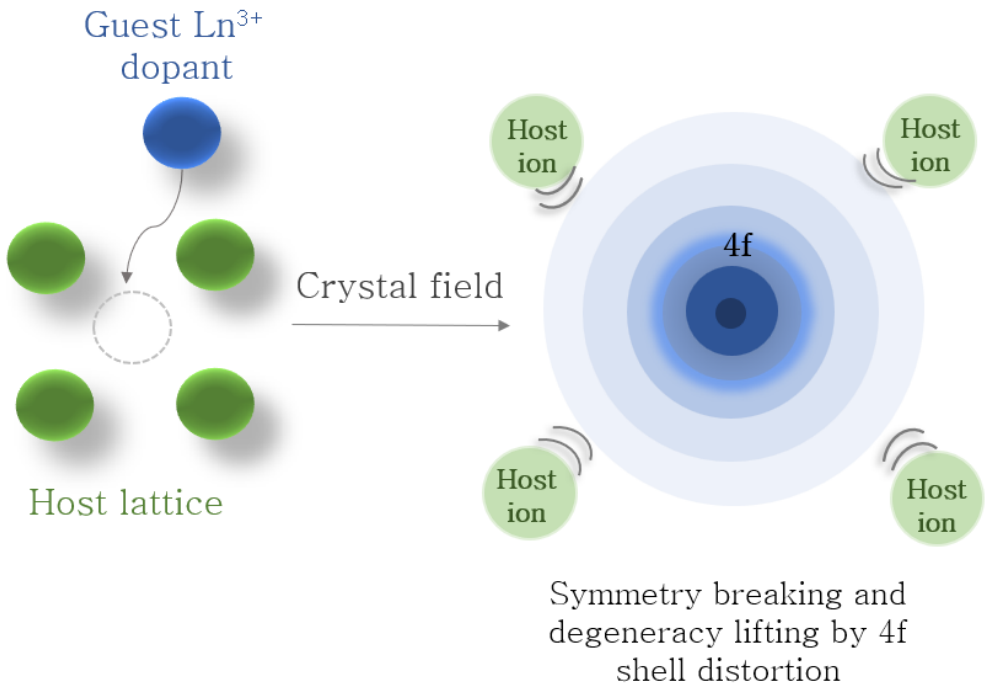

Figure I.11 *Schematic representation of the crystal field effect.*

Indeed, the degree to which *2J+1* degeneracy is lifted depends on the local symmetry point group and the number of levels to which *J* is split can be predicted accordingly (**Table I.1**).

J	0	1	2	3	4	5	6	7	8
Cubic	1	1	2	3	4	4	6	6	7
Hexagonal	1	2	3	5	6	7	9	10	11
Tetragonal	1	2	4	5	7	8	10	11	13
Lower symmetry	1	3	5	7	9	11	13	15	17

Table I.1 *Splitting under point symmetry for integral J.*

The crystal field of a given host material, regardless of its weak influence to change the spectral features of lanthanides ions, plays an important role in determining the transitions within Stark sub-levels. The probability of 4f-4f transitions increases with the number of sub-levels, which depends on the strength of the crystal field. This explains the role of the host material's crystallography in determining the luminescence properties of Ln^{3+}, to which are added other equally important criteria like:

- Compatibility between Ln^{3+} and the host material without modifying the lattice.
- Low phonon energy host material to minimize the non-radiative transitions interfering with the upconversion luminescence.
- Transparency of the host material to upconversion emissions.
- High chemical and thermal stability.

1.4.3 β-$NaYF_4$ host crystal

To complete the design of a performant upconverting probe for use in nanothermometry, it is necessary to judiciously choose a host crystal meeting a maximum of criteria mentioned above to get the best out of Ln^{3+} properties. For this purpose, inorganic fluoride-based materials denoted $AREF_4$ (A for alkali metal, RE for rare earth and F for fluoride), are privileged among a variety of crystals owing to their high chemical stability and their low phonon energies (≃ 370 cm^{-1}) [48, 49], which is ideal to host Ln^{3+} ions. $NaYF_4$ crystal for instance, has been receiving particular attention in this field up until now, owing to its disordered crystal structure arising from the random distribution of Na^+ and Y^{3+} cations, that makes is one of the most efficient host materials for Er,Yb upconverting pair [50 - 52]. More importantly, the hexagonal phase denoted β-$NaYF_4$: Er, Yb shows ten times more upconversion efficiency than cubic phase α-$NaYF_4$: Er,Yb [45, 48]. This is because Ln^{3+} occupy crystalline positions with lower point symmetry C_{3h} in hexagonal $NaYF_4$ compared to the point symmetry O_h of the homologous cubic lattice, which strengthens the crystal field effect in increasing radiative transitions probability within 4f-4f electric dipole. When decreasing the unit-cell volume by doping with relatively small cations, Y^{3+} instead of La^{3+} for instance, the crystal field becomes stronger. Indeed, $NaYF_4$: Er, Yb exhibits two times more upconversion efficiency than $NaLaF_4$: Er, Yb. In addition, hexagonal crystal structure has a more compact form than cubic structure (72 $Å^3$ vs 82 $Å^3$) [53], resulting in shorter Ln-Ln distances. Likewise, studies have also shown that when

varying alkali dopants Na^+ /Li^+ / K^+ having different ionic radius, the Yb-Er distance is modified as a result of unit-cell changing, which can be used in tuning upconversion luminescence [54].

Cubic $NaYF_4$ phase has a fluorite-type CaF_2 crystal structure where Ca^{2+} sites are randomly occupied by Na^{2+} or Ln^{3+} (Y^{3+}, Yb^{3+} and Er^{3+}) ions. When doping with Ln^{3+}, the Y^{3+} in 4a site with O_h point symmetry can be substituted by Yb^{3+} or Er^{3+} ions, and is consequently surrounded by $8F^-$ nearest neighboring ions, and 6 Na^+/Y^{3+} statistically distributed as second nearest neighboring ions. The crystal structure of α-$NaYF_4$: Yb/Er therefore belongs to the $Fm\bar{3}m$ space group (JCPDS No. 77-2042). The space group of β-$NaYF_4$: Er,Yb, on the other hand, was not that straightforward to identify and an enormous controversy was raised on whether its unit cell corresponds to a *P*6 space group, first suggested by Burns, or $P6_3/m$ suggested by Sobolev [49, 53, 55, 56]. In fact, both models exhibit very close X-ray diffractograms, which makes it difficult to identify cation sites and their distribution, while both models agree on the position of $6F^-$ ions. $P6_3/m$ is characterized by one F site and two types of cations sites: the first is a F^- nine-fold coordinated site in the shape of tricapped trigonal prism with C_{3h} point symmetry, occupied randomly either by Na^+ or Ln^{3+}, the second is F^- six-fold coordinated site occupied by Na^+ or a vacancy (**Fig I.12.a**), In contrast, *P*6 space group has two F sites and three cation sites where two F^- nine-fold coordinated are occupied by Ln^{3+} and the third one is occupied by either Na^+ or Ln^{3+} with 50% occupation probability each. Although the debate around β-$NaYF_4$ is not clear-cut [57], most recent studies seem to adhere more to $P6_3/m$ space group (**Fig I.12.b**), with evidence supported by techniques like site symmetry breakdown monitored by high-resolution luminescence spectroscopy [49, 55, 58].

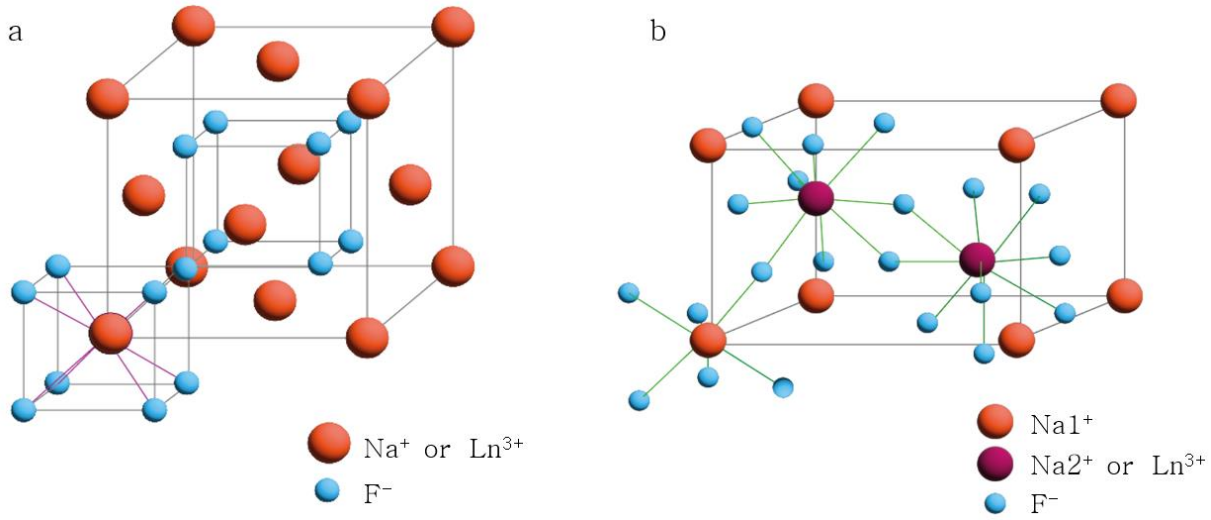

Figure I.12 a. *Cubic lattice of $NaYF_4$.* ***b.*** *Hexagonal lattice $NaYF_4$ (reproduced from [58]).*

1.4.4 Tuning Ln^{3+}-doped materials up-converting performance

With the growing interest around using Ln^{3+}-doped materials for their excellent luminescence properties involving the upconversion process, studies have not been limited to find the best host material for dopant, but also aspired to enhance these properties within the best materials. Many elements have been proven to contribute to tuning the performance of the Ln^{3+}-doped materials.

- **Particle size and surface passivation:** Ln^{3+}-doped materials used as probes for nano-thermometry are mostly made in the form of nanoparticles mainly for biological applications where the nanoprobes are supposed to invade the cell to sense temperature. They are therefore referred to as UpConverting NanoParticles (UCNP). F. Wang and his co-workers have found a relationship between $NaGdF_4$: Yb,Tm nanoparticles size and surface quenching effect [59, 60]. When the UCNP size is reduced, the specific surface increases and more dopants are brought into the surface while they were before confined in larger nanoparticles. As a result, dopants become more exposed to many quenching triggers like solvents, ligands or impurities. When coating the $NaGdF_4$: Yb, Tm with a $NaGdF_4$ shell, smaller nanoparticles displayed a stronger emission, which further confirms the surface quenching effect (**Fig I.13**). Coating UCNP with an undoped $NaGdF_4$ shell by epitaxial growth of the crystal indeed serves as a surface protecting layer, which is in literature referred to surface passivation effect using core/shell strategy.

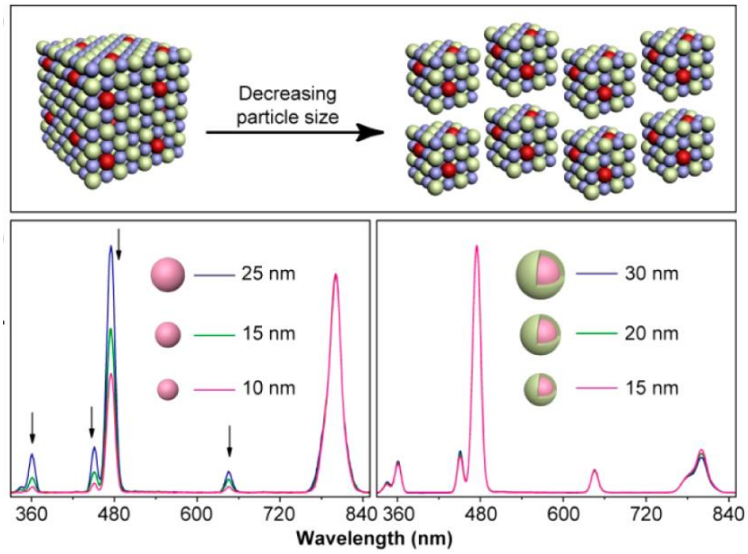

Figure I.13 Top: *schematic representation of specific surface increase with reducing NPs size.* ***Bottom****: Emission spectra of different size particles with and without coating, the coated NPs*

exhibits emission with similar intensities regardless of their size, which confirms the surface quenching effect [59, 60].

- **Crystal lattice physical manipulation:** UCNP crystal structure modulation is used to enhance luminescence properties by reducing the distance between Ln^{3+} ions and increasing the strength of the crystal field, which both result from the host crystal deformation. Numerous techniques have been documented for this purpose:

  - Mechanical constraint: By applying a significantly high pressure reaching 25 GPa on UCNP using a diamond cell anvil, Wisser *et al.* [61] reported an enhancement of $NaYF_4$: Yb/Er properties.

  -Electric field: Hao *et al.* [62] have demonstrated upconversion luminescence enhancement by applying a low voltage electric field on a co-doped Er,Yb ferroelectric $BaTiO_3$-based thin film host material. Ti^{4+} is dislodged in the direction of the electric field, while O^{2-} goes in the opposite direction of it. As a consequence, Ti^{4+} and O^{2-} ions get closer to each other in the tetragonal lattice and lower the symmetry around Ln^{3+} dopants thus increasing 4f-4f transition probability.

  - UCNP annealing: Klier *et al.* [63] studied the evolution of upconversion luminescence of $NaYF_4$: Er, Yb nanoparticles under annealing from 300 °C to 600 °C where they observed a phase transition from cubic to hexagonal $NaYF_4$ between 300 and 600 °C, and a return to cubic phase above 600 °C.

- **Plasmonic enhancement:** Several studies have reported the enhancement of the absorption cross-section, lifetime and energy transfer rate between Ln^{3+} ions when coupled with surface plasmon resonance, with frequencies that depend on the shape, size and the distance between noble metals like Au/Ag and the UCNP [64 - 67].

1.5 Intracellular temperature measurement: challenging issues and perspectives

Despite the excellent properties of UCNP nanothermometers and the significant efforts to optimize their performance, their application in a biological medium such as the intracellular space remains a great challenge and is prone to considerable bias. These challenges can be summarized in the following points.

1.5.1 Biological windows and accuracy of temperature measurement

Before using any upconverting nanothermometers to sense temperature in biological tissues, it remains crucial to first have a complete knowledge of tissue characteristics related to its scattering and absorption which can systematically interfere with the light path of the incident excitation light to attain the nanothermometers, and the quality of the emitted signal, thus affecting the accuracy of temperature measurement [68]. Absorption is related to the different biological tissue components like hemoglobin, yellow pigments like b-carotenes, bilirubin and melanin absorbing in the visible range, whereas NIR absorption is mainly caused by water and lipids. Scattering, on the other hand, is especially associated with the morphology and texture of tissues [69]. Considering these aspects, it is important to identify the wavelength ranges where the overall tissue contribution of both absorption and scattering are the least influent. The allowed wavelength regions must above all exclude blue light excitation or UV that are known to trigger photochemical reactions [70]. These ranges are known as the biological windows (or optical windows OP) divided into three main wavelength ranges (**Fig I.14**) [71], [72]:

- **The 1st biological window BW-I (750-950 nm):** This window is characterized by a dominant blood absorption and mild water absorption. It is also characterized by the autofluorescence of the tissue arising from the absorbed energy released in the form of radiative emission, which can cause significant background noise overlapping with UCNP emissions.

- **The 2nd biological window BW-II (1000-1350 nm):** This window also suffers from water absorption but offers a much better signal-to-noise ratio than BW-I because of lack of tissue autofluorescence in this region.

- **The 3rd biological window BW-III (1500-1800 nm):** Water absorption is strongly present in this window as well, but the latter offers an advantage over BW-II which is a high penetration depth because of low scattering in the long wavelength region.

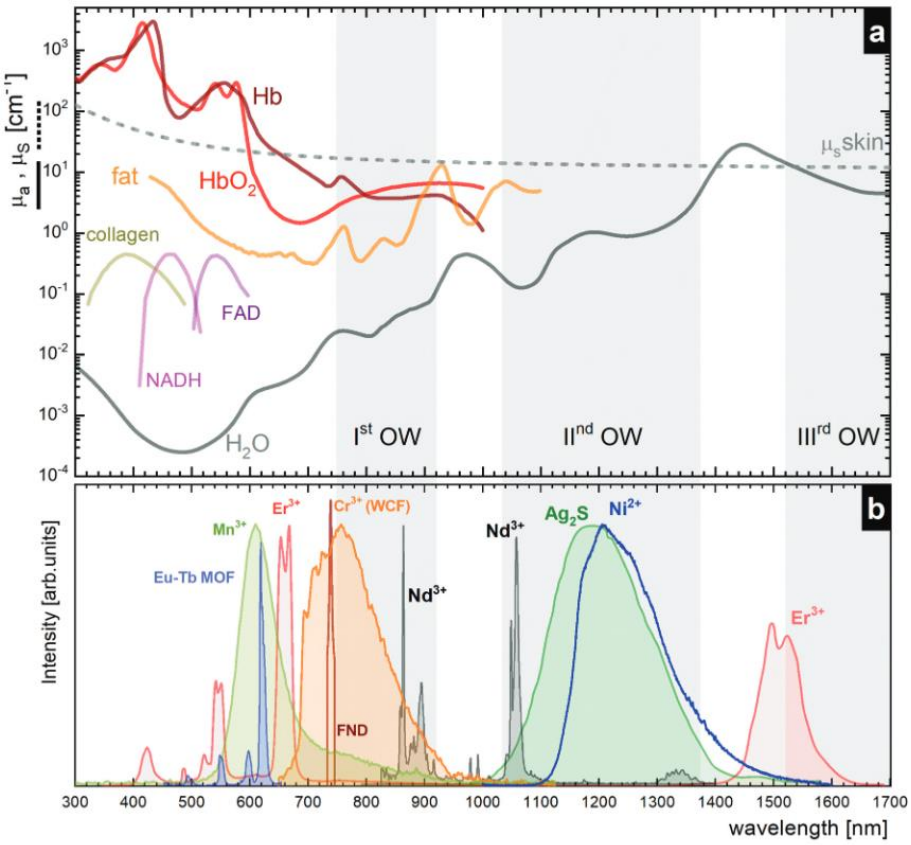

Figure I.14 a. *Luminescent thermometers Vs. tissue spectroscopy.* ***b.*** *Ln^{3+} (Er^{3+}, Nd^{3+}) transition metal ions (Ni^{2+}, Cr^{3+}, Mn^{3+}), Ag_2S quantum dots, Eu-Tb metal-organic frameworks (MOFs), fluorescent nanodiamonds (FND) and optical windows (OW) 1st, 2nd and 3rd indicating preferable spectral ranges [72].*

With that being said, it remains challenging to find an upconverting sensitizer-activator combination both absorbing and emitting in the biological windows (ideally BW-II) while maintaining an optimal upconversion luminescence performance, regardless of the versatility of Ln^{3+} luminescence. For instance, the use of Yb^{3+} as a large cross-section sensitizer to enhance the upconverting luminescence gives rise to an issue in a biological environment as Yb^{3+} absorption at 980 nm overlaps with significant absorption of water, thus resulting in a partial loss of the incident excitation wavelength, and a conversion of the absorbed light into vibrations (stretching and bending modes of H-O-H) that generates heat and results in temperature increment around the probe. Tm^{3+}- and Nd^{3+}- single-doped nanothermometers (without Yb^{3+} as

a sensitizer) are widely employed in biological environment owing to their NIR-to-NIR upconversion in the BW-I, ranging from 700 to 800 nm for Tm^{3+} and from 800-950 nm for Nd^{3+} depending on the excitation wavelength and the host crystal.

In the context of biological application, Nd^{3+} in particular has gained extra attention and ranks among the most extensively studied. In fact, when Nd^{3+} is placed within the SrF_2 host lattice (SrF_2: Nd), it exhibits an interesting emission band in the BW-II around 1060 nm which is widely adopted in nanothermometery in biological medium. It also exhibits and an emission band around 1320 nm in the BW-II, but which overlaps with water absorption at 1430 nm and was proven to have a higher impact than Yb^{3+} absorption in SrF_2: Nd,Yb. However, **Fig I.13** shows that emissions bands of Nd^{3+} are still subject to minimal water absorption in the BW-II [46]. This quenching issue caused by water absorption can be reduced through a surface passivation strategy by coating the UCNP with an inert shell, which has been proven to be efficient in reported studies [60].

In contrast, Er^{3+}-single doped nanothermometers are characterized by NIR-to-visible emission mostly led by cross-relaxation processes, which at the same time decrease the luminescence yield of Er^{3+}. When coupled with Yb^{3+} as a sensitizer and placed in $NaYF_4$ host matrix, Er^{3+} shows an improved upconverting luminescence besides exhibiting the strong green thermally coupled bands to which water is totally invisible. $NaYF_4$: Er, Yb nanothermometer is certainly not suitable for a biological application but represents an ideal probe for temperature measurement and calibration curve establishment in an aqueous medium, to bring into evidence some thermometric aspects which are not necessarily related to the thermometer itself (already demonstrating excellent luminescence properties), but to highlight the effect of the components around it like ligands, solvents or coatings. Nevertheless, some studies have reported successful Er^{3+} emission band shifting to the BW-III in the presence of Ho^{3+} along with Yb^{3+} as a sensitizer [71, 73].

1.5.2 Calibration

Calibrating nanothermometers becomes essential when transitioning between different environments, because the distinct physiological conditions in each environment can lead to various interferences in temperature measurements. Looking at it from a biological standpoint, variations in tissue properties can result in differences in light absorption and scattering effects [68]. Hence, the importance of calibration as an integral step in nanothermometry is underscored. However, repetitive calibration tends to be a laborious task and is considered one of the major challenges of intracellular temperature measurement. Within this framework, the concept of primary nanothermometers described by Balabhadra *et al.* [74] (more detail in **Chapter. IV**) could be a promising approach to overcome the calibration repetition all the while using Ln^{3+} ratiometric luminescence nanothermometry.

1.5.3 Biocompatibility

Measuring the temperatures in an intracellular environment requires nanoprobes endocytosis (**Fig I.15**). A successful nanoprobe uptake strongly depends on the nanoplatform's size, surface chemistry, chemical stability, dispersibility and stiffness. The standards value of each of these properties also vary based on the type of the targeted cells [75, 76].

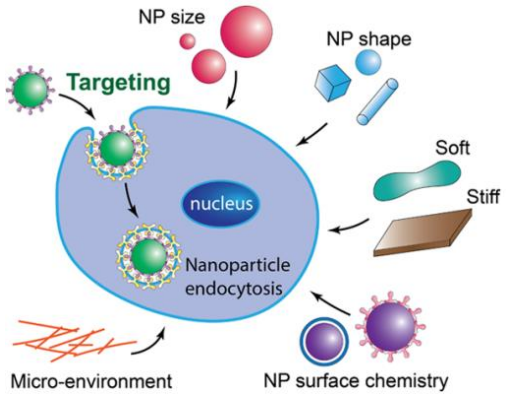

Figure I.15 *Parameters influencing cellular endocytosis [76].*

In the case of targeting tumors in the scope of theranostic application, control over the size of the nanoparticles is important to selectively reach malignant cell through the enhanced permeability and retention effect (EPR) illustrated in **Fig I.16**.

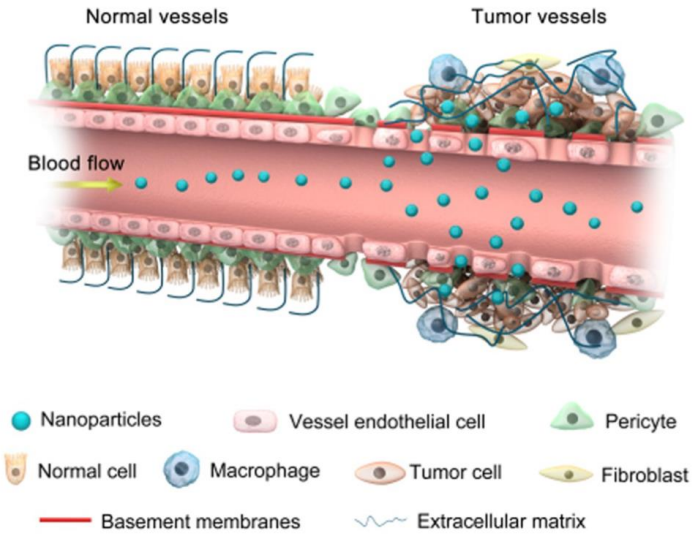

Figure I.16 *Selective accumulation of nanoparticles in tumoral tissue with EPR effect [77].*

1.5.4 Heat transfer at the nanoscale

In analogy to the challenges faced in measuring intracellular temperature using conventional thermometers, treating malignant cells using standard radio-frequency or microwave ablation techniques for hyperthermia without causing collateral damage to surrounding tissues proves unfeasible. These techniques require delicate handling of induced temperature increment often monitored by conventional thermometers like thermocouples or optical fibers, thus adding more invasiveness to the practice. As a substitute, hyperthermia using plasmonic or magnetic nanoparticles for intracellular heat release is one of the most explored approaches in cancer treatment. However, intracellular nano-heaters performance is almost negligible when predicting it using Fourier's heat law, which raises a major skepticism around hyperthermia significance at the nanoscale [78]. Several approaches have been investigated to have a deep insight into this problematic, but most of the time faced some estimation limitations linked to the size, the total volume, the heat capacity and the transient heating process of the nano-heater relatively to the thermal conductance and the size of the cell.

Alternatively, local temperature measurements of the nano-heaters using different kinds of nanothermometers like QDs, GFP, in an aqueous media have been reported by several studies but were also limited by the distance between the nanothermometer and the nano-heater. Moreover, they are at risk to be separated when using them for in vivo applications if the nanoplatforms are chemically and morphologically different, due to biological aspects like chemical surface, size-dependent EPR effect, and cell uptake [68]. To overcome this issue,

ratiometric temperature measurement using Ln^{3+}-doped nanomaterials, could be a potential route to accompany hyperthermia nano-heaters, given the multiple reported advantages, notably the possibility of nanoplatform multi-functionalization, which could be one way to place a nanothermometer and a nano-heater within the same nanoplatform and with controlled distances.

Chapter II.

Hollow Periodic Mesoporous Organosilica Nanoparticles (HPMO NPs) as model functional nanoplatforms

2.1 Introduction

This chapter is dedicated to the study of Hollow Periodic Mesoporous Organosilica Nanoparticles (HPMO NPs), as we are interested in investigating the structural properties of a Periodic Mesoporous Organosilica (PMO) shell, independently from the presence of a functional core. Their synthesis involves a multi-step approach using the hard template strategy, where amorphous silica nanoparticles serve as a hard template for depositing a PMO layer.

The use of the hard template route is favored over alternative methods such as soft templating including vesicle templates and water-oil-in-water emulsions [79 - 81]. While these approaches have been extensively explored in the literature because of the convenience of one-pot processes, they often struggle to result in monodisperse nanoparticles, primarily because of difficulties in achieving thermodynamic stability. Polystyrene-based hard template (PS) is one of the promising strategies to fabricate uniform and monodisperse hollow nanoplatforms, but require a prior surface treatment to enhance the adhesion between PS and the mesoporous silica/ hybrid silica layer to deposit [82]. Furthermore, silica-based hard template is chosen for the synthesis of the model HPMO NPs because the same template is used as a spacer between the upconverting nanothermometer (UCNP) and the PMO shell, subsequently sacrificed to obtain the yolk/shell nanoplatforms (**Chapter. III**).

This chapter starts with an introduction to the sol-gel technology used to elaborate silica and hybrid silica materials, it outlines the chronological evolution of PMO materials leading to the development of HPMO NPs.

Next, a structural characterization of a reference phenylene-bridged HPMO sample (HPMO-A) is presented. Finally, an examination of structural variations in HPMO NPs is conducted, with a focus on how they depend on both size and chemical composition.

2.2 Periodic Mesoporous Organosilica (PMO): Litterature review

2.2.1 Introduction to sol-gel

2.2.1.1 Early silicon chemistry and sol-gel technology for inorganic silica-based materials

Silicon Si is considered as the 8th most abundant element in the universe and the 2nd in the Earth's crust. Given its good affinity with oxygen, Silicon can be found in silica form (silicon dioxide, SiO_2), comprising materials such as sand and dust, or free silica like quartz that represents 12-14 wt% of the lithosphere. It can be also found in many other chemical forms like silicate minerals accounting for 75 wt% of the lithosphere [83] and silica soluble species like silicic acids. The latter, when found in water surfaces of lakes, oceans and seas, it goes through a chemical transformation called "Silicification" carried out by unicellular organisms called "Diatoms", a kind of primitive micro-algae that transform the silicic acids monomers into a biogenic silica shell called "frustule" around the living cell, through an intracellular series of chemical reaction known as polymerization [84]. Thus, representing the first natural manifestation of the sol-gel process. Diatoms frustules are not only the natural embodiment of the sol-gel process, but also exhibit a highly distinctive morphology with regularly structured wall porosity (**Fig II.1**), which has served as a source of inspiration for the advancement of modern functional materials based on the sol-gel technology [85].

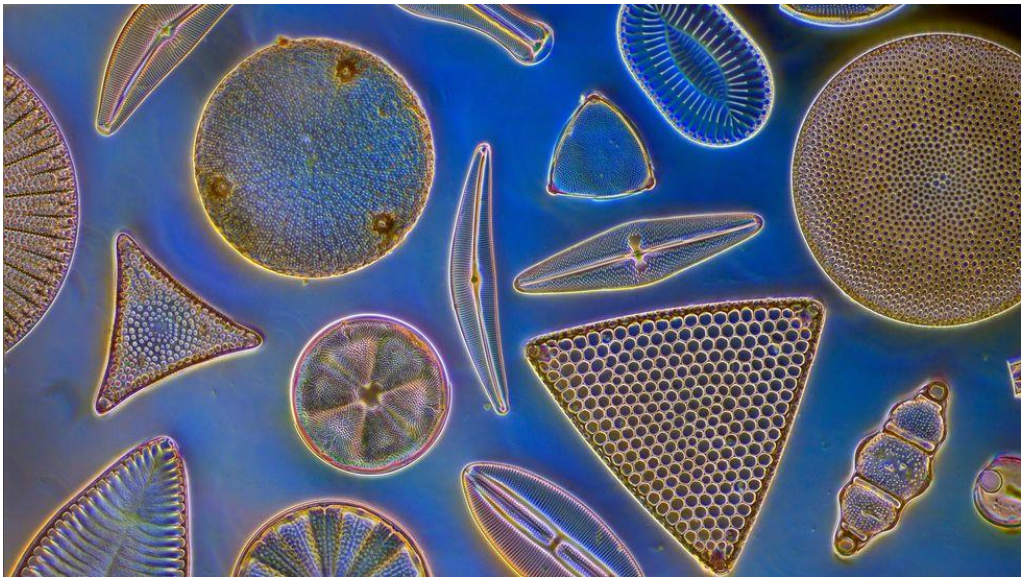

Figure II.1 *Dark field microscopy image of Diatoms with blue background (Credits: Alamy).*

Sol-gel process was the first time witnessed in 1640 by J. B. van Helmont while dissolving the sand in an alkaline solution to form what he described as a “water glass”, which precipitated again in the form of silica sand after acidification. He declared, following that experiment, that it is possible to make glass using silicon chemistry in mild conditions only by varying the solution pH, when glass production had always been based on sand melting at very high temperatures [86, 87]. Van Helmont’s findings were fundamental for the emergence of the so-called “soft chemistry”. Indeed, this concept remains today a very popular and gainful strategy among scientists and industrials wiling to minimize energy use, through methods privileging ambient temperatures, catalysis and pH changing.

At that time, successful attempts to optimize van Helmont’s “water glass” experience took place, notably by T. Berman in 1779, but sand was still the only silica source employed to perform the sol-gel reaction, until the development of the first silicon precursor, a crucial turning point in the sol-gel pathway. Indeed, in 1824, J.J. Berzelius synthesized silicon tetrachloride ($SiCl_4$) after isolating silicon from potassium fluorosilicate, and in 1844 J.J. Ebelmen used it to obtain silicic ethers by adding absolute ethanol to it. Two years later, J. J. Ebelmen observed the formation of a transparent solid glass after exposing silicic ethers to a humid atmosphere. The discovery of the sol-gel has therefore been made official and Ebelmen was acknowledged as its founder. Upon this discovery, Graham introduced in 1864 the words “hydrosol” and “hydrogel” to distinguish the liquid and the gelatinous form of silicic acid hydrates [88]. In the meantime, the development of new different silicon compounds continued to receive a lot of interest, mainly silicon-carbon covalently bonded precursors.

In 1863, C. Friedel and J.M. Craft developed tetraethylsilane ($Si(C_2H_5)_4$), which inspired A. Ladenburg in 1871 to develop ethyl silicate with one hydrolyzable ethoxy group (Et_3SiOEt, Et= C_2H_5) aiming to prepare the first silanol compound Et_3SiOH [86]. This subsequently led to development of tetraethyl orthosilicate (TEOS) and tetramethyl orthosilicate (TMOS), which are today universally used to prepare pure silica materials.

In 1939, W. Geffcken and E. Berger pioneered the industrial utilization of the sol-gel method by their single oxide optical coatings for Schott Glaswerke company and the first sol-gel patent was published in the same year. Different sol-gel made products like thin films, optical glass and aerogels have succeeded since that and reached a large-scale production [89].

Today, the sol-gel chemistry offers the ability to produce a wide range of oxide materials in various forms, including monoliths, thin films, fibers and powders. This versatility, encompassing different materials and shapes, has made this process highly appealing in technological sectors like optics, electronics and biomaterials.

2.2.1.2 Sol-gel process

Sol-gel refers to a chemical process where a colloidal suspension of very small solid particles in a liquid called "sol" is transformed into a three-dimensional "gel" with infinite viscosity. This transformation is based on a sequence of hydrolysis-condensation reactions, that typically take place in an aqueous solution at room temperature, which is why sol-gel falls into the category of soft-chemistry processes. The precursors are commercially available, they consist on alkoxides $M(OR)_n$ where *M* can be either metalloid like silicon or a metal like aluminum, zirconium, titanium etc, *n* is the number of alkoxy groups *(-OR)* linked to metal, and *R* is an alkyl group with the formula C_nH_{2n+1}. As sol-gel reaction is slow under neutral conditions, the use of a basic or acidic catalyst becomes necessary.

The stages leading to the formation of a solid metal oxide begin with the hydrolysis of dissolved alkoxides upon the introduction of water. Subsequently, the hydrolyzed oligomers engage in a polycondensation reaction, leading to the creation of a network of cross-linked molecules, gradually transforming into a highly viscous gel (aging stage). This gel having a solid appearance, actually still entraps a considerable amount of solvent. The expulsion of solvent is performed under mild conditions drying to form a dense xerogel of glass or ceramic material. Moreover, highly porous materials with very low density, known as aerogels, can be obtained using the supercritical drying [87].

In the case of silicone alkoxides $Si(OR)_4$, the hydrolysis and condensation mechanisms go as following:

- **Hydrolysis:** The alkoxysilane *Si-OR* undergoes a transformation in which its alkoxy group *(-OR)* is substituted with a hydroxy group *(-OH)* upon reaction with a water molecule. This results in the formation of silanols *Si-OH* and the release of an alcohol molecule *R-OH*.

$$Si(OR)_4 + H_2O \rightarrow HO{-}Si(OR)_3 + R{-}OH$$

- **Condensation:** The hydrolyzed precursor molecules undergo condensation, where the silanol groups *Si-OH* either react with each other followed by the release of a water molecule (oxolation (1)), or with another alkoxy group followed by the release of an alcohol molecule (alkoxolation (2)). This results in the creation of *Si-O-Si* bonds referred to as "siloxane".

(1) $(OR)_3{-}Si{-}OH + HO{-}Si{-}(OR)_3 \rightarrow (OR)_3\,Si{-}O{-}Si\,(OR)_3 + H_2O$

(2) $(OR)_3{-}Si{-}OR + HO{-}Si{-}(OR)_3 \rightarrow (OR)_3\,Si{-}O{-}Si\,(OR)_3 + R{-}OH$

The kinetics of hydrolysis and condensation, responsible for the growth of polymeric clusters shaping the network, dictate the structure and properties of the final gel. Several parameters, such as temperature, precursor and solvent selection exert influence on these reaction rates. As for the choice of the catalyst, it is directly connected to the material's structure and porosity, defining its intrinsic physical properties [90, 91] . The catalysis pathways are as follows:

- **Basic catalysis:** In the presence of a base catalyst (e.g., NH_4OH, NaOH), hydroxide ions *(OH^-)* exhibit greater nucleophilicity compared to water molecules, and thus, they function as nucleophilic agents by initiating attacks on silicon centers (**Fig II.2**). The hydrolysis under basic condition is the fastest because the replacement of alkoxy groups by hydroxy groups only increases the stabilization of the negatively charged silicon intermediates, thus further accelerating the hydrolysis rate. At the commencement of condensation, 6 silanol sites are already available *($(OH)_3Si$-O-$Si\,(OH)_3$)*. This trigger multiple condensation reaction occurring simultaneously, and result in a highly dense interconnected network.

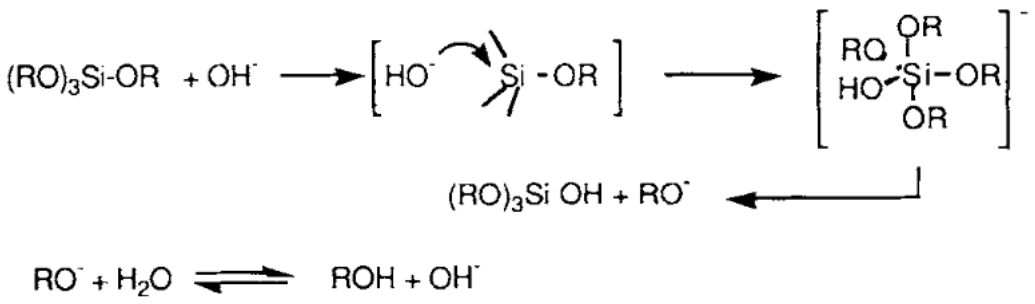

Figure II.2 *Hydrolysis mechanism under basic catalysis [92].*

- **Acidic catalysis:** The silicone alkoxide goes through a penta-coordinated transition state (**Fig II.3**) with the H^+ protonation occurring under acid catalysis (HCl, H_2SO_4, HNO_3), turning the silicon alkoxide more prone to nucleophilic attack, and promoting the hydrolysis process. The condensation step usually targets terminal silanols, and result in chain-like structures.

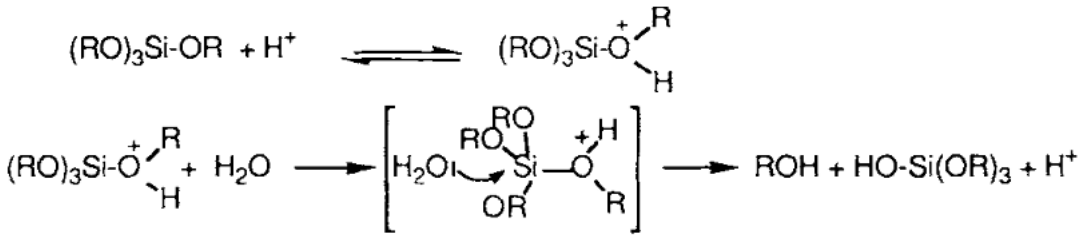

Figure II.3 *Hydrolysis mechanism under acidic catalysis [92].*

- **Nucleophilic catalysis**: This catalysis is realized in the presence of fluorides in a neutral medium (NaF, NH_4F) and has a similar mechanism to that of bases. The replacement of alkoxy groups by hydroxy groups is achieved in two steps: (i) the nucleophilic attack of the fluoride ion (F^-) on the silicon center and the formation of a reversible penta-coordinated intermediate state, (ii) the hydrolysis of Si-F bond by water (**Fig II.4**).

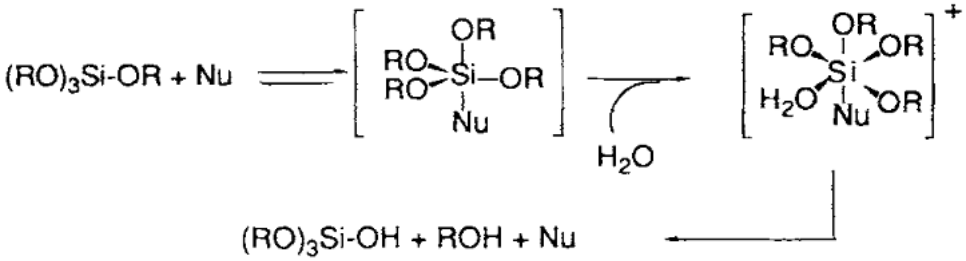

Figure II.4 *Hydrolysis mechanism under nucleophilic catalysis, where Nu= nucleophile corresponds to the fluoride ion (F^-) [92].*

2.2.1.3 Silica nanoparticles

In 1968, Stöber pioneered the synthesis of spherical and monodisperse particles from an aqueous solution of silicon alkoxides, alcohol and ammonia as a catalyst [93]. He could obtain particles with a size ranging between 50 nm and 1 μm by varying the type of the alcohol and the silicon alkoxide precursor (tetraalkyl orthosilicates). Stöber's findings indicate that ammonia serves as the catalyst responsible for the spherical morphology of nanoparticles. Larger particles are achieved with increased ammonia concentration, while the rate of condensation is predominantly influenced by the water content in the system. Subsequently, numerous researchers expressed their interest in understanding the kinetics governing nucleation and growth mechanisms, that play a key role in determining the uniformity of silica NPs. Several studies were reported in modelling these mechanisms [94 - 100]. Based on these models, two nucleation and growth mechanisms can be distinguished:

- **The monomer addition model:** This model was proposed by Matsoukas and Gulari [100] and is consistent with the LaMer's model [101], a widely used theoretical model that describes the process of nucleation and growth in chemical reactions, particularly in the context of colloidal chemistry and nanoparticle synthesis. LaMer and Dinegar [101] suggest that the formation of particles occurs in a brief period of homogenous nucleation, when monomers reach a critical limiting super-saturation concentration (**Fig II.5**), considered as the nucleation threshold. The consumption of these monomers results in their concentration decrease below the saturation limit, and the growth of nuclei starts with a "self-sharpening" mechanism, through the diffusion of molecules to the surface of particles, with the growth of relatively small particles being favored over the large ones. In the case of silica nanoparticles synthesis, the use of ammonia as a catalyst both increases the hydrolysis rate and the solution pH, resulting in negatively charged particles' surfaces ($Si\text{-}O^-$ groups), which stabilize them against aggregation. Their growth is progressively achieved by a monomer addition mechanism. Here, Matsoukas and Gulari suggest that the nucleation is initiated by the condensation of at least two hydrolyzed silicon alkoxides. Nucleation is therefore governed by the hydrolysis rate of monomers, and has a key role in determining the final size of silica nanoparticles.

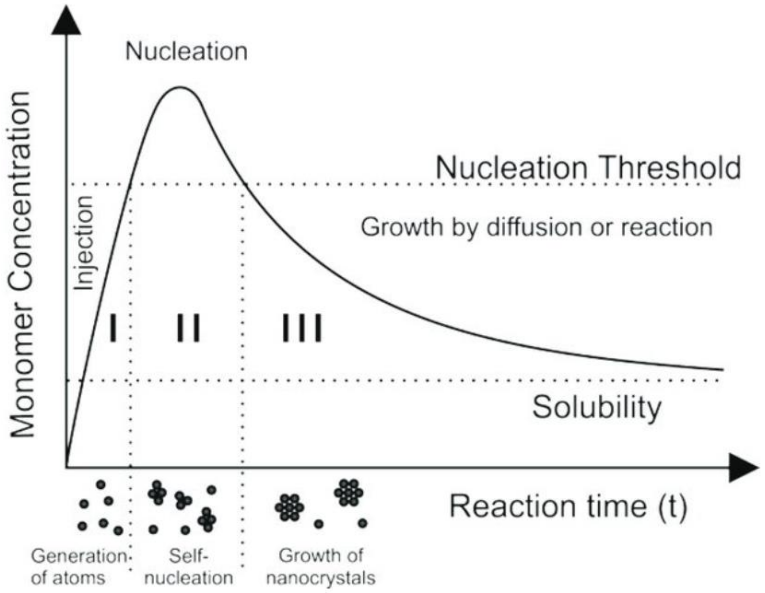

Figure II.5 *LaMer diagram describing nucleation and growth of particles as a function of time and concentration.*

- **Aggregative growth model:** This model was proposed by G.H. Bogush and C.F. Zukoski [96]. Here the formation of monodisperse silica NPs goes through two stages, the first is the nucleation of small unstable primary particles in the supersaturated solution, and second is the fast aggregation of these particles to form stable ones.

Other studies focused on finding the optimal conditions to achieve monodisperse silica NPs [102 - 104], where the impact of each Stöber reaction component on the hydrolysis and condensation rates is depicted through the variation of the water/precursor ratio, ammonia and ethanol concentrations. The variation of the size and the uniformity of silica nanoparticles based on these parameters is then examined. The findings from these studies on the influence of individual components on NPs size and dispersity are often not consistently aligned. This can be attributed to the difference in the syntheses conditions, including hydrodynamic factors such as the stirring rate, the type and the size of the stirrer and vessels, affecting hydrolysis and condensation kinetics as well, and usually not described in literature.

2.2.2 From inorganic to hybrid silica materials

Modern sol-gel technology has expanded to the development of glass materials with very fine and performant intrinsic properties to meet different industrial needs, through novel hybrid silica precursors containing one or more organic moieties. In 1985, Schmidt [105] brought in a new family of organically modified silicate referred to as "ORMOSILs" with the idea to create composites on the atomic scale. ORMOSILs consist of silica precursors with one or more hydrolysable ethoxy groups (Si-OEt) that are replaced by an organic moiety linked to the Si atom. The number *n* of organic *R* linked to the Si atom can range from 1 to 3, and reduces the number *f* of hydrolysable ethoxy groups (Si-OEt) (**Fig II.6**) serving as a Si-O-Si network forming.

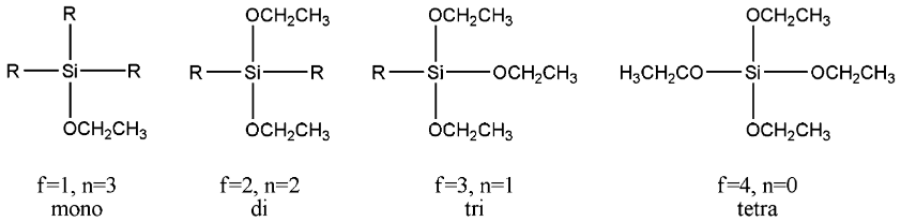

Figure II.6 *Types of ORMOSILs functionalization, starting from a tetra silicon alkoxide (n=0) with no functional organic group R [87].*

The emergence of ORMOSILs was the starting point for the development of organic-inorganic hybrid compounds called "Silsesquioxanes" containing pendant organic groups *R*, thus providing versatile chemistry by enabling a wide range of possible functionalization, within a silica network with various structures (**Fig II.7**) [106, 107].

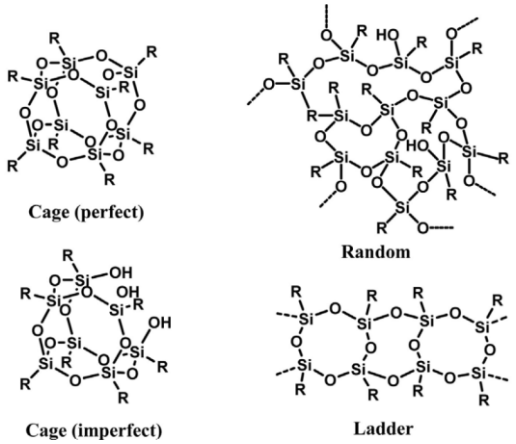

Figure II.7 *Different structures of silsesquioxanes [106].*

Later, bridged organosilane compounds were developed (**Fig II.8**). They are composed of an organic moiety attached to two or more trialkoxy silyl groups through a non-hydrolysable Si-C bond, thus bridging between at least two Si atoms. The incorporation of molecular blocks through bridging organosilanes was employed the first time by D. A. Loy and Kenneth J. Shea in 1992 [108] to engineer the structural properties of silica-based material at the molecular scale. For example, porous silica materials like xerogels with very high specific surface area can be obtained by oxidation to selectively remove the organic part of the hybrid silica matrix, or by the chemical cleavage of Si-C bond with fluoride anion as reported by M. Wong Chi Man *et al*. [109]. The flexibility of the molecular blocks could be varied by changing the organic bridging groups, and can be used to control the porosity of the amorphous silica networks [110]. Other properties can be tuned depending on the organic moiety, like the hydrophobicity, the mechanical properties, the hydrothermal stability and the morphology [111].

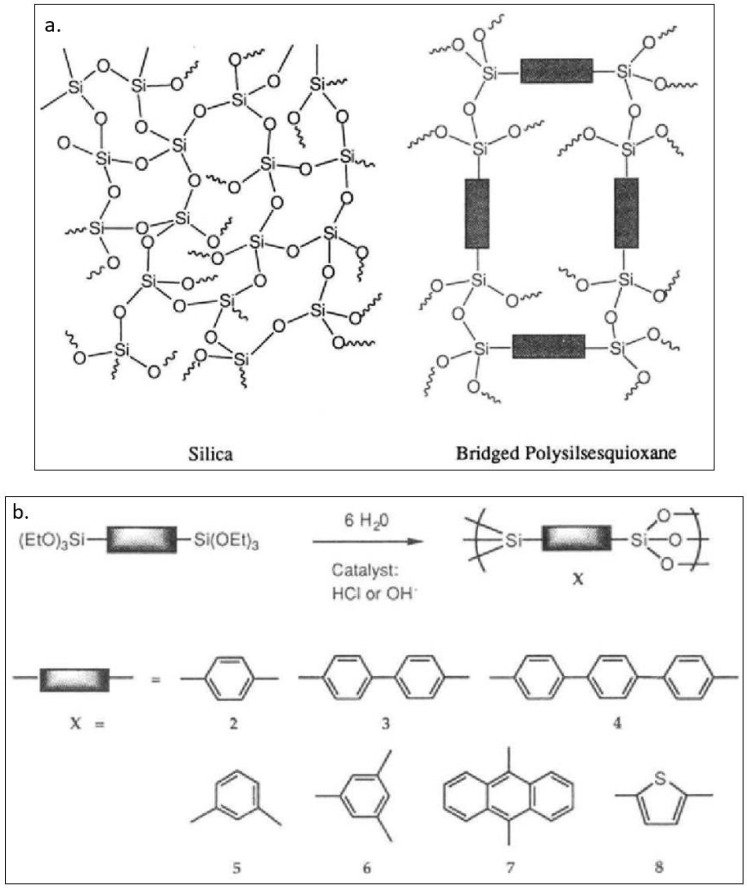

Figure II.8 a. *Difference between a pure silica network and bridged polysilsesquioxane.*
b. *Diverse arylene-bridged organosilanes used to prepare hybrid xerogels [108].*

One of the first bridged silsesquioxanes was prepared using arylene-bridged organsilane precursors known for their rigidity, a good thermal stability and very high specific surface area

arising from the presence of pores with size ranging between 10 and 50 Å. Bridged silsesquioxanes can be obtained in mild conditions by simply using a sol-gel reaction to hydrolyze and polycondense arylene-bridged monomers, under acidic, basic or nucleophilic catalysis (**Fig II.8.b**). To date, 1,4-bis(triethoxysilyl)benzene (BTEB) firstly reported par D.A. Loy and K. J. Shea [108, 112], is the most commonly used arylene-bridged organosilane. It is obtained by the Barbier-Grignard reaction using 1,4-dibromobenzene, magnesium, TEOS an THF as solvent (**Fig II.9**). After work-up, the product is purified by distillation.

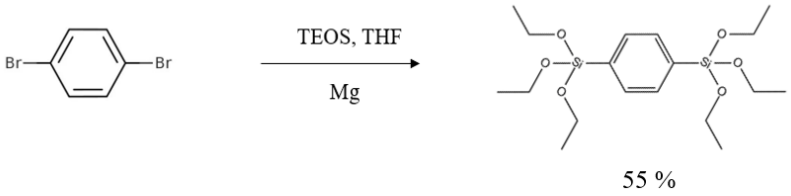

Figure II.9 *Synthesis reaction of BTEB precursor.*

Aliphatic bridged organosilane monomer precursors with alkylene bridging moieties were reported in 1993 by K. J. Shea and H. W. Oviatt. They are prepared by hydrosilylation of alkyldienes with triethoxysilane using Speier's catalyst (H_2PtCl_6) in isopropanol or ethanol. One of the most popular alkylene-bridged organosilane is the ethane-bridged one, (1,2-bis(triethoxysilyl)ethane) denoted BTSE and is also commercially available as BTEB. Ethenylene-bridged organosilane (1,2-bis(triethoxysilyl)ethene) denoted BTSEENE is also a widely used precursor and is commercially available as a mixed 80:20 E : Z isomers. In this case, the pure E-isomer can be prepared following the methathesis reaction of vinyltriethoxysilane (VTSE) with Grubbs' first-generation catalyst as reported by P. Van Der Voort in 2009.

2.2.3 Mesostructured organic-inorganic hybrid materials

2.2.3.1 Development

The growing interest around porous materials with a high specific surface area, and with well-defined and uniform pore size distribution for various application like adsorption, catalysis, gas storage etc, led to the development of mesoporous silica material with a pore size exceeding the maximum pore size of zeolites for instance (15 Å). One of the first mesoporous silicate materials figure in the work of K. Kuroda, Chuzo Kato and co-workers (1990) [113] who

synthesized porous (2-4nm) single layered polysilicate kanemite in an alkyltrimethylammonium chloride solution and showed that the pore size can be varied by changing the alkyl chain length of the alkyltrimethylammonium ion. Later, mesoporous silica material famously known as the MCM-41, were pioneered in 1992 by J. S. Beck et *al.* [114] working for the Mobil Oil company, knowing that an older procedure patented in 1971 by V. Chiola and co-workers lead previously to materials that are similar to MCM-41 [115] (*V. Chiola, J.E. Ritsko, C.D. Vanderpool, US Patent 3 556 725, 1971*). MCM-41 are characterized by highly ordered mesoporous structure arising from the use of quaternary ammonium surfactant aggregates like cetyltrimethylammonium bromide (CTAB) acting as a structure directing agent (SDA) and co-assembling with silicate species in solution. The pore size is dictated by the length of the alkyl chain, which is why surfactant with long alkyl chains (n> 8) were privileged in order to obtain mesopores, whereas the short alkyl chains only result in amorphous or zeolite-like materials. X-ray diffraction analysis is used to monitor the highly periodic MCM-41 materials exhibiting a diffraction pattern with peaks in the diffraction planes (100), (110) and (200), characteristic of a hexagonal arrangement of mesopores with a space group *p6mm*, and a unit cell parameter that can be deduced by $a= 2d_{100}/\sqrt{3}$.

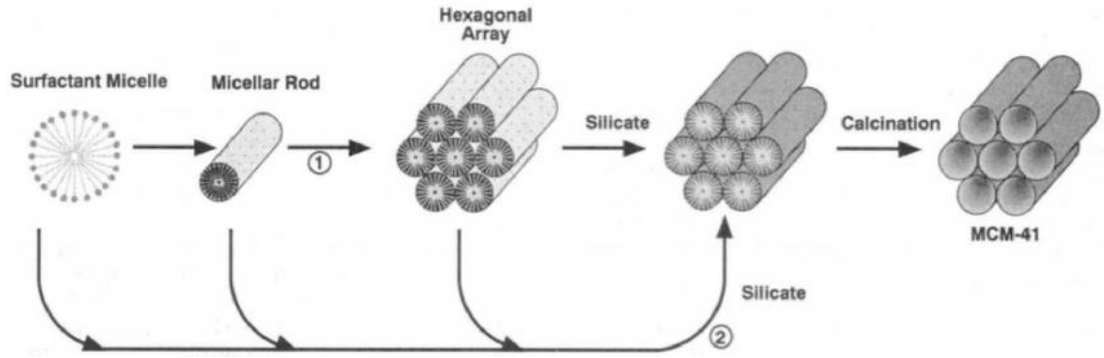

Figure II.10 *Schematic representation of mechanism of MCM-41 formation using surfactant aggregates suggested J. S. Beck et al [114].*

After their discovery, the mechanism of MCM-41 formation was not straightforwardly clear-cut. At that time, two mechanisms were suggested (i) the formation of the hexagonal array of micellar rods precedes the formation of silica around the template, which was described as a true liquid crystal mechanism (**Fig II.10**), (ii) the arrangement of micelles is conditioned by the formation of silicates, described as a cooperative liquid crystal mechanism. The latter was introduced by G. D. Stucky *et al.* [116] and was explored in several other works [117, 118]. J. C. Vartuli et *al.* [119], for instance, demonstrated that the cubic structure MCM-48, and the lamellar structure MCM-50, both belonging to the same family of mesoporous silica (M41S),

were obtained by varying the ratio of surfactant to silica concentration (**Fig II.11**). Nevertheless, since then, the intricacies of such complex mechanism have remained a subject of ongoing debate. Recently, X. Cattoën *et al.* [120] developed a new experimental approach to address this challenge, by coupling pH measurement with light diffusion. The findings indicate that the precursor monomers undergo initial hydrolysis and adsorption on the surface of spherical micelles due to strong electrostatic forces. Subsequently, they undergo a rapid transformation into rod-like micelles at a higher hydrolysis rate. This transformation is followed by the aggregation of micelles and the condensation of neighboring silanols.

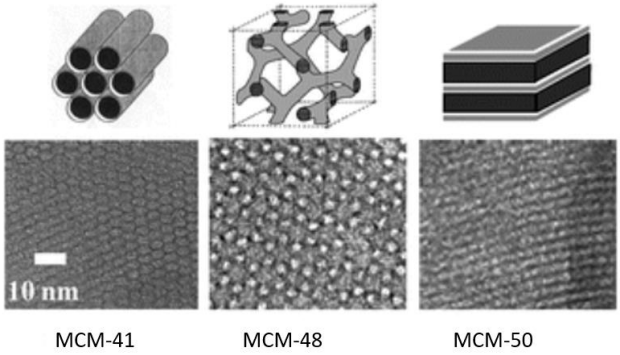

Figure II.11 *The M41S family of mesoporous silica [121].*

The cooperative mechanism is only valid in the case of negatively charged silica species co-assembling with a positively quaternary ammonium long chain surfactant, this synthetic pathway is termed S^-I^+. When using acidic catalysis, silica species become positively charged, the manifestation of the cooperative liquid crystal mechanism through electrostatic integration with a cationic ion requires the presence of a mediator anion X^- ($S^+ X^- I^+$). Inversely, when an anionic surfactant is used in basic conditions, a mediator cation X^+ is required ($S^- X^+ I^-$). In case of the use of nonionic surfactant like polymers, the cooperative interaction between silica and the surfactant can still happen through hydrogen bonds [122, 123].

MCM-41 materials were succeeded by the introduction of a new material in the family of mesoporous silica, known as the SBA-15 reported by G. D. Stucky and coworkers [124]. It has the unique feature of 2D hexagonal periodically arranged large mesopores with a unit cell of 11.8 nm, arising from the use of P123 block copolymer as an SDA co-assembling with TEOS in acidic conditions.

The triumph of the MCM-41 family of materials served as a great inspiration for the elaboration of Periodic Mesoporous Organosilica (PMO). In 1999, three research groups independently achieved the synthesis of PMO using bridged organosilane compounds described in the previous section. Inagaki *et al.* [125] prepared a highly ordered PMO material using ethane-bridged organosilane precursors with octadecyltrimethylammonium chloride (ODTMA) as SDA in basic conditions. Simultaneously, G. A. Ozin *et al.* [126] used ethene-bridged organosilane in the presence of CTAB as SDA to achieve the PMO in basic conditions as well. Likewise, A. Stein [127] achieved the same material using the same conditions as Ozin's.

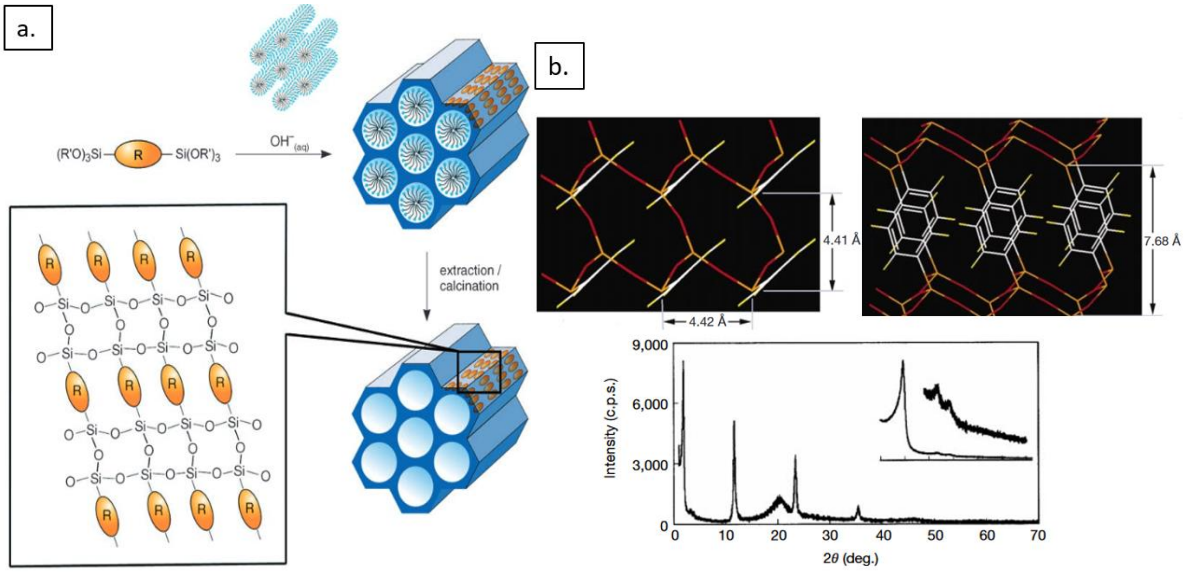

Figure II.12 a. *Schematic representation of the PMO structure with a crystal-like wall structure [123].* ***b.*** *Structural model of molecular periodicity promoted by benzene aromatic ring π-π stacking, and the corresponding d-spacings calculated from the X-ray pattern [128].*

In 2002, Inagaki and co-coworkers reported PMO materials that not only exhibit well periodically ordered mesopores, but also a molecular-scale periodicity resulting in a crystal-like wall structure (**Fig II.12.a**). This was demonstrated by X-ray diffraction with the presence of additional sharps peaks in the intermediate scattering angle, with d-spacing of 7.6, 3.8 and 2.5 Å (**Fig II.12.b**) corresponding to the molecular periodicity promoted by the π-π stacking of the phenylene-bridged organosilane employed as a precursor [128].

2.2.3.2 Surfactants as structure directing agents (SDA): Definition and properties

The Mobil Oil company's pioneering use of a surfactant, referred to as a "crystal liquid template" to synthesize the first mesoporous silica material [114], marked a groundbreaking development in the domain of porous materials. Since that, surfactants have been extensively used as soft templates to obtain materials with highly ordered and narrow sized-porosity. Indeed, they possess the unique capability to self-assemble in an organized manner within a liquid medium, under specific chemical and thermodynamic conditions, in a similar way to that of a solid crystal. Their variety enabled the development of multiple strategies to shape the pore size and structure.

a) Classification

Surfactant are amphiphilic chemical compounds composed of a hydrophilic (polar) head group soluble in aqueous media, and a hydrophobic (non-polar) tail made of a long hydrocarbon chain. Surfactant can be classified as ionic when the hydrophilic head is charged, and non-ionic when it is not charged. Ionic surfactants include cationic with a positively charged head, like quaternary ammonium surfactants comprising cetyltrimethylammonium bromide (CTAB), anionic surfactants with a negatively charged head, and zwitterionic surfactants (positive and negative charges). Non-ionic surfactants are generally block copolymers consisting of two or more alternating polymer blocks bonded in a linear or branched way. These blocks can have distinct chemical and physical properties (**Fig II.13**).

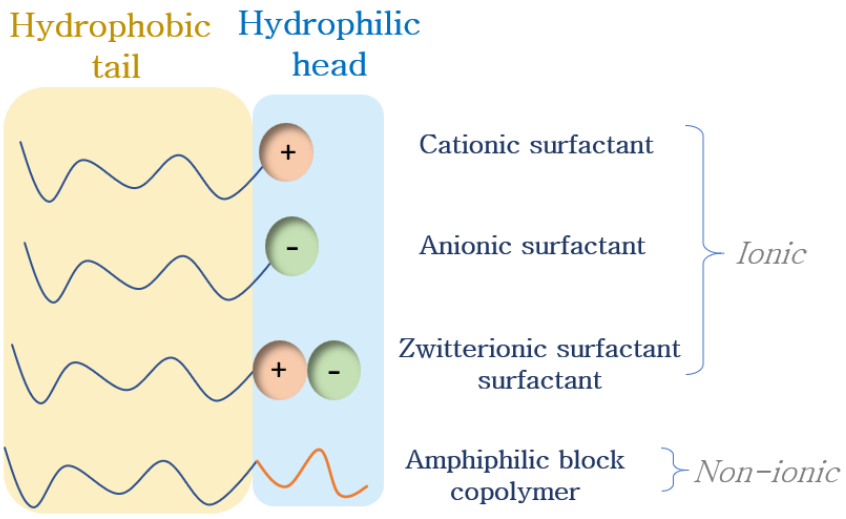

Figure II.13 *Classification of surfactants.*

b) The Critical Micelle Concentration (CMC)

Surfactants have the particularity to self-assemble in a way to form well-arranged aggregates in a solution, driven by the purpose to minimize the interfacial tension between the hydrophilic and hydrophobic regions. When present in small concentrations in water, the surface tension is high and surfactant molecule are situated at the interface between water and air. These molecules begin to self-assemble only when they reach a concentration above which the interface between water and air is saturated. This concentration is known as the Critical Micelle Concentration (CMC). The aggregation of surfactant molecules in the form of micelles result in the decrease of the surface free energy γ because the contact between hydrophobic alkyl chains and water is reduced (**Fig II.14**).

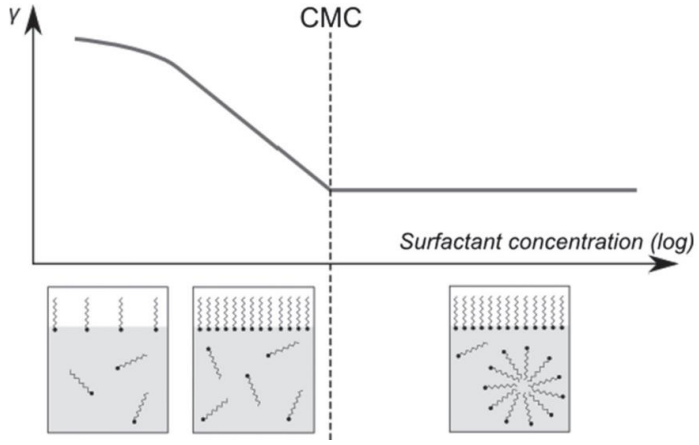

Figure II.14 *Schematic representation of the evolution of surface tension γ as a function of surfactant molecules concentration in the solution [129].*

The geometry of micelles can be found in various shapes based on how the interactions occur at the headgroup and the hydrocarbon chain according to Israelachvili [130]. These interactions are described by the packing parameter denoted *P*, reflecting the packing geometry of micelles based on the curvature of surfactant molecules, and which can be used to predict the shape, the size and the stability of micelles (**Fig II.15**). It is a dimensionless value estimated based on the surface of the headgroup a_0, the volume of the hydrocarbon chain *v* and its critical length l_c with the following equation (II.1):

$$P = \frac{v}{a_0 \, l_c} \qquad \text{(II.1)}$$

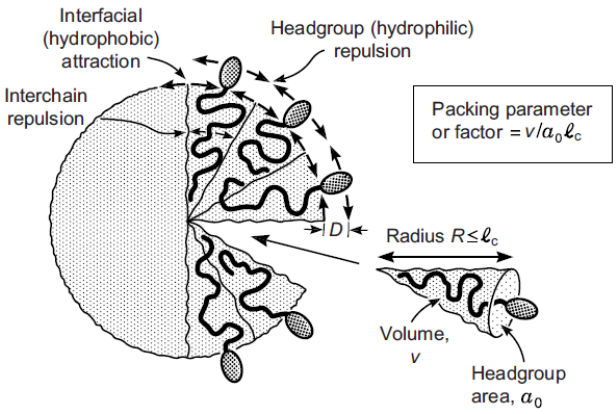

Figure II.15 *Surfactant molecules features and the possible interactions between them determining micelles geometry.*

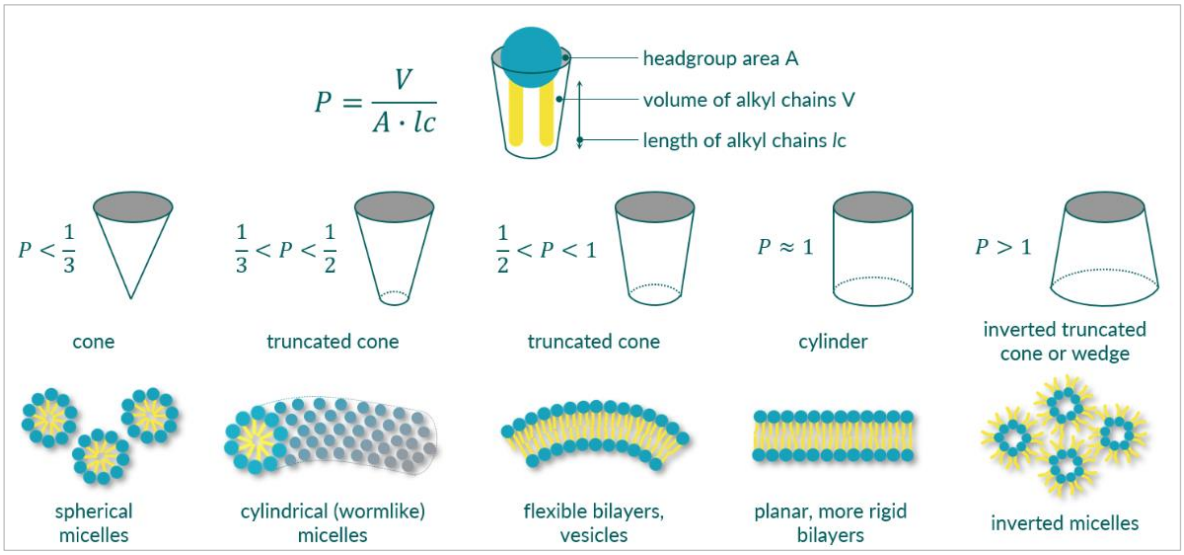

Figure II.16 *Packing parameter ranges and the corresponding micellar shapes*[1].

2.2.4 From bulk to Periodic Mesoporous Organosilica (PMO) nanoparticles

In the recent decades, the use of nanotechnology has found application in various domains dealing with very fine processes like the controlled drug release and cellular delivery in biomedicine, energy storage, catalysis and adsorption, miniaturization of electronic devices etc. The outstanding properties exhibited by the periodic mesoporous silica and hybrid silica motivated the development of the nanoscale colloidal version of these materials by the synthesis of the mesoporous silica nanoparticles (MSN) and PMO NPs with well-defined size, morphologies and tunable mesopores size and organization. These nanomaterials hold

[1] The various phospholipid aggregates - Phospholipid Research Center (phospholipid-research-center.com)

significant appeal due to their exceptional properties, including the high surface-to-volume ratio, versatility, biocompatibility and physiochemical stability [131 - 133].

Ozin and co-workers [134] were the first to explore the elaboration of mesoporous silica materials in various geometrical shapes. The first submicrometric spherical mesoporous silica nanoparticles type MCM-41 were synthesize by K. K. Unge *et al.* [135] who modified the Stöber process used to prepare monodisperse colloidal dense silica particles, simply by adding a cationic surfactant to the sol-gel reaction and obtained MSN with size ranging from 400 nm to 1100 nm. Smaller nanometric sizes were reported afterwards, which were prepared in very diluted conditions and where the size and monodispersity of the MSN could be controlled by varying the pH and the molar ratio of reactants [136 - 138].

More recently, greater attention was directed toward the synthesis of PMO NPs [139]. These nanomaterials possess superior properties compared to those of MSN, mainly their enhanced biocompatibility and biodegradability, an outstanding versality enabling numerous functionalization, and tunable hydrophobicity [140 - 142]. PMO NPs can be synthesized following the same MSN synthesis pathway, only the inorganic silica source is replaced by a bridged organosilane precursor. One of the commonly tackled challenges in the synthesis of PMO NPs is the precise control of pore structure and NP size [143] in order to align with biomedical requirements, which includes adhering to defined maximum NP size for cellular uptake [144, 145].

2.2.5 Hollow Periodic Mesoporous Organo-silica Nanoparticles (HPMO-NPs)

Hollow NPs are exceptionally attractive as nanoplatforms with their notable storage capacity, thanks to the core cavity which make them ideal to be used as nanocontainers. Early works reported on such nanoplatform were especially dedicated to metallic and metal oxides shells [146 - 149]. In most of cases, silica NPs or polystyrene were employed as hard templates and subsequently etched by HF and THF respectively to form the hollow structure.

The synthesis of the first hollow periodic mesoporous organo-silica NPs can be considered as fortuitous. M. Fröba and co-workers [150] synthesized a composite core/shell system, with the core made of silica NPs prepared by Stöber process, on which, in one sample a periodic

mesoporous silica shell was deposited using TEOS as an inorganic silica source and CTAB as SDA, and in the other sample a PMO shell is deposited using phenylene-bridged organosilane as a precursor and CTAB. In this work, the effect of the synthetic conditions was studied by varying the reaction temperature from room temperature to 100 °C. Interestingly, for the silica/PMO core/shell NPs synthesized at 60 °C, 80 °C and 100 °C, a partial shrinkage of the silica core was observed which started at the interface between the PMO and silica, resulting in the formation of a void space. Whereas for the silica/mesoporous silica NPs, the silica core was intact, however, the surface of the NPs became less smooth (**Fig II.17**).

The fact that the reduction of the silica core volume only occurred in the case of silica/PMO system only proves that the PMO shell exhibits better stability compared to silica under high-temperature and basic conditions. Consequently, only the core silica is susceptible to the hydrolysis, which is why it is selectively targeted. For the silica/mesoporous silica system, the mesoporous silica shell was clearly weakened under the same conditions, which therefore modified the surface texture prior to reaching the core silica.

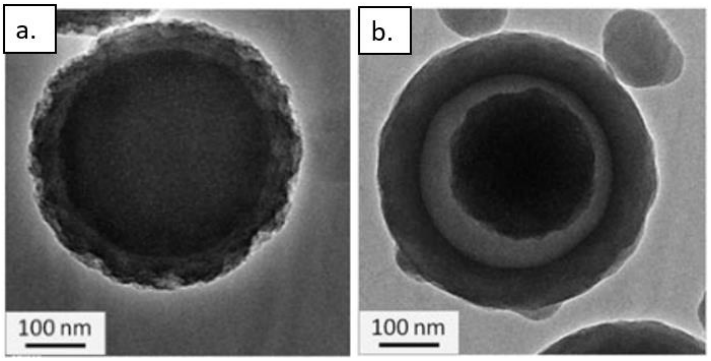

Figure II.17 a. *Core/shell NPs synthesized at 100 °C composed both of a pure silica core, a mesoporous silica shell.* ***b.*** *and mesoporous organosilica shell [150].*

This inspired the fabrication of hollow periodic mesoporous organosilica NPs (HPMO) [151], hollow mesoporous organosilica NPs (HMON) [152] prepared using more than one bi-silylated precursor or the hollow mesoporous silica NPs (HMSN) [153] (**Fig II.18**). Here the silica hard template can also be used to support the PMO layer with a chemical nature closely resembling that of inorganic silica. The hard template is selectively etched using an alkaline hot water etching strategy [152]. The hydrolysis of the hybrid silica network by nucleophilic attack of OH^- is prevented by the steric hindrance of the organic moiety as suggested by M. Fröba *et al.* [150], or by the abundance of Si-C bonds in the PMO network that helps to stabilize the shell [151].

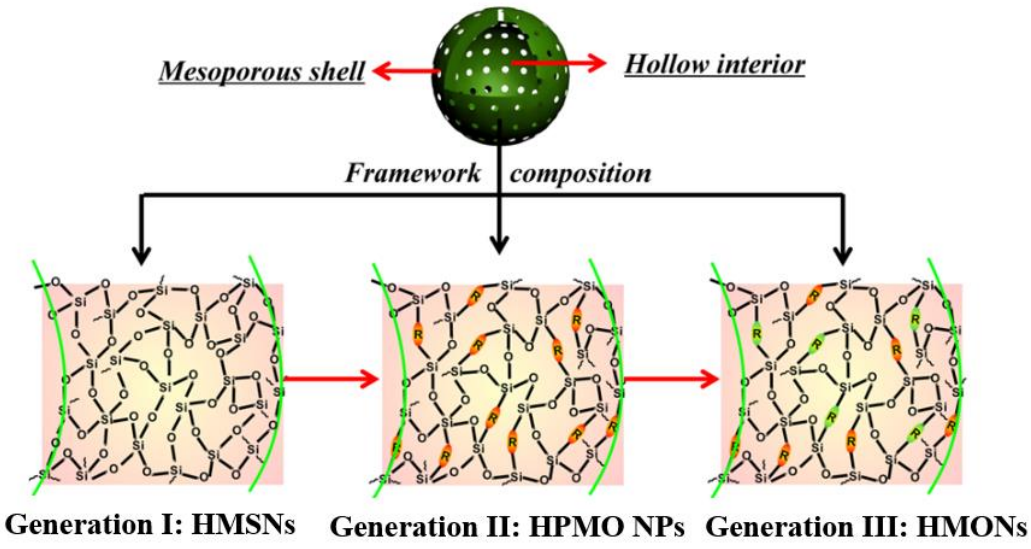

Figure II.18 *Schematic representation of the different types of silica/hybrid-silica based hollow NPs [152].*

Other studies suggest that this selective etching is supported by the presence of the cationic surfactant [154], which plays a role in the stabilization of the mesoporous silica shell and also promote the acceleration process of the silica core etching. The alkaline etching agent usually employed is Na_2CO_3 solution rather than HF or NaOH solution which can be too aggressive and result in NPs collapsing if the etching is not well controlled. Only few works were reported on the size tuning of hollow NPs, targeting the synthesis of NPs smaller than 50 nm which are the most challenging to achieve. These NPs are mainly considered HMONs (**Fig II.18**), because either there is no use of surfactant forming the liquid crystal template to obtain uniform mesopores with a well-defined size [155], or TEOS is used as a co-precursor with the bridged organosilane to favor the deposition on the inorganic silica shell [156]. In their work, W. Fan *et al.* [156] synthesized mesoporous silica by the co-assembly of TEOS with a surfactant (CTAC) which is used as a hard template, then a mixture of BTEB and TEOS are subsequently added to form the mesoporous organosilica in the same pot. This means that the thickness of the shell is limited by the amount of surfactant that did not contribute to the formation of the mesoporous silica seeds, and cannot be controlled separately.

The deposition of the layer of PMO by the co-assembly of a bridged organosilane with SDA remains indeed very challenging. Usually, a spontaneous nucleation occurs and the consumption of monomers results in the formation of independent organosilica NPs instead of

being used in building the shell. T. Okubo *et al.* [155] encountered this issue even when following a surfactant-free synthesis, and suggest that the amount of the precursor, even when used in excess, is not responsible of the formation of additional organosilica NPs. They suggest that the available surface of the hard template plays a key role in controlling the hydrolysis and condensation rates of precursor's monomers. The hydrolysis rate of monomers exceeds the co-condensation rate between precursor monomers and silanols groups on the surface of silica hard template, when the available surface area is low. Consequently, the spontaneous nucleation and growth of independent organosilica NPs is initiated when the solution is saturated with hydrolyzed monomers.

In this work, we aim to study systematically the relationship between the structure of PMO shell and the size of the HPMO NPs. For this matter, we were interested in tailoring the size of HPMO NPs in a range between ~ 50 and 500 nm. The size tuning challenge is addressed and the synthesis protocol is developed to achieve uniform small sized-HPMO NPs, using a single bridged-organosilane co-assembling with a surfactant (Generation II, ***Fig II.18****). The capacity to tune the chemical composition of the shell is also demonstrated, and its impact on the PMO network structure will be discussed as well in the next section.*

2.3 Synthesis and study of a reference HPMO compound

2.3.1 Synthesis strategy of HPMO NPs

The strategy adopted to synthesize spherical and monodisperse HPMO NPs is based on the use of a hard template (introduced in the previous part). The multi-step chemical approach starts with the preparation of amorphous silica NPs acting as spherical hard templates. The PMO layer is then deposited on the silica hard template (**Fig II.19**). The affinity between the PMO and silica is one among several reasons to adopt silica hard template over the other strategies. The synthesis steps are further detailed in the following sections.

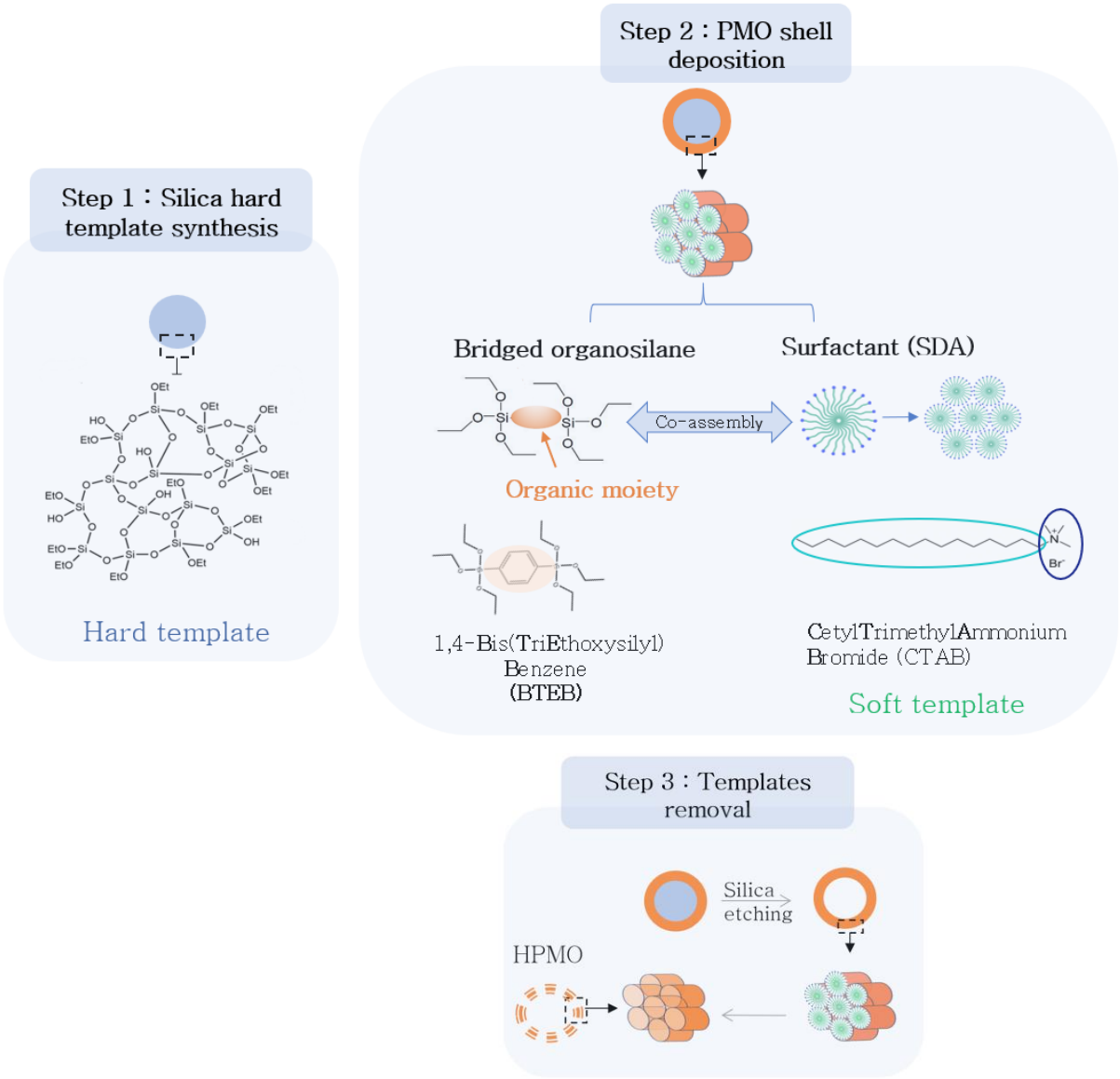

Figure II.19 *Schematic representation of the synthesis steps of HPMO NPs using dual templating strategy.*

2.3.2 Silica hard template synthesis

2.3.2.1 Synthesis

Silica seeds used as a hard template are synthesized by a sol-gel reaction is conducted under alkaline conditions with the use of NH_4OH as reaction catalyst and TEOS as the inorganic silica precursor (II.2) following the Stöber process [93], resulting in the formation of spherical amorphous and dense silica (**Fig II.19**).

$$Si(OC_2H_5)_4 + 2\,H_2O \xrightarrow{NH_4OH} SiO_2 + 4\,C_2H_5OH \qquad \text{(II.2)}$$

2.3.2.2 Morphology: Microscopy characterization

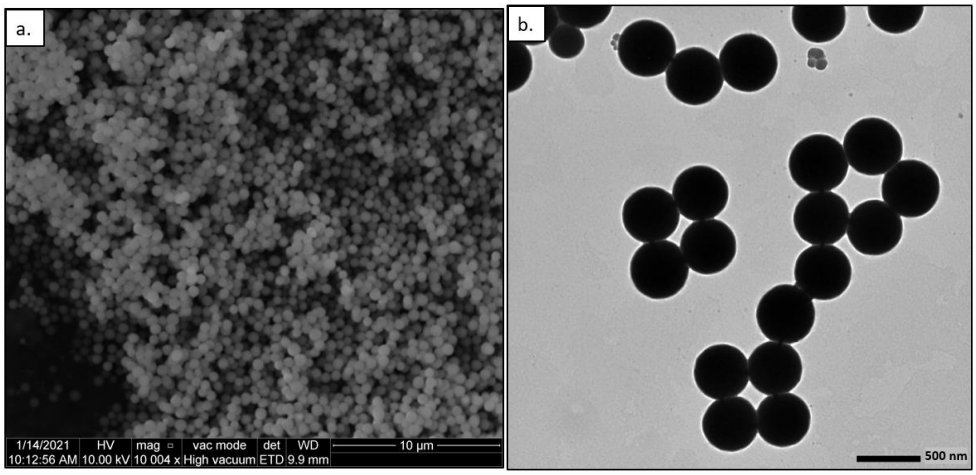

***Figure II.20 a**. SEM and **b.** TEM images of the reference silica NPs denoted SiO_2-HT.*

Fig II.20 displays the as-prepared silica NPs, subsequently used as a hard template for the deposition of the PMO shell. The large-scale SEM image (10 µm) of a dry powder of NPs shows remarkable monodisperse NPs. The high magnification images obtained by TEM is employed in Digimizer software to measure the mean diameter from an average of 100 NPs. The diameter of this reference hard template is 471 ± 18 nm.

2.3.2.3 Structural characterization

The structural characterization of the silica network composing the hard template NPs is studied using a FT-IR analysis in the mid-infrared region (MIR: 4000-400 cm^{-1}). Spectra are obtained after recording 64 scans, at room temperature using a Bruker Tensor 27 spectrometer equipped with a KBr beam splitter and DTGS pyroroelectric detector. KBr pellets are prepared using 0.5

mg of sample and 300 mg of KBr and are dried at 90 °C for 72 h to remove water absorbed in the KBr.

The recorded FT-IR spectrum of silica NPs is displayed in **Fig II.21** and assignments of the vibrational fingerprints are summarized in the **Table II.1**. The intense and sharp signal in the region between 1100 cm^{-1} and 1200 cm^{-1} is characteristic of polycondensed silica massive and is assigned to Si-O-Si antisymmetric stretching vibration (ν_{as} Si-O-Si). Symmetric Si-O-Si (ν_s Si-O-Si) are exhibited at 802 cm^{-1}. The Si-OH stretching (ν Si-OH) vibrations are found at 950 cm^{-1} and structural OH stretching vibrations ν(OH) are expected around 3400-3700 cm^{-1}, but difficult to discern because they are mixed with ν(OH) of water molecules. Small peaks in the 2800-3000 cm^{-1} range correspond to the C-H stretching vibrations (ν_s and ν_{as} and CH_2 /CH_3) of the ethoxy groups of TEOS, indicating that there is still some remaining non-hydrolyzed Si-OEt and non-polycondensed Si-OH in the silica network. Finally, the band at 468 cm^{-1} is assigned to Si-O-Si bending vibrations and the band at 580 cm^{-1} is of unknown origin (**Table II.1**).

Silica materials synthesized using the conditions described in *2.3.2.1*, and exhibiting these spectral features usually have an amorphous structure enriched with framework defects due to the abundance of Si-OH [157]. This structure is ideal for the etching step because it facilitates the diffusion of the etching agent and the breakage of Si-O-Si bonds [153].

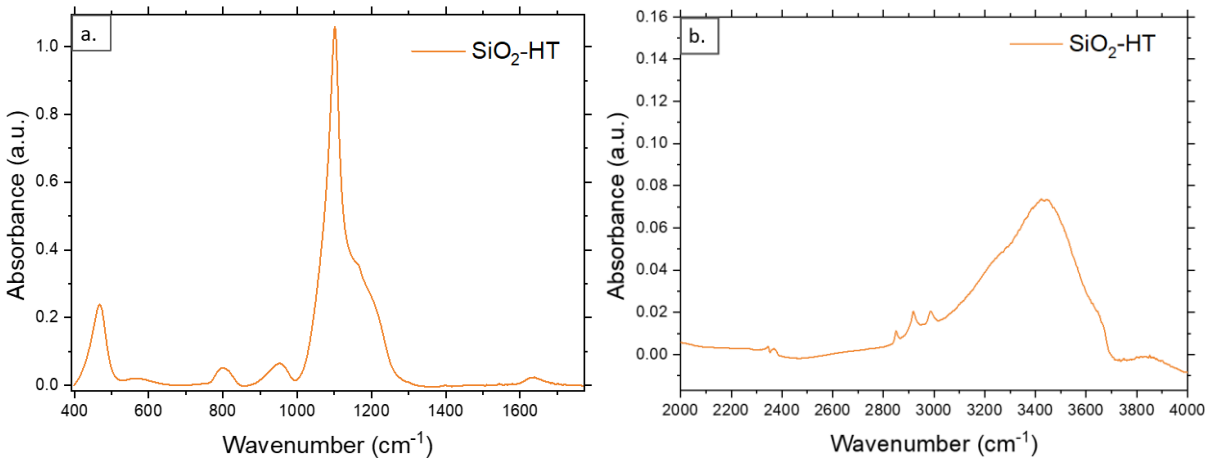

Figure II.21 a: *FT-IR spectrum of silica NPs hard template in the 400-1700 cm^{-1} region.* ***b:*** *FT-IR spectrum in the 2000-4000 cm^{-1} region.*

Vibrations	Attribution
468 cm^{-1}	Si-O-Si bending vibrations [158]
802 cm^{-1}	Si-O-Si symmetric stretching [158]
950 cm^{-1}	Si-OH stretching [158]
1100 cm^{-1}	Si-O-Si antisymmetric stretching [158]
1150-1160 cm^{-1}	Si-O-C stretching [159]
1633 cm^{-1}	H_2O bending
2800-3000 cm^{-1}	C-H antisymmetric stretching (CH_2, CH_3) [160]
3000-3500 cm^{-1}	O-H stretching of H_2O Si-OH [160]

Table II.1 *Detailed vibration attribution of silica NPs spectrum in* ***Fig II.21****.*

The surface charge of silica NPs is determined using Zeta potential analysis. The mean Zeta potential value is determined from the peak of the Gaussian fit curve in **Fig II.22** and corresponds to - 41.7 ± 0.05 mV which is in accordance with average reported values [161]. Thus, indicating that the as-prepared colloidal silica NPs have a negatively charged surface, which can be justified by the presence of $Si\text{-}O^-$ on the surface of these NPs. This aspect is important in the sense that it does not only maintain the dispersion of the NPs in the solvent through repulsion forces that prevent from the agglomeration of NPs, but the negative charges also play a key role to attract the positively charged headgroup of the cationic surfactant molecule (CTAB), which in its turn co-assemble with the bridged-organosilane precursors, thus favoring the deposition of the PMO layer as discussed in the next step.

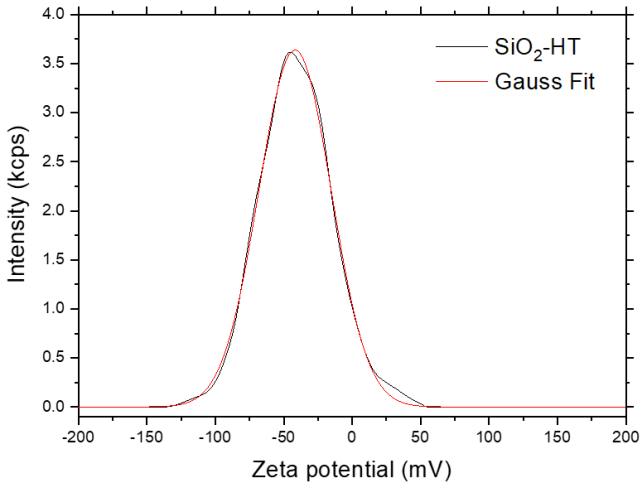

Figure II.22 *Zeta potential analysis of the colloidal suspension of the reference SiO_2-HT. The red curve corresponds to a Gaussian fit.*

2.3.3 PMO deposition

2.3.3.1 Synthesis

The PMO layer is formed by a classical sol-gel reaction in the presence of a cationic surfactant serving as a soft template (**Fig II.23**), also known as the structural directing agent (SDA). The latter forms micelles subsequently aggregating into cylinders while co-assembling with the bi-silylated precursor during its hydrolysis and polycondensation, thus leading to the formation of a mesostructured hybrid silica framework as previously discussed in the state of art.

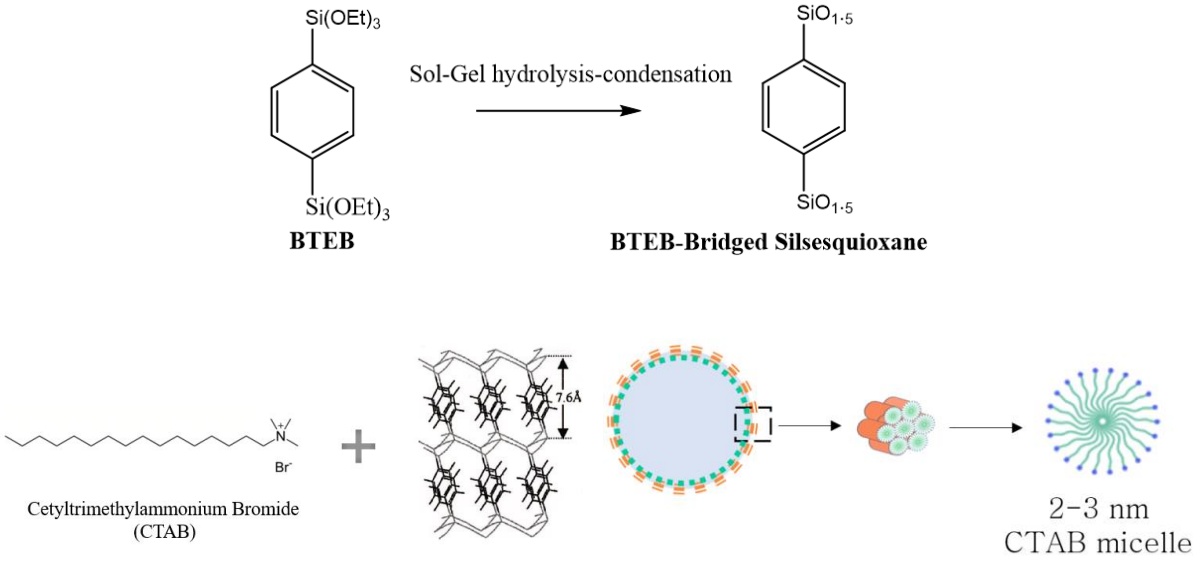

Figure II.23 *Schematic representation of the co-assembly between the cationic surfactant (CTAB) and the phenylene-bridged organosilane (BTEB) to form a periodic mesoporous organosilica (PMO) structure with a molecular-scale organization in the walls [162].*

2.3.3.2 Morphology: Microscopy characterization

Fig II.24 displays electron micrographs (SEM, TEM and HRTEM) of the silica NPs with the deposited PMO shell. The large-scale SEM image **(a)** show that the uniformity and monodispersity of the sample is maintained after the PMO deposition sol-gel reaction. The PMO shell can be distinguished from the silica hard template with the obvious contrast in the TEM image **(b)**, which can be justified by the porous nature of the shell, making it relatively less dense than the amorphous silica hard template. Based on this contrast, the PMO shell thickness can be also measured using Digimizer software, in addition to the total size of the core/shell structure. The mean diameter of SiO_2-PMO and shell thickness are estimated to 587

± 32 nm and 59 ± 8 nm respectively. The HRTEM image in **(c)** consists on a cross-section image of a single SiO_2-PMO NP obtained after slicing a solid resin containing the sample in the powder form. The image shows a clear difference between the silica hard template structure and the PMO shell. This suggest that the PMO layer deposited on the surface of dense and amorphous silica hard template is composed of radially oriented mesochannels. The latter are not always perfectly continuous all along the thickness of the shell.

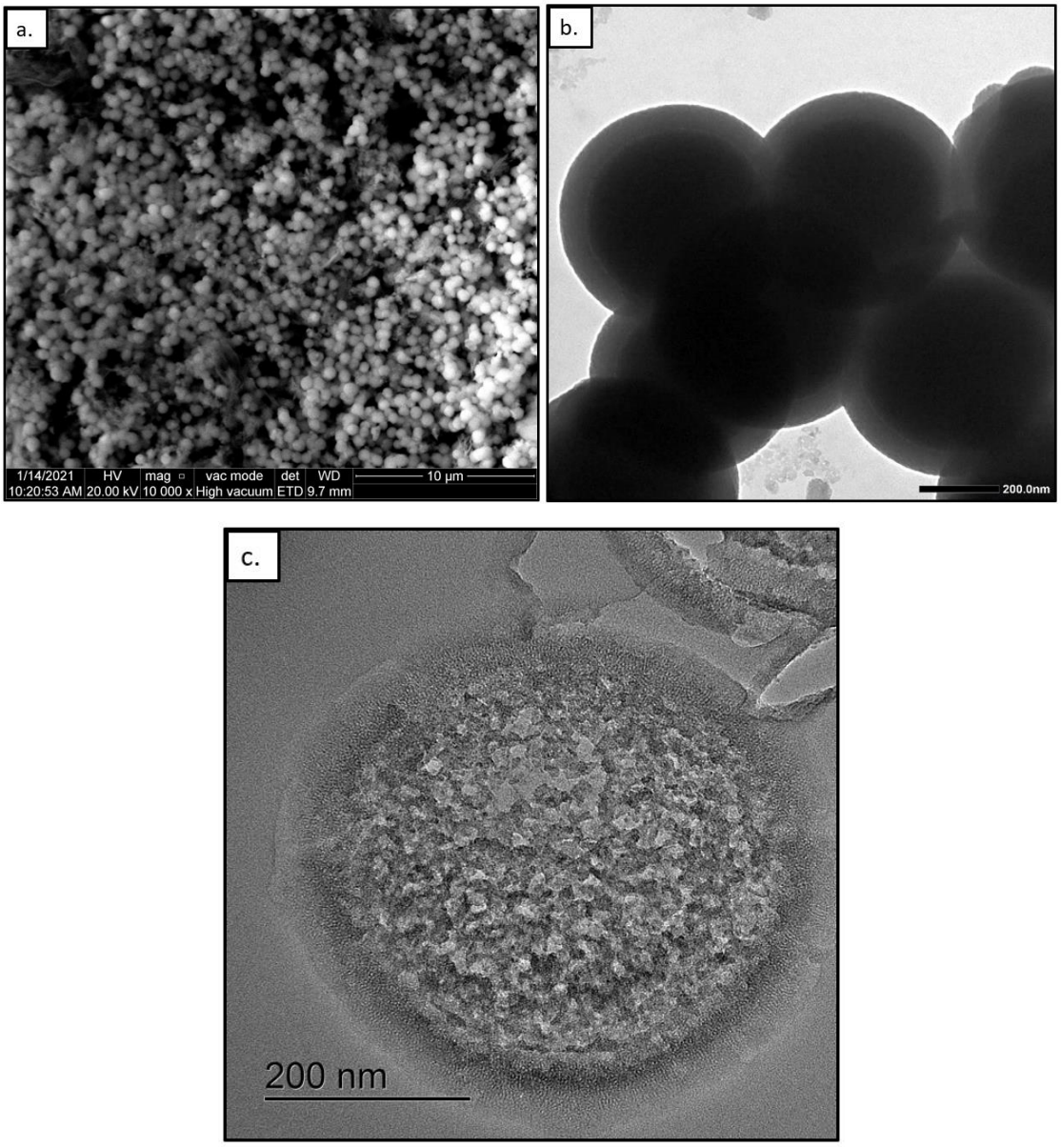

***Figure II.24 a**. SEM and **b.** TEM **c.** HRTEM micrograph of the reference silica NPs after the deposition of the PMO layer. This sample is denoted SiO_2-PMO.*

2.3.3.3 Structural and textural properties: FT-IR and N_2 sorption characterization

a) FT-IR analysis

In order to qualitatively evaluate the success of the elaboration process, spectra of the samples through the different stage of HPMO synthesis are recorded. FT-IR analysis is performed using the same experimental conditions described previously (*2.3.2.3*).

FT-IR spectrum is exhibited in the **Fig II.25**, and compared with the previous silica NPs spectrum. Spectra displayed in the range from 400 cm^{-1} to 1700 cm^{-1} **(Fig II.25.a)** are mainly dominated by silica features previously discussed, as expected. After coating with the PMO, the spectral contribution of silica decreases significantly. As a matter of fact, based on the sizes and morphologies obtained from TEM micrographs and considering the spherical geometry, one can roughly estimate the volume ratio of dense silica (56 %) and of PMO (44 %) for the sample SiO_2-PMO. The ratio of intensity between the two bands (Ir = I ν_{as} SiOSi/I δ SiOSi) is therefore divided by 2, and the ν_{as} Si-O-Si peak becomes broader than the SiO_2-HT one, suggesting the presence of polycondensed BTEB.

The SiO_2-PMO spectrum is also marked by the appearance of the band at 523 cm^{-1} corresponding to the aromatic ring deformation (δ ring) [163], characteristic of the phenylene-bridged organosilane (BTEB), thus indicating a successful deposition of the phenylene-bridged PMO layer.

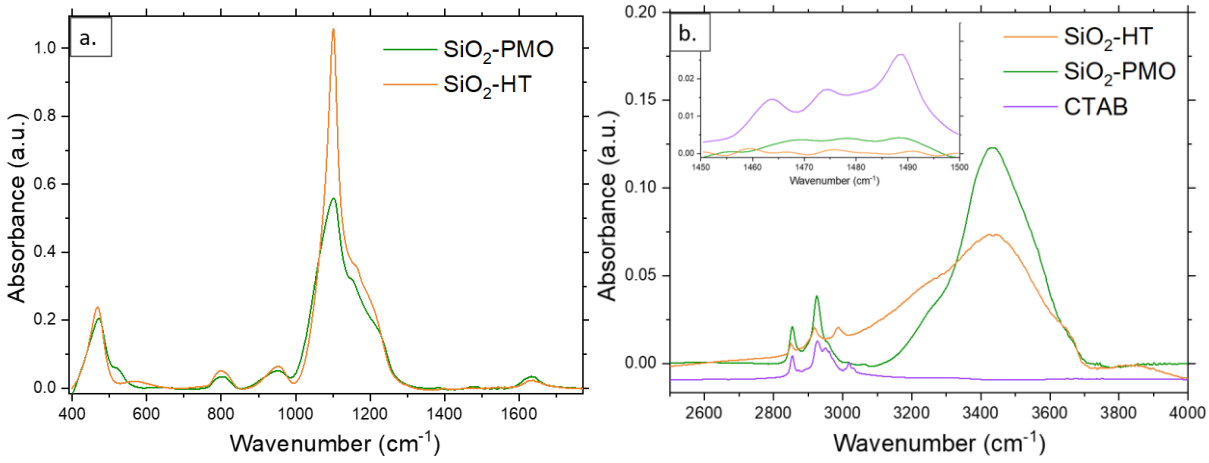

Figure II.25 a: *FT-IR spectra of the NPs before (SiO_2-HT) and after the deposition of the PMO layer (SiO_2-PMO) in the 400-1700 cm^{-1} region and* ***b:*** *in the 2000-4000 cm^{-1} region.*

Furthermore, spectra in **Fig II.25.b** show several peaks in the 2800-3000 cm^{-1} region arising from ν_{as} and ν_s C-H vibrations, signing the presence of CTAB. In the case of SiO_2-HT, the weak C-H vibration peaks are attributed, as mentioned before, to the CH_2 and CH_3 of the non-hydrolyzed ethoxy groups (Si-OEt). For the SiO_2-PMO sample, these vibrations arise from the long alkyl chain of the CTAB molecule as exhibited by the CTAB spectrum. The low intensity C-H modes are also found in the 1400-1500 cm^{-1} [164]. Therefore, the IR spectra demonstrate the presence of both BTEB and CTAB in the SiO_2-PMO NPs.

b) Textural analysis using nitrogen sorption at low temperature

The analysis of nitrogen physisorption isotherms is one interesting tool to characterize the textural properties of these HPMO NPs due to the porous nature of the hybrid silica shell. More details about the utilization of this technique are given in the next section *(2.3.4.3)*.

The sorption isotherm of the SiO_2-PMO sample displayed in **Fig.II.26** show very weak adsorption and form a flat plateau from the lowest relative pressures to gas saturation. The specific surface area estimated using the BET method is equal to 60 $m^2.\ g^{-1}$ that could be associated with the external surface of the large core/shell NPs. This value is clearly low for a material that is supposed to be mesoporous, as suggested by the HRTEM image in **Fig II.24.c**. In fact, this result confirms that the structured mesochannels are still filled with CTAB in this stage of the synthesis, thus preventing gas adsorption.

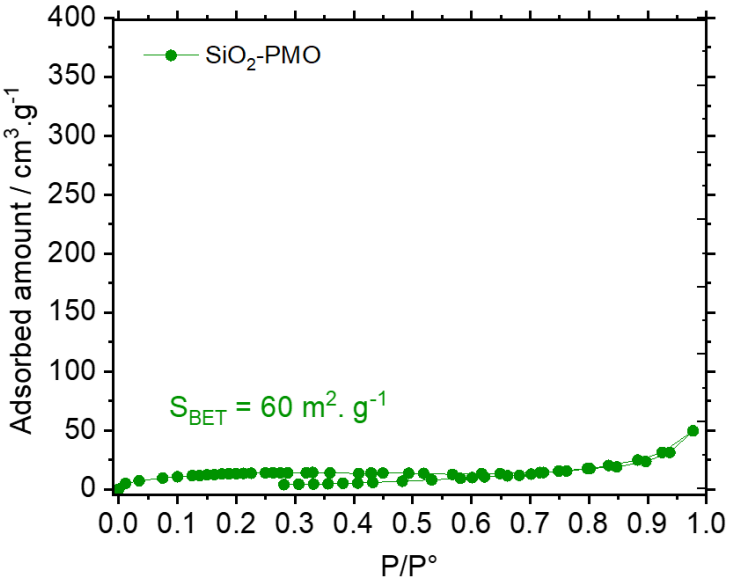

Figure II.26 *Nitrogen sorption isotherm of the SiO_2-PMO sample.*

2.3.4 Formation of HPMO NPs

2.3.4.1 Removal of the hard and the soft template

The hard template is removed by an alkaline hot water etching using a weak base like Na_2CO_3 where silica is dissolved by the coordination of OH^- with Si atoms, thus breaking Si-O-Si bonds [165]. Hollow structures are achieved after 1 h of etching in an aqueous solution of Na_2CO_3 at 80 °C, while the surfactant is still occupying the mesopores (**Fig II.27**). The etching time and the Na_2CO_3 concentration should be carefully controlled, otherwise, even the PMO shell may collapse.

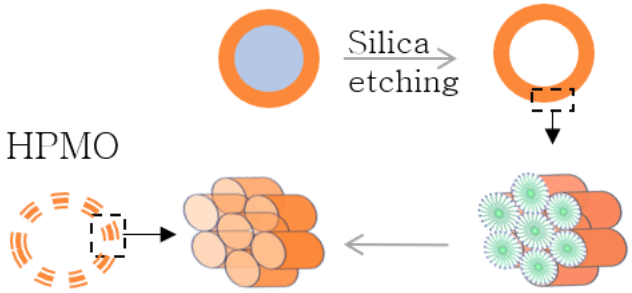

Figure II.27 *Schematic representation of hard and soft templates removal.*

The soft template (CTAB) removal is performed by an acid treatment using an ethanolic solution of hydrochloric acid under reflux. In fact, a cation exchange occurs between the cationic surfactant forming an ionic bond with $Si\text{-}O^-$ present in the PMO framework [166], and the H^+ of the hydrochloric acid [167, 168]. The mesopores are emptied in the final step of the elaboration process (**Fig II.27**). The following characterization are performed to validate this synthesis steps.

2.3.4.2 Morphology: Microscopy characterization

The successful etching of silica hard template can be clearly observed by the comparison of SEM images in **Fig II.28.a** and **Fig II.28.b.** Indeed, the difference in the core/shell contrast between SiO_2-PMO and HPMO-A is significant and indicates that the NPs interiors are actually hollow. Hollow structures are confirmed by TEM image in **Fig II.28.c**, and a mean diameter of 587 ± 32 nm can be deduced **Fig II.28.e**. The mesostructure of the PMO shell is clearly exhibited by the HRTEM image in **Fig II.28.d**, showing the inner side surface of the HPMO NP shell with stacked mesopores having a narrow size distribution.

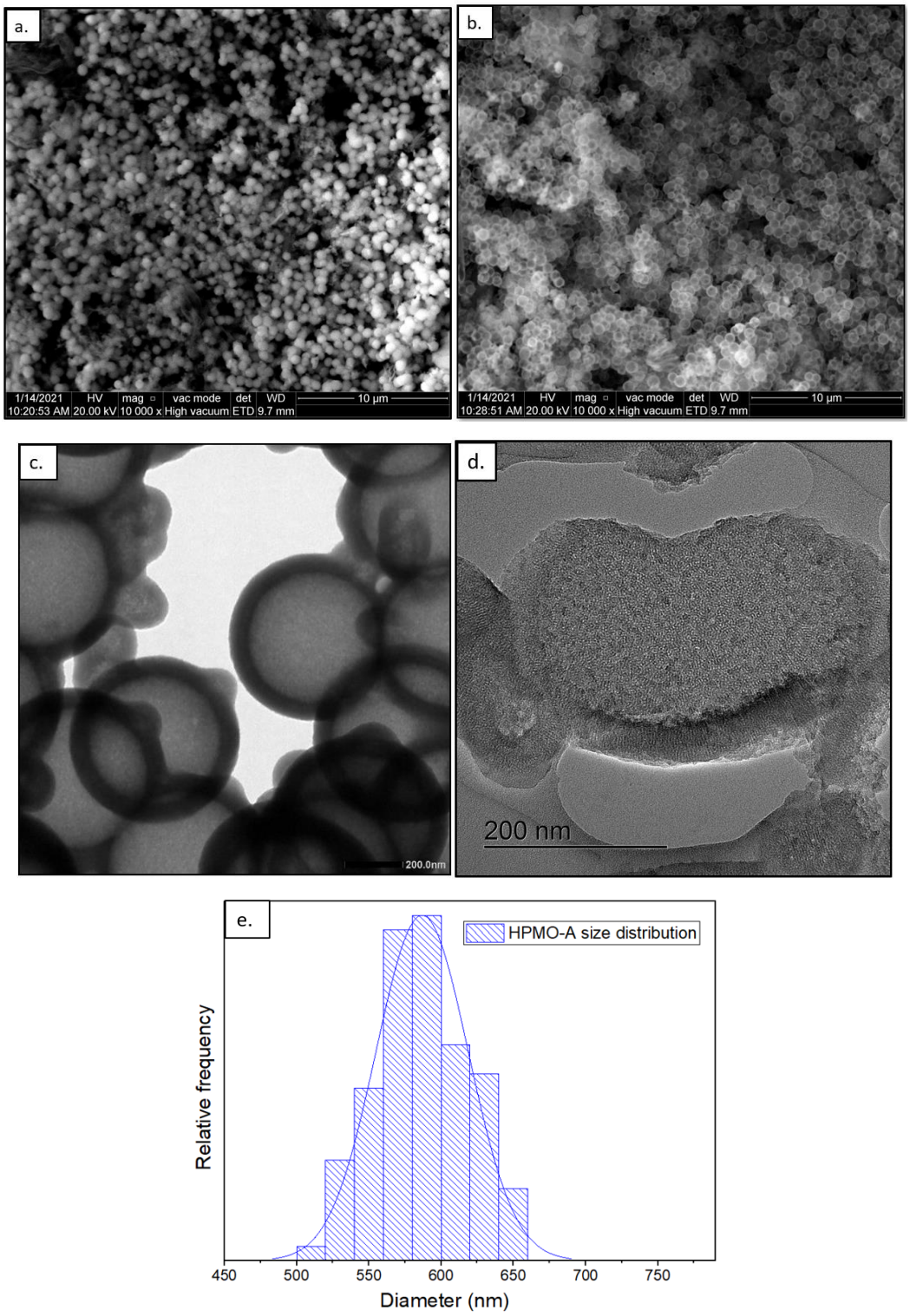

Figure II.28 a. *SEM image of NPs before silica etching.* ***b.*** *SEM and* ***c.*** *TEM* ***d.*** *HRTEM images of the reference HPMO NPs obtained after the etching of the silica hard template. This sample is denoted HPMO-A.* ***d.*** *Size distribution of HPMO-A NPs.* ***e.*** *Size distribution of HPMO-A NPs.*

2.3.4.3 Structural characterization: FT-IR characterization

FT-IR spectrum of the sample HPMO-A after the removal of both the silica hard template and CTAB, is added to the previous spectra for comparison (**Fig II.29.a**). Here, the ratio Ir = I *ν* SiOSi/I *δ* SiOSi is even more modified compared to SiO_2-HT and SiO_2-PMO (from 2.5 to 8 between SiO_2-PMO and HPMO-A), which confirms silica etching. The *ν* Si-O-Si maximum band is downshifted by -15 cm^{-1} which suggests a lower polycondensation of the material, expected for a PMO framework compared to dense inorganic silica [169, 170]. The characteristic band of the BTEB at 523 cm^{-1} is preserved after the silica etching which suggest that the local arrangement of the PMO structure is not impacted.

To conduct a more detailed analysis of the material before and after silica etching, a linear combination is performed, comprising 44 % HPMO-A and 56 % SiO_2-HT (Fig **A.1**, appendix A). It shows that the same spectrum of SiO_2-PMO is reproduced. This means that the etching of the silica does not imply significant re-condensation at the level of the PMO.

The removal of CTAB from mesopores can be deduced from **Fig II.29.b**. The intensity of CTAB features in the 1300-1500 cm^{-1} range and in the 2100-2800 cm^{-1} are very weak in HPMO-A compared to SiO_2-PMO, signing the efficiency of CTAB removal.

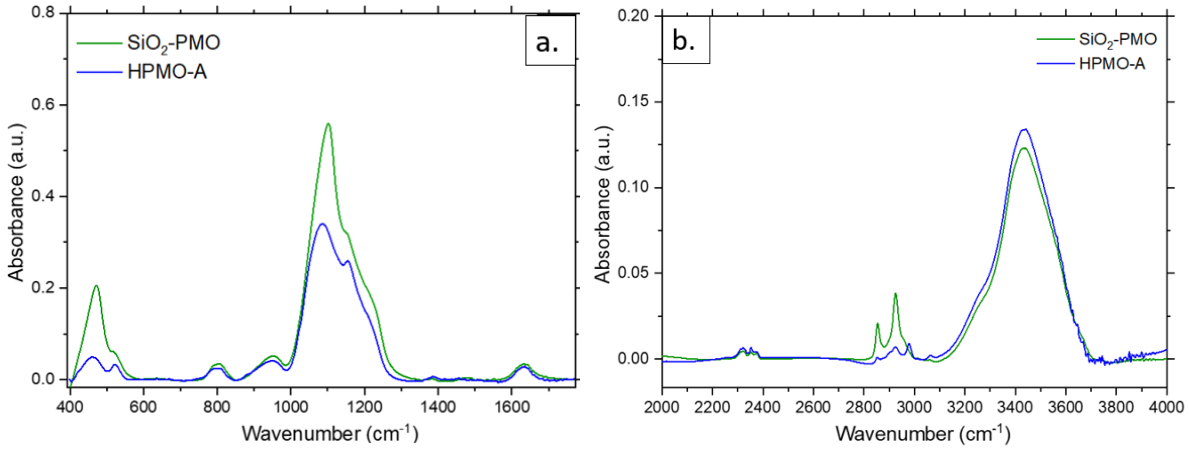

Figure II.29 a. *FT-IR spectra of the obtained HPMO NPs denoted HPMO-A after the removal of both silica hard template and CTAB in the 400-1700 cm^{-1} region and* ***b.*** *in the 2000-4000 cm^{-1} region.*

From our experimental results, the BTEB vibrational fingerprints are difficult to identify because they are mainly mixed with silica vibrational features. The IR response of the BTEB precursor has been simulated. DFT results are compared to the experimental spectrum of BTEB precursor. The vibration attributions of the overall calculated spectrum are presented in the

Table A.1 (appendix A). The calculated spectrum of BTEB precursor reproduces the vibrational fingerprints of the experimental one. The polycondensed BTEB (HPMO-A) is marked by the appearance of the polycondensed silica bulk between 1000-1200 cm^{-1}, broadening the band with the intensity of the peak at 1150 cm^{-1} increasing relatively to the maximum of Si-O-Si feature at 1100 cm^{-1}. The disappearance of the band at 687 cm^{-1} (in plane δ ring of BTEB) is also observed (**Fig II.30**).

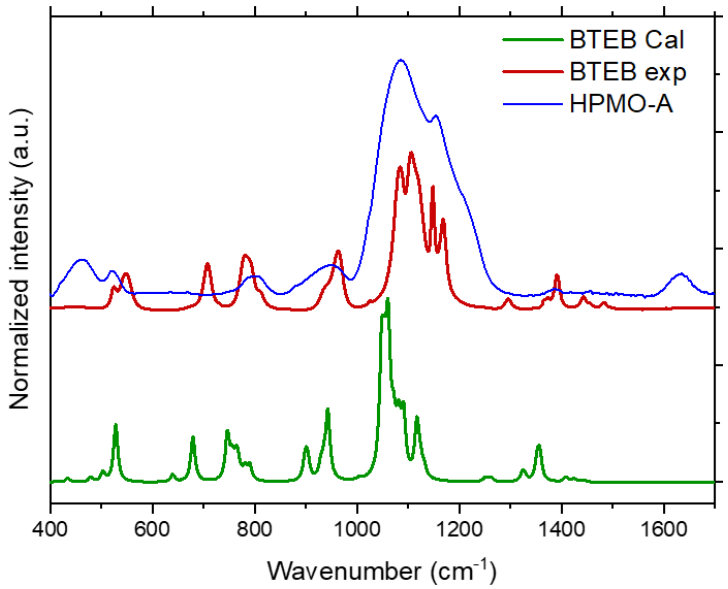

Figure II.30 *Comparison between calculated and experimental spectra of one BTEB molecule and polycondensed BTEB material (HPMO-A).*

A special attention is drawn to the frequency region between 400 and 800 cm^{-1}. A DFT simulation of BTEB IR spectra as a function of π-π stacking is performed according to the model proposed by S. Inagaki *et al.* [128] for one isolated BTEB molecule, four then twelve molecules. Simulated spectra suggesting π-π interactions and the corresponding spectra are presented in **Fig II.31**. The symmetries of the low frequency modes are given in **Table II.2**. The two modes exhibiting pure out of plane and in plane deformations of the aromatic ring in 503 cm^{-1} and 528 cm^{-1} respectively. When π-π stacking is established, these modes collapse. The peak around 528 cm^{-1} found only in the isolated molecule of BTEB is attributed to the in-plane deformation of BTEB aromatic ring. We show from the three calculated spectra that the development of ordered structures arising from π-π stacking induces the disappearance of the peak at 528 cm^{-1} and the appearance of low frequency modes below 500 cm^{-1}. We clearly observe in the experimental spectrum (HPMO-A) a band at 523 cm^{-1} but also a broad weak band at lower frequency around 460 cm^{-1} suggesting π-π interactions. It is difficult to conclude on this point because silica contribution (δ Si-O-Si) cannot be excluded in this frequency region.

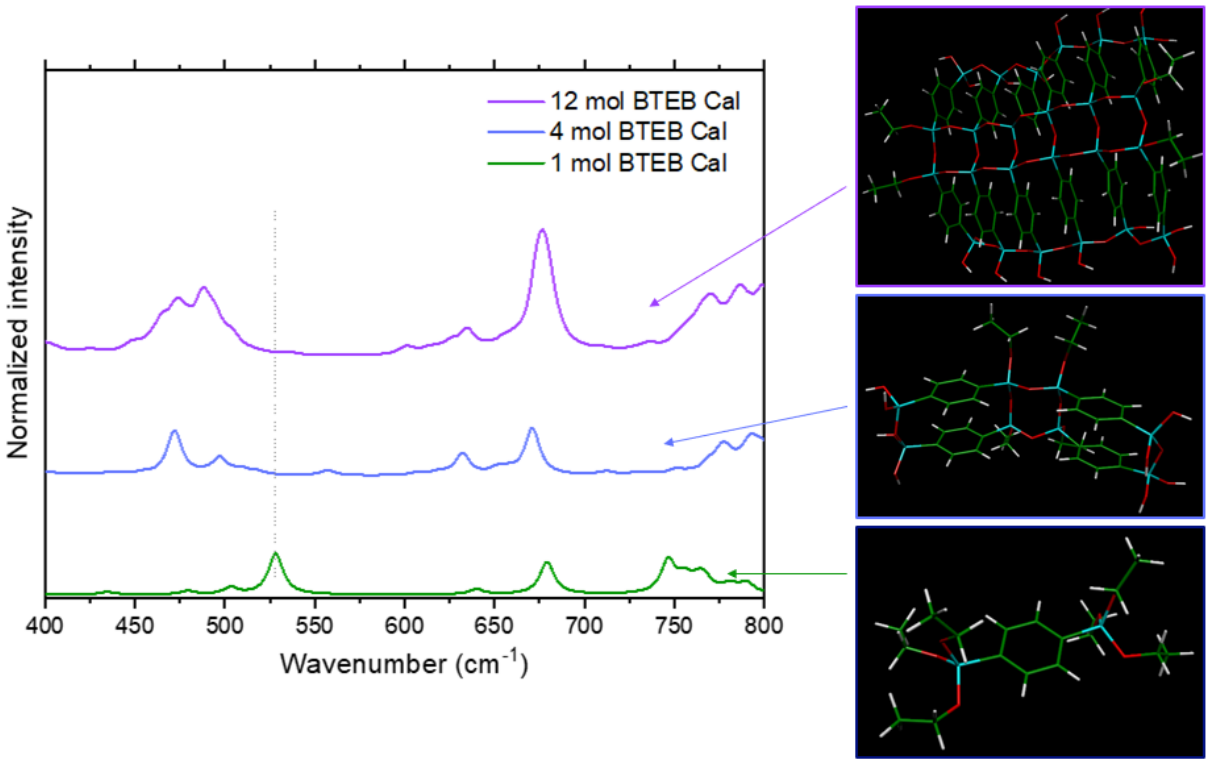

Figure II.31 *DFT IR calculated spectra of 1 BTEB molecule, 4 and 12 polycondensed BTEB molecules in the 400-800 cm^{-1} region.*

479 cm^{-1}	503 cm^{-1}
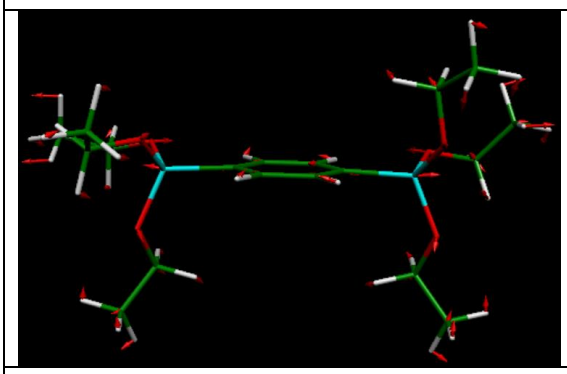	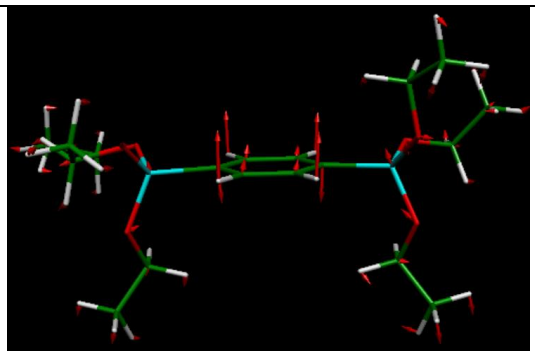
528 cm^{-1}	639 cm^{-1}
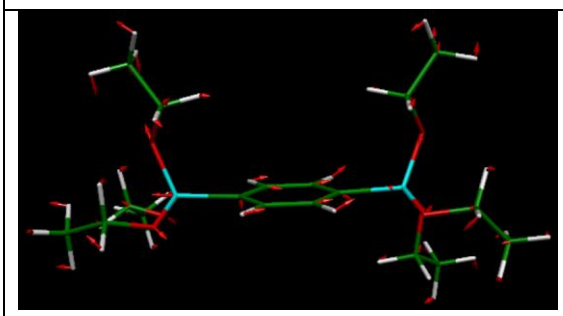	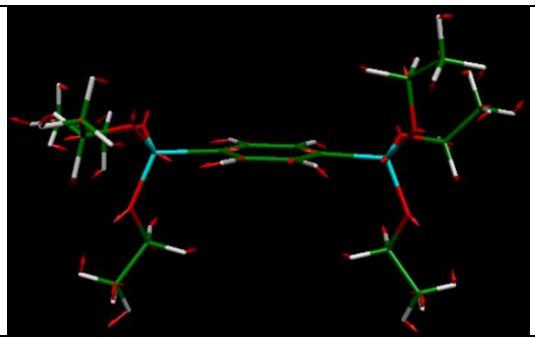
687 cm^{-1}	783 cm^{-1}
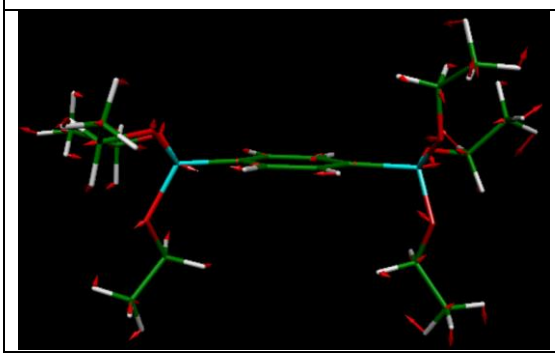	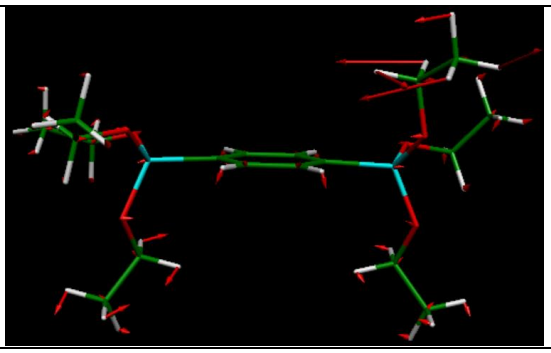

Table II.2 *Aromatic ring deformation modes with animations based on DFT calculations.*

2.3.4.4 HPMO NPs mesostructure analysis

a) Mesopores structuring: X-ray diffraction/diffusion characterization

The hydrolysis and polycondensation of a bridged-organosilane precursor while simultaneously co-assembling with aggregates of surfactant micelles forming a sort of liquid-crystal, results in the formation of highly ordered mesoporous material with a crystal-like wall structure [128] referred to as periodic mesoporous organosilica (PMO). The structural arrangement of the mesopores is maintained even after the removal of the liquid-crystal template, and is therefore worth studying using X-ray diffraction (XRD° or small angle X-ray scattering (SAXS)) to analyze the mesopores organization. The X-ray pattern in the small *q* wave vector shown hereafter in **Fig II. 32** is typically assigned to a highly organized 2D hexagonal lattice with the space symmetry group *p*6*mm*.

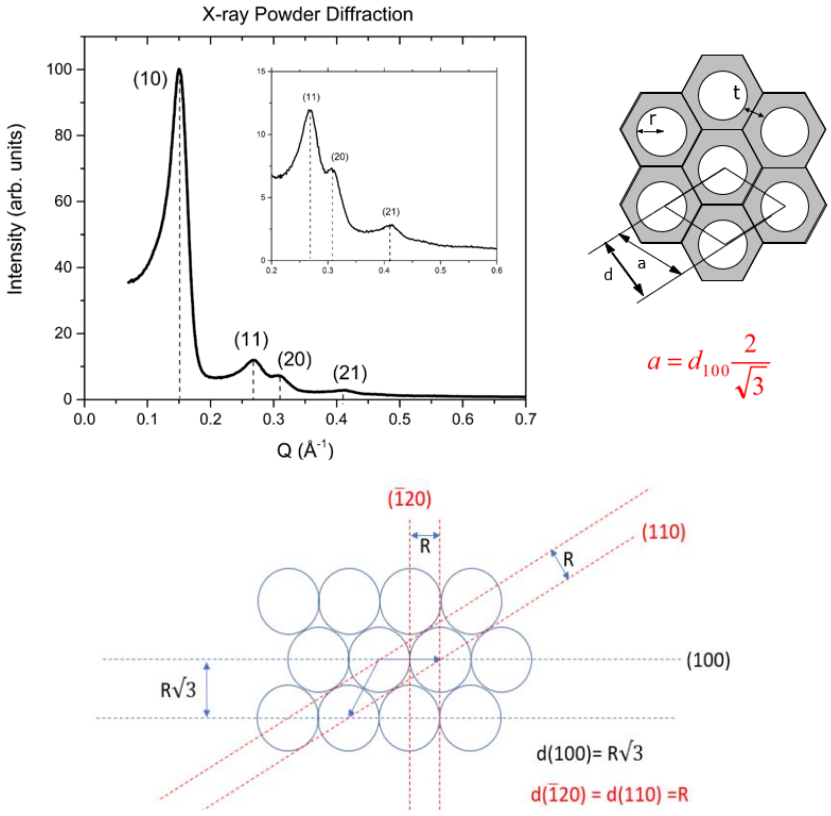

Figure II.32 *Typical X-ray pattern of 2D hexagonal mesoporous material, from MCM-41 reference bulk material [171].*

The first three diffraction peaks position at *q* values of 1.5 nm^{-1}, 2.7 nm^{-1} and 3.1 nm^{-1} corresponds to the diffraction planes (100), (110) and (200) respectively, with *q* (110) = $3^{1/2}$ *q* (100) and *q* (200) = 2*q* (100) if we assume the geometrical representation also shown in the **Fig. II. 32**. The lattice parameter or the unit cell corresponding to the centre-to-centre spacing can

be calculated using the equation $a = 4\pi/q_0\sqrt{3}$ and is equal to 4.7 nm in this case. The pore size is driven by the length of the surfactant alkyl chain and thus, the peak positions of HPMO-A are expected to be analogous to the MCM-41 material because the same cationic surfactant is employed.

The SAXS profile of HPMO-A exhibited in **Fig II.33** shows two peaks at q =1.7 nm^{-1} and q = 3.2 nm^{-1} (*i.e.*, diffraction planes (100) and (110) respectively), assigns to a hexagonal arrangement of mesopores with a lattice parameter a = 4.3 nm which is close to the reported value [171]. The first peak q (100) is not very intense, and the second peak q (110) is barely observed whereas the q (200) corresponding to the second order of q (100) is not observed. This data is not totally aligned with the ones shown in **Fig II.32**, because we believe that the mesostructure of a PMO layer undergoes some modification under the curvature effect imposed by the spherical hard template. Consequently, a slight disorder within the PMO layer is expected. This result suggests a moderate hexagonal organization of the mesostructured shell.

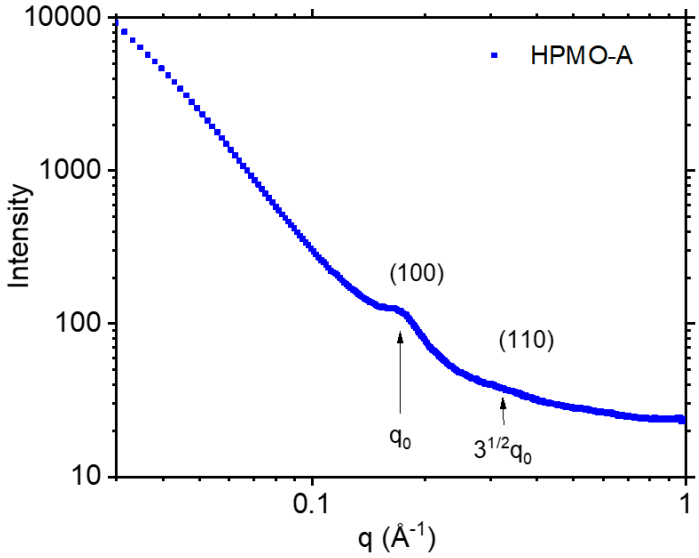

Figure II.33 *SAXS signal of the reference material HPMO-A in the small wave vector.*

b) Textural properties of HPMO NPs using nitrogen sorption analysis

Nitrogen sorption analysis is a well-established characterization method exclusively dedicated to analyze the textural properties of porous materials, involving the pore size and structure that can be deduced from the physisorption isotherms and the hysteresis loop shape, as well as the specific surface area resulting from the overall porous structure and which can be calculated using the Brunauer-Emmett-Teller (BET) method.

The current terminology used to classify the pore size according to the IUPAC is the following [172]:

- Micropores: pore diameter (d) < 2 nm
- Mesopores: 2 nm < d < 50 nm
- Macropores: d > 50 nm

Based on the previous X-ray data, the pore sizes of the HPMO material are in the range of 2 to 4 nm which is consistent with a typical diameter of a CTAB micelle, and also consistent with the appellation "Hollow Periodic Mesoporous Organosilica" and underscores the significance of nitrogen sorption as an effective structural characterization tool.

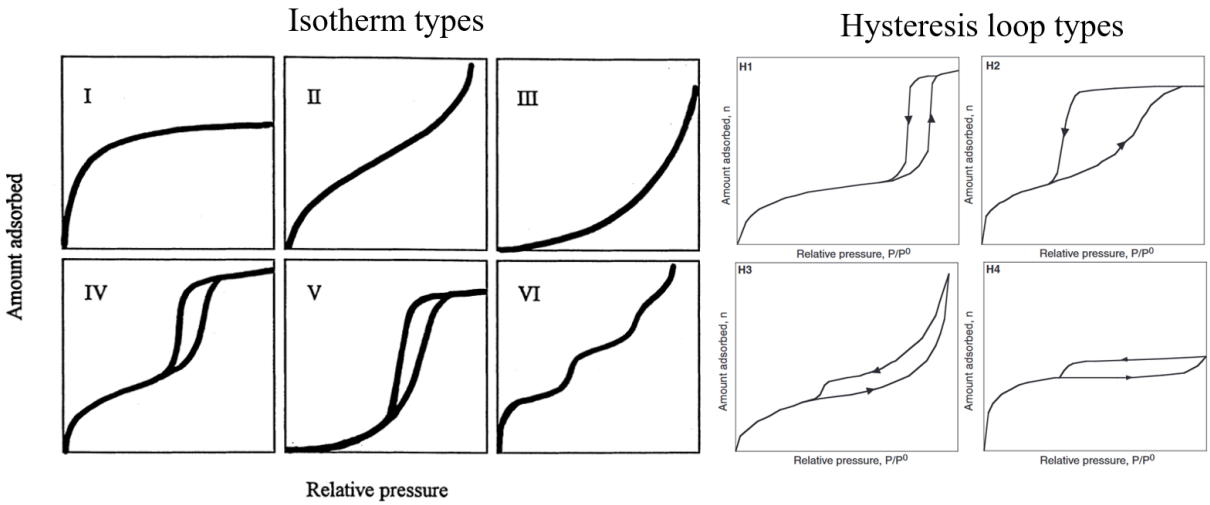

Figure II.34 *Physisorption isotherms and hysteresis loops classification defined by IUPAC* [173, 174].

The different possible isotherms are depicted in **Fig II.34**, and are classified from type I to VI according to the IUPAC definition. They reflect the evolution of physisorption behavior and the adsorbed amounts as a function of the relative gas pressure p/p°, where p° is the saturation pression of the adsorptive, at a given temperature. Nitrogen is classically used as an adsorptive gas at 77 K, but its utilization remains limited for a quantitative analysis of micropores with a size under 0.7 nm [175].

Isotherm type I is usually attributed to microporous material adsorption because of the high gas uptake in the lowest relative pressures, while type II and III are rather attributed to a non-porous or microporous material with high gas uptakes around high relative pressures, where a strong adsorbate/adsorbent interaction in type II can be distinguished from weak ones for type III,

where a quantitative adsorption is observed near saturation [173]. Sorption isotherms type IV and V are attributed to mono- and multilayer adsorption usually exhibited by mesoporous materials and also have hysteresis loops that are associated with capillary condensation, which correspond to gas-liquid phase transition at relative pressure lower than the saturation one, which generally happens starting from a pore width greater than 4 nm for a nitrogen adsorption at 77 K in cylindrical pores for instance [176]. Finally, type VI reflects a multistep adsorption behavior. The occurrence of a capillary condensation is usually accompanied by the formation of a hysteresis loop, whose pattern can be sometimes employed to have an idea on the shape of the pores and their rigidity [176, 177]. The hysteresis loop can be a result of two possible phenomena (**Fig II.35**):

- **Neck-bottle shape pores:** when the pores have a neck-bottle shape, the large part of the pore is filled first through the narrow neck. During the desorption, the adsorbed amount occupying the large pores cannot be desorbed before the blocking neck zone is totally emptied at low relative pressures. When the neck width is relatively not too small from the inner pore, the desorption may occur at a relative pressure which is the same as the percolation threshold and may be used to have an idea on the size of the pore neck. When the neck width is lower than a critical value, around 5 to 6 nm when using nitrogen as an adsorptive at 77 K, the desorption of gas in the inner pores is constrained through a spontaneous formation of gas bubbles inside the condensed liquid, consequently, the evacuation of the inner pore occurs before the neck. This phenomenon is referred to as “cavitation”, and is associated with the observed sharp step-down and a forced closure of the hysteresis loop in the desorption branch, which is the lower limit of the capillary condensation. In this case of the sorption of the nitrogen, this closure can be observed at $p/p^{\circ} = 0.42$.



Figure II.35 Left: *Illustrative representation of the cavitation.* ***Right:*** *Pore blocking effects with different neck widths.*

- **Metastable adsorption:** This effect is generally observed for cylindrical pores with an open end and where the capillary condensation occurs only at high relative pressures because of the metastability of the adsorbed multilayer. The thermodynamic equilibrium is only achieved during the desorption, thus explaining the mismatch responsible for the formation of a hysteresis loop.

Some of the hysteresis loop types described in the **Fig II.34** from IUPAC classification correspond to the cases described above. The H1 type corresponds to the metastable adsorption effect, the H2 to the cavitation one, and the H3 to pore blocking one [178]. The type H4 has the similar hysteresis loop to that of H3, the only difference is that the adsorption branch of H4 is a mixture of an isotherm of type I and II, because largest gas uptake occurs at low relative pressures and correspond to a large amount of micropores [176].

Before analyzing the sorption isotherm of the reference phenylene-bridged HPMO NPs, it is worth noting that the nitrogen adsorption amounts before and after removal of CTAB exhibit huge differences, which confirms even more that the presence of the surfactant prevents the nitrogen adsorption inside the mesopores. Indeed, the BET surface goes from 60 $m^2. g^{-1}$ to 833 $m^2. g^{-1}$ after the removal of the surfactant, thus indicating a successful mesopores emptying.

The sorption exhibited by HPMO-A (**Fig II.34**) is mixture of type I and type IV, with an obvious steep uptake in the $p/p^\circ = 0.2$ region, indicating the presence of a narrow distribution of mesopores with a size ranging between 2 and 4 nm [174], which is consistent with the average diameter of CTAB micelle [179, 180]. The type H3 hysteresis pattern indicates the presence of a progressive capillary condensation at higher relative pressures, the loop closure at $p/p^\circ = 0.42$ corresponds to the nitrogen cavitation at the lower limit of the capillary condensation.

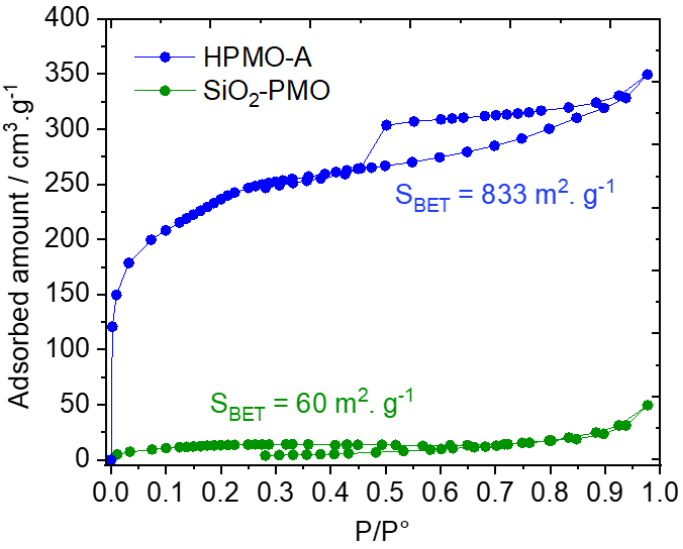

Figure II.36 *Isotherm sorption analysis of HPMO NPs before and after surfactant removal.*

In the study reported by M. Fröba and co-workers [150], nitrogen sorption isotherms of the materials before and after the core silica shrinkage were compared. Strong hysteresis loops in addition to the nitrogen cavitation effect appears only on the material having the hollow structure.

2.3.5 HPMO NPs synthesized in the absence of ethanol

Given the dual role of ethanol, serving as a solvent for organic compound like bridged organosilane precursors, and as a co-surfactant participating in micelle formation [181, 182], we were interested in investigating how the PMO shell structure is modified when following a chemical process not involving ethanol.

2.3.5.1 TEM characterization

A comparative table displaying TEM images of samples synthesized in the presence and in the absence of ethanol is displayed in **Fig II.37**. Some interesting differences can be observed (i) numerous tiny NPs are formed independently from the hard template, (ii) the mean thickness of the deposited PMO layer is smaller in HPMO-A SE than in HPMO-A. The average thickness is 32 ± 2 nm against 59 ± 8 nm. Actually, since BTEB and CTAB are weakly soluble in water alone, an important amount of these components co-assembles to form small nanoparticles instead of contributing in the PMO shell building.

	Synthesized in the presence of ethanol	Synthesized in the absence of ethanol (HPMO-A SE)
587 nm HPMO-BTEB	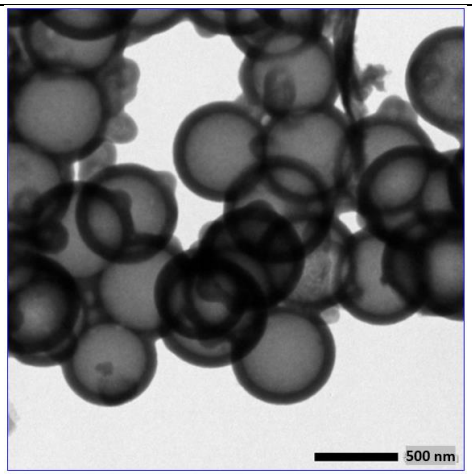	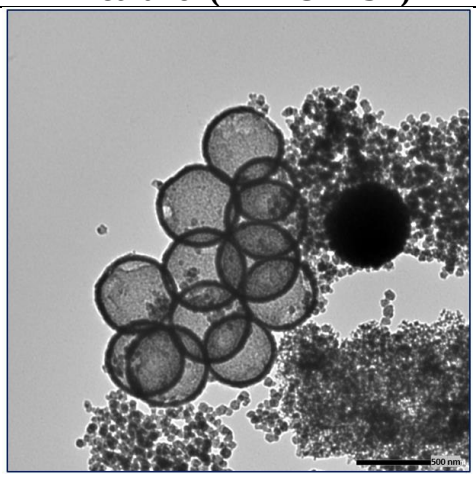

Figure II.37 *TEM images of HPMO NPs obtained using ethanol in the first column of the table, and obtained without using ethanol in the second column of the table. Samples in each line correspond to HPMO NPs having similar mean size because the same hard template size was employed. The sample of the first column are already shown in* ***Fig II.28****. and are only serving for comparison in this table.*

2.3.5.2 Small angle X-ray scattering (SAXS): Mesopores periodicity

SAXS analysis of the HPMO NPs synthesized in the presence of ethanol (HPMO-A) and without ethanol (HPMO-A SE) are presented in the **Fig II.38**. We can observe that for HPMO-A SE, the q_0 position corresponding to the (100) diffraction peak is downshifted to a lower value of 1.3 nm^{-1} which corresponds to a higher value of the characteristic distance equal to 4.8 nm, against 3.6 nm for the HPMO-A. The calculated lattice parameter a is also higher, 5.5 nm for HPMO-A SE against 4.3 nm for HPMO-A. The increase of the lattice parameter indicates a mild enlargement of mesopores when the materials is not prepared in an ethanolic solution. Several reported studies discussed the solvent/co-surfactant dual role of ethanol. When used in an important amount, ethanol serves as a solvent and result in a decrease of the packing parameter of micelles, which reduces their size. When a small amount of ethanol is used, the latter rather serves as a co-surfactant with CTAB, consequently, the packing parameter is increased and micelles swell. When no ethanol is used at all, the latter will still be produced in small amounts in the early stages of the sol-gel reaction, and serves as a co-surfactant here as well. As the size of mesopores is related to the initial size of micelles, the swelling induces mesopores enlargement. This is consistent with SAXS results showing an increase of the lattice parameter for HPMO-A SE.

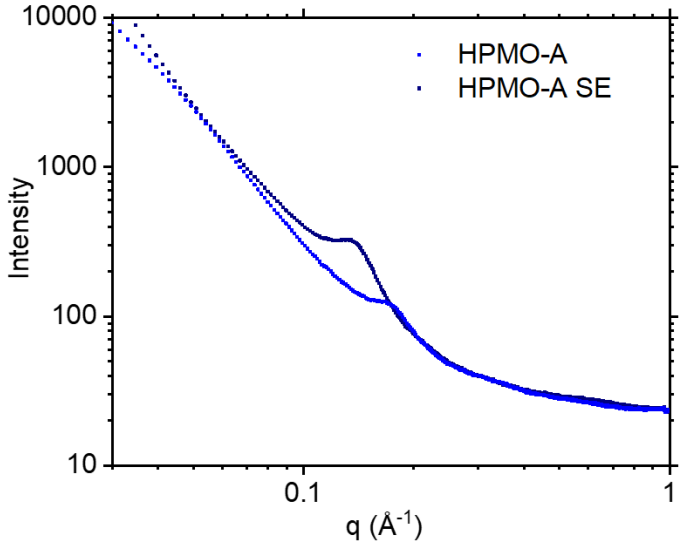

Figure II.38 *SAXS analysis of phenylene-bridged HPMO NPs synthesized with (HPMO-A) and without ethanol (HPMO-A SE).*

2.4 Size tuning of Hollow Periodic Mesoporous Organo-silica Nanoparticles (HPMO-NPs)

2.4.1 Strategy of HPMO NPs size tuning

The strategy for tailoring HPMO-NPs size depends on the capacity to synthesize spherical and monodisperse silica NPs using the Stöber process. After the deposition of the PMO layer on the hard template with a well-defined size, silica cores are etched and the resulting HPMO NPs conserve the size of the hard template as schematized in **Fig II.39**. The thickness of the PMO layer, can be also be tuned by varying respectively the amounts of the bridged organosilane precursor and the surfactant co-assembling with it.

In order to study the modification of the PMO shell structural properties as a function of the hard template size, phenylene-bridged organosilane precursor (BTEB) is used to synthesize all the HPMO NPs with the different sizes.

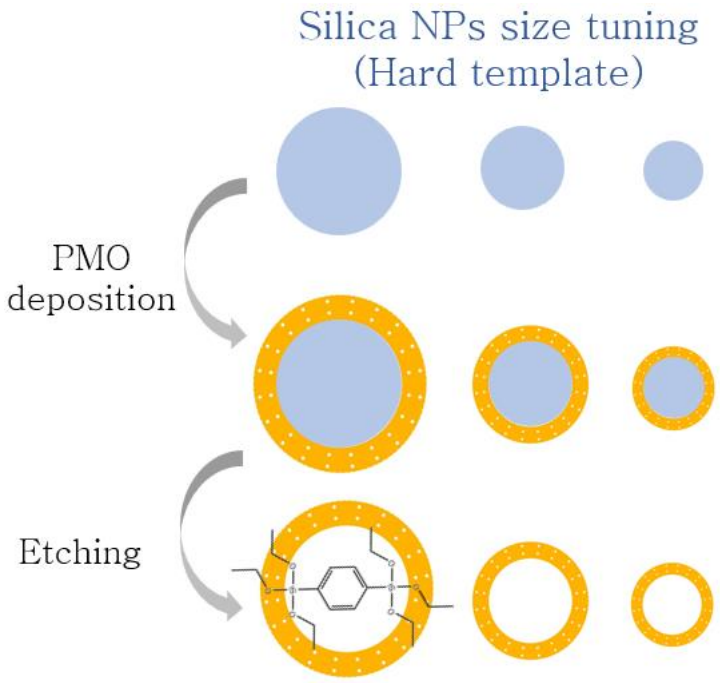

Figure II.39 *Schematic representation of HPMO NPs size tuning strategy based on the hard template approach.*

2.4.2 Size tuning of silica NPs (hard template)

2.4.2.1 Synthesis

The synthesis of spherical and monodisperse silica hard templates with different sizes is performed by varying the amounts of the Stöber process components as shown in the **Table II.3**. The amounts used to obtain the largest monodisperse silica seed denoted T1 and is considered as the reference sample (used to obtain HPMO-A). Smaller NPs are obtained by modifying the sol-gel components amounts relatively to T1.

SiO_2 NPs	**H_2O (ml)**	**TEOS (ml)**	**NH_4OH (25%) (ml)**	**Ethanol (ml)**	**Monodisperse**	**Mean diameter (nm)**
T1 (ref)	2	1.2	0.7	15	Yes	471 ± 18
T2	1	1.2	0.7	15	No	310 ± 12 /141 ± 8
T3	1	0.6	0.7	15	Yes	180 ± 7
T4	0.75	0.45	0.7	15	Yes	147 ± 7
T5	0.5	0.3	0.7	15	Yes	90 ± 5
T6	0.15	1.1	0.62	15	Yes	32 ± 1

Table II.3 *Sol-gel reaction's component amounts used obtain silica NPs with different sizes. Mean diameters are measured using Digimizer software from TEM images displayed in* ***Fig II.40****.*

2.4.2.2 TEM characterization

TEM images of the resulting silica NPs are displayed in **Fig II.40**. The first attempt to decrease the silica NPs (T2) relatively to the reference sample T1 consisted in dividing the amount of water which is the main actor in the hydrolysis of the precursor. The rest of the reagents amounts and the experimental conditions were kept the same. This led to a polydisperse sample with a bimodal size distribution of silica NPs. When changing the amount of TEOS the same way as water (T3), monodisperse NPs of 180 nm are obtained. To further decrease NPs size, amounts of TEOS and water are decreased while keeping a water/TEOS volume ratio of 1.6. For the smallest NPs (T6), a small quantity of water is used against a considerable amount of TEOS, and the amount of NH_4OH, acting as a catalyst is slightly decreased. The achieved silica NPs are all spherical and quite monodisperse with a mean size ranging between ~ 30 and 470 nm.

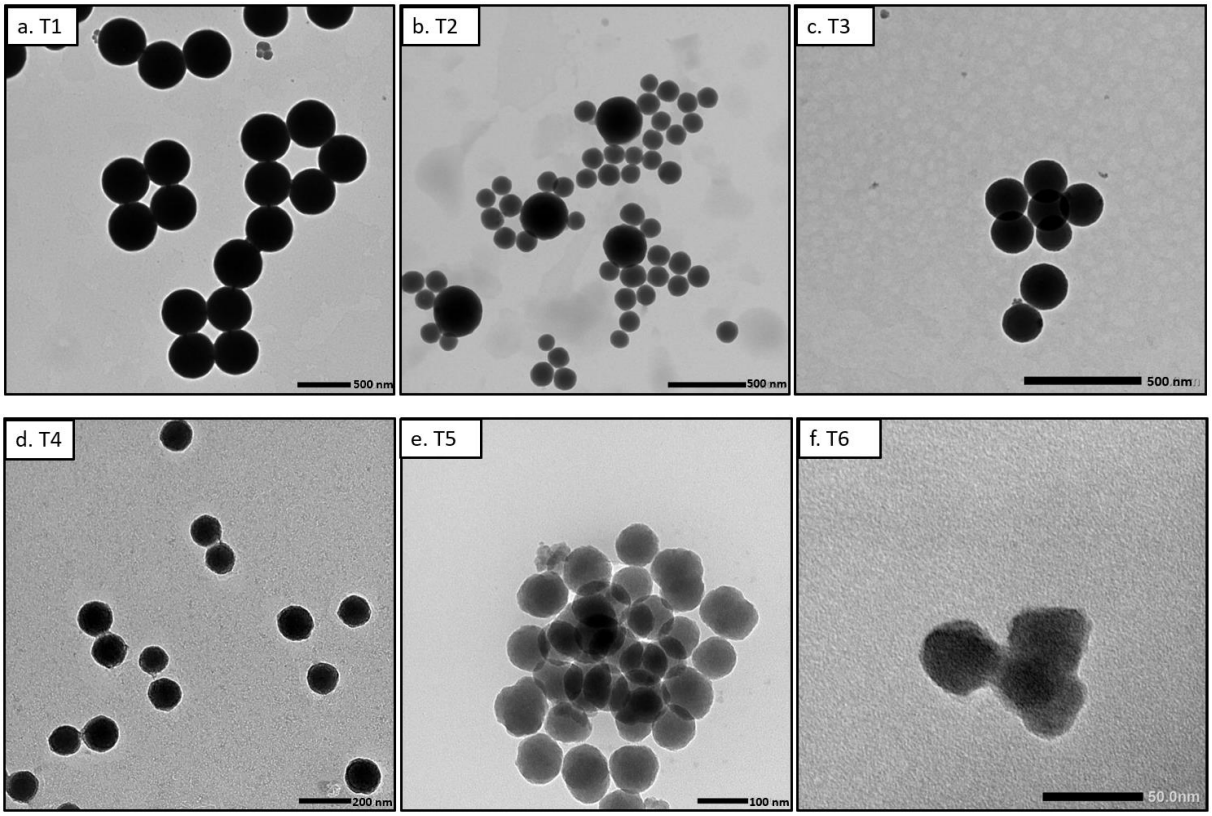

Figure II.40 *TEM micrographs of the as-prepared silica hard templates (SiO_2-HT) with tailored sizes.*

2.4.3 Size-tuned phenylene-bridged (BTEB) HPMO NPs

2.4.3.1 Synthesis

Phenylene-bridged organosilane (BTEB) and CTAB as a structure directing agent are used to deposit a PMO shell on silica NPs (T1, T3, T4 and T6 from **Fig II.40**) using the reagents amounts in the **Table II.4**. The detailed synthesis protocols are presented in the experimental section. It is noteworthy that only the reference T1-HPMO-A is synthesized using a one pot reaction following a previous reported work [152]. This one pot reaction consists on adding a mixture of 24 ml of water and 2 ml of ethanol and the rest of the components for the next step of the synthesis (PMO deposition), to the same pot containing the as-prepared silica NPs.

Considering the fact that ethanol serves as a solvent in the synthesis of silica nanoparticles and that some ethanol and water are generated or consumed during the sol-gel reaction, when introducing additional water and ethanol into the mixture to initiate the PMO deposition, the water-to-ethanol ratio can be estimated to approximately 1.2. This one pot reaction cannot be applied to the other hard template sizes, because when modifying the size of silica NPs using Stöber process, the yielded volume fraction is not the same. As a consequence, when keeping

the same reaction pot, most of the reaction volume containing a mixture of ethanol and water as a solvent is not occupied by the silica seeds to be coated. This excess of water and ethanol in the presence of surfactant micelles and a catalyst favors the spontaneous nucleation of independent PMO NPs, besides the coating hard templates. As it was also noticed by T. Okubo *et al.* [155], the excess of BTEB is not the cause behind the formation of these PMO NPs, but it is the insufficient hard template available surface, relatively to the amount of solvent.

HPMO-NPs	**H_2O (ml)**	**Ethanol (ml)**	**NH_4OH (25%) (ml)**	**CTAB (mg)**	**BTEB (ml)**	**Mean diameter (nm)**	**Mean shell thickness (nm)**
T1-HPMO-A (ref)	24	2	0.672	64.1	0.2	587 ± 32	59 ± 8
T3-HPMO-C	12	10	0.35	32	0.1	358 ± 11	85 ± 3
T4-HPMO-D	6	5	0.175	16	0.1	236 ± 7	51 ± 3
T6-HPMO-B	2	1.66	0.056	5.4	0.0165	43 ± 4	5.2 ± 0.7

Table II.4 *Reagents amounts used to deposit the PMO layer on different sizes of hard templates. The total size and PMO shell thickness are measured using Digimizer software from TEM images displayed in* ***Fig II.41****. The name of each HPMO sample starts with a T number, which corresponds to the size of silica hard templated used, as listed in* ***Table II.1****.*

This issue was encountered in all the attempts aiming to coat the small sized hard templates without modifying the one pot reaction (**Fig A.2**, appendix. A). This has two consequences: (i) samples are not uniform, and it is almost impossible to separate the PMO NPs from the HPMO NPs neither by using filters nor by centrifuging, because they usually have a close size and they definitely have the same surface chemistry. (ii) An important amount of surfactant and precursor are directed toward forming the PMO NPs instead of being deposited as shells. The resulting shell thicknesses in this case are usually random and thinner than expected and cannot be predicted based on a given reaction protocol. To overcome this issue, the only solution is to wash and collect the silica seeds by centrifugation directly after the end of the Stöber reaction, and re-disperse them in a new mixture of water and ethanol suiting their volume fraction, while keeping a water to ethanol ratio of 1.2. This method is followed for the three other samples, and the amount of CTAB/BTEB/NH_4OH can be modified in a way to vary the shell thickness as well.

2.4.3.2 TEM characterization

TEM images of the obtained HPMO NPs with different sizes are displayed in the **Fig II.41**. Spherical and monodisperse HPMO NPs with voids conserving the diameter of the etched hard templates are successfully prepared. The homogeneity of the samples is also successfully achieved using the strategy described above and no additional PMO NPs were formed independently from hard templates. The mean diameters and shell thicknesses are mentioned in **Table II.4**.

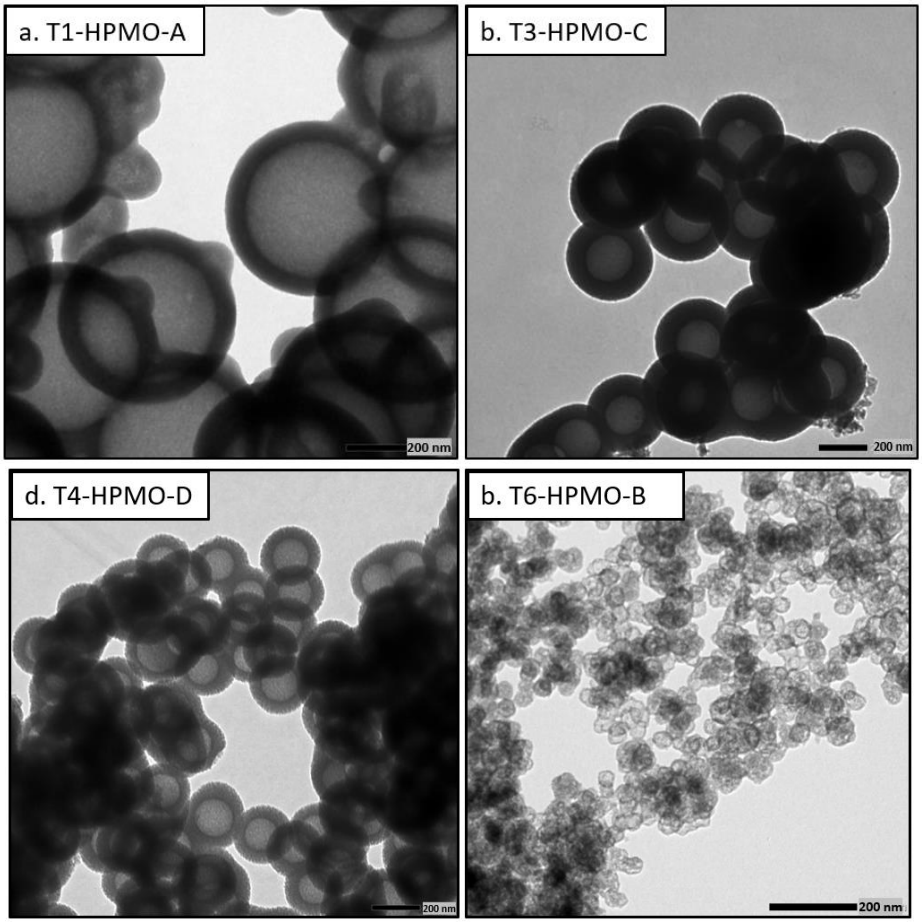

Figure II.41 *TEM images of the as-prepared size-tuned phenylene-bridged HPMO NPs, the scale bare of all the images is 200 nm.*

2.4.3.3 Nitrogen sorption analysis

Nitrogen sorption analysis is used to follow the structural evolution of the PMO shell as a function of the different sizes HPMO NPs, through the analysis of the sorption isotherms and the specific surface area calculated using BET method (S_{BET}). The four sample with different sizes prepared using the same bridged organosilane precursor (BTEB) have different isotherm profiles and different S_{BET} values indicating the presence of textural differences between these

materials. All the materials exhibit a mixture of type I and type IV sorption isotherms (**Fig II.42**) which can be deduced from the high uptake at very low p/p°, and have hysteresis profile type H3, except for T6-HPMO-B that exhibits a mixture of H2 and H3 hysteresis profiles. The reference material T1-HPMO-A exhibits a steep slope at very low p/p° indicating a high affinity between nitrogen and the surface of the material. This could be due to the presence of some micropores. These are likely scarce as the extent of adsorption is rather moderate at the first inflexion of the sorption isotherm ($p/p^{\circ} = 0.05$), that is where the micropores are filled with nitrogen. More importantly, a clear substep is observed $p/p^{\circ} = 0.2$, indicating the presence of small mesopores with a narrow pore distribution around 2.5 to 3 nm according to the Kelvin law. This is in accordance with the diameter of a CTAB micelle. Above $p/p^{\circ} = 0.3$, the nitrogen uptake gradually increases until saturation with a rather flat plateau reflecting a low external surface. This is consistent with the large size of T1-HPMO-A (587 nm), therefore offering a low external surface.

Compared to T1-HPMO-A, T3-HPMO-C and T4-HPMO-D have a higher and steeper slope at very low p/p° (<0.1). It can be deduced that these materials are more microporous than is T1-HPMO-A. Beyond the micropores filling, at higher relative pressure, the adsorbed amount keeps increasing gradually in all the region between 0.1 and 0.9. Above $p/p^{\circ} = 0.6$. The higher slope in the case of T4-HPMO-D, confirms that this sample is made of smaller particles than T3-HPMO-C. In terms of porosity, the main difference between these two materials lies in the sorption curve in the case of T3-HPMO-C that becomes flatter from $p/p^{\circ} = 0.5$ onwards. This suggests that this material has a large range of mesopores (between 2 to 6 nm according to the Kelvin law), whose filling with nitrogen is therefore complete beyond $p/p^{\circ} = 0.5$. Whereas in the case of T4-HPMO-D, there is no such as phenomenon, as the adsorbed amount increases without any trace of saturation before bulk condensation of nitrogen at high relative pressure. The slope of the curve in this region can be interpreted by assuming an adsorption process through a multilayer mechanism around the aggregated particles of T4-HPMO-D. This interpretation would be consistent with the occurrence of a large H3 hysteresis loop.

T6-HPMO-B is characterized by a less visible substep at $p/p^{\circ} = 0.2$ indicating the presence of small mesopores too. Unlike T1-HPMO-A having the flat saturation plateau, T6-HPMO-B exhibits a steady increase of the adsorbed amounts, once the small mesopores are filled, until saturation. The adsorption isotherm strongly increases from $p/p^{\circ} = 0.75$. This is the evidence of

the existence of large mesopores. The hysteresis loop is also different in two ways (i) it is larger compared to that of T4-HPMO-D and (ii) the branches are not parallel. These observations are also related to the presence of large mesopores whose emptying is strongly delayed to the lower relative pressures.

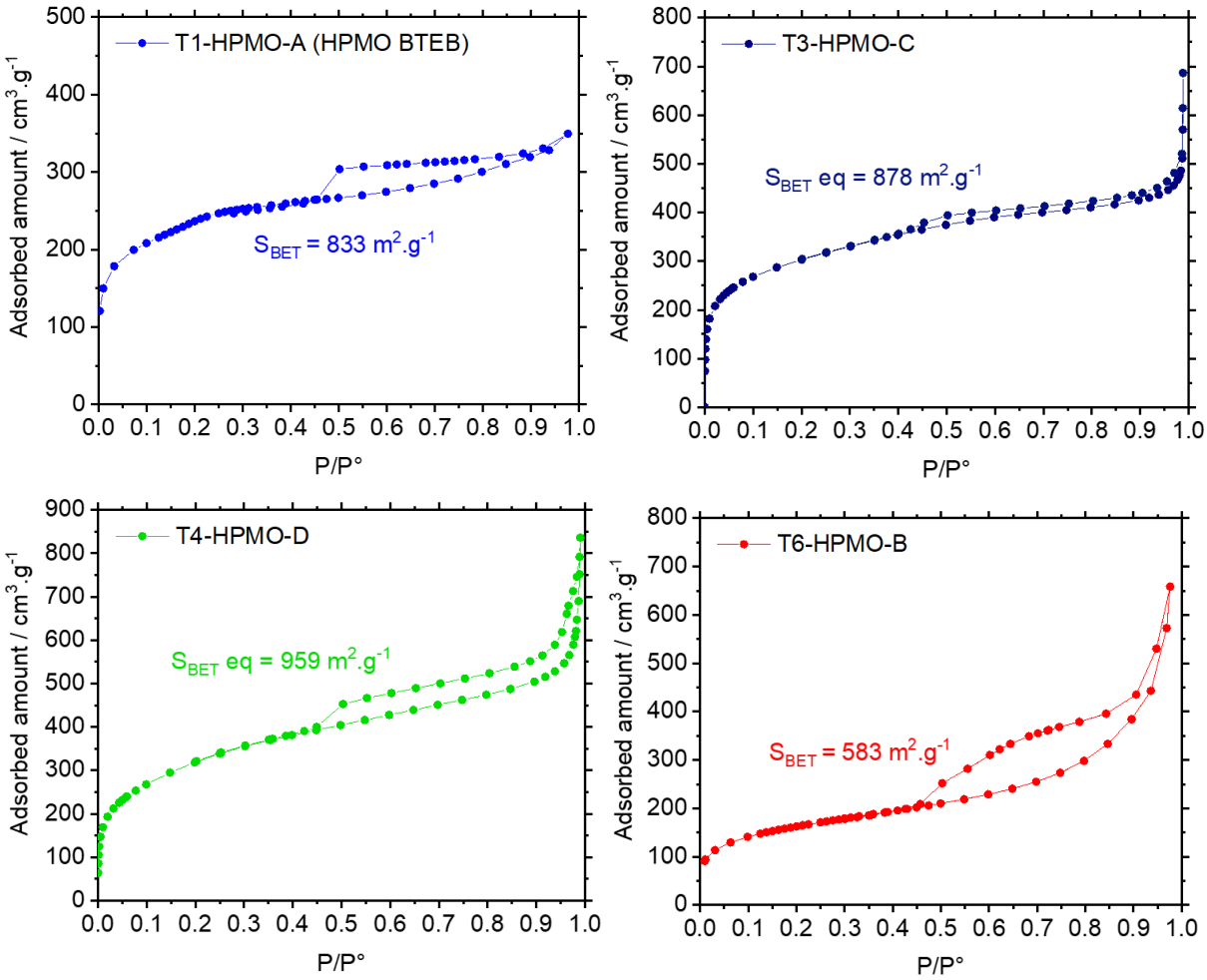

Figure II.42 *Nitrogen sorption analysis of sized-tuned phenylene-bridged HPMO NPs.*

No clear correlation between HPMO NPs size and nitrogen uptake can be concluded based on these results, even if we consider HPMO NPs having the same shell thickness and different hollow cores (T1-HPMO-A and T4-HPMO-D). This is because these materials differ in terms of porosity. Indeed, T1-HPMO-A has small mesopores around 2 nm, T3-HPMO-C has both micropores and a small population of mesopores at around 3 nm, T4-HPMO-D has more micropores than T3-HPMO-C while T6-HPMO-B has a high population of large mesopores.

2.4.3.4 Small angle X-ray scattering (SAXS): Mesopores structuring

SAXS profiles displayed in **Fig II.43** are used to rate the mesopores organization following a 2D hexagonal structuring for each size of phenylene-bridged HPMO NPs. The reference material T1-HPMO-A has a 2D hexagonal mesopore structure and a lattice parameter a= 4.3 nm. T3-HPMO-C and T4-HPMO-D show less mesopore structuring compared to T1-HPMO-A, by exhibiting a very broad peak at the same position of q_0. For T6-HPMO-B, diffraction peaks are hardly distinguished.

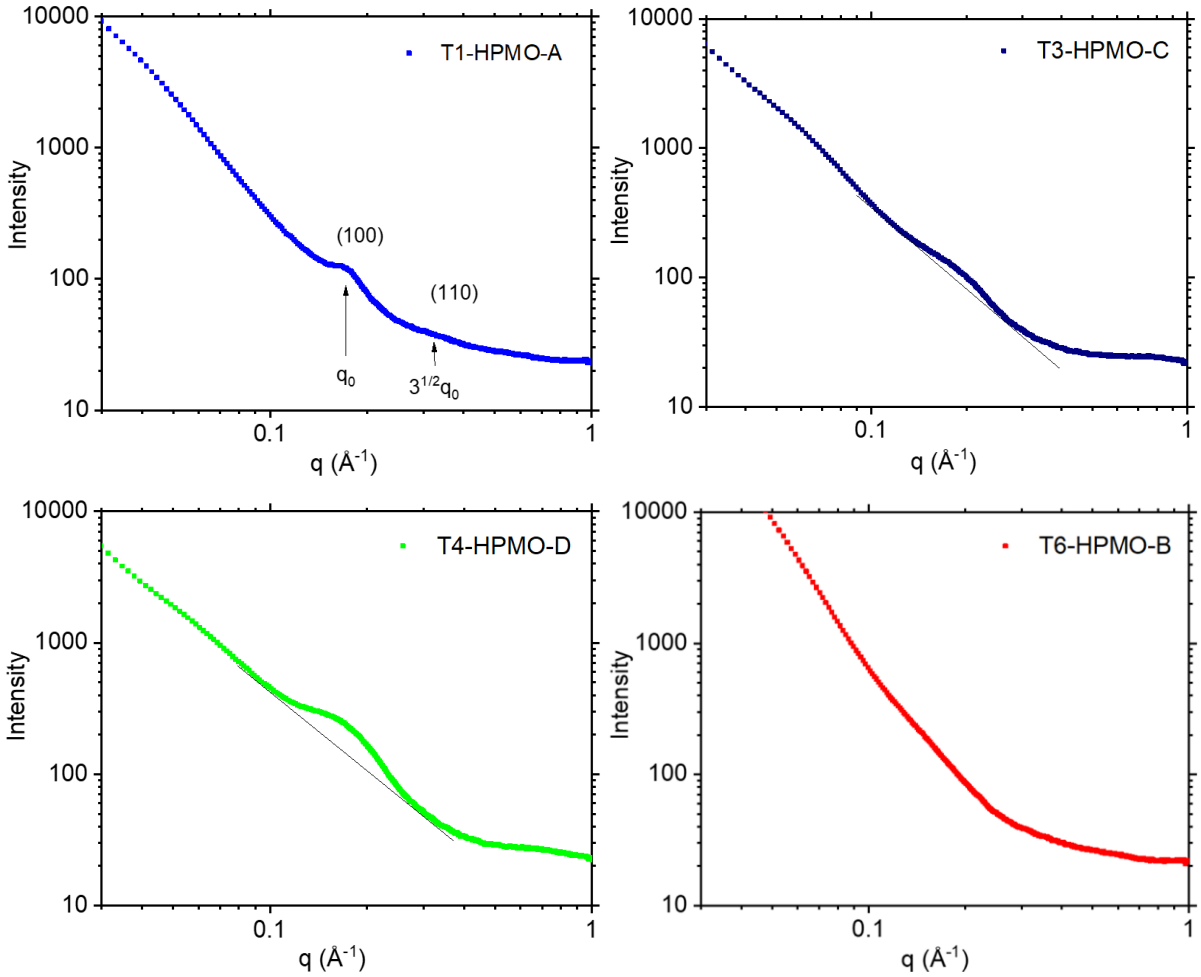

Figure II.43 *SAXS profiles of the size-tuned phenylene-bridged HPMO NPs.*

The samples having broad peaks reflecting a disordered mesopore structuring in the small wave vector, (T3-HPMO-C and T4-HPMO-D) are also the ones exhibiting both mesopores and micropores populations. In contrast, T6-HPMO-B exhibiting a similar adsorption isotherm shape in the low p/p° region to that of T1-HPMO-A, show no sign of diffraction peak. This is

expected given the small NPs size (43 nm) and the very thin PMO shell (5 nm). Here again, there is no direct correlation between the size of HPMO NPs and the mesopores structuring.

FT-IR spectra of the as-prepared BTEB HPMO NPs with the four different sizes are presented in the **Fig II.44**. All spectra have in common the same two peaks at 1150 cm^{-1} and around 523 cm^{-1} which are characteristic vibrations of the phenylene-bridged organosilane (BTEB) aromatic ring. The first peak corresponds to the stretching vibration of Si-C of the phenylene bridging moiety and the second corresponds to the out of plane deformation of the aromatic ring. All spectra also have the Si-O-Si antisymmetric stretching vibration in the 1000-1100 cm^{-1} region as discussed previously. The peak position is significantly downshifted to the low frequencies for T3-HPMO-C and T4-HPMO-D ($\Delta\nu$ = - 44 cm^{-1}), which suggests a lower polycondensation of these materials. The ratio of intensities between the υ Si-O-Si peak in the 1000-1100 cm^{-1} region and the peak at 520 is lower for T3-HPMO-C and T4-HPMO-D compared to T1-HPMO-A and T6-HPMO-B, 1.04 against 11 respectively.

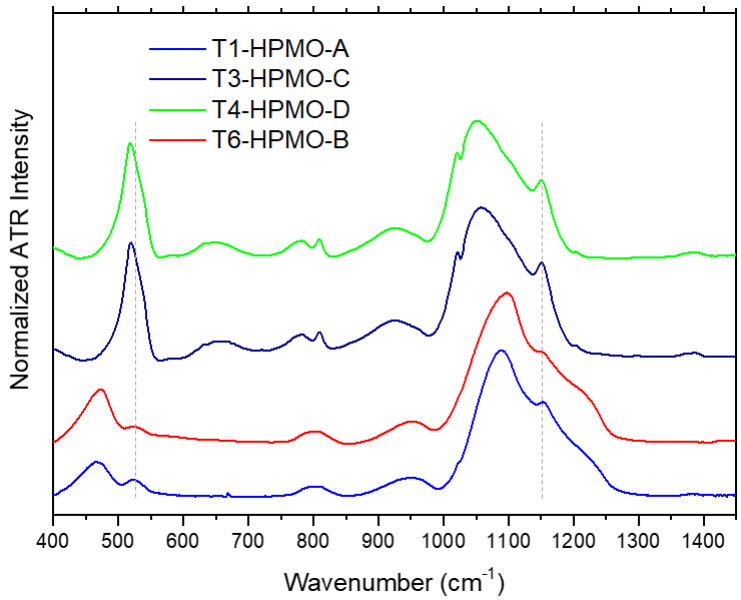

Figure II.44 *FT-IR spectra of the size-tuned phenylene-bridged HPMO NPs in the 400-1400 cm^{-1} region. Spectra are normalized on the ν_{as} Si-O-Si band at 1100 cm^{-1}.*

The latter are also characterized by a broad peak in the 1000-1200 cm^{-1} region and an additional peak at 470 cm^{-1} which is not found in the two other spectra, the latter is assigned to the bending vibration of Si-O-Si and signs that amorphous silica is still present in the sample even after the etching. T3-HPMO-C and T4-HPMO-D have additional peak in the region around 650 cm^{-1}, 808 cm^{-1} that corresponds to C-H vibrations of the aromatic ring, which, according to F. Lin *et al.* [183] correspond to a lack of molecular periodicity by π-π stacking. When the phenylene-

bridged PMO walls are composed of well-arranged aromatic rings, the C-H vibrations in the aromatic rings are blocked and their corresponding vibrations are absent in FT-IR spectra. This is not the case for T3-HPMO-C and T4-HPMO-D. In addition, they exhibit weak bands around 1380 cm^{-1}, assigned to C-H bending vibrations of non-hydrolyzed ethoxy groups (Si-O-CH_2-CH_3) [160], thus supporting the low polycondensation concluded from the downshift. These bands are not found in T1-HPMO-A and T6-HPMO-B. From these results, we can notice that the samples having low π-π interactions (T3-HPMO-C and T4-HPMO-D) are also the ones displaying a very disordered structure and a mixture of mesopore/micropore population.

To conclude, based on the structural analysis performed using nitrogen sorption analysis, SAXS, and FT-IR results on the size-tuned phenylene-bridged HPMO NPs, and despite the structural changes induced by the variation of hard template's surface curvature, no linear correlation with the size could be deduced.

2.5 HPMO NPs prepared using different bridged organosilanes

2.5.1 Single shell

2.5.1.1 Strategy

In order to investigate the effect of the bridged organosilane precursor type on the structural properties of the PMO shell, three precursors other than BTEB are used to prepare HPMO NPs with fixed sizes, obtained using the same silica hard template size (**Fig II.45**).

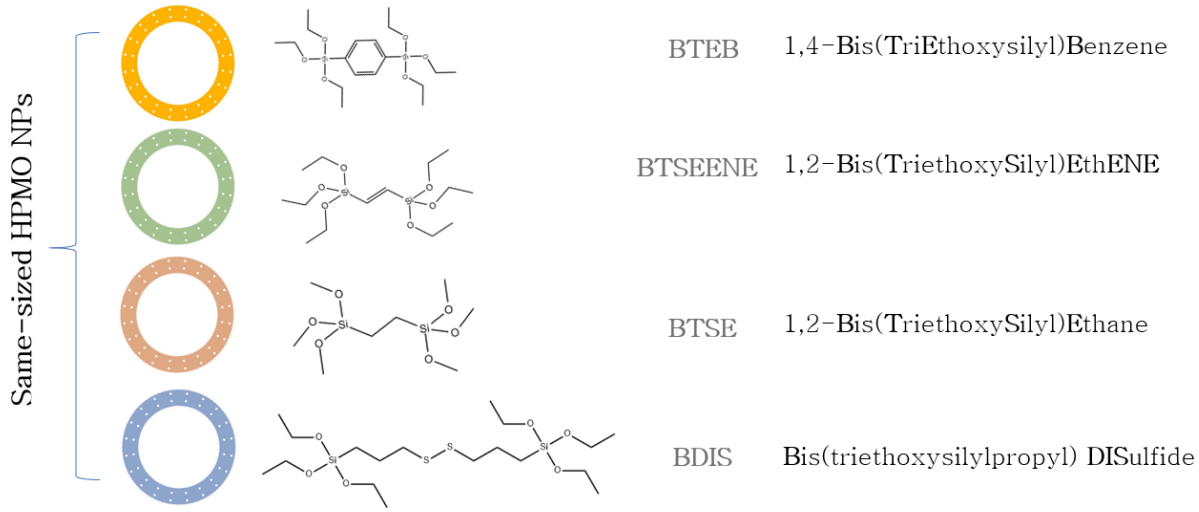

Figure II.45 *Nomenclature of bridged organosilane precursors used to synthesize HPMO NPs.*

2.5.1.2 TEM characterization

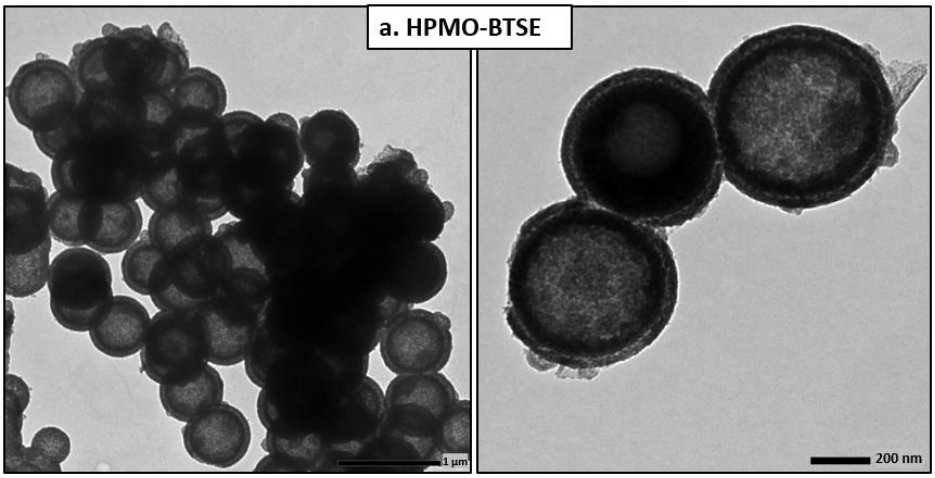

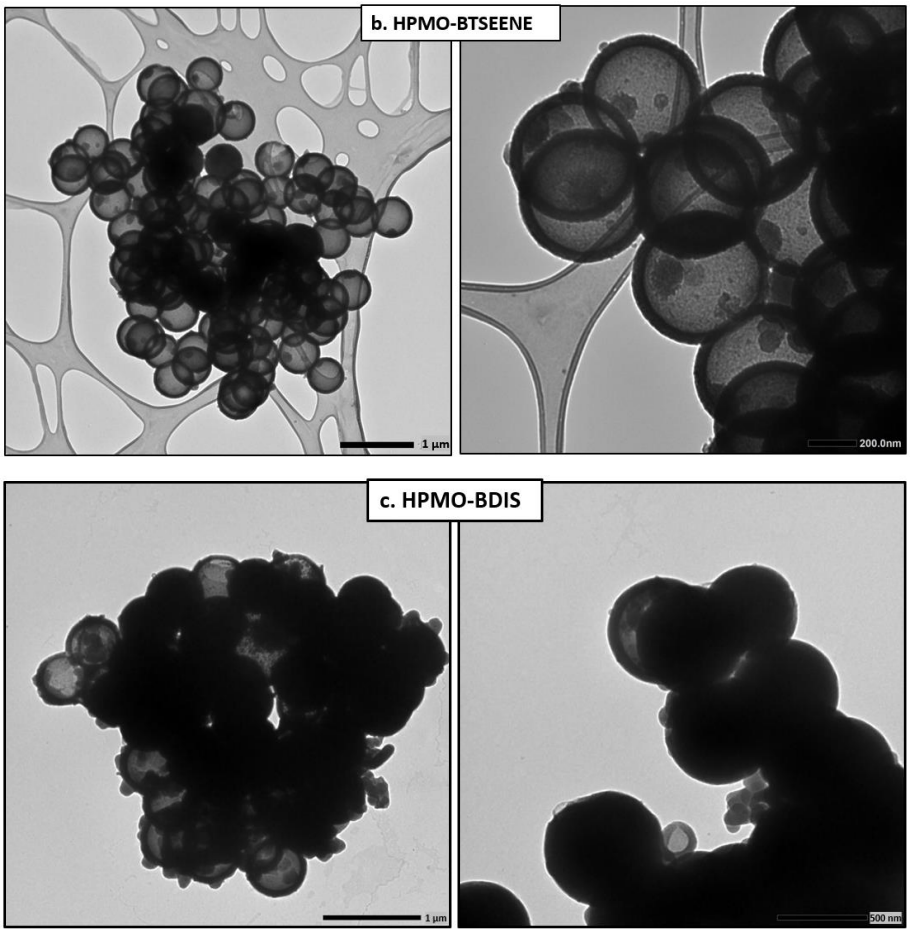

Figure II.46 *TEM images of HPMO NPs prepared with bridged-organosilane precursors other than BTEB.*

HPMO NPs with similar size and different PMO composition are displayed in **Fig II.46**. PMO shells in the distinct samples also have the same average shell thickness as the reference material synthesized using BTEB (T1-HPMO-A). Based on TEM micrograph observation, HPMO-BTSE seems to have a different texture than all the rest of the HPMO, and the shell seems to be quickly fragilized by the etching based on the visible contrast in the PMO shell revealing one grey line between two dark lines that almost look like a double shell, the etching even seems to impact the shell before the silica hard template is totally etched. HPMO-BTSEENE looks similar to HPMO-BTEB (T1-HPMO-A), some leftover of silica hard template can be noticed in the form of small grey nano-objects inside the HPMO. Whereas for HPMO-BDIS, hollow particles are found but most of the observed NPs are not successfully etched even though the same synthesis steps (described in the experimental section) are respected for all the nanomaterials. These differences might be originated from the properties of the mesostructured

shell of every HPMO nanomaterials and are further investigated using nitrogen adsorption and X-ray analysis.

2.5.1.3 Nitrogen adsorption: Specific surface area analysis

Sorption isotherms of HPMO NPs made of different bridged organosilane precursors are shown in **Fig II.47**. T1-HPMO-A (HPMO BTEB), HPMO BTSEENE and HPMO BTSE share the same general features in terms of porosity. Indeed, these materials exhibit a bimodal porosity, as shown by the uptakes at low relative pressure (p/p° between 0.15 and 0.3 which corresponds to pore diameters of ~2 nm) and an inflexion on the adsorbed amounts at high relative pressure which can be attributed to the presence of large mesopores.

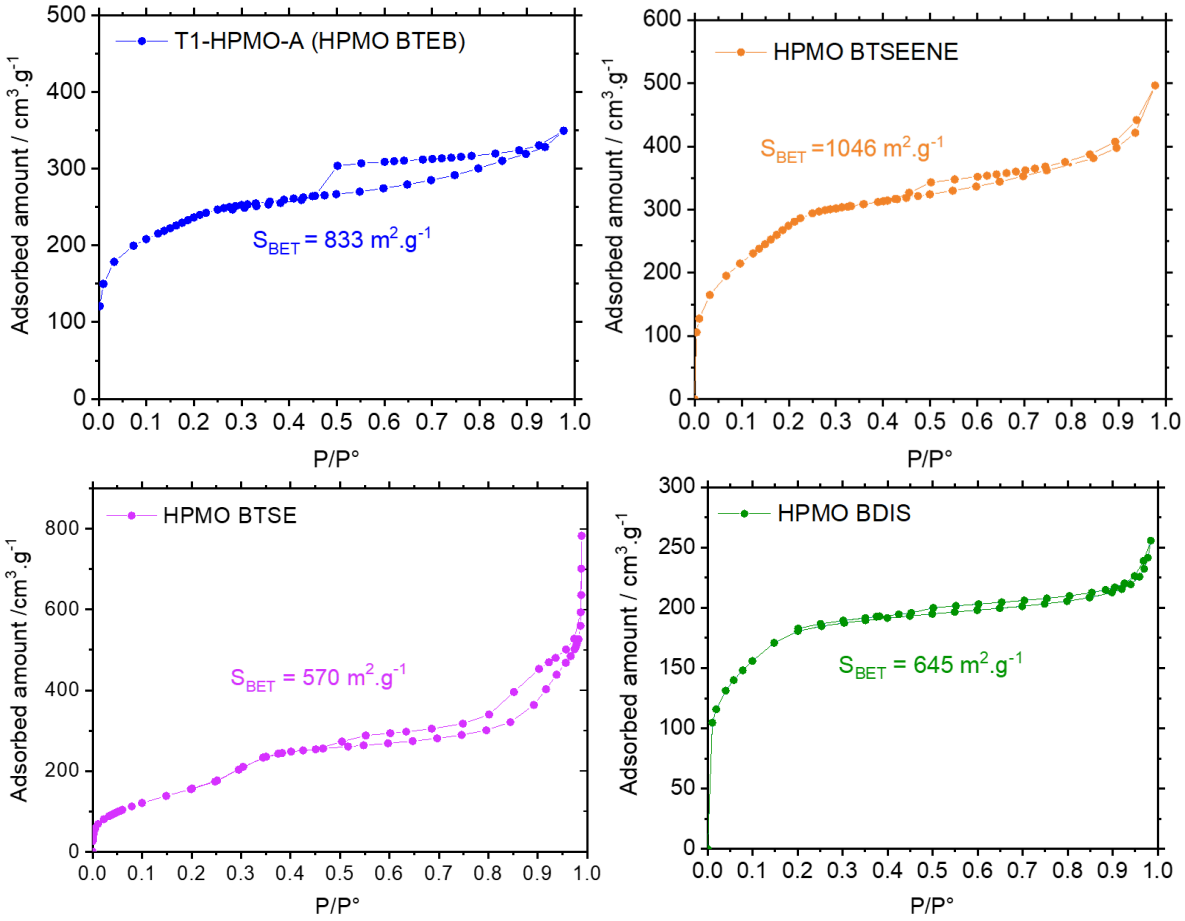

Figure II.47 *Nitrogen sorption analysis of HPMO NPs with different PMO chemical composition. T1-HPMO-A is the reference material corresponding to HPMO BTEB.*

However, these materials also exhibit some differences in terms of specific surface area, which is associated to the different observed porosities. HPMO BDIS is characterized by only an uptake at low relative pressures (p/p° <0.2) which indicates that the structure is principally composed of micropores. As the "knee" of the sorption isotherm is located at a quite high

relative pressure (p/p° = 0.15), these micropores can be likely classified as supermicropores, as they have a pore diameter located between 1 nm and 2 nm. From p/p° = 0.2 upwards, the uptake gradually increased following a monolayer-multilayer mechanism on the external surface of the material up to saturation. This can be evidenced by the flat plateau obtained.

2.5.1.4 Small angle X-ray scattering (SAXS): Mesopores periodicity

SAXS analysis is also performed for HPMO NPs synthesized using different bridged-organosilane precursors. The four samples displayed in **Fig II.48** exhibit the same main peaks at q_0 (100) and $3^{1/2}\,q_0$ (110) diffraction planes typical of a 2D hexagonal phase. Some differences can be observed between the diffraction profiles likes the HPMO BTSEENE and HPMO BTSE having a sharper and more intense peak in the (100) diffraction plane compared to HPMO BTEB. HPMO BTSE have a slightly shifted value of both q_0 and $3^{1/2}\,q_0$, the peaks are also very broad compared to all the other HPMO NPs.

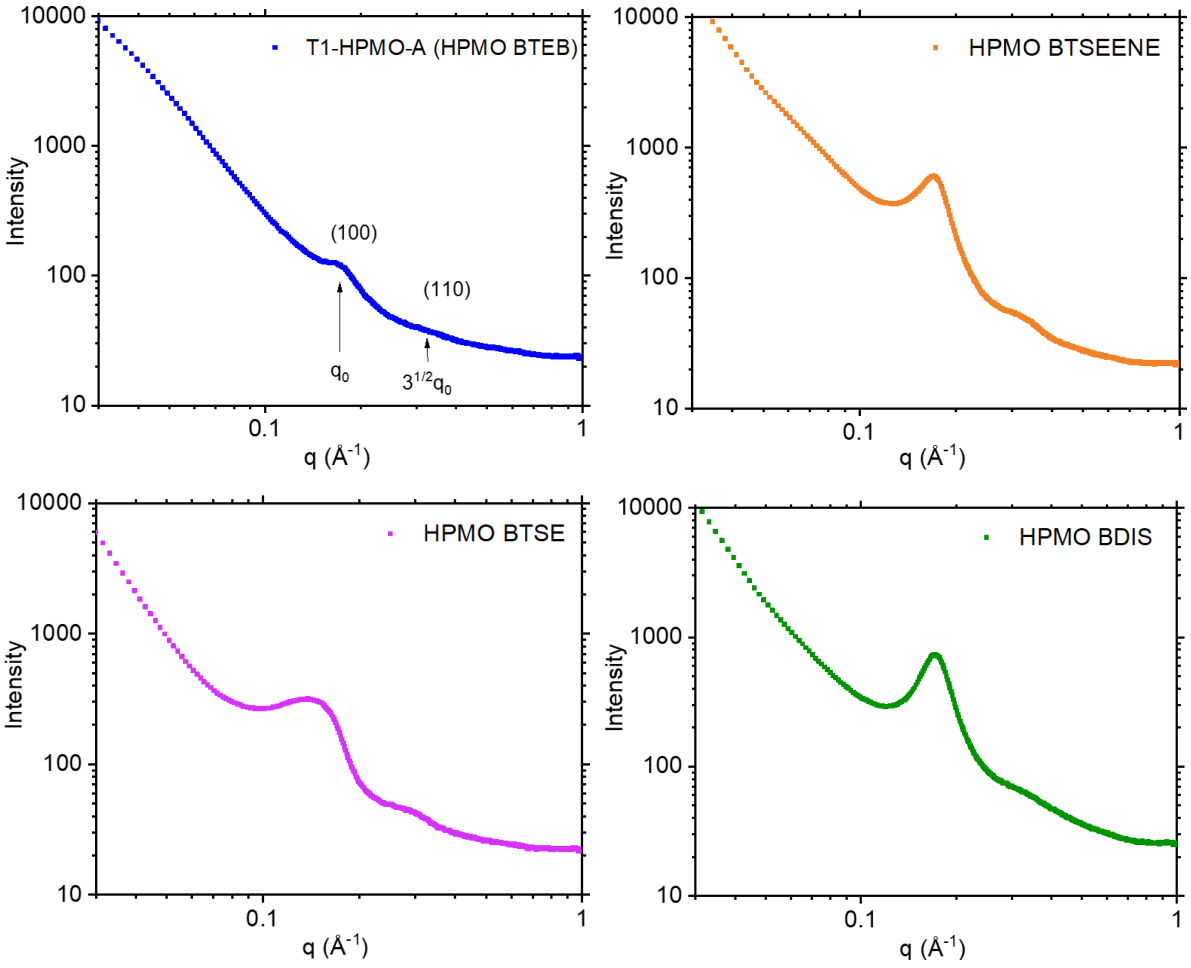

Figure II.48 *SAXS analysis of HPMO NPs with different PMO chemical composition.*

The lattice parameter for HPMO BTSE is therefore higher than that of the other samples (5.2 nm against 4.3 nm), despite using the same surfactant (CTAB) to obtain the mesoporous structure. This suggest that the mesopores 2D hexagonal structuring is conserved by slightly enlarged.

Since the only variable in this experiment is the bridged organosilane precursor, these differences are mainly attributed to the precursor's nature, specifically the type of bridging organic moiety. The difference between the four bridged organosilane precursor molecules is shown in the **Fig II.45**. BTEB have 3 double bonds in the aromatic ring, BTSEENE have only one, BTSE have none and BDIS also have non but a longer bridging moiety.

In a recent study, A. Birault *et al.* [184] investigated the variation of a bulk PMO material structuration as a function of three different bridged organosilane precursors BTEB, BTSEENE, and BTSE (**Fig II.49**). It was shown that PMO is more or less structured based on the flexibility of the organic moiety and that BTEB is the most rigid and is more susceptible for molecular-scale organization thanks the π-π stacking, BTSEENE is semi-rigid with the single double-bond and BTSE is less rigid and is less likely to be organized at a molecular scale.

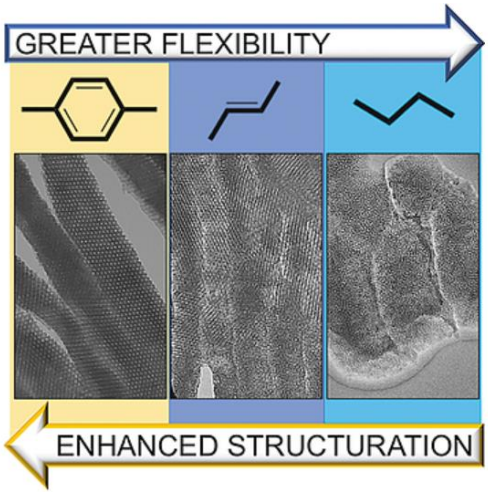

Figure II.49 *PMO structuration as a function of flexibility of the bridged organosilane* [184].

If we extend this argument to the PMO layer deposited on a curved surface, the rigidity of the organic moiety would lead to a contrasting effect. In this case, the curvature of the hard template's surface imposes constraints. The precursor's degree of flexibility might influence the quality of mesopore structuring and molecular-scale organization. Indeed, the most flexible precursor according to A. Birault *et al.* [184] which is BTSE, exhibits at 2D hexagonal structure with very broad diffraction peak indicating that the mesopores size distribution is broad. This

suggests that the precursor's flexibility leads to a slight increase in mesopore size to accommodate curvature, all while maintaining effective structuring. This phenomenon also accounts for the reduced specific surface area. In contrast, HPMO BTEB with the rigid bridging moiety, has the weakest diffraction peaks. HPMO BTSEENE defined as a semi-rigid, have a sharp and intense peak in the diffraction plane (100), reflecting a narrow mesopores distribution (the deviation from the average characteristic distance is not very important compared BTSE), and the 2D hexagonal pattern is also present. Therefore, monodispersed mesopores size and high organization are both obtained with BTSEENE, unlike BTEB and BTSE that exhibit two extreme behaviors.

The rigidity of HPMO BDIS in the other hand, was not discussed but A. Birault *et al*. [184]. However, a reported study by J. Croissant *et al.* [141] showed that it is not possible to synthesize PMO NPs based on 100 % BDIS precursor, and that it is necessary to mix it with another precursor with a good molecular-scale organization capacity, like BTSEENE, and that the ratio of the two components determines the PMO structure. However, the single shell HPMO BDIS was synthesized using 100% BDIS precursor co-assembling with CTAB. Interestingly, the corresponding SAXS diffractogram shows a sharp peak in the diffraction plane (100) and a second one at (110) which indicates the presence of a 2D hexagonal pattern, but surprisingly the adsorption isotherm hardly signs the presence of mesopores and mainly exhibits supermicropores. Besides, when looking at the TEM images of the HPMO BDIS NPs (**Fig II.46 and Fig A.3** appendix A**)**, statistically, there is more non-hollow NPs than hollow ones even after etching. All these points may indicate that the mesopore organization for HPMO BDIS is only superficial. BDIS could be co-assembling with micelles, but the long chain of its organic moiety and the absence of a π-π stacking most likely prevent it from the molecular-scale organization (compared to BTEB). Therefore, the molecular periodicity in the walls is not favored all along the shell thickness, and the formation of radial pores with open endings leading to the interior of the NPs becomes less probable, especially if we consider that the presence of a liquid crystal template facilitates the etching process, as it was suggested by N. Zheng *et al.* [154] (cationic surfactant-assisted selective etching). In contrast, HPMO BTSE appears to be more permeable thanks to its flexibility, and could even allow silica oligomers resulting from etching to re-diffuse through the shell and re-polycondense on the inner side of the shell **(Figure A.3**, appendix A), knowing that alkaline etching using a weak base like Na_2CO_3 is a reversible chemical process.

2.5.1.5 FT-IR analysis

IR spectra of the HPMO NPs made using different bridged organosilane precursors in the region between 400 and 1600 cm^{-1} are displayed in the **Fig II.50.a**. The comparison between spectra of silica NP (SiO_2-HT) and spectra of distinct HPMO NPs suggest that the latter are dominated by silica vibrational features discussed previously. Some differences can be discerned between spectra corresponding to characteristic vibrational fingerprints of each bridged organosilane precursor like the BTEB aromatic ring vibrations at 523 cm^{-1} and the Si-C vibration 1150 cm^{-1}. The Si-C vibration of the BTSEENE, on the other hand, is found in slightly shifted position at around 1193 cm^{-1} [185]. BTSE and BDIS HPMO have some common vibrational signatures related to the presence of CH_2-CH_2 in the organic bridging moiety characterized by the vibrational bands at 852 cm^{-1}, 1166 cm^{-1}, and the Si-CH_2 (ν Si-C) also found for both material at 1270 cm^{-1} [111, 186]. A difference of the band shape from 1000 cm^{-1} to 1300 cm^{-1} is also quite different between spectra, and can be related to the different vibrational patterns of the distinct organic moieties. In the 2000-4000 cm^{-1} region (**Fig II.50.b)**, ν_{as} (C-H) peaks corresponding to non-hydrolyzed ethoxy groups of the precursors are more visible in HPMO-BDIS than the rest of materials, whereas ν (O-H) of H_2O and Si-OH peaks are intense in both HPMO-BTEB and HPMO-BTEB, which may indicate that these materials adsorb more water molecules than the others.

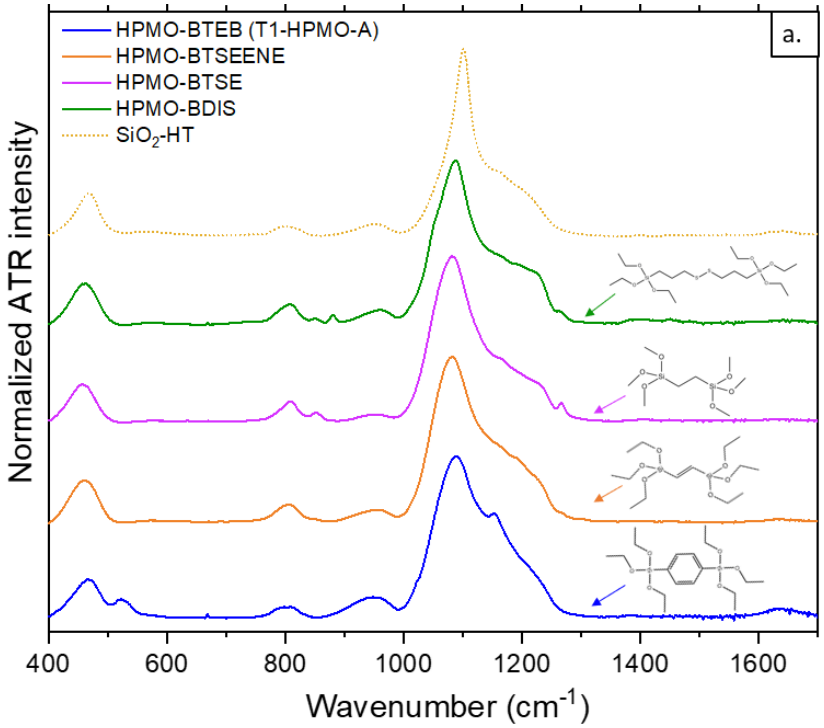

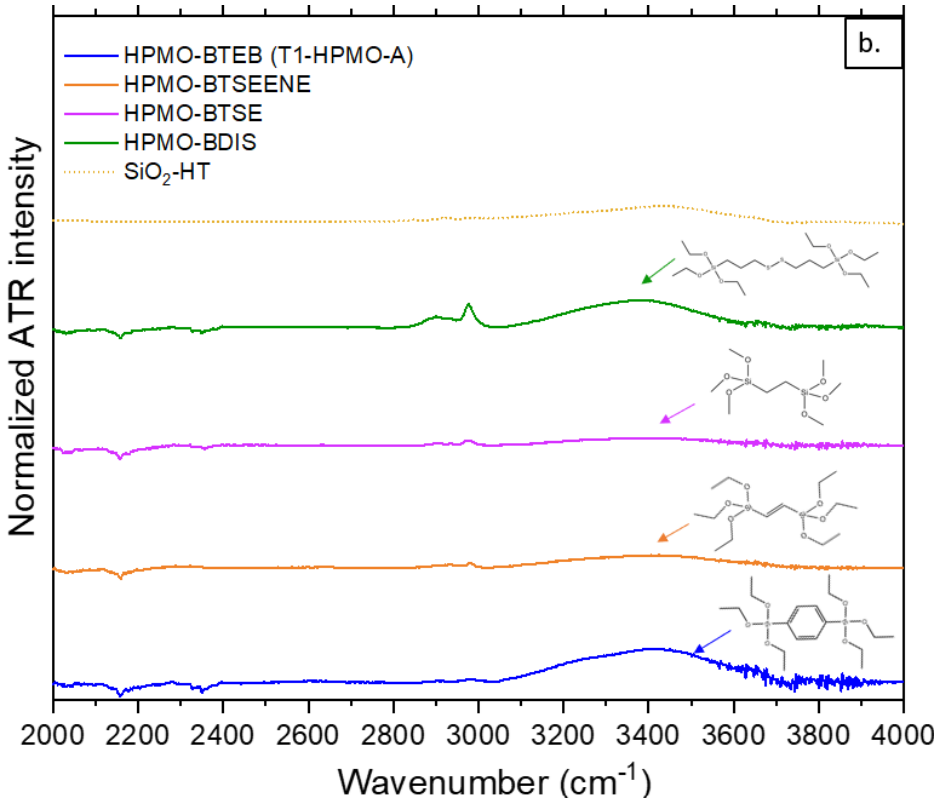

Figure II.50 *FT-IR spectra of HPMO NPs with different PMO chemical composition. The bridged organosilane precursor molecule corresponding to each spectrum is indicated with an arrow.* ***a.*** *In the 400-1600 cm^{-1} region.* ***b.*** *In the 2000-4000 cm^{-1} region.*

In summary, this approach has allowed us to highlight the interrelationship between (i) the mesopores structuring and distribution, (ii) the flexibility of the bridging moieties and their molecular scale structuring, and how it conditions the specific surface area and the permeability of the shell.

2.5.2 Toward a double-shell nanoplatform

The purpose of creating a double-shell structure is to multi-functionalize the platform by the use of a second PMO layer of a distinct chemical composition that can host a different molecule than the first shell for instance. The feasibility of the PMO double shell structures is not widely mastered and the attempt to make one is verified in this part of this chapter. After validating the possibility to tailor the size of HPMO NPs only by modifying the size of the hard template, the same strategy could be used to obtain double-shelled HPMOs with a well-defined range of size.

The main motivation behind creating a double shell structure for this work is to be able, in future works, to graft gold NPs in the PMO shell that could be utilized to exalt the UCNP

performance through surface plasmon resonance demonstrated in the literature. For this, BTEB HPMO NPs (T1-HPMO-A type) is first synthesized, on which is added a second layer composed of a mixture with molar percentage of 75% of BTSEENE and 25% of BDIS **Fig II.51**. In a previous reported work, J. Croissant *et al.* [141] showed that it is not possible to obtain a PMO structure using 100% of BDIS as a precursor and that it must be necessarily mixed with another bridged organosilane to form a PMO. For this reason, in the current work, BDIS is mixed with BTSEENE.

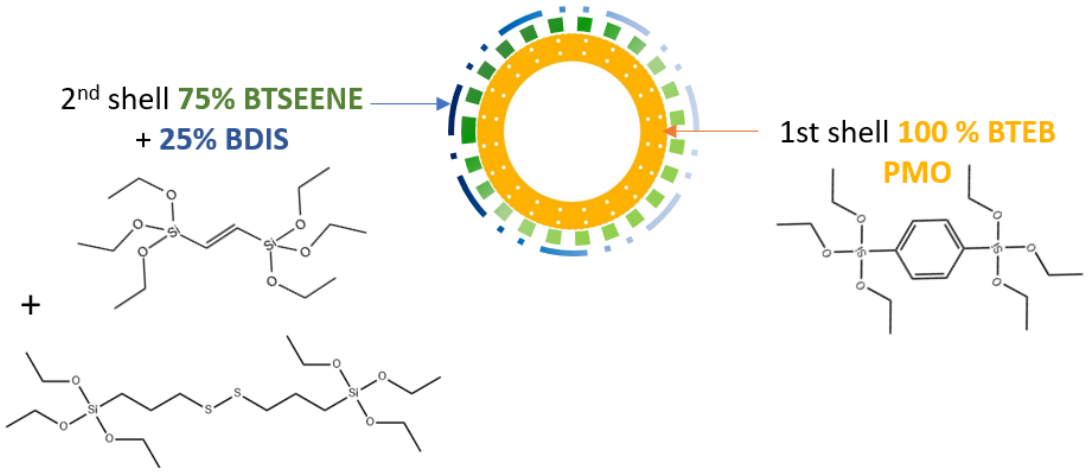

Figure II.51 *Representative scheme of the double-shell PMO nanoplatform.*

2.5.2.1 Microscopy analysis

HRTEM image in **Fig II.52.a** show clearly the hollow structure with a double-shell PMO and a void between the two layers in all the present NPs. This void is less clear in the nanoparticle in **Fig II.52.c.** The mapping of Si, O and S elements show a very dense distribution of Si and O in the shell of the HPMO and less in the central zone that correspond to the back of the hollow nanoparticle. The S element is also present in the shell, indicating a successful integration of the disulfide moieties of BDIS inside the second shell BTSEENE PMO. Given the low molar percentage of BDIS (25%) compared to BTSEENE (75%) as shown in **Fig II.52.c**, the density of S in the red elemental map is relatively low and occupy only a small portion of the overall PMO shell.

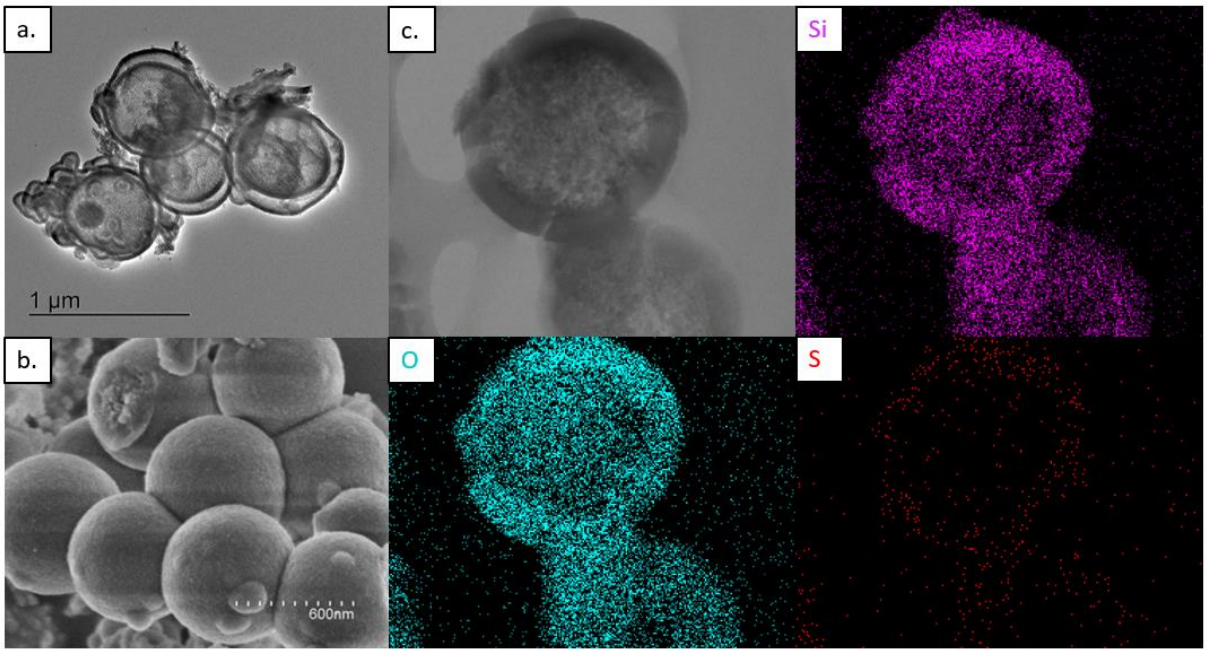

Figure II.52 *Images of the double-shell HPMO obtained using* ***a.*** *HRTEM,* ***b.*** *SEM and* ***c.*** *Elemental analysis using STEM-EDX with the grey picture being the electronic image, and the corresponding elemental map of silicon (pink), oxygen (blue) and sulphur (red).*

2.5.2.2 FT-IR analysis

IR spectra of the as-prepared double-shell HPMO NPs DS-BTEB-BTSEENE/BDIS composed of a first BTEB shell and second 75% BTSEENE/25% BDIS is displayed in **Fig II.53**. When compared with spectra of the single shelled BTEB HPMO and BTSEENE HPMO, both fingerprints of the Si-C vibrations of the organic moieties are found in the double shell spectra around 1150 cm^{-1} and 1193 cm^{-1}, besides the aromatic ring deformation at 520 cm^{-1}.

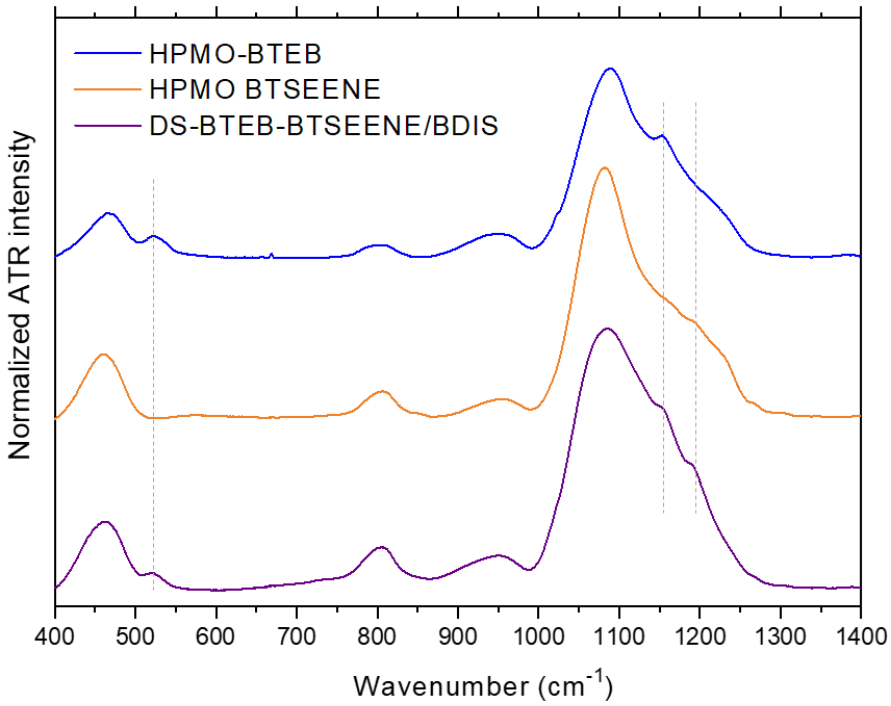

Figure II.53 *FT-IR spectra of the as-prepared double-shell HPMO NPs compare with the single shells HPMO BTEB and HPMO BTSEENE.*

2.5.2.3 Textural analysis

N_2-sorption isotherm of the double shell HPMO NPs displayed in **Fig II.54.a** is very similar to the isotherm of the single shelled of HPMO BTEB (T1-HPMO-A) in **Fig II.42**. It is a mixture of type I and type IV isotherms and a hysteresis loop type H3. The low p/p° region show very low nitrogen uptake, meaning that the presence of micro-porosity is very low. The steep substep around $p/p^\circ = 0.2$ observed for previous HPMO materials is present. The uptake in the region is very important, which indicates the presence of a large amount of mesopores. The S_{BET} calculated for this double shell HPMO is 932 m^2/g which is slightly higher than the single shell HPMO BTEB alone. The SAXS diffractogram in **Fig II.54.b** shows a broad peak assigned to the (100) diffraction plane with a valued of q_0= 1.5 nm^{-1} corresponding to a characteristic distance of 4.1 nm and a unit cell parameter a= 4.8 nm. These values are slightly higher than HPMO BTEB. The second diffraction peak of the (110) is hardly discernable.

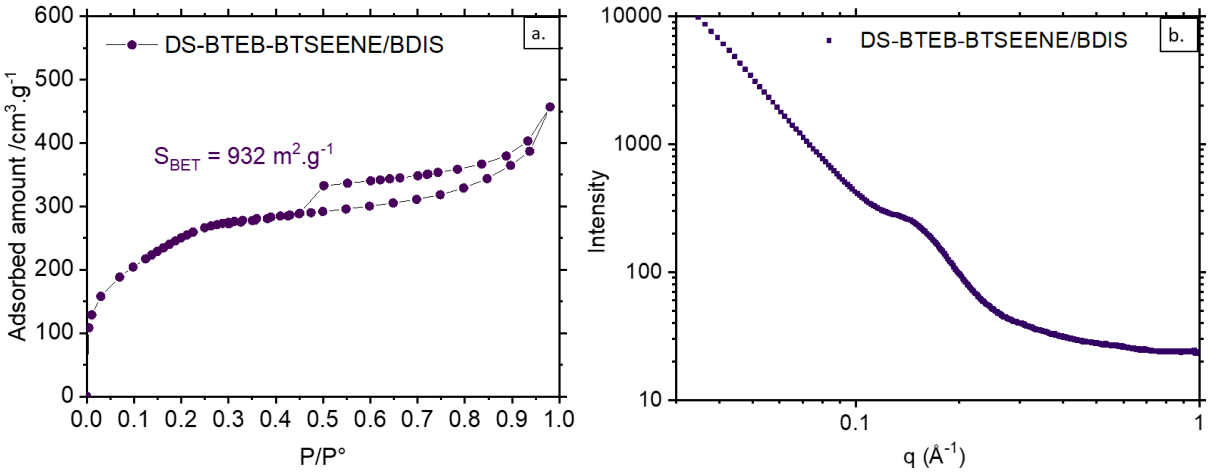

Figure II.54 a. *Nitrogen sorption analysis,* ***b.*** *SAXS analysis of the as-prepared double shell HPMO NPs.*

In conclusion, the incorporation of the disulfide propyl moiety in the BTSEENE mesostructured framework was successfully achieved. This incorporation led to the modification of the structural arrangement of mesopores within the second shell, as it can be deduced from the SAXS profile of this samples, exhibiting a single broad diffraction peak, a big downshifted compared to the previous materials. The double shell nanoplatform where one hollow particle is mobile inside another hollow particles is only observed in some few NPs (**Fig II.52.a**), and could be obtained for a bigger number of NPs using a more intense etching. Indeed, the first hollow double-shell NPs to be reported was by Z. Teng *et al.* [187] who obtained hollow structures with spaced multilayers by performing an etching in hydrothermal conditions. In perspective, the molar ration between BDIS and BTSEENE can be adjusted in a way to control the amount of gold to be grafted using thiol functional groups.

2.6 Experimental section

2.6.1 Synthesis of phenylene-bridged HPMO NPs with different sizes (HPMO BTEB)

2.6.1.1 Hard template synthesis

In a 100 ml two-necked flask, a mixture of 2 mL of deionized H_2O, 1.2 mL of TEOS and 0.7 mL of NH_4OH (25%) are dissolved in 15 ml of absolute ethanol. The temperature is set to 30 °C and the mixture is left to react for 1h under a 750-rpm magnetic stirring. The amounts of H_2O, TEOS and NH_4OH are modified according to the Table II.3 (2.4.2) to obtain silica NPs with different sizes.

2.6.1.2 PMO layer deposition

- In the case T1-HPMO-A (reference sample)

To the pot containing silica NPs, a mixture of 24 mL of deionized H_2O, 2 mL of absolute ethanol, 0.672 mL of NH_4OH (25%) and 64.1 mg of CTAB, is added drop wise. The mixture is left to stir for 40 mins at 30 °C. Then, the temperature is switched to room temperature and 0.2 ml of BTEB (0.504 mmol) is added. The reaction is left for 6 h.

- In the case of T3-HPMO-C, T4-HPMO-D and T6-HPMO-B

After 1 h of reaction, silica seed are first collected by high-speed centrifugation (10000-16000 rpm), and washed with water twice before re-dispersing them in the new mixture of water/ethanol with amounts described in Table II.4 (2.4.3). The reaction is left for 6 h.

- In the case of HPMO-A SE (without ethanol)

After the synthesis of silica hard templates, the latter are collected by centrifugation and washed with water, then re-dispersed in a mixture of 24 mL of deionized H_2O, 0.672 mL of NH_4OH (25 %) and 64.1 mg of CTAB, and left to stir for 40 mins at 30 °C. After that, the temperature is switched to room temperature and 0.2 mL of BTEB (0.504 mmol) is added. The reaction is left for 6h.

2.6.1.3 Hard template etching

After the 6 h of PMO deposition, the NPs are collected, washed with water, and re-dispersed in a solution of 3.18 g of Na_2CO_3 in 50 mL of deionized water. The temperature is set to 80 °C and the etching is left for 1h under 750 rpm stirring. Then, the NPs are collected by centrifugation and washed 3 times by deionized water.

2.6.1.4 CTAB removal

The collected NPs are re-dispersed in a solution of 1 mL of HCl (35%) in 80 mL of ethanol, the temperature is set to 80 °C and the reaction is left overnight under reflux. The NPs are then collected and washed several times by water/ethanol.

2.6.2 Synthesis of HPMO NPs using different bridged organosilane precursors

The synthesis steps of HPMO-BTSE, HPMO-BTSEENE, HPMO-BDIS are the same as HPMO BTEB (T1-HPMO-A) except the volume of precursors should be adjusted to the same molar amount (0.504 mmol). 0.185 mL, 0.184 mL and 0.232 mL respectively. Silica etching and CTAB removal steps are the same as described above.

2.6.3 Synthesis of the double shell HPMO NPs

First, HPMO BTEB (T1-HPMO-A) is synthesized. Here the PMO BTEB deposition is left for 2h, after which a mixture of 0.138 mL BTSEENE (0.387 mmol, 75%) and 0.058 mL BDIS (0.126 mmol, 25%) is added simultaneously, using two propipettes at once. Then the NPs are collected, the etching step and CTAB removal are performed the same way as described before.

2.7 Conclusion

In this chapter, we focused on the development of core-shell structures of nanometric dimensions. The nanostructures were developed from size-controlled silica nanoparticles (NPs) encapsulated in a Periodic Mesoporous Organosilica (PMO) shell. We were then interested in investigating the relationship between the structure and physicochemical properties of these low-dimensional systems.

The first objective was to demonstrate the ability to build nanosized core-shell systems. This involved two main challenges. The first one was the preparation of monodisperse silica NPs serving as hard templates following the Stöber process, and the deposition of the PMO shell on the silica NPs all the while maintaining the homogeneity and the uniformity of the sample. We show that the control of the PMO deposition in a way to avoid the formation of core-free separately-formed PMO nanoparticles depends on the hard template volume fraction in the total volume reaction.

The second objective was to size-tune HPMO NPs. Herein we demonstrate successful preparation of HPMO NPs with a size ranging from 50 to 500 nm using phenylene-bridged organosilane as precursor, by adapting the PMO deposition process for each size of hard template. It should be noted that the elaboration protocols optimized in this section are transposable to the encapsulation of upconverting nanoparticles (UCNP) serving as nanothermometers, in a PMO layer (**Chapter.III**). Indeed, the results obtained from HPMO systems will contribute in the development of multifunctional nanoplatforms. These nanoplatforms involve the encapsulation of small core/shell nanoparticles (approximately 50 to 100 nm).

A multiscale study of the structural properties of the NPs based on their diameter was performed using electronic microscopy (SEM, TEM, HRTEM), X-ray diffraction, FT-IR and nitrogen sorption analysis. The different NPs exhibit a disordered 2D hexagonal mesopore structuring, which seem to be strongly affected by the mesopores/micropores population distribution. IR results suggest that the samples having low π-π interactions are more likely to have a disordered mesopores structuring.

Additional analysis was conducted on HPMO NPs synthesized in the presence and in the absence of ethanol as a solvent. Here the size of mesopores appeared strongly affected by this parameter. The absence of ethanol serving as a solvent, and the systematic release of ethanol during the early stage of the sol-gel reaction, lead to the participation of alcohol molecules with short alkyl chain in the role of co-surfactant alongside CTAB. This causes an increase of the packing parameter and an enlargement of micelles.

The third objective was to prepare HPMO NPs with tuned PMO composition having similar mean sizes and shell thicknesses. It was achieved simply by varying the bridged organosilane precursor used in the reaction, while fixing all the other reaction parameters, including the molar amounts of the different precursors. We have demonstrated the feasibility of preparing such nanoparticles using BDIS, BTSEENE and BTSE precursors. However, some issues still need to be tackled. We could notice in some samples that some NPs are still holding the hard template even after the etching step. While for other samples, HPMO BDIS for instance, the hard template has not been removed for most of the NPs. This raises a question about the real mechanism behind the etching process, whether it is only time-dependent or structure dependent as well, and whether the mesopores structuring affects the permeability of the shell and consequently the etching quality.

After conducting a multiscale analysis, we proposed that the structure of the PMO shell, as determined by the distribution of mesopore sizes and their arrangement, is primarily influenced by the size of the hard template. This template size alters the curvature of the structure. It is also conditioned by the flexibility of the bridging organic component of the selected bridged organosilane precursor.

Finally, the synthesis of the double mesostructured shell was tried out. The first layer is BTEB-based and the second layer is made from a mixture of BTSEENE and BDIS. The incorporation of disulfide moieties was confirmed from the elemental analysis using EDX. This method can serve for additional multifunctionalization like gold NPs grafting.

Chapter III.

Encapsulation of $NaYF_4$: Er, Yb-based upconverting nanothermometers in a PMO shell

3.1 Introduction

In the previous chapter, the synthesis of Hollow Periodic Mesoporous Organosilica Nanoparticles (HPMO NPs) using a dual templating strategy, with well-defined size and PMO chemical composition were the object of structural properties' investigation. They will serve as a model system to construct a more complex nanoplatform, by following a similar synthesic approach (**Fig III.1**).

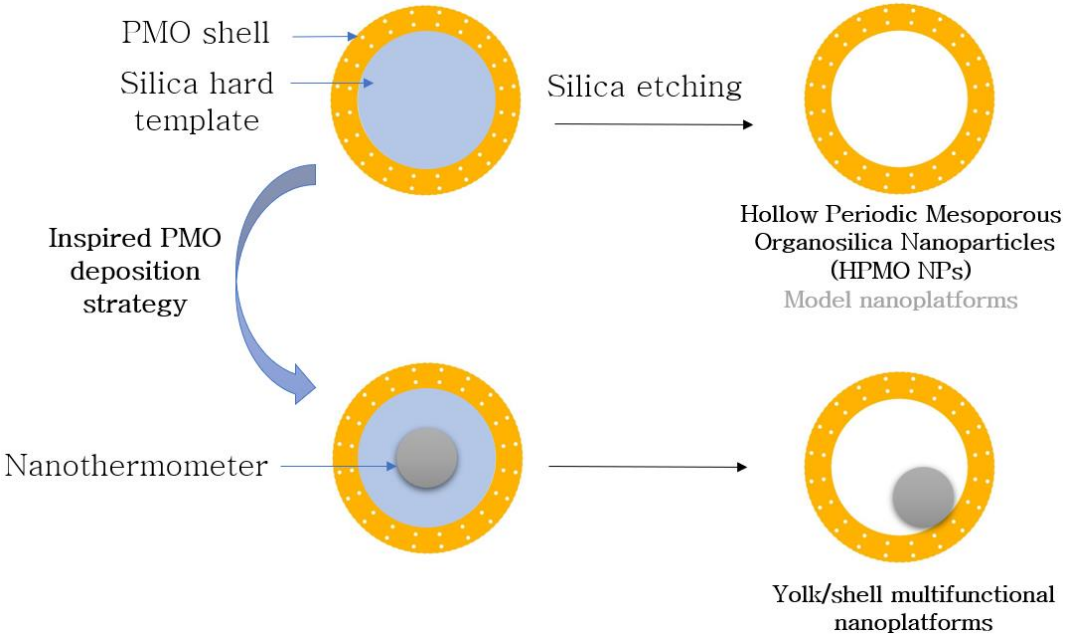

Figure III.1 *Schematic representation of HPMO NPs synthesized using the hard template strategy as model nanoplatform to synthesize multifunctional nanoplatforms.*

Indeed, the current interest in nanoplatforms design has expanded beyond the basic core/shell structure and led to an emerging new generation of complex nanostructures targeting limitless possibilities of multi-functionalization. During the past decade, many kinds of sophisticated nanoplatforms were conceived and introduced to nanomaterials field, bringing a wide range of potential applications to explore. Among them the core/multi-shell nanoplatform, the yolk shell or the nano-rattle, the satellite-core/shell (multi-core inside the same shell) and the Janus nanomaterials [188, 189], all illustrated in **Fig III.2**. These structures hold many advantages like the possibility of hierarchical multi-functionalization, a high surface to volume ratio that could be further enhanced by adopting a mesostructured shell, and an impressive versality.

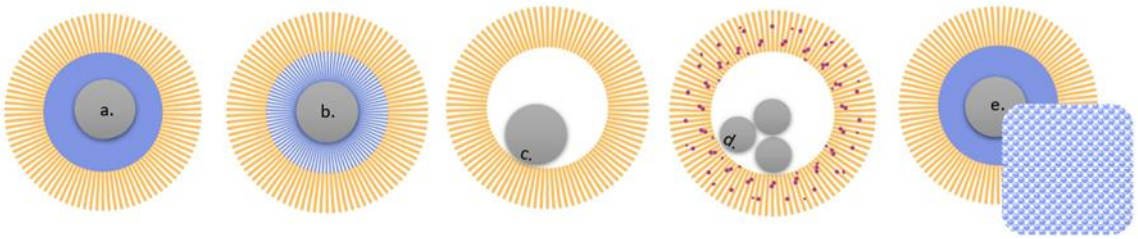

Figure III.2 *Schematic representation of different types of multifunctional nanoplatforms.* ***a.*** *Functional core encapsulated in a first dense silica-shell and a second layer of mesoporous silica/hybrid silica, the dense silica can be considered as a hard template and is therefore sacrificial leading to (c) after etching [190 - 195].* ***b.*** *Double-shell of mesoporous silica/hybrid silica (PMO) shell using different precursors [196].* ***c.*** *Yolk/shell or "nano-rattle" structure with a mobile core inside the mesoporous shell [197 - 199].* ***d.*** *Multi-cores encapsulated in a single mesoporous shell, the purple dots represent the precursor diffusing through the mesostructured interface and reaction inside the nanoplatform to form several cores. This method is called "Ship in the bottle"[199, 200] .* ***e.*** *Janus structure consisting of two totally different kind of nanoplatforms (spherical and cubic or other) merging to form a composite asymmetrical nanoplatform, composed of a functional core inside a layer of dense silica (sacrificial), then a layer of mesostructured silica that can host a hydrophilic molecule, in addition to a mesostructured hybrid silica-based (PMO) nano-cube to host hydrophobic molecules [197, 201, 202].*

The different nanoplatforms continue to receive a special attention in several fields more specifically in biomedicine area for theranostic applications, with the purpose of coupling both diagnostic (bioimaging, nanothermometry) and therapy (drug delivery, PDT, etc.) functionalities within the same nanoplatform. Many published works have expressed such interest and addressed distinct challenges concerning the application of these systems [139, 203 - 205], like how these nanoplatforms can be chemically and structurally designed in order to host a specific kind of therapeutic molecule for instance or to construct a nanoreactor. Other concerns are centered around the mastering of the size/shape tuning of such complex system while maintaining uniformity, biocompatibility and good dispersibility. The easily accessible functionalities clearly multiply the number of issues to deal with to create a complete nanoplatform, and the strategies to prepare them as well.

The aim of this chapter is to synthesize a multifunctional nanoplatform consisting of a functional core acting as a nanothermometer confined in hierarchical double-layer of silica/hybrid silica frameworks through a three-steps approach.

These three steps are addressed in this chapter:

1) The synthesis of UpConverting NanoParticles (UCNPs) serving as functional cores.

2) UCNP encapsulation in the first layer of amorphous silica (SiO_2).
3) UCNP-SiO_2 encapsulation in the second PMO layer which is of the same nature of an HPMO shell.

The following section is dedicated to the synthesis of $NaYF_4$: Er, Yb UpConverting NanoParticles (UCNP). Some strategies reported in the literature are described.

3.2 Elaboration of $NaYF_4$: Er, Yb (UCNP)

3.2.1 Synthesis strategies

$NaYF_4$: Er,Yb was for the first time reported as an efficient upconverting phosphor in 1972 by N. Menyuk *et al.* [206] It was prepared upon heating a mixture of ultra-pure Ln fluorides (YF_3, YbF_3 and ErF_3) up to 750 °C in HF gas, before adding a 20-wt% of dried NaF. It was next placed in a platinum crucible and heat treated at 200 °C then at 1000 °C under argon atmosphere. In 1998, N. Martin *et al.* [207] prepared $NaYF_4$: Yb, Pr microcrystals using a co-precipitation of Ln^{3+} oxides with NaF with no post thermal treatment. The transformation from cubic to hexagonal phase was slowly achieved by heating at 80 °C for 15 days. Later on, L. Liang *et al.* [208] reported the synthesis of hexagonal doped and undoped $NaLnF_4$ under mild hydrothermal conditions (220 °C), using a teflon-lined stainless-steel autoclave. The reaction lasted for 2 days.

Since 2003, many research groups have been developing new strategies to synthesize nanosized spherical $NaYF_4$: Er, Yb with controlled size and morphology, especially with the growing interest of using upconverting materials in biological applications. The first $NaYF_4$: Er,Yb nanoparticles were prepared by G. S. Yi *et al.* [209] by a co-precipitation method using EDTA (Ethylene Diamine Tetraacetic Acid) as chelating agent to form complex with RE with the aim to separate between growth and nucleation stages to obtain uniform particles as postulated by LaMer [101]. The size distribution of the nanoparticles could be controlled from 37 to 166 nm by varying the EDTA amounts. However, this strategy requires a post treatment reaching 600 °C to obtain the hexagonal phase, which is detrimental since heating at such high temperatures leads to agglomeration, particle size modification and mixed hexagonal and cubic crystal phases. Moreover, EDTA can be carbonized due to annealing. Consequently, surface modification using any organic ligand is subject to carbonization. The sought

hydrophilic/hydrophobic character of nanoparticles surfaces is therefore suppressed, and redispersion in organic/inorganic solvents becomes difficult, as well as multi-functionalization using core/shell systems. To address this, Zeng *et al.* [210] followed the solvothermal route with the use of the teflon-lined autoclave to obtain β-$NaYF_4$: Er,Yb, because it enables the utilization of relatively low temperatures (140-200 °C), thanks to the additional pressurization created inside the autoclave which helps to increase the solubility of solids above the critical point of the solvent [211], along with using EDTA for particle size control. They also report the use of CTAB dissolved in ethanol to move from spherical to rod-shaped upconverting nanomaterials, promoted by the worm-like micelles. One of the advantages of the solvothermal route is that the reaction composition can be adjusted in several ways to tune the surface chemistry, the shape and the size of β-$NaYF_4$: Er, Yb, while still operating at low temperature. In this scheme, organic additives including chelating agents and polymers like EDTA, CTAB, PVP or PEI are used to produce hydrophilic UCNP following what is referred to as the hydrophilic ligand-assisted solvothermal method, while organic additives like oleic acid are used for the hydrophobic ligand-assisted solvothermal method. Organic additives-free solvothermal method is also possible by using the polyols like glycol, ethylene glycol (EG), diethylene glycol (DEG) or glycerol, acting both as high boiling point solvents (198-290 °C) and ligands controlling the UCNPs sizes. D. Chen *et al.* [212] showed that the use of different polyols following the same solvothermal method results in different sizes of nanoparticles. In fact, the length of the polyol chain plays an important role in determining the size of the nanoparticle during the growth stage, due to the steric hindrance that prevents reactants to reach nanoparticles. However, the absence of the stabilizing ligands in the case the organic additives-free solvothermal method makes it difficult to totally manipulate the reaction in order to obtain well defined sizes and shapes of NPs, and to re-disperse in any kind of solvent (polar or non-polar). Besides, adsorbed ligands on NPs surface is a prerequisite for post-functionalization. Despite the numerous benefits provided by the solvothermal method, it still presents some limitations when it comes to monitor the synthesis process and have more insight into nanoparticles formation mechanism. That is because the autoclave is not as transparent as a chemistry flask, and it should remain closed throughout the whole reaction. Consequently, sampling becomes unfeasible. In addition to this, specialized autoclave vessels often come with a high cost.

Since 2006, a new strategy to synthesize highly crystalline and monodisperse $NaYF_4$: Er,Yb nanoparticles using thermal decomposition has been explored [213], pioneered by G. S. Yi *et*

al. [214] and inspired from J. E. Roberts' [215] method to decompose lanthanides trifluoroacetates $Ln(CF_3COO)_3$ and form lanthanides fluorides LnF_3 at around 250 to 300 °C, and from Y.W. Zhang *et al.* [216] who performed the thermal decomposition of $La(CF_3COO)_3$ in a mixture of octadecene and oleic acid to control the size and shape of LaF_3 nanoparticles. Similarly, G. S. Yi *et al.* decomposed Ln $(CF_3COO)_3$ precursors (Ln= Y, Yb, Er) providing Ln^{3+} ions and fluorine at the same time, and CF_3COONa as a source of sodium in oleic acid/octadecene mixture (OA-OCD), or in oleylamine (OM) alone. Octadecene is used as a non-chelating high boiling point solvent (315 °C) and oleic acid is used as a long hydrocarbon chain capping ligand that controls the growth of the upconverting nanoparticles and ensures their dispersibility in an organic solvent. Oleylamine can act both as organic solvent and a capping agent [213]. The effect of temperature is also highlighted in the study, where G. S. Yi *et al.* [214] showed by using X-ray diffraction that for 1h reaction, the cubic phase is dominant at 300 °C, whereas at 320 °C a mixture of both cubic and hexagonal is found. The crystal becomes totally hexagonal only at 330 °C.

Z. Li *et al.* [217] suggested a user-friendly method to prepare oleic acid capped β-$NaYF_4$: Er,Yb aiming to avoid the presence of toxic fluorinated species coming from trifluoroacetates precursors or other fluoride reactants like NH_4F, NaF in excess while using high temperatures, and which must be eliminated by extreme ventilation otherwise they threaten the user's safety. The idea is to completely consume the fluoride source at room temperature to form $NaYF_4$ nuclei. For this purpose, stochiometric amounts of NH_4F (fluoride source) and NaOH (sodium source) are dissolved in methanol, and added to a homogenous solution of $LnCl_3$ in a mixture of octadecene and oleic acid and left to stir at room temperature, thus marking the beginning of nucleation. The methanol is subsequently evaporated and the mixture is heated up to 300-330 °C where the growth of crystals on the nuclei takes place. This method is known as the methanol-assisted organic phase, belonging to the thermal decomposition category. It is one of the most attractive routes because it enables the separation between nucleation and growth stages leading to monodisperse and high quality UCNP, in addition to the fact that the decomposition of fluoride reactants no longer presents a danger during the synthesis. Besides, simple inorganic salts precursors like Ln^{3+} chlorides can be used. Before adding methanol solution of dissolved NH_4F and NaOH, $LnCl_3$ must be totally dissolved in the organic mixture of octadecene and oleic acid at 150 °C to form a homogenous solution then left to cool down. However, Ln^{3+} oleate complexes precursors can be prepared to skip the dissolution step and to avoid the difficulty to extract the NaCl by-product [218, 219]. $LnCl_3$ (Ln= Y, Yb, Er) can be

either purchased or synthesized by dissolving Ln_2O_3 in HCl at high temperatures then evaporating the solvent under vacuum. The Ln^{3+} oleate are obtained following J. Park *et al.* [220] method to synthesize oleate metal complexes. Ln^{3+} oleate (Ln-OA) can be directly added to a mixture of NH_4F dissolved in OCD and OA, stirred at room temperature for nucleation, and are boiled at high temperatures to start the crystal growth process.

Only few groups reported the synthesis of β-$NaYF_4$: Er,Yb materials using other techniques like water-in-oil microemulsion in which the size of nanoparticles depends on the size of micelles [221], and the ionic liquid method considered as a "green" route using water instead of organic compounds, and low temperatures (<200 °C) [222]. These approaches were not extensively investigated because of very weak control over nanoparticles shape, size and dispersity [223]. In general, thermal decomposition and solvothermal method continue to be the most commonly employed as they provide high yield and high quality UCNP and represents the best candidates for the core/shell type post-functionalization. Information about both methods is summarized in the table below.

Methods	Characteristics	Sub-methods	References
Solvo(hydro)-thermal method	- Hexagonal $NaYF_4$: Er, Yb obtained at lower temperatures (200 °C) compared to the thermal decomposition method. - Adjusted synthetic protocols to obtain both hydrophilic and hydrophobic NPs. - Expensive specialized reaction vessels. - Long reaction time (2h-24h). - Neither reaction tracking, nor sampling can be done.	Organic additives-free (Polyol process: glycol, EG, DEG, glycerol)	[212]
		Hydrophobic ligand-assisted (OA)	[224, 225]
		Hydrophilic ligand-assisted (EDTA, CTAB, Cit^{3+}, PEI, PVP, PAA)	[210, 226 - 229]
Thermal decomposition	- Synthesis in oxygen-free atmosphere and inert gas protection. - High temperature needed (300-330 °C) - High boiling organic solvents and organic additives to stabilize and control NPs size. - Only hydrophobic NPs are obtained, re-dispersible in non-polar solvent like hexane, cyclohexane, or toluene.	Trifluoroacetates precursors	[214, 230 - 233]
		Other precursors (Oleates, acetates etc.)	[218, 219, 234 - 236]

	- Post-synthetic surface modification needed for hydrophilic reconversion. - Versality in controlling the size and shape of uniform, monodisperse and highly crystalline β-$NaYF_4$: Er, Yb, with well understood mechanisms. - Short reaction (60-90 mins) and high yield. - Pure hexagonal phase $NaYF_4$: Er, Yb NPs obtained at temperatures starting from 300 °C.	Methanol-assisted organic phase	[217, [237 - 242]

Table III.1 *Main advantages and drawbacks of solvo(hydro)-thermal and thermal decomposition methods [48, 213, 223].*

3.2.2 Phase, size and morphology tuning of β-$NaYF_4$: Er, Yb

The relevance of the crystallographic structure in determining the luminescence properties of the $NaYF_4$: Er, Yb upconverting phosphors was previously mentioned in **Chapter. I**. It is clear from the overall synthesis strategies cited above that the common motivation relies on finding the optimal method to obtain uniform and monodisperse $NaYF_4$: Er, Yb NPs in the hexagonal phase, which demonstrated remarkable upconverting yield surpassing the cubic phase one. Tailoring the preparation of these NPs with (i) well-defined size and morphology, (ii) a variety of sizes to meet different application demands, is one of the main challenges, which in turn, justifies the numerous synthetic approaches [243].

Most reported works have related these features to the synthesis parameters like the concentration of lanthanides precursors, the fluoride and sodium source [210, 224, 227], the amount and nature of the capping ligand, the choice of solvent, and the crystal doping [58], [244]. Some works have particularly focused their interest in the mechanism of hexagonal $NaYF_4$: Er, Yb formation, through the comprehension of the complex kinetic process governing the nucleation and the growth of the nanocrystal. Y. Li and co-workers [224] reported the role of temperature and NaF to Ln ratio in the control of the particle size of $NaYF_4$: Er,Yb, and stated that the formation of the hexagonal phase, first goes through the formation and the evolution of the metastable cubic phase. In fact, the transition to the thermodynamically stable hexagonal phase only occurs when the system is supplied with enough energy to overcome the dynamical energy threshold, which can be realized by raising temperature [234]. C. H. Yan *et al.* [232] were the first to extensively investigate the nucleation and growth mechanism of $NaYF_4$: Er,Yb nanocrystals to clearly understand how it is involved in the cubic to hexagonal

phase transition (α→β) and its correlation to particle size using the trifluoroacetate approach (**Table III.1**). They postulate that the α→β transition actually does not immediately take place once the temperature reaches 330 °C, but that α nanocrystals goes through a series of changes before transforming into β nanocrystals, which they referred to as the "delayed nucleation pathway". This process can be divided into two possible paths depending on the initial precursor's concentration, described as following:

- **Promoted Ostwald-ripening process (path (A) figure. III.3):** Monomers are few or completely consumed, the smaller nanocrystals quickly re-dissolve and release monomers due to the high surface energy and the high solubility of the thermodynamically unstable cubic phase, and large hexagonal nanocrystals grow at their expense. This effect is known as the Oswald ripening or maturation. It results in a broad NPs size distribution and is therefore not favorable to obtain monodisperse NPs with predictable size.

- **Restricted Ostwald ripening process (path (B) figure. III.3):** When monomers of (CF_3COO) Na are used in enough quantity or in excess, the Ostwald ripening process is restricted, meaning that the small cubic phase nanocrystals are rather stable and do not re-dissolve because their growth rate is higher than the larger ones. The particle size increases in a uniform way at the same time as phase transition, as long as the monomer concentration and the temperature thresholds are reached.

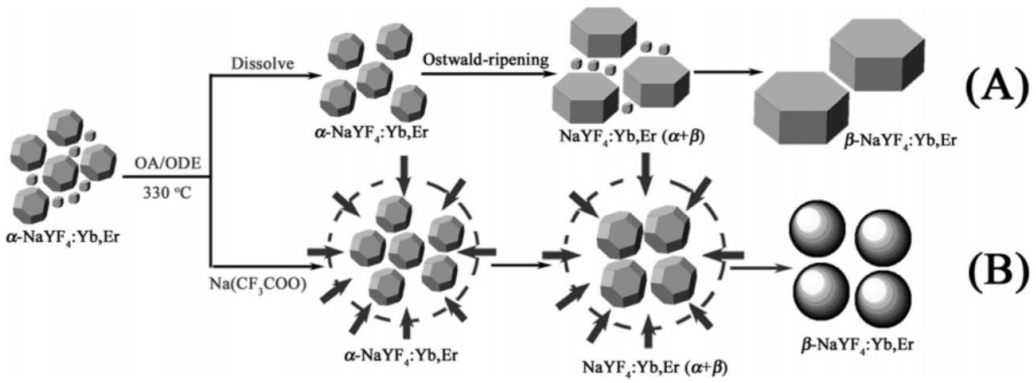

Figure III.3 *Schematic representation of the two possible pathways of α→β phase transition of $NaYF_4$: Er,Yb nanocrystals during nucleation and growth stages with* ***(A):*** *Promoted Ostwald-ripening process and* ***(B):*** *Restricted Ostwald-ripening process [232].*

M. Haase *et al.* [245] also studied the nucleation/growth processes, and further investigated the role of precursors concentration in ruling α→β phase transition. Thermal decomposition using oleate precursors were used, and several β-$NaYF_4$: Er, Yb batches were prepared by varying NaF/Ln^{3+} ratio where x in $Na_{1-x}YF_{4-x}$ is ranging between 0 to 4/9. The results show that the sodium content plays a crucial role in the nucleation of the β phase NPs. In fact, when the latter is low, nucleation of the β phase follows an Ostwald ripening process as described by C. H. Yan *et al.* [232], (α→β) phase transition is therefore incomplete which results in mixed phase and broad size distribution of NPs. When the system is sodium-deficient with even low NaF to Ln^{3+} ratio, the α→β phase transition does not occur at all even after long time heating at high temperature. When adding more sodium and fluoride precursors to all the sodium-deficient systems, a complete transition to β phase successfully happened. In contrast, when initially using increased NaF to Ln^{3+} molar ratio, monodisperse and very small (sub-10 nm) β-$NaYF_4$: Er, Yb are obtained, and the size can be further decreased by increasing the molar ratio. Finally, we can conclude from M. Haase *et al.* [245] and C.H. Yan *et al.* [232] reports that size, phase transition, NPs monodispersity (broad or narrow) and uniformity (mixed or pure phase) are ruled by one of the nucleation and growth modes of α nanocrystals schematized in **Fig III.3**, dictated by the stochiometric NaF to Ln^{3+} molar ratio, for doped ($NaYF_4$: Er,Yb) and undoped ($NaYF_4$) material.

In 2010, X. Liu *et al.* [58] reported a novel approach for a simultaneous control over the phase and the size of $NaYF_4$: Er, Yb by doping the crystal lattice with Gd^{3+}. It was demonstrated that when the low-symmetry cation sites known to be occupied by either Na^+ or Ln^{3+} (Y, Yb, Er), with Y^{3+} (r = 1.159 Å) being replaced with larger radius lanthanide ions like Gd^{3+} (1.193 Å), the electron cloud distortion becomes more important and the hexagonal phase crystal transition is consequently favored even at temperatures lower than the α→β transition normal temperature threshold (300-330 °C). Indeed, X. Liu *et al.* [58] showed that it is possible to synthesize spherical, monodisperse and pure phase β-$NaYF_4$: Er,Yb using the methanol-assisted organic phase thermal decomposition (**Table III.1**) at 230 °C when doping with 30 % of Gd^{3+}. Whereas the same synthesis in the absence of Gd^{3+} does not even enables the nucleation α phase, and yields only NaF crystals. This approach also enables the tuning of NPs size below 10 nm which is explained by the fact that electron charge density increases on the surface of the nanocrystals as a result of replacing Y^{3+} by Gd^{3+} which generates F^- ions repulsion, and limits their diffusion to the surface of the nanocrystal. Doping with Gd^{3+} does not interfere with the upconversion

process of the sensitizer-activator pair Er, Yb responsible of the strong green emission, because its energy gap goes well beyond the Er, Yb one, and the lowest excited level of Gd^{3+} ($^6P_{7/2}$) emits in the UV region. Likewise, Y. Zhang *et al.* [239] used the same principle of the surface electron density to produce the inverse effect and increase uniformly the particles size of β-$NaYF_4$: Er,Yb by using Lu^{3+} as a doping agent because it has a smaller ionic radius than Y^{3+} and does not interfere with Yb-Er upconversion neither. Size tuning of β-$NaYF_4$: Er, Yb from 20 nm to 200 nm was reported, by varying doping level of Lu^{3+} from 0 to 50 %.

In the next section, two synthesis routes from the ***Table III.1*** *are tested in order to achieve uniform and monodisperse pure hexagonal phase of $NaYF_4$: Er, Yb: a pseudo hydrothermal method using PEI, and the thermal decomposition method.*

3.2.3 Synthesis of β-$NaYF_4$: Er, Yb NPs

3.2.3.1 Hydrophilic-ligand assisted route using PEI

The first attempt to synthesize $NaYF_4$: Er, Yb NPs in this work was performed by a modified PEI-assisted route reported by X. liu *et al.* [228] where PEI (Polyethylenimine) is used as capping agent to control the size of NPs besides being a biocompatible polymer and offers a potential path for post functionalization [48]. The protocol was modified by replacing the Teflon-line autoclave by a 100 mL three-necked flask (pseudo hydrothermal), increasing the temperature up to 300 °C to compensate the lack of pressurization, and by scaling-up the reagents amounts.

The synthesis goes as the following: 0.373 g of branched PEI (Mw ~25 000) is mixed in 22.4 mL of EG under vigorous stirring for 30 min in the flask, then a previously prepared mixture of 0.28 g of NH_4F, 0.18 g NaCl, 0.35 g of $YCl_3.6H_2O$, 0.012 g of $ErCl_3.6H_2O$ and 0.103 g of $YbCl_3.6H_2O$ in 15 mL of EG was added, and temperature is fixed to 120 °C after which a yellow color solution is observed. The temperature is progressively increased to 300 °C and left to react for 4 hours under reflux. The solution is left to cool down then the NPs are collected by centrifugation at 8000 rpm for 10 min and washed 3 times with water.

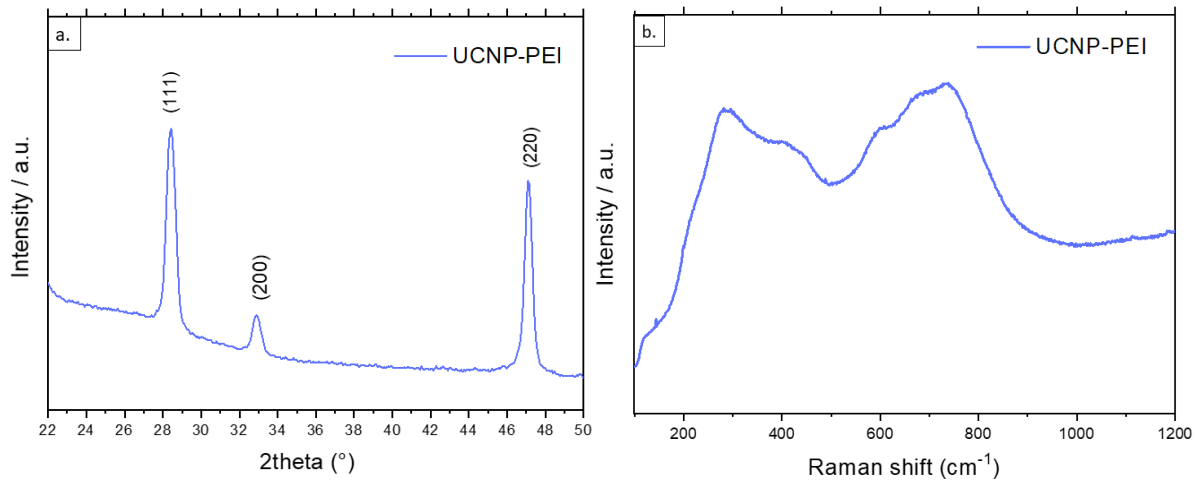

Figure III.4 a: *X-ray diffraction analysis (WAXS),* ***b:*** *Raman spectrum of the as-prepared UCNP-PEI obtained using an excitation wavelength of 532 nm.*

The diffractogram of UCNP-PEI in **Fig III.4.a** exhibits three sharp peaks at θ = 28.39 °, θ = 32.92 ° and θ =47.16 ° corresponding respectively to the following d-spacings: 0.32 nm, 0.27 nm and 0.19 nm attributed to the crystallographic planes (111), (200) and (220). These diffraction peaks are characteristic of a pure α $NaYF_4$: Er,Yb, in good agreement with the calculated pattern (JCPDS file number PDF 77-2042, card No. 16-334) [214, 232, 246].

The crystal structure of $NaYF_4$: Er, Yb is also supported by Raman analysis as the cubic and hexagonal phases are known to exhibit two different vibrational fingerprints reported in the literature. Raman spectrum displayed in **Fig III.4.b** shows two predominant broad peaks at 285 cm^{-1} and 730 cm^{-1}, also characteristic of the α-$NaYF_4$: Er,Yb [63, 247].

We can therefore conclude that the synthesis of $NaYF_4$: Er, Yb NPs following the PEI and without using autoclave only yielded a cubic phase despite the adjustment of the protocol used by X. liu *et al.* [228] (shifting to a higher temperature (300 °C), for a 4 h reaction). The temperature should probably be raised above 300 °C to obtain hexagonal phase nanocrystals, however the EG boils at 197 °C, and the reaction is exposed to a potential disturbance with the boiling and reflux process.

3.2.3.2 *Thermal decomposition by methanol-assisted organic phase: Synthesis of β-$NaYF_4$: 2% Er, 18%Yb (UCNP-OA)*

For the second attempt, we decided to choose thermal decomposition method pointed out for the past decade, as is it the most promising strategy and rapid reaction so far to prepare highly reproducible and pure hexagonal phase $NaYF_4$: Er,Yb, thanks to the use of the high boiling non-polar solvent (such as OCD) supporting temperatures ranging between 300-330 °C, and the organic capping ligand (such as OA) that ensures the stabilization and the size control during the growth of NPs. The methanol-assisted organic phase is supposed to facilitate the introduction of a mixture of inorganic compounds like sodium and fluoride precursors to the organic phase composed of OCD and OA at room temperature through a polar organic solvent like methanol. The resulting oleate capped NPs are hydrophobic and should be subsequently dispersed in a non-polar organic solvent. This is not considered as an important issue for post functionalization because the hydrophobic oleic acid ligand can be easily replaced by a hydrophilic one through a ligand exchange process that will be discussed later in this chapter.

a) Key parameters influencing the synthesis

The preparation of UCNP-OA is performed by modifying slightly a reported procedure [242], but still needs to be meticulously monitored by paying attention to certain apparent details occurring during the reaction, and which could completely change the quality of the as-prepared nanoparticles. These tips are usually not described in literature and are pointed out in the following points:

- **Oxygen-free synthesis:** we mentioned previously in **Table III.1** that this synthetic route requires an oxygen-free atmosphere and an inert gas protection. In fact, the organic compounds are sensitive to oxidation, and oxygen leaking in the vacuum line leads to synthesis failure. The oxygen contamination can be spotted with the solution aspect as described in **Fig III.5.b**.

- **Precursors amounts:** The amounts of precursors are very low and should be carefully weighed and introduced in the three-necked flask while ensuring that the lanthanide chloride crystals ($LnCl_3$) do not stick on the wall of the flask, otherwise the stochiometric ratios are not maintained due to non-solubilized species. Consequently,

the doping levels (2% Er^{3+}, 18% Yb^{3+}) are not respected and the desired crystal phase also risks to be missed. The fluoride source (NH_4F) and sodium source (NaOH), usually come in the form of powder or pellets and should be completely dissolved in methanol before addition considering the significant role of NaF to Ln^{3+} ratio in affecting the size, crystal phase, purity of the phase and the monodispersity.

- **Methanol suppression:** It is important to make sure that methanol is completely evaporated at 70 °C, before increasing the temperature up to 300 °C, otherwise the solution becomes dark brownish which is a sign of synthesis failure **(Fig III.6.b)**.

b) Preparation

Lanthanide chlorides dissolution: A mixture of 0.16 g (0.8 mmol) of $YCl_3.6H_2O$, 0.05 g (0.18 mmol) of $YbCl_3.6H_2O$ and 0.005 g (0.02 mmol) of $ErCl_3.6H_2O$ is added to a mixture of 15 mL OCD and 6 mL OA in a three-necked 100 mL flask. The system is degassed under vacuum and flask is heated up to 150 °C and left to stir for 30 mins to dissolve all the precursors and obtain a homogenous solution. The mixture is then left to cool down at room temperature while maintaining the vacuum throughout the cooling process. The color of this solution at this stage is a clear and very pale yellow (white wine color). The conservation of an oxygen-free atmosphere at this point of the synthesis is crucial. An oxygen leaking can be concluded when the yellowish solution becomes turbid, meaning that a part of precursors has precipitated into crystals, and most of them will fail to contribute in producing the hexagonal phase $NaYF_4$: Er, Yb NPs. It is noteworthy that the colors of the solution throughout the whole process is a good indicator of the success of a high quality β-$NaYF_4$: Er, Yb.

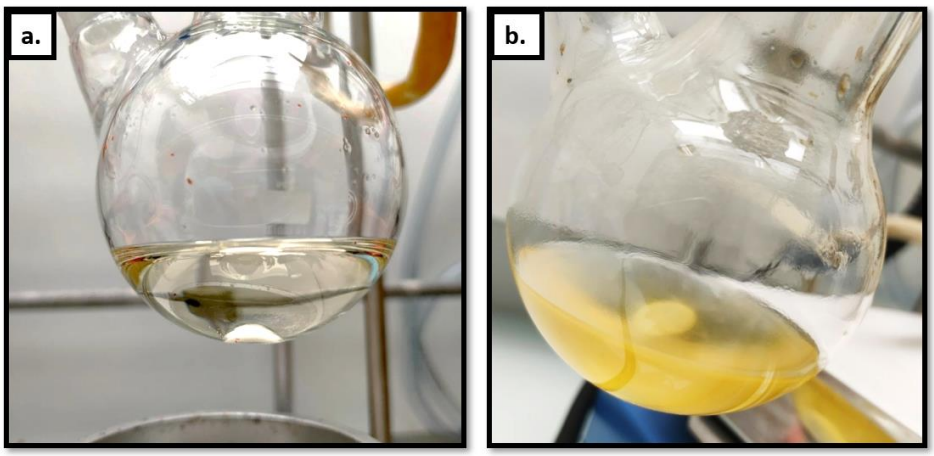

Figure III.5 *Images of the solution of $LnCl_3$ dissolved in the mixture of OA and OCD after 30 mins cooling. In* ***(a)*** *the clear solution is a good sign and signifies that the vacuum has been maintained*

*successfully, and the next step can be performed. In **(b)**, the solution became turbid because of Ln-nanocrystal precipitation.*

Methanol-assisted addition of NH_4F and NaOH: 0.1 g (2.5 mmol) of NaOH and 0.15 g (4 mmol) of NH_4F are dissolved in 10 mL methanol, and added dropwise to the $LnCl_3$ mixture in the flask, the solution suddenly becomes turbid **(Fig III.6.a**) indicating the formation of the first NaF nuclei. The mixture is left to stir at room temperature for 2 h, then progressively heated to 70 °C to evaporate the methanol. To ensure the complete removal of methanol, the reaction is further heated to 100 °C for some minutes, then the reaction is put under a gentle flow of nitrogen and heated up to 320 °C and left to react for 1h. The mixture is left to cool down before adding 10 mL ethanol to precipitate the nanoparticles.

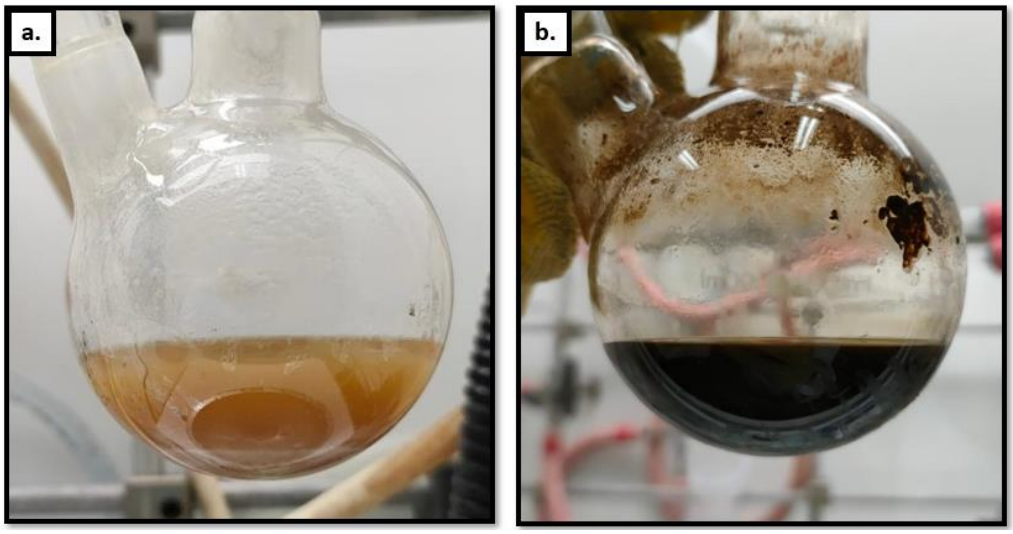

Figure III.6 *Final solution images showing the color difference when the methanol is completely suppressed from the solution in image **(a)**, compared to when traces of methanol are still present in solution, therefore disturbing the reaction and resulting in a brownish solution in image **(b)**.*

It is worth mentioning that in order to obtain a $NaYF_4$: Er, Yb crystal, stochiometric molar ratio of 1 mmol Na, 1 mmol Y (including Er^{3+}, and Yb^{3+}) and 4 mmol F (1:1:4) is supposed to be followed. However, we noted before that the ratio of NaF to Ln^{3+} is involved in controlling the size and uniformity of NPs, and that increasing this ratio can yield monodisperse relatively small NPs. Therefore, a small excess of sodium can be fixed based on the desired NPs size and especially, to ensure the phase purity and uniformity of the sample. The compounds molar ratio used in this synthesis is respectively 2.5:1:4 where 1 mmol of Y^{3+} contains 80 % of Y^{3+}, 18 % Yb^{3+} and 2 % Er^{3+}. The amount of Y varies with the respect of the doping percentage of the Er, Yb pair, but also in case of adding a third Ln^{3+} like Gd^{3+} or Lu^{3+} to tune the size of UCNPs.

NPs collection (Fig III.7): The resulting mixture is centrifuged for 10 min at 8000 rpm to collect the oleate-stabilized NPs, washed several times with ethanol to eliminate the by-product

like Cl-compounds and NaF, and then re-dispersed in cyclohexane with a concentration of approximately 7 mg/mL. The washing using non-polar organic solvent like cyclohexane, hexane or toluene should be avoided because they are able to solubilize the stabilizing ligand OA. As a consequence, the NPs are agglomerated and the post-functionalization becomes a challenging task.

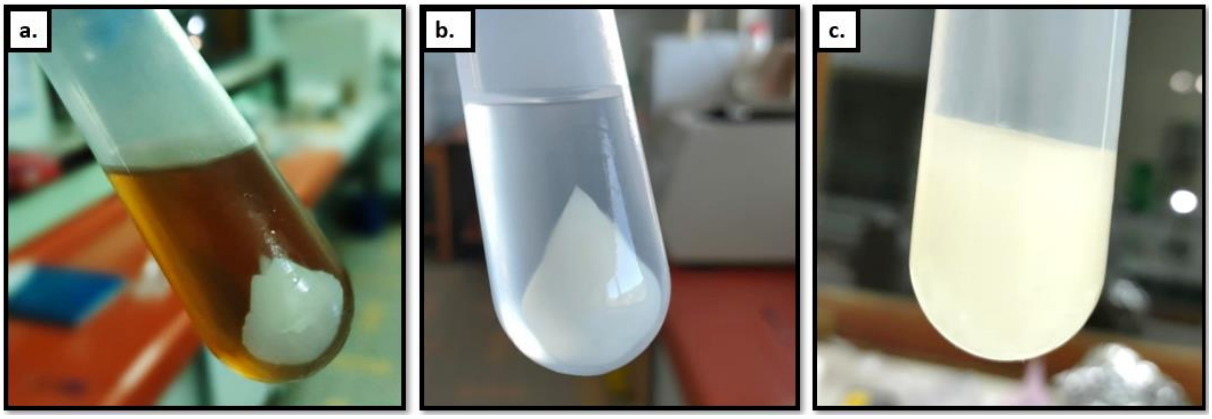

Figure III.7 a. *Image of the first centrifugation to collect the oleate-stabilized NPs.* ***b.*** *Image of the collected NPs following washing with ethanol.* ***c.*** *Homogenous redispersion of the NPs in cyclohexane.*

3.2.3.3 TEM analysis of the as-prepared $NaYF_4$: 2% Er, 18%Yb (UCNP-OA)

Two samples were prepared using the same synthesis procedure described in *3.2.3.2.* One of the samples (UCNP-OA-S2) underwent a premature precipitation of Ln-nanocrystal at room temperature before the addition of the methanol mixture containing NH_4F and NaOH, which is due to an oxygen leaking as shown in **Fig III.5.b**, that happened accidentally because the tubes linked to the vacuum pump were not robust enough. When the latter were replaced with new ones, a good vacuum was applied to the system. In this case, no leaking occurred and no precipitation was observed as shown in **Fig III.5.a**. This sample will be denoted (UCNP-OA-S1). The characterization and comparison between both samples is interesting to find out how the premature precipitation affects all the rest of the reaction, and consequently the quality of the final product.

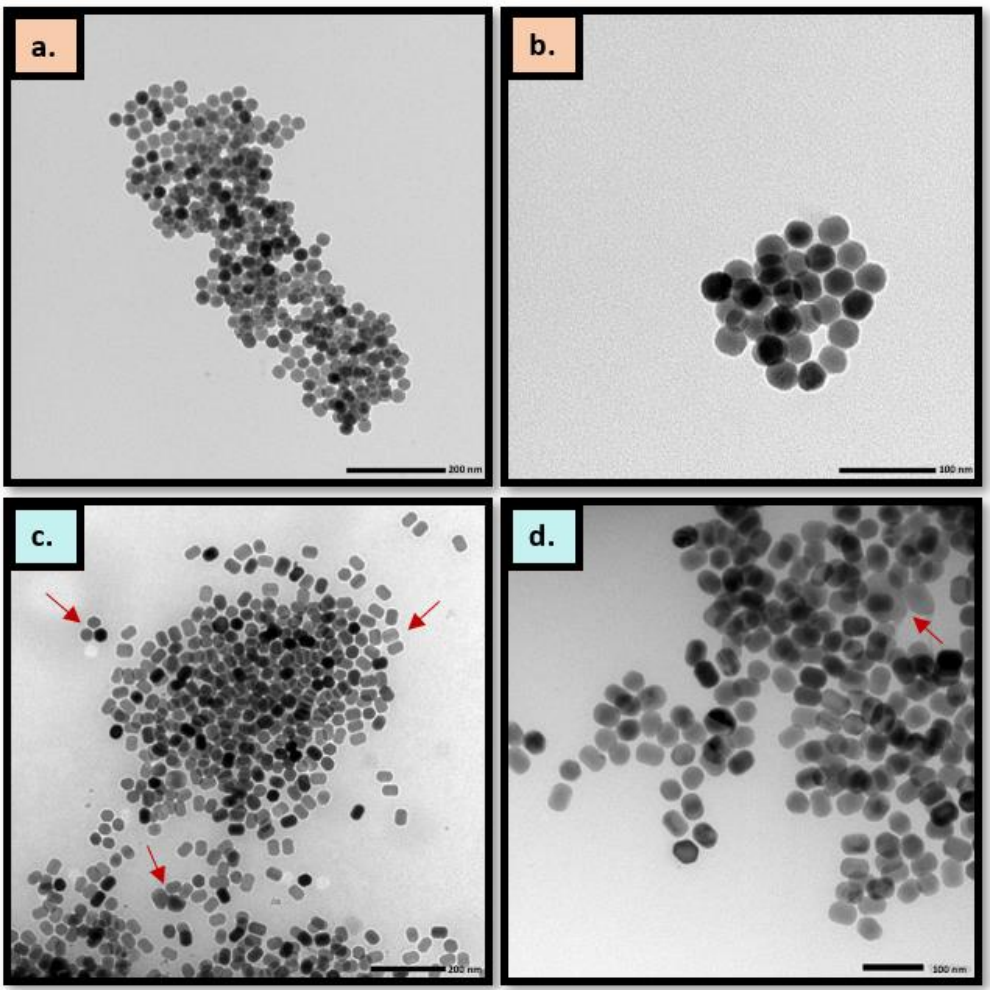

Figure III.8 *TEM analysis of the as-prepared $NaYF_4$: 2% Er, 18%Yb. Top micrographs correspond to UCNP-OA-S1* ***(a, b)*** *sample, and bottom images to UCNP-OA-S2* ***(c, d)****. Left column corresponds to 200 nm scale images and right column to 100 nm scale. The red arrows in* ***(c, d)*** *indicate the three NPs shapes found in UCNP-OA-S2 sample: spherical, rod-shape, and big nanocrystals with irregular form.*

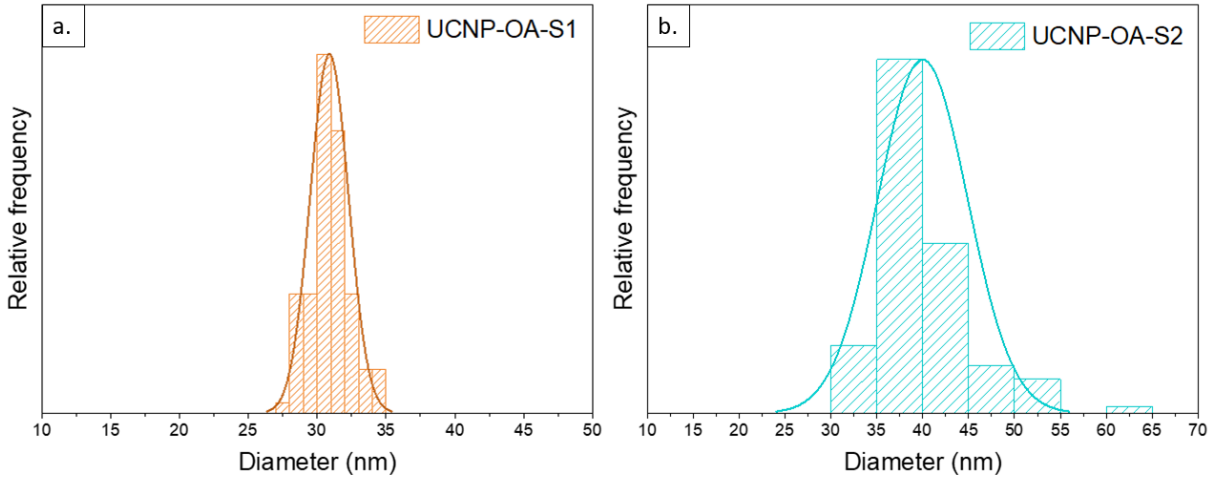

Figure III.9 *Size distribution of* ***a.*** *UCNP-OA-S1 and* ***b.*** *UCNP-OA-S2 obtained by measuring the diameter of 100 NPs from each TEM micrograph in* ***Fig III.8*** *using Digimizer software.*

3.2.3.4 $NaYF_4$: Er, Yb Crystal phase: XRD analysis

The X-ray diffractogram of UCNP-OA-S1 displayed in **Fig III.10.a** shows five sharp peaks at θ = 30.05 °, θ =30.87 °, θ = 34.86 °, θ = 39.74 ° and θ = 43.58 °, corresponding respectively to the following d-spacings: 0.3 nm, 0.29 nm, 0.26 nm, 0.23 nm and 0.21 nm. They are attributed to the diffraction plane (110), (101), (200), (111), (201) strongly matching with the β phase pattern of $NaYF_4$: Er,Yb nanocrystals (JCPDS PDF 28-1192, card No. 16-334) [214, 246, 248]. The diffractogram does not show the presence of any additional peaks belonging to the α phase, suggesting that UCNP-OA-S1 contains pure β phase nanocrystals. UCNP-OA-S2 on the other hand exhibits only one small peak indicated by an asterisk, which corresponds to NaF (200) diffraction plane [219, 246, 248 - 250]. The nanorod shape could be originated from the growth of the crystal in the direction of the a-axis with a d-spacing of 0.23 nm between (200) planes.

Raman spectra of both UCNP-OA-S1 and UCNP-OA-S2 in **Fig III.10.b** showed very close vibrational fingerprints, with three dominant sharp peaks from 200 cm^{-1} to 400 cm^{-1} characteristic of the lattice phonon of hexagonal phase of $NaYF_4$: Er, Yb. The two other peaks from 450 cm^{-1} to 700 cm^{-1} were attributed to the organic capping ligand (OA) [246, 251], while they were assigned by D. Yuan *et al.* [233] to the of Na-F bond vibration signature. The discrepancies between X-ray diffraction and Raman analysis may be associated to the difference in the probed volumes and a dominant Raman signal of the β phase despite the small amount of β-$NaYF_4$: Er, Yb, nanocrystals in UCNP-OA-S2 sample. Some slight differences in the vibrational features between UCNP-OA-S2 and UCNP-OA-S1 can be noticed like small shifts and line broadening, that can be justified by the difference in nanocrystals size and shape and their effect on the phonon confinement [251, 252].

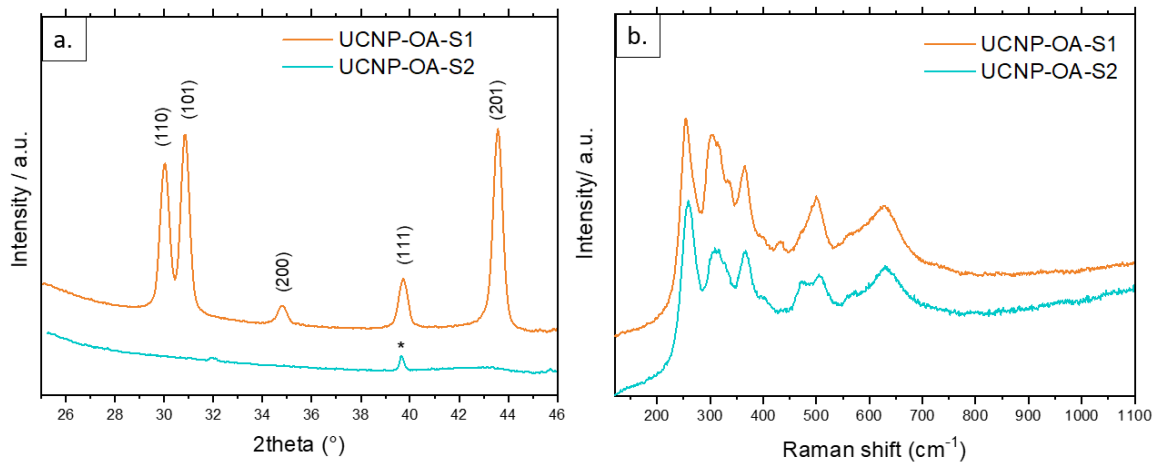

Figure III.10 a: *X-ray diffraction analysis (WAXS).* ***b:*** *Raman spectra of the as-prepared UCNP NPs using a 532 nm excitation wavelength.*

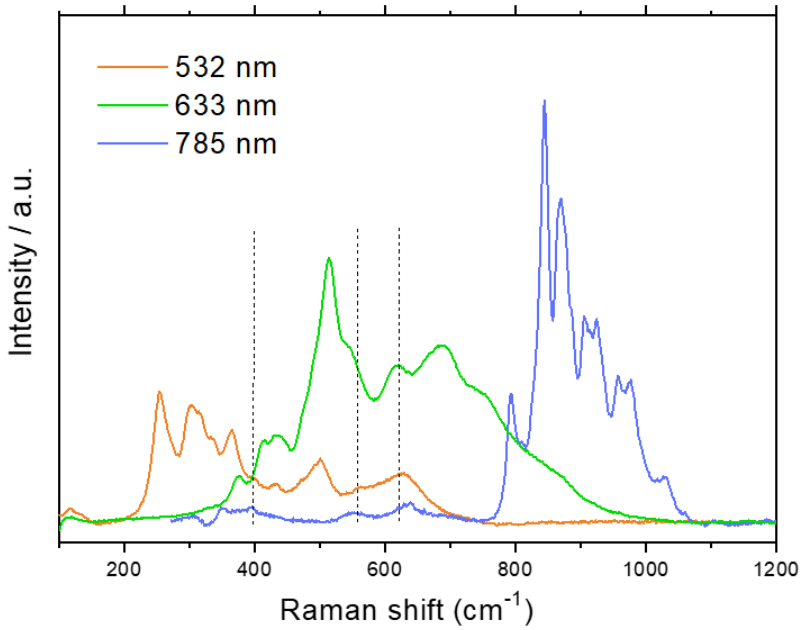

Figure III.11 *Raman spectra of UCNP-OA-S1 obtained using three excitation wavelengths, orange:532 nm, red: 633 nm and brown: 785 nm. The dashed lines are used to identify the common vibrational peaks.*

Interestingly, when exciting pure hexagonal $NaYF_4$: Er, Yb nanocrystal at different excitation wavelengths **Fig III.11**, vibrational fingerprints with shifted peak positions are obtained. R. Janjua *et al.* [253] suggested that these peaks arise from Ln^{3+} luminescence rather than Raman scattering, because peaks are shifted by a constant value when using different laser wavelengths. This was disapproved by many reported works all agreeing that the peaks are originated from the lattice phonon vibrations of β-$NaYF_4$: Er,Yb [49, 50, 247], and especially D. Yuan *et al.* [233] who showed that the same vibrational pattern is obtain in both doped and undoped β-$NaYF_4$ crystal. Nevertheless, whatever is the interpretation of the signal changing

with the incident excitation wavelength, it remains a signature of the hexagonal phase $NaYF_4$: Er, Yb nanocrystals, and is highly useful to characterize these materials.

3.2.3.5 Discussion

The above-presented characterization results demonstrate that even when employing the same synthetic procedure for UCNP preparation, the quality of the resulting nanoparticles is highly sensitive to the precise control of synthesis conditions, which must be managed with a great care. Indeed, the morphological distinction between UCNP-OA-S1 and UCNP-OA-S2 observed in TEM images **Fig III.8** could be justified by the observed premature precipitation of Ln-nanocrystals and its impact on the nucleation/growth kinetics of the UCNP, therefore resulting in bigger nanocrystals, with non-uniform shape and a large distribution for UCNP-OA-S2. This could be supported by the absence of both α and β phases diffraction peaks, because if the non-uniformity and dispersity of this sample were arising from a sodium-deficient system leading to an Ostwald ripening growth of β phase as described in **Fig III.3**, mixed phases (β+ α) would appear. But in this case, the system is in excess of sodium, the premature precipitation of Ln-nanocrystals before reacting with the mixture of NaOH and NH_4F in the methanol-assisted process resulted in an enormous NaF to Ln^{3+} ratio. A part of Na^+ and F^- reacted with the remaining small amount of non-precipitated Ln^{3+} to form some spherical β-$NaYF_4$: Er, Yb, and the vast majority formed NaF nanorods, thus confirming the effect of NaF to Ln^{3+} in affecting not only crystal structure and the size of UCNPs, but their morphology as well, which was emphasized in many reported works [224, 234, 254]. NaF nanocrystals are capped with OA as well, which is why they are not eliminated even after washing several times with ethanol [219].

The first step of the synthesis of the multifunctional nanoplatforms has been achieved successfully. The sample UCNP-OA-S1 exhibiting the expected morphological and structural characteristic is selected, and will be used to study the next synthesis steps which are (i) the coating with the amorphous silica layer, (ii) the PMO layer addition.

3.3 Encapsulation of $NaYF_4$: Er, Yb nanoparticles

3.3.1 Surface modification

The expanding interest in using functional nanomaterials in the biomedical field for some specific applications like bio-imaging diagnostic, photodynamic therapy (PDT), hyperthermia or drug delivery therapy, raised the question of the biocompatibility of the functional nanomaterials including UCNPs, knowing that most of them are toxic and are by no means suitable for a straightforward use in human body. This led to a new challenge in the nanotechnology sphere revolving around how such nanomaterials can be modified in order to make them well adapted to such biological environments, while preserving their functionality. The most evident way to address this issue is through surface modification of the NPs, which by the same means, must be contributing in a better dispersibility of the NPs in aqueous media, especially hydrophobic NPs like oleate-capped UCNPs. Surface modification can be realized in various ways depending on the targeted application and can be divided into two categories:

Ligand engineering: It consists in ligand adsorption on the surface of the NPs for surface functionalization. By using different terminated hydrophilic chemical functional groups, hydrophobic to hydrophilic NPs conversion can be achieved and NPs can be linked to diverse biomolecules through bioconjugation. Ligand engineering can be performed in different techniques.

- Ligand exchange **(Fig III.12.a)**: in this method, the original ligand adsorbed on the surface of NPs and conferring the hydrophobic character is replaced by another hydrophilic ligand using a surfactant or a bifunctional polymer, thus promoting a better dispersibility in aqueous solvents and additional functionalization. It is usually applied to NPs prepared following the thermal decomposition in high temperature boiling organic solvent involving the use of a hydrophobic ligand like OA. Many examples of ligand exchange of NPs were reported in literature. Like the replacement of OA by poly (acrylic acid) (PAA) having hydrophilic carboxylic groups COOH on their surface enabling their water dispersion and covalent coupling with biomolecules like antibodies, proteins [213, 255]. The -COOH layer can be obtained using PEG diacid (HOOC-PEG-COOH) as well [256]. The transfer of NPs to an aqueous solution can be also achieved by an amino-modified poly (ethylene oxide) s (PEO) coupled with poly (ethylene

imine)s (PEI), thus layering the NPs surface with -NH_2 terminated molecules known by their high biocompatibility and bioconjugation capacity [257]. Other molecules like PVP, citric acid, cysteine, glycine, 2-aminoethyl dihydrogen phosphate (AEP) and biotin were also used for the same purposes [258].

- Ligand oxidation **(Fig III.12.b)**: Here, OA is not exchanged by any other hydrophilic ligand, but its carbon-carbon double bond (C=C) is oxidized by Lemieux-von Rudloff reaction using $KMnO_4/NaIO_4$, and turned into a hydrophilic pendant carboxylic functional group (-COOH). This method was applied the first time on UCNP by C. Huang *et al.* [259] and was later adopted by other groups [225, 260].

- Ligand attraction **(Fig III.12.c)**: This method consists in adding an amphiphilic block co-polymer with a hydrocarbon chain side attracted to the original hydrophobic ligand with strong Van Der Waals interactions. The other hydrophilic side of the polymer enables the dispersion of NPs in aqueous solutions. G. Chow *et al.* used an octylamine and isopropylamine modified poly (acrylic acid) (PAA) amphiphilic polymer, so as the octyl and isopropyl alkyl chains are attracted to the octadecyl group of oleylamine (the original hydrophobic ligand OM), while the terminal carboxyl group (-COOH) of PAA tends outward, thus enhancing their hydrophilicity [261].

- Layer by layer engineering **(Fig III.12.d)**: Surface modification following this method is carried out by alternating oppositely charged layers of polyions assembled with electrostatics interactions. It is one of the most attractive approaches because it not only offers multiple pathways for versatile functionalization, but also enables a precise control of the overall layers thickness, biocompatibility and a very good colloidal stabilization of NPs in solution through charges repulsion. But this route is exclusive to hydrophilic UCNP [48, 262].

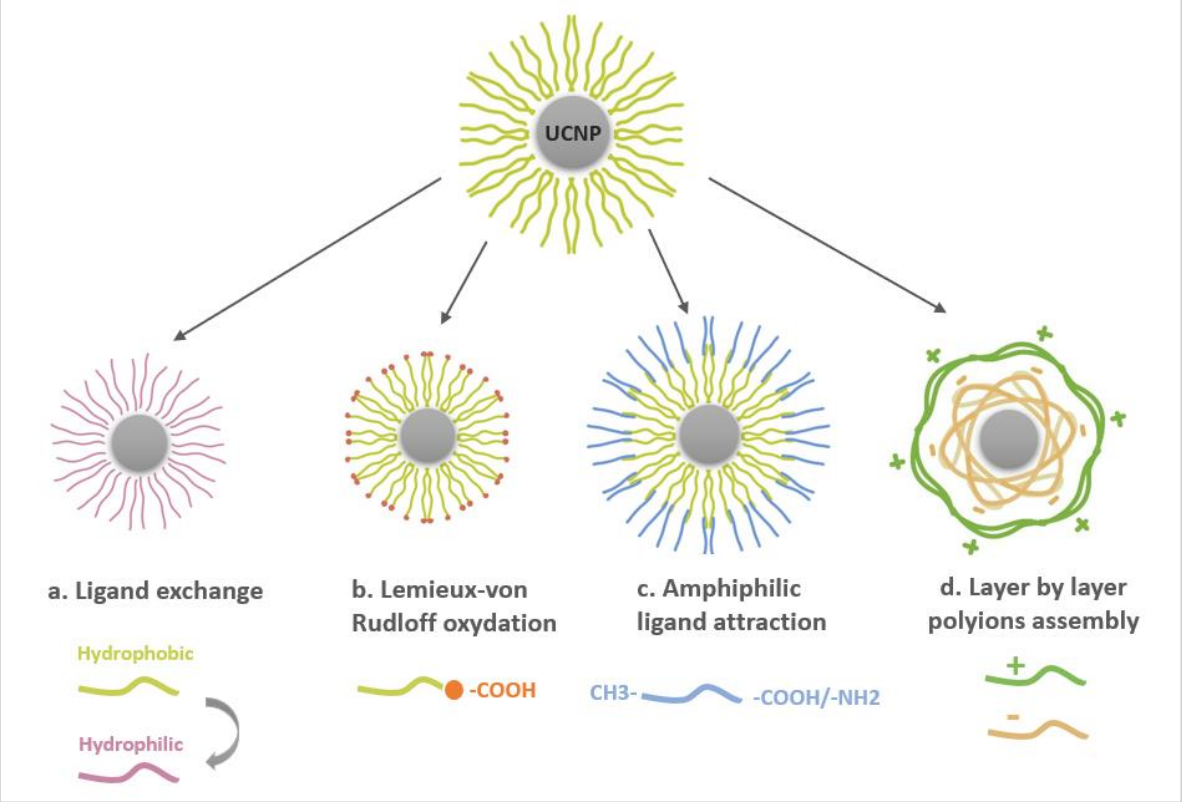

Figure III.12 *Different strategies of the oleate-capped UCNP surface modification.* ***a.*** *Hydrophobic surface to hydrophilic surface conversion by ligand exchange.* ***b.*** *Oxidation of the C=C bond of OA by Lemieux-von Rudloff oxidation.* ***c.*** *Surface modification by coupling OA with an amphiphilic polymer.* ***d.*** *Alternative layer by layer deposition of negatively and positively charged polyions.*

Encapsulation: The second category of surface modification is based on UCNP encapsulation in an inert shell, mostly dense silica deposited on the surface of the functional nanocrystal by hydrolysis and condensation of siloxane monomers. It is known as the surface silanization method and is one of the most widely adopted approaches to modify the surface of nanomaterials like UCNP. Encapsulating a functional core inside a solid-state layer leads to the formation of a "core/shell" structure, which has known a significant rise and a prominent research interest for the last two decades in a wide range of nanotechnology fields, most particularly in the biomedical and pharmaceutical areas [263]. The coating not only serves as a protecting layer in case the functional core is prone to thermal or chemical modification when interacting with an external environment, but also prevents living organisms like cells from the potential cytotoxicity of this functional core. For this aim, silica and mesoporous silica have been extensively utilized because they demonstrate a good biocompatibility [264, 265], and can be exploited in many different ways for additional functionalization, like molecules grafting for gene targeting, drug loading/delivery and others. More importantly, the silica coating can provide a surface passivation effect and is therefore beneficial for the optical performance of

UCNP. The shell thickness can be controlled and it can be used as a spacer or a linker to a second shell, thus creating a more complex nanoplatform with multilayers for hierarchical multifunctionalities. Silanization can be achieved either by using inorganic silica source like TEOS, or a monosubstituted alkoxysilane like APTES ((3-Aminopropyl) triethoxysilane) that offers an amino function (-NH_2) that can be used for surface bioconjugation [266, 267]. Silica can also be co-assembled with a surfactant forming a crystal liquid template to obtain a mesoporous silica coating.

3.3.2 UCNP silica coating

The lack of affinity between and inorganic hydrophilic silica and the hydrophobic oleate-capped UCNP requires an intermediate step of surface modification following one of ligand engineering methods described in **Fig III.12**, to enable a successful silica layer deposition and a uniform coating of NPs following a sol-gel process. There are two possible ways to achieve this.

Silanization supported by ligand attraction: Prior to silica deposition, an amphiphilic polymer or a surfactant with a hydrophilic head and a long alkyl tail is attracted to OA hydrocarbon chain by hydrophobic interactions as described in **Fig III.13**. The surface of the modified NPs becomes hydrophilic and can support a silica deposition. Several works have reported surface silanization of functional cores using CTAB as a surface modification agent. Concomitantly, the latter also act as a mesostructure directing agent (SDA), and co-assembles with silica species to form a mesoporous silica structure [190, 268, 269].

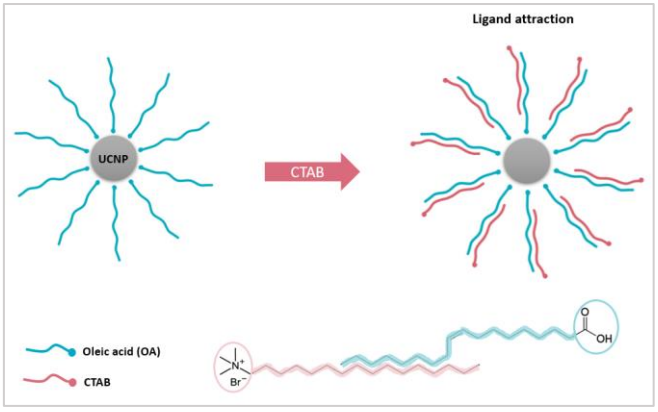

Figure III.13 *Scheme of surface hydrophilization of oleate-capped UCNP using CTAB for hydrophobic attraction. The polar head of CTAB tends outward the nanoparticles, which gives it a hydrophilic character.*

Silanization supported by ligand exchange: In the case of deposition of dense and amorphous silica without the formation of mesopores, a total removal of the original hydrophobic ligand (OA) and replacement with a hydrophilic ligand is required prior to silica coating. This process is carried out through a reverse microemulsion route where OA is usually replaced by Igepal co-520, a non-ionic surfactant capable of stabilizing water-in-oil microemulsions. First, ligand exchange occurs between OA and Igepal co-520, then the modified NPs are dragged in the water emulsions composed of ammonia stabilized by Igepal co-520, where silica species hydrolyze and condense to form a coating around the trapped functional core, with ammonia acting as a catalyst of the sol-gel reaction. Y. Ying *et al.* were the first to describe this process in 2005 [191]. At that time the ligand exchange mechanism was only ascribed between the original hydrophobic ligand (OM or OA) and Igepal co-520. In 2008 the same author reported that the ligand exchange can also occur between negatively charged silicate species of hydrolyzed TEOS and OM. Later on, G. H. Li *et al.* [193] confirmed the ligand exchange between OA and Igepal co-520 initially, the adsorption of Igepal co-520 on the surface of the functional NPs (Fe_2O_3 NPs in the reported work) helps them to be transferred to the ammonia emulsion also stabilized with Igepal co-520, then a second ligand exchange occurs between hydrolyzed TEOS and Igepal co-520 which was proven by FT-IR analysis**.** Subsequently, silica grows at the ammonia/cyclohexane interface as shown in **Fig III.14**.

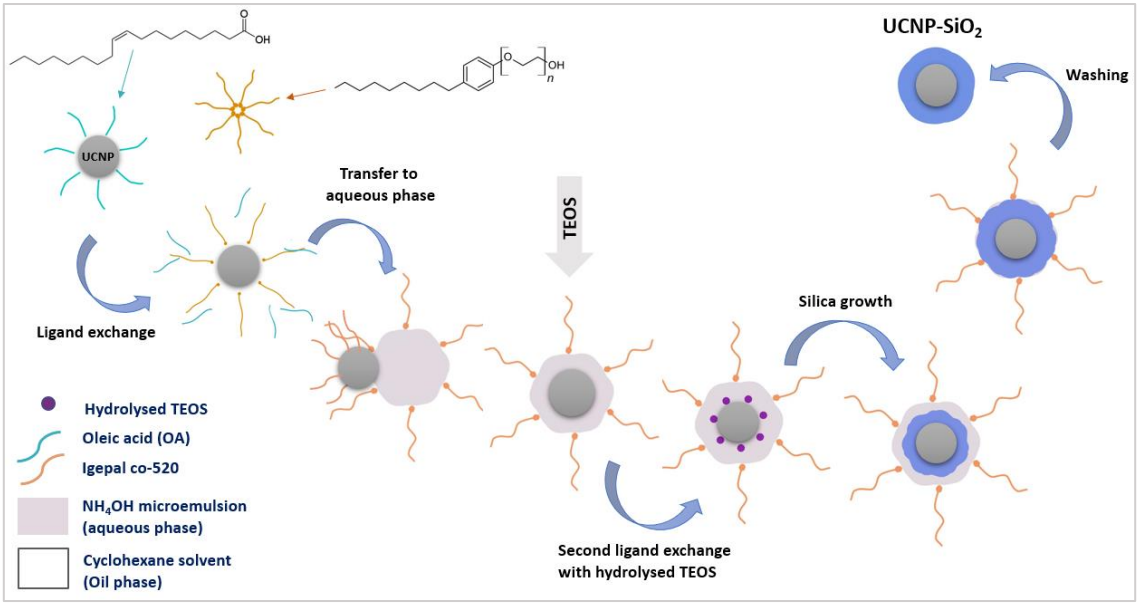

Figure III.14 *Water-in-oil reverse microemulsion mechanism for UCNP encapsulation in silica shell. The NH_4OH micro-droplets represents the water phase emulsion in a cyclohexane solution representing the oil phase. (Reproduced from [193]).*

Reverse microemulsion is by far the most utilized method to encapsulate oleate-capped UCNP in dense silica, and was reported by many research groups [194, 195, 242]. However, there is still an ongoing and almost inevitable challenge about this strategy, which is the difficulty to obtain a 100 % single functional core entrapped in a silica shell. In fact, different scenarios may take place, like more than one functional nanoparticle being encapsulated in the same shell, some NPs can miss the encapsulation, and the most recurrent scenario is when several empty silica nanoparticles are formed in addition to the core/shell structure. Coating all the functional cores individually with a silica layer means that there should be as much number of NPs as the aqueous domains in the solution to obtain a one-to-one encapsulation. Quantifying the number of NPs is not an evident task, and measuring the total mass of NPs is not relevant because for the same mass of NPs with different sizes, the number of NPs is not the same, and for the same size of NPs with different chemical composition, the number of NPs is not the same neither. That is why it remains difficult to establish a universal procedure for silica coating using a reverse micro-emulsion strategy. The only way to achieve uniform and single core encapsulation is by controlling the number and size of the aqueous domains in the organic solution through the variation of Igepal co-520 to ammonia amounts ratio as reported by M. Zhang *et al.* [270] and adapting it as function of the size of the NPs as demonstrated by G. H. Li *et al.* [193]. Indeed, decreasing the size of the aqueous domain relatively to the size of the functional core will only allow the insertion of one nanoparticle per aqueous domain, and would also decrease the thickness of the silica shell, because the smallest is the size of the ammonia

droplets the less space is available for the hydrolysis/growth of TEOS monomers. With the aim of increasing the shell thickness, both TEOS and ammonia amounts can be increased, but they should all be carefully balanced all the while taking into consideration the size of the functional core in such a way to avoid the formation of core-free silica NPs and the encapsulation of more than one core in the silica shell.

3.3.3 PMO shell deposition

Only few works reported the synthesis of a yolk/shell structure made of a functional mobile core inside a PMO shell, with the key difference between their procedures being the silica etching strategy. The Ship in bottle strategy **(Fig III.1.d)** on the other hand does not involve any silica etching step and is therefore easier, because it is based on the synthesis of HPMO NPs first (discussed in detail in Chapter.II) and their introduction in a UCNP synthesis batch, where the precursors start to diffuse through the mesopores and form UCNP nanocrystals inside the core cavity of the HPMO under specific conditions described by X. Chen *et al.* [200], thus leading to multiple small mobile core inside a PMO shell that eventually merge to form a single core after a calcination step.

In case of the yolk/shell nanoplatforms synthesis using the classical route of the layer-by-layer deposition followed by the etching of the sacrificial silica, the reported works can be divided in two categories depending on the etching strategy described below. The limitations of each method and the challenges in applying any of them to create the intended yolk/shell $NaYF_4$: Er, Yb@PMO are discussed below.

Organosilica-assisted etching method: In some reported works [196, 197, 271], the void between the functional core and the PMO shell is created by the silica etching induced with the simultaneous growth of the PMO layer. D. Zhao *et al.* demonstrated that the void space can be tuned by varying the interval time (from 0.5 to 5 min) between the addition of NaOH (catalyst) and the bridged organosilane precursor at a temperature of 80 °C. The high temperature and a pH equal to 12 promote a quick degradation of the amorphous silica layer into silica monomers, which contribute in the growth of the PMO shell.

Surface-protected hot water etching: One of the well-known strategies to perform silica etching is the surface-protected hot water etching reported by Y. Yin *et al.* [272] where a

polymer like PVP is used as a protecting agent adsorbed on the surface of a silica nanoparticle. Consequently, the alkaline hot water etching cannot rapidly attack the silica surface because it is already forming bonds with the PVP layer. Instead, the OH^- diffuse inside the nanoparticles and gradually etch the silica from the center of the NP to the surface. In its way to dissolve the core of the NP, the etching agent creates a sort of porosity on the surface and near the surface of the NP thus turning it permeable and increasingly diffusive **(Fig III.15)**.

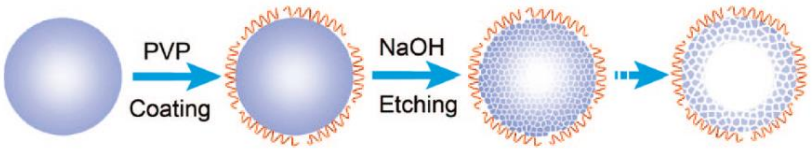

Figure III.15 *Scheme of the surface-protected hot water etching strategy applied to simple dense silica nanoparticles [272].*

By controlling the time reaction of the alkaline hot water etching, a hollow structure with a porous surface can be obtained. This procedure is one of the suggested strategies found in literature to prepare hollow structure, and was used by many research groups to prepare different yolk/shell nanostructures [273, 274]. Indeed, it can be applied to a simple dense silica NP like schematized in the **Fig III.15**. where only the surface of the NP is conserved and thus regarded as a shell. It can also be applied to a core/shell structure with the purpose to etch the inner part of the shell while the surface remains intact which results in a yolk shell structure **(Fig III.16)**, this implies a rigorous control over the etching time. Lastly, it can be applied to a core/double-shelled nanoplatform, where the intermediate layer is sacrificial (hard template) and supposed to be completely etched, and the second layer is protected with PVP but is also susceptible to etching from the inner side. The latter case is found in the work of X. Chen *et al.* [275] who reported a procedure to prepare mobile UCNP inside a hybrid silica layer following a PVP surface-protected hot water etching. Later, the same protocol was used M. Kaczmarek *et al.* [199] to encapsulate nanothermometers in a yolk/shell nanoplatform.

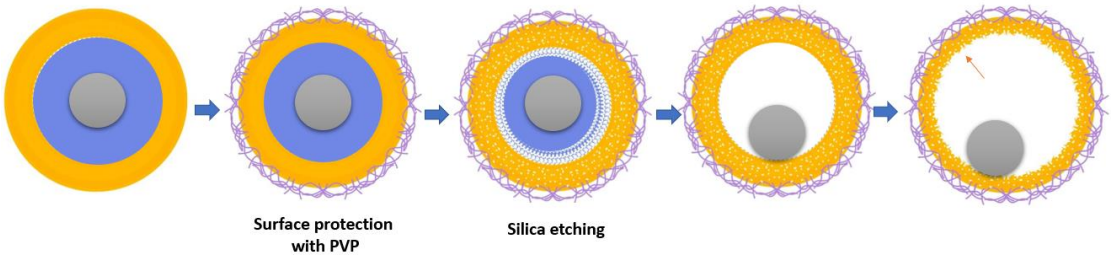

Figure III.16 *Schematic illustration of sacrificial silica etching steps using PVP surface protection strategy, this method is the same as described in* ***Fig III.15****. Here, silica represents a sacrificial intermediate layer, and the top layer is the one protected with PVP. In the last step, when there is no more sacrificial silica to etch, and that the etching process is carried out for a long time, the inner side of the second layer start etching.*

It is important to highlight that the surface protection using a polymer was initially adopted because no surfactant was used to form a mesostructured shell. In fact, when using a crystal liquid template to form a mesoporous silica/organosilica shell by the employment of a cationic surfactant as structure directing agent (SDA), like CTAB, deposited on a silica hard template, as long as the cylindrical micelles of the surfactant are still occupying the mesopores, they act as a pillar to the whole shell structure and protect it from etching. This means that the shell is not impacted by the diffusion of OH^- and directly dissolve the hard template and surface protection. The use of PVP is not needed in this case. This etching strategy is known as "the cationic surfactant-assisted selective etching strategy" and was first reported by N. Zheng *et al.* [154] who demonstrated the critical role of CTAB in promoting the amorphous silica hard template etching over the mesoporous shell. Therefore, the absence of SDA use during the formation of a silica or an organosilica layer has two consequences: the surface protection using PVP becomes essential otherwise all the nanostructure collapses, which in turn leads to the formation of randomly organized and non-uniform pores than can also eventually collapse if the alkaline hot water etching is prolonged.

3.4 Synthesis of multifunctional nanoplatforms through multilayered material engineering

With the purpose of encapsulating $NaYF_4$: Yb, Er-based nanothermometer in a PMO shell in a way to achieve a yolk/shell type multifunctional nanoplatform, the ship-in-the bottle route appears to be attractive because of its simplicity, especially that mastering HPMO NPs

preparation with different sizes and composition was also demonstrated in the present work (Chapter.II), but is still not convenient for our study because it does not result in high quality encapsulated UCNP. Indeed, the number and the size of UCNP per each HPMO NP is not well controlled following the Ship in the bottle procedure, which leads to a non-uniform distribution from one yolk/shell NP to another.

Whereas for the organosilica-assisted etching method, most of the studies reporting the use of this strategy in the context of yolk/shell NPs, were centered on the use of Fe_2O_3 NPs as functional cores, which can be easily separated and collected using a magnet. When following the same reported protocols for non-magnetic UCNP that can only be collected via centrifugation, the additional core-free PMO nanoparticles that are inevitably formed in the solution, are hardly separable from the PMO coated functional core (these mechanisms will be discussed in detail in the experimental part). The second inconvenience about the growth-induced etching is that it is not possible to collect the sample in the step before silica etching, as this procedure consists in a one pot strategy and the silica is etched at the same time as the PMO growth, unless the time, the temperature and the pH of solution are adjusted in such a way to avoid this effect. Y. Deng *et al.* [202] proposed a procedure to prepare yolk/shell PMO nanoplatforms without the etching of a sacrificial silica layer. Again, Fe_2O_3 NPs were collected by a magnet and no additional impurities could be detected after the separation, which does not necessarily mean they do not exist. However, Y. Deng *et al.* [202] highlighted the importance of ethanol presence in forming an isotropic PMO layer. Therefore, the organosilane precursor was first mixed with a small amount of ethanol before addition, which helps to increase both the solubility of CTAB and the hydrophobic precursor.

The hot water etching after surface protection by PVP in the other hand is not useful, as the use of an SDA like CTAB is essential to for a PMO layer and would imply the stabilization of this layer against etching.

In fact, none of the described procedure above can be used to achieve the desired nanoplatform for the current work, because of the following points:

- The functional NPs should be monodisperse, which implies that the synthesis of the multifunctional nanoplatform should begin with the synthesis of UCNP, and be followed by the multi-step deposition of encapsulating layer.

- The homogeneity of the sample should be straightforwardly attained without the need to perform any separation using magnetization or filtration.

- The deposition of the hybrid silica shell should be performed in the presence of an SDA co-assembling with the bridged organosilane precursor in order to obtain structured mesopores with a narrow size distribution.

In order to meet all these criteria at once, a new protocol is developed to control the PMO deposition when moving from large silica hard template to small ones. In this case the etching strategy followed to obtain the yolk/shell structure should be the cationic surfactant-assisted selective etching strategy **(Fig III.17)**. To date, no work has been reported on the preparation of yolk/shell nanoplatforms encapsulating UCNP or any other functional core while using this route.

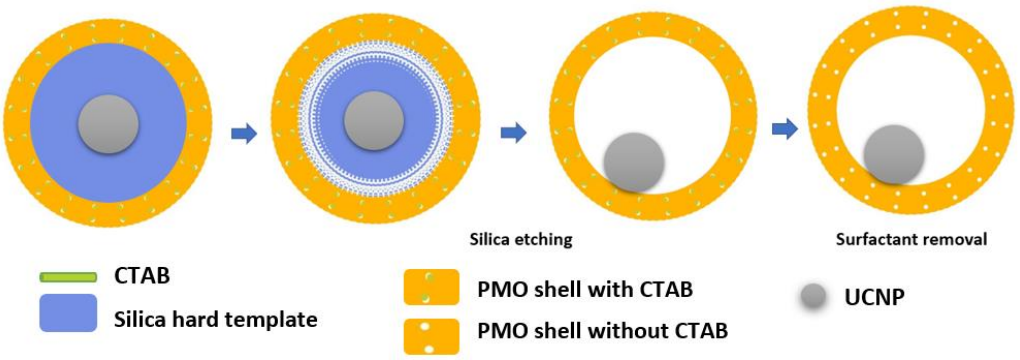

Figure III.17 *Schematic illustration of the etching process following the cationic surfactant-assisted selective etching strategy. The top layer is not impacted and does not need to be protected on the surface by PVP (unlike in the* ***Fig III.16****) the surfactant is removed in the last step after the silica etching, resulting in mesoporous shell.*

The preparation of the UCNP@PMO with yolk/shell are prepared first by encapsulating UCNP in a layer of amorphous silica according to the reverse micro-emulsion method described in **Fig III.14**. The silica layer is acting as a sacrificial hard template subsequently etched leading to the creation of a void. It also acts as medium for the deposition of the PMO layer given their good affinity. The deposition of the PMO layer is performed by the co-assembly of a liquid crystal template formed by the aggregation of cationic surfactant micelle cylinders (CTAB) with a bridged organosilane precursor. The etching process is carried out according to the steps described in **Fig III.17** using an alkaline hot water etching.

In the next experimental section, the UCNP presented previously (UCNP-OA-S1) is first coated with a silica layer, then a PMO one. It is noteworthy that the several unsuccessful attempts toward high-quality samples according to the criteria described above, served to understand the mechanisms ruling the homogeneity of the samples, and will be first discussed.

3.4.1 1st coating of UCNP with silica layer (UCNP-S1@SiO_2)

3.4.1.1 Preparation

Two silica encapsulation samples obtained using two slightly modified protocols and the resulting TEM characterization are presented and discussed in this section.

- ***UCNP-S1@SiO_2-A***

UCNP-OA-S1 in **Fig III.9 (a, b)** are coated with a silica layer following a reported procedure using the reverse microemulsion method [242]. In a 100 mL flask, 0.5 mL of the oleate-capped UCNP dispersed in a solution of cyclohexane (≃ 5-7 mg/mL) is mixed with 6 mL of anhydrous cyclohexane and 0.1 mL of Igepal co-520, then 0.4 mL of Igepal co-520 and 80 µL of NH_4OH (28%) is added to form a microemulsion and stirred until the solution becomes transparent. 40 µL of anhydrous TEOS (99.99%) is added to the mixture, and it is left to stir for 2 days at 30 °C and 600 rpm. The silica coated UCNP are precipitated using 5 mL of ethanol, collected by a centrifugation at 8000 rpm and washed 3 time with water/ethanol solution then either used directly for the next step of PMO coating or re-dispersed in water for further use.

- ***UCNP-S1@SiO_2-B***

The above procedure was slightly modified in another attempt to prepare silica coated UCNP. The amount of Igepal co-520 was not added in two steps, but the whole 0.5 mL of it was mixed with 6 mL of anhydrous cyclohexane and left to stir for few minutes for homogeneous solution before adding the same amounts of NH_4OH and TEOS. The rest of the synthesis is all the same.

3.4.1.2 TEM analysis of the as-prepared UCNP-S1@SiO_2

TEM micrographs in **Fig III.18** corresponding to the samples exhibit two different results. UCNP-S1@SiO_2-A have a thick silica layer of ≃ 20 nm and several empty silica NPs as pointed out with a red arrow in the TEM image, while UCNP-S1@SiO_2-B have a thinner silica shell ≃ 10 nm and homogenous composition with no apparent core-free silica NPs. TEM micrographs displayed in **Fig III.19** show unsuccessful attempt to coat UCNP with silica layer, that are worth discussing because they show how much delicate is the method of silica coating using a ligand exchange by the reverse microemulsion method. The image in **Fig III.19.a** show very agglomerated UCNP covered by the same silica layer. For UCNP in **Fig III.19 (a,b)**, statistically only few UCNP are covered with silica layer among a large number of core-free silica NPs.

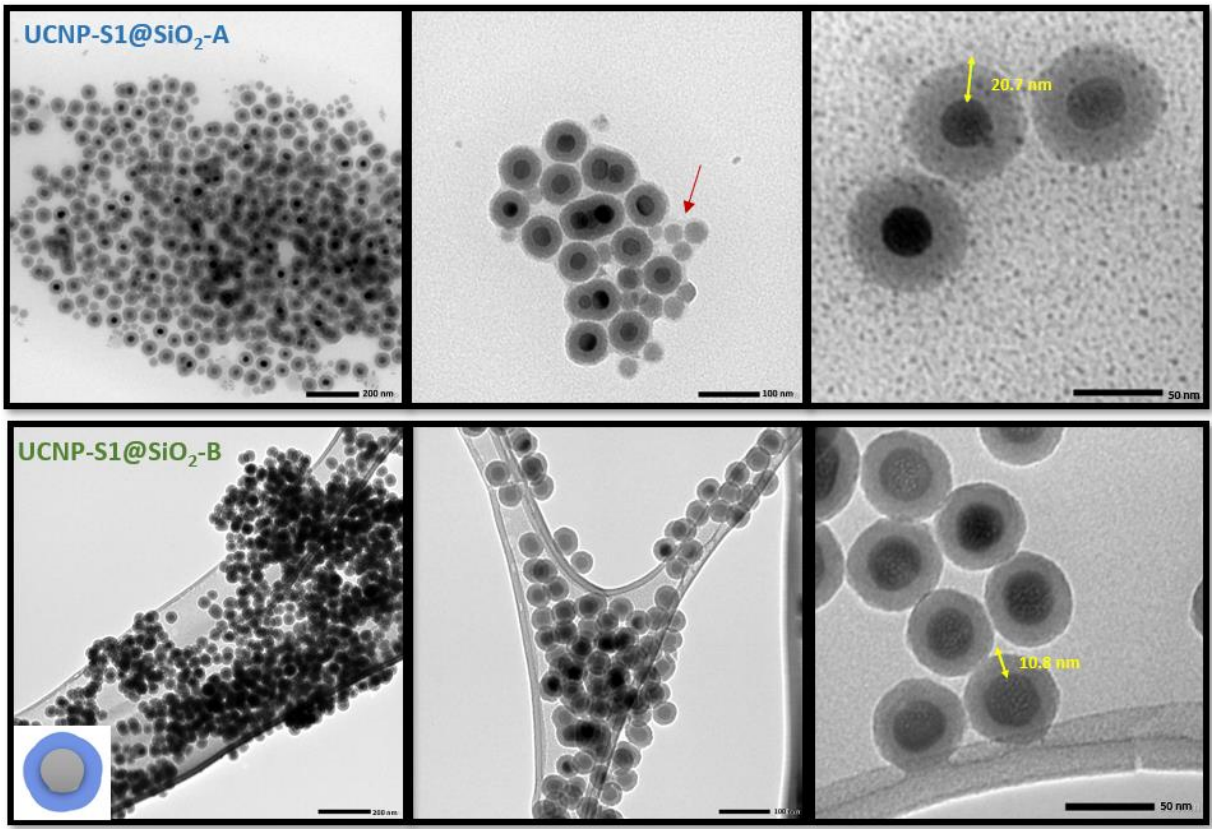

Figure III.18 *TEM micrographs UCNP-OA-S1 coated with silica in two synthesis with modified procedures.* ***Top:*** *UCNP-S1@SiO_2-A images with 200, 100, and 50 nm respectively from left to right, the red arrow points out the core-free additional silica NPs in this sample, and the yellow arrow indicates the thickness of the silica shell around 20 nm.* ***Bottom:*** *UCNP-S1@SiO_2-B.*

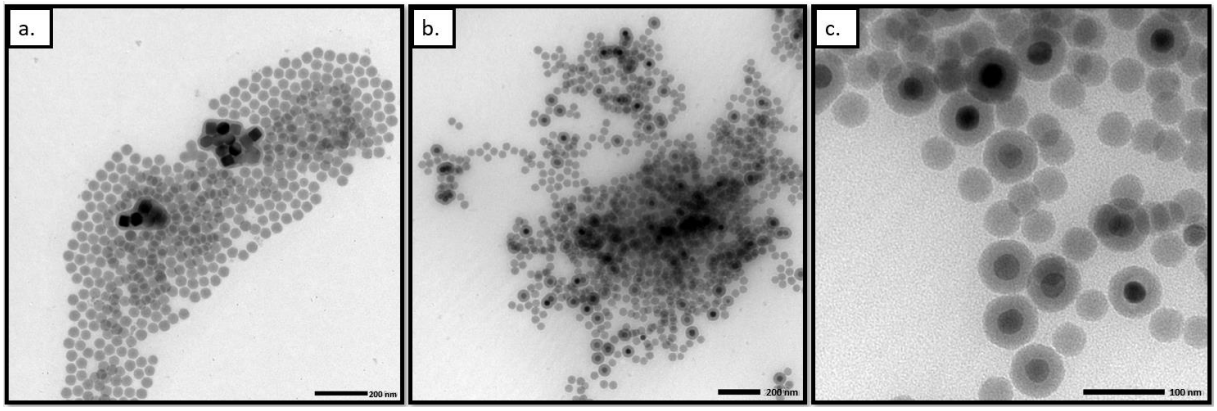

Figure III.19 *TEM micrographs of failed homogeneous UCNP silica coating.* ***a:*** *Agglomerated UCNP coated in one layer of silica and a large number of core-free silica NPs.* ***b, c:*** *Few silica-coated UCNP compared to core-free silica NPs in 200 and 100 nm scale bars respectively.*

The size distribution analysis using TEM micrographs show two different diameters of silica-coated UCNP **(Fig III.20 (a,b))**. Both samples have the same core diameter because the same UCNP core sample is used for the silica coating (UCNP-OA-S1 from **Fig III.9**). Only the shell thickness is different, around 20 nm for UCNP-S1@SiO_2-A and 10 nm for UCNP-S1@SiO_2-B, which is why they have different mean sizes: 62 ± 3 nm and 47 ± 2 respectively. Zeta potential measurement displayed in **Fig III.20.d** indicates a value of -15.6 mV of the silica-coated UCNP suspended in deionized water, which is justified by the typical negatively charged surface of silica due to the presence of $Si\text{-}O^-$ species [276].

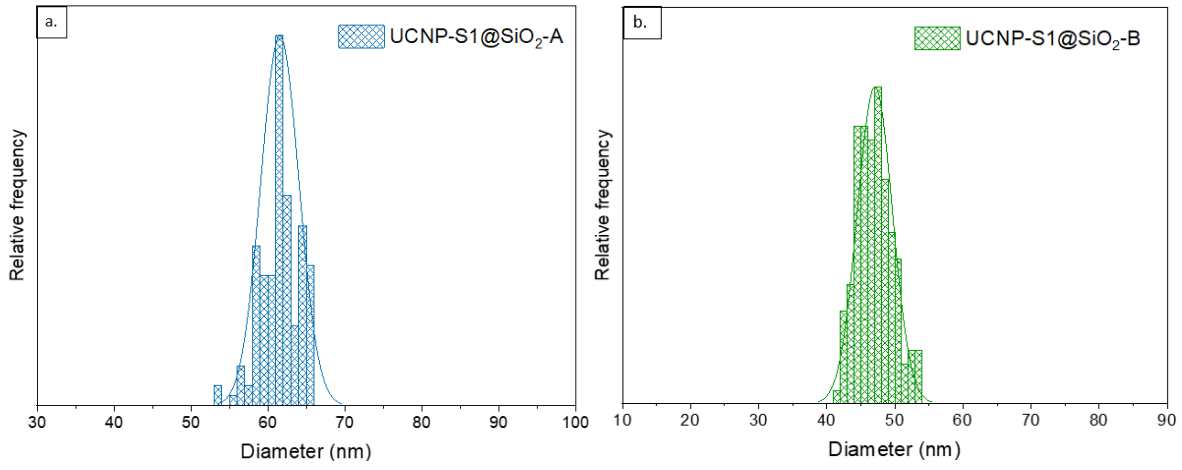

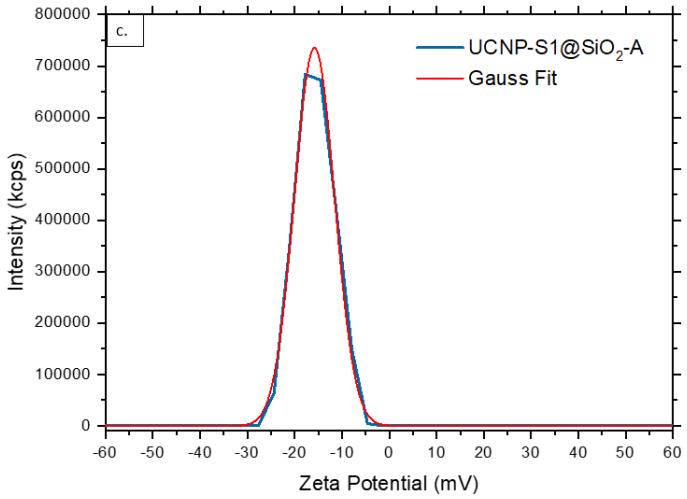

Figure III.20 *Size distribution and dispersion analysis.* ***a, b:*** *Diameters of UCNP-S1@SiO_2-A and UCNP-S1@SiO_2-B respectively measured from TEM micrographs using Digimizer software.* ***c.*** *Zeta potential measurement of UCNP-S1@SiO_2-A dispersed in deionized water, the blue curve is fitted using a Gaussian function in red.*

3.4.1.3 Discussion

The difference in the silica shell thickness and the homogeneity of the samples (presence/absence of core-free silica NPs) can be explained by the modified preparation steps. The impact of the addition order of Igepal co-520 might seem negligible but turns out to be significant in this reverse microemulsion method. In the first batch the Igepal co-520 amount was split into two parts between two steps, the first 0.1 mL of the surfactant is mixed with cyclohexane and the dispersed UCNP and left to stir for some minutes during which a part of the surfactant molecules already started the ligand exchange which consist on substituting OA on the surface of the hydrophobic UCNP by Igepal co-520 (**Fig III.14**). The other part of surfactant molecules formed the first micelles with the hydrophobic alkyl chains being directed toward the solvent because of the good affinity with cyclohexane. After adding ammonia and the remaining 0.4 mL of surfactant, the ammonia fills the already existing Igepal co-520 micelles to create water-in-oil microemulsions stabilized with the surfactant. Simultaneously, more microemulsions are being formed as a result of additional Igepal co-520 added to the flask. In the second preparation, the amount of Igepal co-520 is used all at once in one step before ammonia addition. In their explanation of the mechanism of silica coating using the reverse micro-emulsion route, G. H. Li *et al.* [193] brought out the role of ammonia content in affecting the shell thickness, and tried several ammonia to Igepal co-520 ratios to tune it. Indeed, when the amount of ammonia is increased relatively to the amount of surfactant, the size of the aqueous domain increases and the shell gets thicker. Concomitantly, as ammonia

acts as a catalyst, increasing its content leads to the speed up consumption of hydrolyzed TEOS monomers in a short time, resulting in a spontaneous nucleation, which is responsible of the formation of the small core-free silica. This is because the concentration of the supplied monomers becomes lower than the homogeneous nucleation concentration threshold and as long as it is above the solubility concentration, spontaneous nucleation will take place, according to LaMer [101]. The addition of TEOS to compensate the consumed concentration must be done in this case, but should not exceed the homogeneous nucleation concentration (or the saturation concentration) otherwise it leads to a spontaneous nucleation and formation of core-free silica NPs as well. G. H. Li *et al.* [193] suggest to modify TEOS concentration in the same way as the ammonia content in order to increase the silica shell thickness.

Here, the ammonia to surfactant ratio has been increased indirectly in two possible ways for the preparation of UCNP-S1@SiO_2-A: either the two steps addition of Igepal co-520 in the flask has changed the ratio of ammonia to surfactant, or the use of a syringe in a two steps addition of the viscous Igepal co-520 has increased the error in the true surfactant volume compared to a one step addition used UCNP-S1@SiO_2-B. In both cases, the ratio of ammonia to Igepal co-520 increases because the ammonia amount was kept unchanged and TEOS as well, while Igepal co-520 amount does change. Consequently, a spontaneous nucleation too place, leading to the formation of the small silica NPs as shown in the **Fig III.18 (Top)**. In contrast, no independent silica NPs were detected for UCNP-S1@SiO_2-B where a one-step addition of Igepal co-520 were followed. This procedure was repeated several times and still resulted in homogenous silica-coated UCNP.

The agglomeration of UCNP in **Fig III.19.a** happened as a result of collecting the as-prepared UCNP by centrifugation then drying them with the intention of measuring the dry weight yield and weighing a precise amount of UCNP. This must be avoided because once NPs are dried, they are hardly re-dispersed because agglomerates have been already formed. Consequently, the reverse microemulsion will hardly result in individual UCNP encapsulation, and most of the aqueous domains will remain empty because the size of agglomerated NPs does not suit the size of emulsions. That is why, after washing the as-prepared UCNP, they should be conserved with the proper concentration in cyclohexane, where they are kept stabilized by steric repulsion coming from the adsorbed OA ligand on their surface. Another common mistake is to use insufficient amount of UCNP compared to the number of available microemulsion droplets, which results in few silica-coated UCNP next to a high amount of core-free silica NPs (**Fig**

III.19 (b, c)), and that, independently from the nucleation/growth rate effect that could also bring to the same result under certain circumstances.

Lastly, the washing step is critical because it is important to use the right solvent to wash NPs without removing the capping ligand on their surface (OA). Solvent like cyclohexane, hexane and toluene must be avoided because OA is quite soluble in these. Instead, washing NPs several times with a water/ethanol mixture should be adopted even though it turns out to be a tedious task because of hydrophobicity of oleate-capped UCNP. If OA ligand is removed as a result of wrong washing, agglomerates are formed even when the NPs are kept in cyclohexane. Moreover, when NPs are not well stabilized in the solvent, they are not homogeneously dispersed in the volume sampled using the micropipette, and the amount of UCNP used for the silica step risks to be insufficient. In this case, both consequences in **(a)** and **(b,c)** of the **Fig III.19** can occur.

3.4.2 Yolk/shell nanoplatforms synthesis (UCNP@void@PMO)

The way to obtain the yolk/shell structure UCNP@void@PMO is based on similar steps for the preparation of HPMO NPs, using again BTEB as bridged organosilane precursor and CTAB as the structure-directing agent for the PMO formation. The only contrast relies on the presence of an additional functional core nanoparticles and that the hard template here is situated between the core and the PMO shell (**Fig III.1**). Silica is subsequently etched, hence resulting in movable UCNP inside PMO shell.

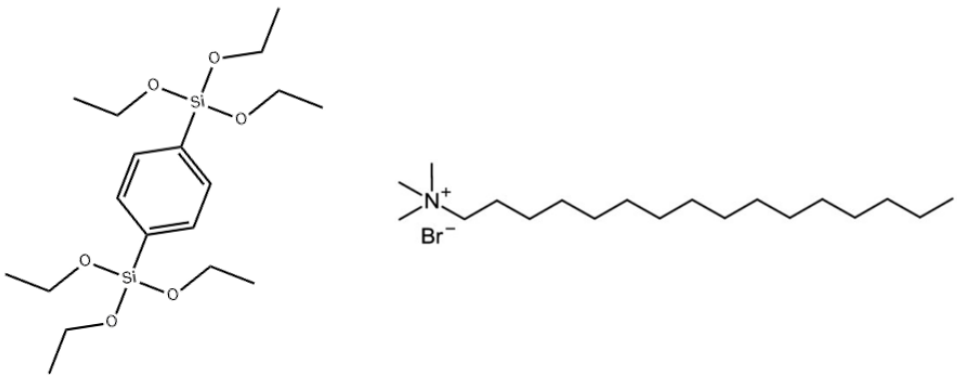

Figure III.21 Left: *1,4-Bis(triethoxysilyl)benzene (BTEB) used as a bridged organo-silane precursor.* ***Right:*** *Cetyl Trimethyl Ammonium Bromide (CTAB) surfactant used a structure directing agent (SDA).*

3.4.2.1 PMO deposition: Series of samples A

A second layer deposition on the silica-coated UCNP consisting in hybrid silica co-assembled with a surfactant was so far the most challenging task. The obtention of uniform and monodisperse UCNP@SiO_2@PMO NPs was not straightforward. The approach to prepare these nanoplatforms went through several adjustments before reaching its optimal form. The observation of results evolution enhanced the comprehension of the high-quality NPs formation mechanism and how it is governed by the synthetic parameters.

In the next section, failed samples and their evolution through the synthesis adjustments ***(Sample series A)*** *are described and discussed before presenting the successful samples* ***(Sample series B)***.

a) Series of samples A: Preparation

- ***A-PMO-1***

The as-synthesized UCNP-S1@SiO_2-A are re-dispersed in 10 mL of absolute ethanol and conserved for several uses. 1 mL of the dispersion is sampled and added to a 50 mL two-necked flask, to which 1.15 mL of absolute ethanol, 2.6 mL of water, 67 µL of NH_4OH (28%) and 6.4 mg of CTAB was added. The mixture is left to stir at 30 °C for 40 mins before adding 0.02 mL of BTEB and left to react for 6 h at room temperature and 600 rpm. The water to ethanol volume ratio is fixed at 1.2.

- ***B1-PMO***

The as-synthesized UCNP-S1@SiO_2-B (B1) were collected by centrifugation at 8000 rpm. The yield is ≃ 17 mg (wet weight) and is completely redispersed in a mixture of 12 mL of deionized water and 10 mL absolute ethanol (1.2 volume ratio) by 10 min sonicating. To this, 32 mg of CTAB and 0.35 mL NH_4OH (28%) are added and left to stir for 40 min at 30 °C before adding 0.1 mL of BTEB and left to react for 2 hours at room temperature and 600 rpm. The resulting solution was centrifuged at 5000 rpm to collect the NPs, and washed twice with water/ethanol and redispersed in water, this procedure was applied for the rest of the samples.

- ***B2-PMO***

A second batch of UCNP-S1@SiO_2-B (B2) was prepared following the same procedure described in *3.3.2.1*. NPs with reproducible quality and silica shell thickness were obtained. The yielded wet weight (≃ 15 mg) was redispersed in 12 mL of deionized water, to which 32 mg of CTAB and 0.35 mL of NH_4OH (28%) and left to stir for 40 mins at 30 °C. 0.1 mL of BTEB is then mixed with 0.2 mL of absolute ethanol in a hemolysis tube and sonicated before adding it to the flask. The temperature is raised to 80 °C and the reaction is left for 2 hours under reflux.

- ***B3-PMO***

A third batch of UCNP-S1@SiO_2-B (B3) was prepared (≃ 15 mg) and redispersed in 12 mL of deionized water, to which 32 mg of CTAB and 0.35 mL of NH_4OH (28%) and left to stir at 30 °C. After 20 min, 0.2 mL of absolute ethanol was added and after another 10 min 0.1 mL of BTEB in 0.2 mL of absolute ethanol was added and left to react for 2 hours at 30 °C.

Sample	Amount of UCNP-SiO_2 used for PMO deposition (mg)	H_2O/ EtOH Molar ratio	Addition time interval of ethanol	PMO-induced etching	Initial silica shell thickness (nm)	Silica-shell thickness after PMO deposition (nm)	Homogeneity of the sample	T°C after BTEB addition
A-PMO-1	1ml suspension of UCNP-S1@SiO_2-A (≃ <5 mg)	3.87	Added to the mixture since the beginning of reaction	No etching	20	20	Formation of big PMO NPs of 700 nm to 1µm	RT
B1-PMO	17	3.87	Added to the mixture since the beginning of reaction	No etching	10	10	Formation of independent large PMO NPs of 100 to 150 nm	RT
A-PMO-2	22	No ethanol	_	Yes	20	10	Formation of independent small PMO NPs of 25 nm.	80°C
B2-PMO	15	223	Mixed with BTEB and added after 40 mins	Yes	10	0	Formation of independent small PMO NPs of 25 nm.	80°C
B3-PMO	15	96	Mixed with BTEB and added after 20 mins	Yes	10	4-5	Few independent PMO NPs of 25 nm.	30°C

Table III.2 *Summary of the synthetic parameters proper to each sample from series A and the most prominent features observed in the TEM micrographs.*

b) Series of samples A: TEM analysis

All TEM micrographs displayed **Fig III.22** with the corresponding synthesis conditions and characteristics summarized in **Table III.2** are heterogenous because of the presence of either large or small core-free PMO NPs pointed out with red arrows.

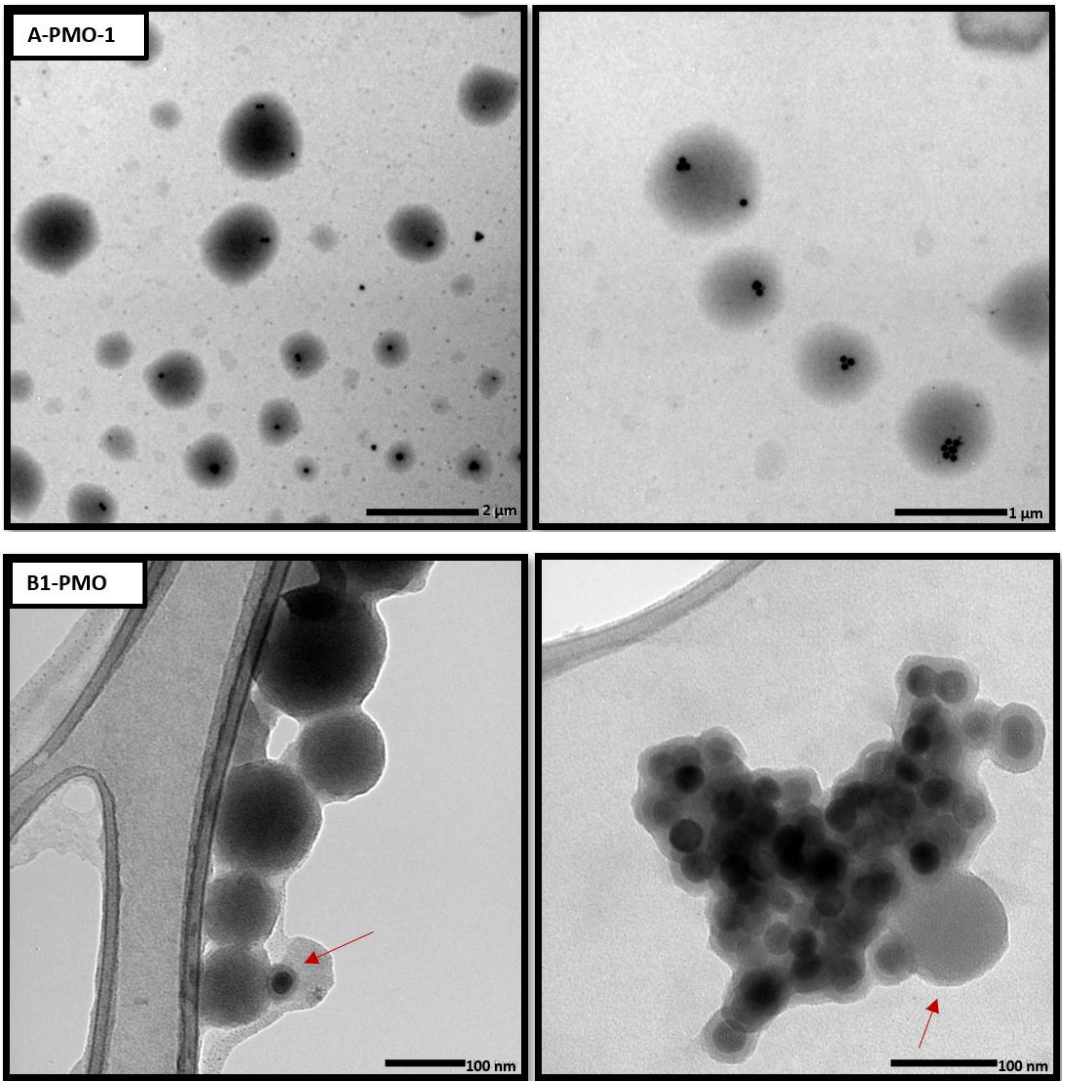

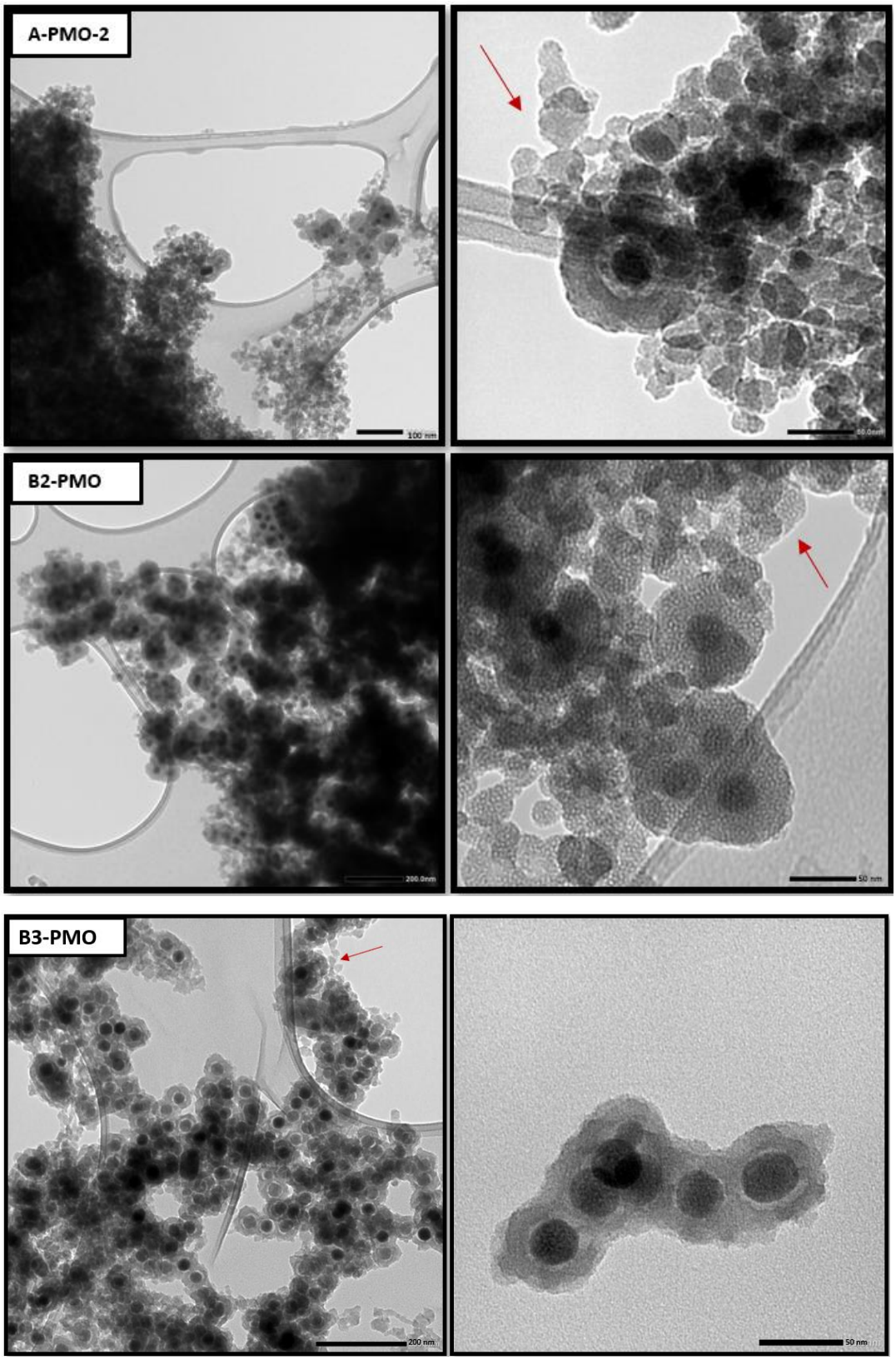

Figure III.22 *TEM micrographs of the series A of samples. The red arrows in the samples B2-PMO, B3-PMO and A-PMO-2 indicate the small core-free individual PMO nanoparticles, the arrow in B1-PMO indicates big core-free PMO nanoparticles.*

3.4.2.2 Analysis and discussion

Homogeneity of the samples

This series of experiments shows several significant aspects that give some indications to achieve an optimized synthesis of yolk/shell UCNP nanoplatforms, and some of them corroborate with the observations made in **Chapter. II** on the synthesis of HPMO NPs with tunable size. However, it does not seem possible to apply exactly the same procedure used to coat the sub-50 nm hard templates NPs with a PMO shell to the silica-coated UCNP, first because here we are dealing with very small amounts of UCNP, which besides do not have the same number of NPs for the same mass. Indeed, UCNP consist of nanocrystals doped with heavy rare earth metals. Nevertheless, what it can be derived from the HPMO NPs size tuning experience is the importance of using the appropriate volume fraction of UCNP-SiO_2 in the reaction mixture, especially in a system composed of both water and ethanol as solvents. Otherwise, the bridged organosilane precursor and surfactant co-assembling tend to form independent core-free PMO NPs in the unoccupied volume of the solution, which results in non-homogeneous sample where PMO NPs are considered as by-products that become difficult to separate. In the case of magnetic nanoparticles this issue can be easily overcome since they can be separated from the by-product using a magnet. Unfortunately, this is not applicable for UCNP and a proper procedure must be developed in order to solve this challenge.

In fact, by looking at the TEM micrographs of the sample A-PMO-1 (**Fig III.22**), several large PMO nanoparticles ranging from 700 nm to 1 µm were detected at the large scale. They randomly entrap one or several UCNP-SiO_2 NPs, while other NPs are free. This result seems to be very close to the work reported by S. Rahmani *et al.* [277] on the encapsulation of UCNP ($BaLuF_5$: Er-Yb and $NaYF_4$: Er**,**Yb nanocrystals) in 1,2-bis(triethoxysilyl)ethane (BTSE) in the presence of CTAB as soft template, knowing that no silica layer is used as medium between the UCNP and the BTSE PMO. This suggest that the reaction conditions favor the formation of large PMO NPs, UCNP-SiO_2 NPs.

The amount of UCNP-SiO_2 in the 1 mL suspension can be estimated to be less than 5 mg, which is not enough even with small volumes of water/ethanol. The small size of the NPs and their small numbers do not favor a precursor/surfactant co-assembly around individual UCNP-SiO_2. When using a larger amount (22 mg) for the sample B1-PMO in a larger solution volume with the same water/ethanol molar ratio, UCNP-SiO_2 were slightly covered with a thin layer of PMO,

but the large PMO NPs were still produced independently from the core/shell structure. This suggests that as long as the amount of core/shell NPs is not perfectly adjusted to water/ethanol mixture, there will always be a formation of PMO NPs. In fact, ethanol plays a key role in this matter, as it is a good solvent for the bridged organo-silane precursor (BTEB) and for the surfactant (CTAB). It is known to act both as either solvent or co-surfactant depending on the used concentration [181]. The kinetics of the co-assembly is accelerated in the blank space of solution (unoccupied by UCNP-SiO_2), and the larger it is, the bigger is the number of PMO NPs. Therefore, most of the monomer use is preferably directed toward the formation of PMO NPs, and the core/shell structures are either ignored or coated with a very thin layer as it is noticeable in **Fig III.22**, **A-PMO-2**.

In the next sample A-PMO-2, no ethanol was used and no large PMO NPs appeared. Instead, a big amount of small PMO NPs of 25 nm were formed (pointed out with red arrow in **Fig III.22**), similar to the HPMO NPs synthesized without ethanol in **Chapter. II**. Their formation is explained by the low miscibility between BTEB and water molecules. Additionally, the CMC of CTAB in water ($9x10^{-4}$ mol/L) is significantly lower than in ethanol (0.24 mol/L) [278], which means that at a concentration of 32 mg of CTAB in 12 mL of water ($7.32\ x10^{-3}$ mol/L above water CMC), the micelles of CTAB have already been formed. While BTEB molecules are hardly soluble in water, their hydrolysis rate is faster than in water/ethanol system [202], and they would rather rapidly co-assemble with CTAB micelles, and form the sub-50 nm core-free PMO NPs. A PMO deposition also occur on the top of core/shell UCNP, as shown in **Fig III.22**. **A-PMO-2**, because some CTAB micelles are adsorbed on the top of the negatively charged UCNP-SiO_2 and co-assemble with hydrolyzed monomers of BTEB. Ethanol release during the early-stage hydrolysis and condensation of BTEB monomers further enhances the development of the PMO shell. However, when the spontaneous nucleation occurs, the amount of precursor is not entirely dedicated to core/shell PMO coating, consequently the prediction and control of the PMO layer thickness can be challenging. To sum up, the results show that on the one hand it is hard to perform PMO deposition while controlling its homogeneity in a water/ethanol system with a molar ratio of 3.87. On the other hand, the suppression of ethanol from the reaction mixture decreases the solubility of both the precursor and the surfactant, thus impacting homogeneity of the sample.

The next solution is to add a small amount of ethanol in such a way to increase the solubility of the monomers. This procedure was reported of Y. Deng *et al.* [202] who mixed BTEB with a

small amount of ethanol (0.2 mL) before addition. We applied this strategy for sample B2-PMO preparation, the formation of core-free PMO NPs has still occurred. When using an additional amount of ethanol (0.2 mL) for B3-PMO just before the addition of the BTEB/ethanol mixture, fewer 25 nm PMO NPs were observed in the TEM micrographs. This can be explained by the influence of the extra ethanol in dissolving any remaining CTAB molecules and enhancing the formation of micelles. These micelles subsequently co-assemble with the hydrolyzed precursor monomers on the surface of the core/shell nanoplatforms. However, complete impurity-free sample could not be attained probably because the water to ethanol molar ratios used in these cases are enormous, 223 and 96 respectively (**Table III.2**).

PMO-induced etching

In the three last samples, an etching of the amorphous silica layer induced by the growth of PMO is observed, like reported in literature. D. Zhao *et al.* [197] varied the time interval between the addition of NaOH and the precursor to obtain different etching thicknesses. But following the results shown in TEM micrographs (**Fig III.22**) and summarized in the table (**Table III.2**), the etching process seems to be occurring in a different manner. In both samples A-PMO-2 and B2-PMO, the core/shell NPs were left to stir with CTAB and ammonia at 30 °C for 40 mins before adding BTEB and raising temperature up to 80 °C. Since the silica-shell thickness of the UCNP-SiO_2 is not the same in the two syntheses (**Fig III.18**) ($\simeq$20 nm for A-PMO-2 and $\simeq$10 nm for B2-PMO), the etching extent is not the same. The TEM micrographs show clearly that for the core/shell NPs that were coated with a PMO layer, the silica shell was etched to the half of the total thickness for A-PMO-2, whereas it was totally etched for B2-PMO resulting in a deposition of PMO directly on the surface of PMO. Therefore, for the same synthetic conditions, around 10 nm of silica in each sample was dissolved. The etching originates from the high temperature (80 °C) and high alkaline condition, and induced by the deposition of PMO like reported by some studies [196, 197]. However, by looking at the TEM micrograph of sample B3-PMO, the etching took place even when maintaining the temperature at 30 °C. This suggests that the silica etching actually occurs since the beginning of the reaction at 30 °C, when the core/shell structure are embedded in the water/ammonia (pH$\simeq$10) solution and before the addition of BTEB. Furthermore, the extent to which silica is etched is based on the time left in the high alkaline solution before addition of the precursor. D. Zhao *et al.* [197] mentioned that the silica etching degree depends on the time interval between the addition of the alkaline agent and the precursor (also true in our case), and that etching of the silica occurs at the same time as the monomer/cationic surfactant co-assembly to form a PMO shell. But the

subtle difference is that the etching is actually triggered by the alkaline agent that hydrolyzes Si-O-Si bonds. Following the introduction of the organosilane precursor, it promptly initiates the formation of a PMO shell under the guidance of the cylindrical micelles of CTAB surrounding the partially etched silica. The distance between the core and the PMO shell is determined by the extent to which the silica shell thickness is reduced and determines the volume of the void as well. After the PMO deposition, the remaining silica keeps dissolving under the high alkaline condition, leading to the formation of the void. The monomers released after silica etching also contribute in the polycondensation of the PMO shell [197]. In case all the silica shell is suppressed before the addition of the precursor, the latter will simply co-assemble on the top of the UCNP, especially that the silica monomers would still be around and would favor the process. This was the case for sample B2-PMO with a 10 nm silica layer that dissolved completely after 40 mins, whereas for A-PMO-2 the silica layer of 20 nm was reduced to half thickness after 40 mins as well. For B3-PMO, the 10 nm silica layer (the same as B2-PMO) was only reduces to 4-5 nm in 20 min only, before the addition of BTEB (**Table III.2**). This indicated that the process of etching is indeed time dependent.

d) Series of samples A: Conclusion

This series of samples provided some information that will be considered in the next yolk/shell UCNP@void@PMO in order to prepare improved nanoplatforms and the following points will be followed for the series of samples B:

- *The amount of UCNP-SiO_2 core/shell NPs should be preferably above 20 mg for 12 mL of water solution (~1.67 mg/mL).*

- *The amount of ethanol to add just before the addition of BTEB should be slightly increased to dissolve the maximum of BTEB/CTAB molecules and avoid the formation of 25 nm core-free PMO NPs.*

- *The duration of UCNP-SiO_2 presence in the alkaline solution should be controlled in a way to avoid the spontaneous etching as we are interested in studying the nanoplatform's luminescence properties when the silica layer is still present.*

3.4.2.3 PMO deposition: Series of samples B

a) UCNP@ SiO_2: Description

The next series of samples are prepared using UCNP-SiO_2 provided with enough quantity from Xiaogang Liu's group from the department of Chemistry of National University of Singapore. The $NaYF_4$ nanocrystals were doped with Lutetium (Lu) in addition to the sensitizer-activator pair (Er, Yb), with the purpose of UCNP size tuning and obtaining the 52 nm size. The characteristics of the core/shell structures are summarized in the following table.

Sample name	Composition	Core size (nm)	Silica shell thickness (nm)
UCNP@1-SiO_2	$NaYF_4$:40%Lu,18%Yb,2%Er	52	13
UCNP@2-SiO_2	$NaYF_4$:40%Lu,18%Yb,2%Er	52	27

Table III.3 *UCNP-SiO_2 NPs characteristics.*

Synthesis of UCNP: *The synthesis of the upconverting nanoparticles (UCNPs) was carried out according to a previously reported procedure (C. D. Brites et al. Nat. Nanotechnol. 11, 851, 2016). In a typical experimental procedure, a 2 mL aqueous solution of Ln $(CH_3CO_2)_3$ (0.2 mol L^{-1}, Ln = Lu, Y, Yb, and Er) was added to a 50 mL flask containing oleic acid (3 mL) and 1-octadecene (7 mL). The mixture was heated to 423 K for 1 h. After cooling down to 323 K, a methanol solution (6 mL) containing NH_4F (1.6 mmol) and NaOH (1 mmol) was added under stirring for 30 min. After removing the methanol through evaporation, the solution was heated at 563 K under argon for 3 h and then cooled down to room temperature. The resulting nanoparticles were washed with ethanol several times and re-dispersed in 4 mL of cyclohexane.*

Coating with amorphous silica shell (~13 nm): *In a standard methodology, amorphous silica (SiO_2) shell was grown onto the surface of the 52 nm ligand-free UCNPs by using polyvinylpyrrolidone (PVP) as a mediator (Y. Wu, J. Xu, X. Qin, J. Xu, X. Liu, Nat. Commun. 2021, 12, 2022). PVP (250 mg) was dissolved under stirring in a 50 mL round-bottom flask containing 5 mL of deionized water and 15 mL of ethanol until its total dissolution. The ligand-free 52 nm $NaYF_4$: Lu/Yb/Er (40/18/2%) UCNPs were added to the flask and kept under stirring for 30 min. Then, a solution of tetraethyl orthosilicate (50 µL) dissolved in ethanol (300 µL) was added to the flask. The mixture was reacted overnight under stirring. $NaYF_4$: Lu/Yb/Er (40/18/2%) @SiO_2 UCNPs were collected via centrifugation at 16500 rpm for 30 mins and washed twice with ethanol.*

b) PMO deposition on UCNP@ SiO_2

- ***UCNP@1-SiO_2@PMO-CTAB***

~23 mg of UCNP-SiO_2-C from the **Table III.3** are re-dispersed in 12 mL of deionized water with 10 mins sonicating bath. To this 32 mg of CTAB and 0.35 mL of NH_4OH (28%) are added and the mixture is left under stirring for 7 mins at 30 °C and 750 rpm stirring rate. Soon after, a first shot of 0.3 mL of absolute ethanol is added to the mixture and left to stir for 3 mins. Then a second shot composed of a mixture of 0.2 mL absolute ethanol and 0.05 mL BTEB is added slowly and dropwise using a micropipette. The color of the suspension does not change immediately. If it is the case and that the color quickly turns toward light grey (**Fig III.23.b**), it would mean that the formation of core-free PMO NPs occurred faster and one can already guess the failure of the synthesis. If the color turns progressively into a translucid opal blue color (**Fig III.23.a**) it indicates that the reaction is going in the good direction toward a homogeneous PMO coating. The reaction is left for 2 h then the opaque white color of the as-obtained solution is centrifuged at 5000 rpm to collect the NPs, then washed several times with water and either preserved as a suspension in water or used directly for the etching step.

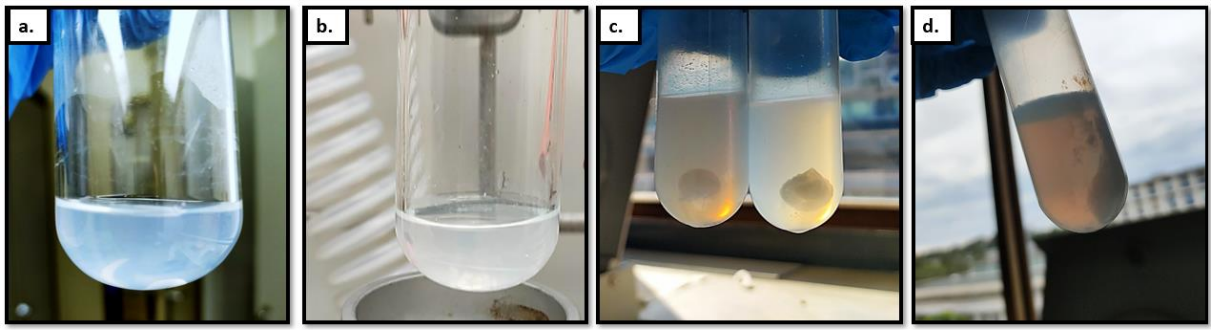

Figure III.23 *Difference between a homogeneous and heterogeneous sample distinguished based on the suspension color in the first 20 mins of the reaction* ***(a-b)****, the centrifuged solution aspect at 5000 rpm* ***(c-d)****.* ***a.*** *Translucid opal blue color when the PMO coating is homogeneous.* ***b****. Greyish solution that is a sign of fast nucleation of small PMO NPs resulting in a heterogeneous sample.* ***c.*** *The volume of precipitated NPs should be reasonably close to the initial UCNP-SiO_2 before PMO coating.* ***d.*** *The yield of collected NPs using the same centrifugation rpm is bigger than expected, meaning that additional PMO NPs were produced.*

- ***UCNP@2-SiO_2@PMO-CTAB***

The same procedure above was repeated for core/shell NPs PMO coating, except that the amount of UCNP-SiO_2-D used is ~ 49 mg.

c) UCNP@SiO_2@PMO-CTAB etching to form a yolk/shell nanoplatform: UCNP@void@PMO-CTAB

A quantity of the as-prepared UCNP@SiO_2@PMO-CTAB is dispersed in a mixture of 25 mL of water and 0.175 ml of NH_4OH (pH=10) in a 100 ml flask. Then the mixture is heated up to 80 °C and left for 1h. The etched NPs are subsequently collected after centrifugation and washing twice with water. The etching is performed while CTAB is still in mesopores.

d) CTAB removal to obtain UCNP@SiO_2@PMO and UCNP@void@PMO samples

The acid treatment using HCl usually used to remove the cationic surfactant from the mesoporous shell is not suitable for nanoplatform containing a UCNP core. Indeed, some preliminary experiments using a diluted HCl solution in ethanol like the one used for HPMO, lead to the decomposition of the UCNP core. Some works reported the use of NH_4NO_3 solution instead to remove CTAB [268]. The procedure goes as following: a quantity of the as-collected NPs is dispersed in 50 mL solution of absolute ethanol containing 0.3 g of NH_4NO_3, the temperature is heated up to 60 °C and the mixture is left to stir for 2 h. The collected NPs are subsequently washed twice with ethanol/water then preserved in water. The same procedure is applied for both samples.

e) Series of samples B: TEM analysis

The deposited PMO layer thickness is quite similar in both samples, mean shell thicknesses 27.9 ± 1.9 nm and 27.8 ± 1.7 nm for UCNP@1-SiO_2@PMO and UCNP@2-SiO_2@PMO respectively are measured using TEM images. The large scale (2 µm) micrograph displayed in **Fig III.24.a** show the homogeneity of the sample, no PMO NPs impurities were detected and the coating is successfully homogenous. We can notice from **Fig III.24.b** that some cores are merged in one PMO layer, which might be caused by the fact that the core/shell NPs were initially not well separated. This proves that the re-dispersion step using sonicating bath is crucial to ensure a total separation of NPs, especially that centrifugation tends to agglomerate them. Nevertheless, they remain very few from a global view. The high-resolution TEM and SEM micrographs in **Fig III.24 (f, g, h)** exhibit the apparent contrast between the layers of the nanoplatforms, with a gradient from black with the high electronic density of the upconverting nanocrystal doped with heavy rare earths, dark grey of medium electronic density of the amorphous dense silica hard template and light grey of the less dense mesoporous layer (PMO). The mesoporous structure is also quite discernible in the **Fig III.24.h**, and the size of the single

mesopore can be estimated between 2 to 3 nm if we consider the scale of the micrograph, and which corresponds to the size of CTAB micelle.

The successful silica etching in both samples is shown in **Fig III.25**. The different silica hard template thicknesses 13 nm and 27 nm (**Table III.3**) left different void volumes after etching. Consequently, the functional core became mobile inside the PMO shell forming a rattle-type nanoplatform (yolk/shell), and falls on the lower side of the NP under gravity effect. The CTAB extraction using NH_4NO_3 ethanol solution was not aggressive for UCNP core unlike HCl solution, it remained intact and the crystallinity of the hexagonal phase $NaYF_4$: Er,Yb is also quite visible (**Fig III.25 (e, f)**).

- **Before silica etching**

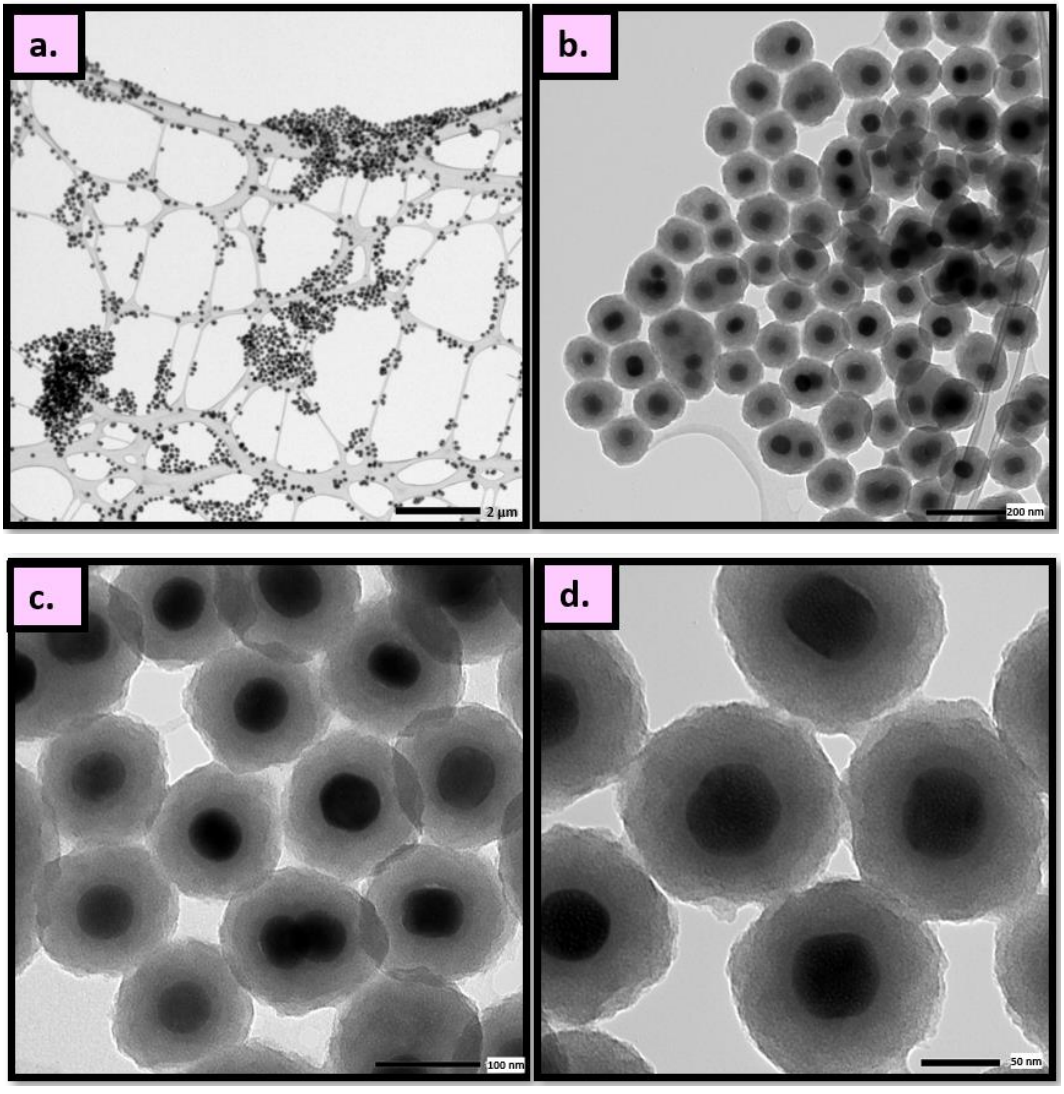

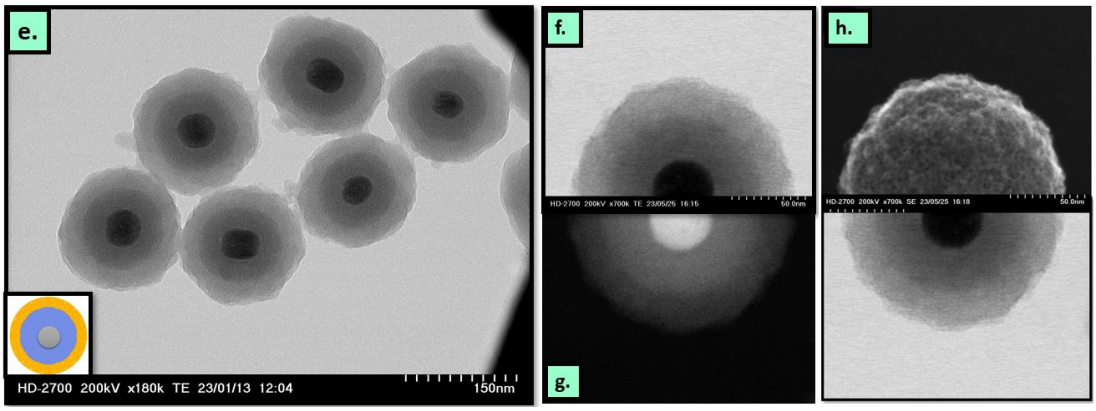

Figure III.24 *TEM micrographs of the as-prepared UCNP@SiO_2@PMO with two different intermediate silica layer thicknesses before the silica etching procedure.* ***(a-d)*** *UCNP@1-SiO_2@PMO sample with a 13 nm silica layer observed in different scales from 2 µm to 50 nm respectively.* ***e.*** *UCNP@2-SiO_2@PMO sample with a 27 nm silica layer with 150 nm scale bar.* ***f.*** *High resolution TEM micrograph of single NP from UCNP@2-SiO_2@PMO showing the contrast of different layers.* ***g.*** *The same NP in dark-field showing inversed contrasts.* ***h.*** *SEM profile showing visible mesoporous structure.*

- **After silica etching**

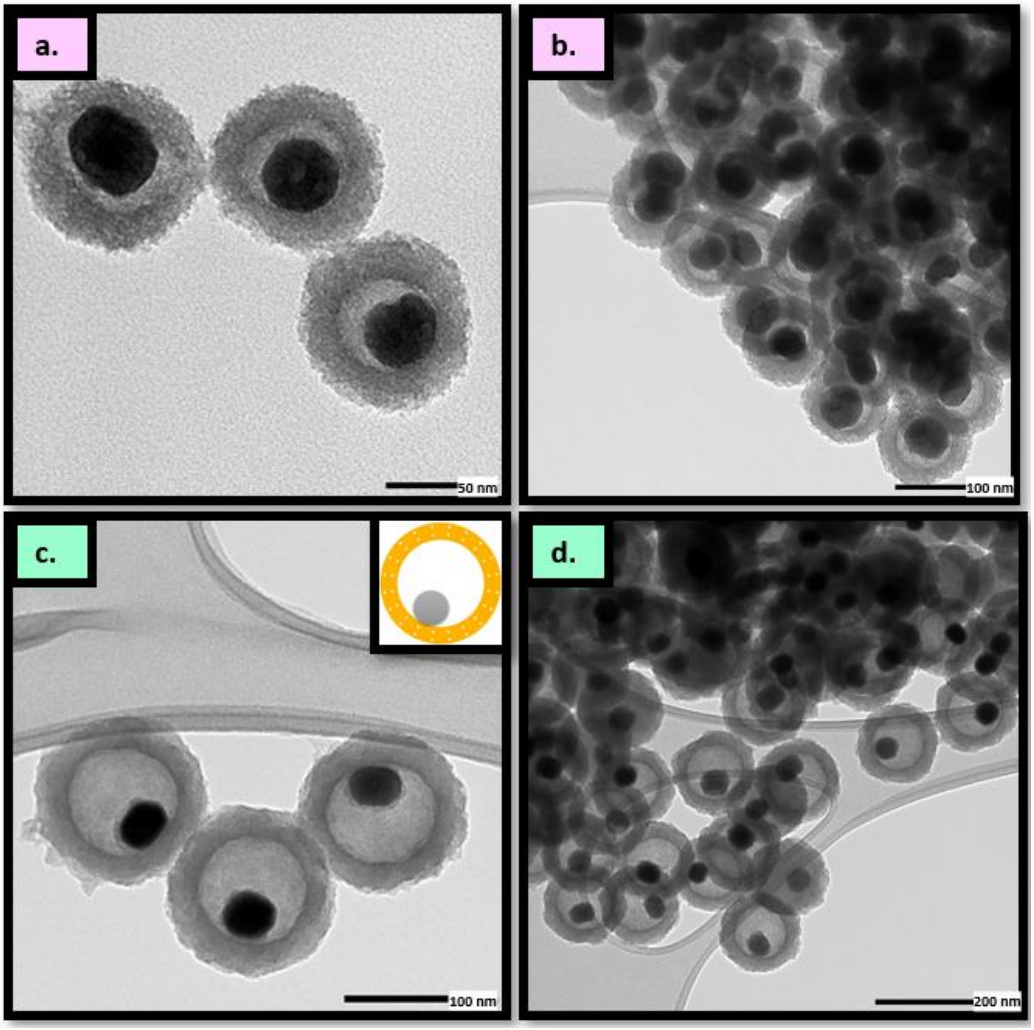

Figure III.25 *TEM micrographs of UCNP-SiO_2-PMO after silica etching (UCNP@void@PMO).* ***a, b:*** *UCNP@1-void@PMO in 50 and 100 nm scale bars respectively.* ***c, d:*** *UCNP@2-void@PMO in 100 and 200 nm scale bars respectively.* ***e, f:*** *High resolution TEM micrographs of both yolk/shell samples.*

f) Series of samples B: size distribution and dispersion analysis

Size distribution are measured from TEM images **Fig III.26 (a, b)**. The mean sizes are 128 ± 6 nm and 166 ± 9 nm for UCNP@1-SiO_2@PMO and UCNP@2-SiO_2@PMO respectively, calculated from a minimum of 100 NP. DLS analysis displayed in **Fig III.26 (c, d)** show a normal distribution of slightly higher NPs sizes than the ones measured from TEM images, the mean sizes are 168 ± 1 nm and 214 ± 1 nm for UCNP@1-SiO_2@PMO and UCNP@2-SiO_2@PMO respectively. The difference in the size is around ~ 40 nm, which could be assigned to the hydrodynamic size of NPs.

The zeta potential analysis in **Fig III.26.c** shows a different value between the sample UCNP@2-SiO_2@PMO, before and after the removal of CTAB, with a slight shift toward higher negative values after the removal (+ 4.7 mV).

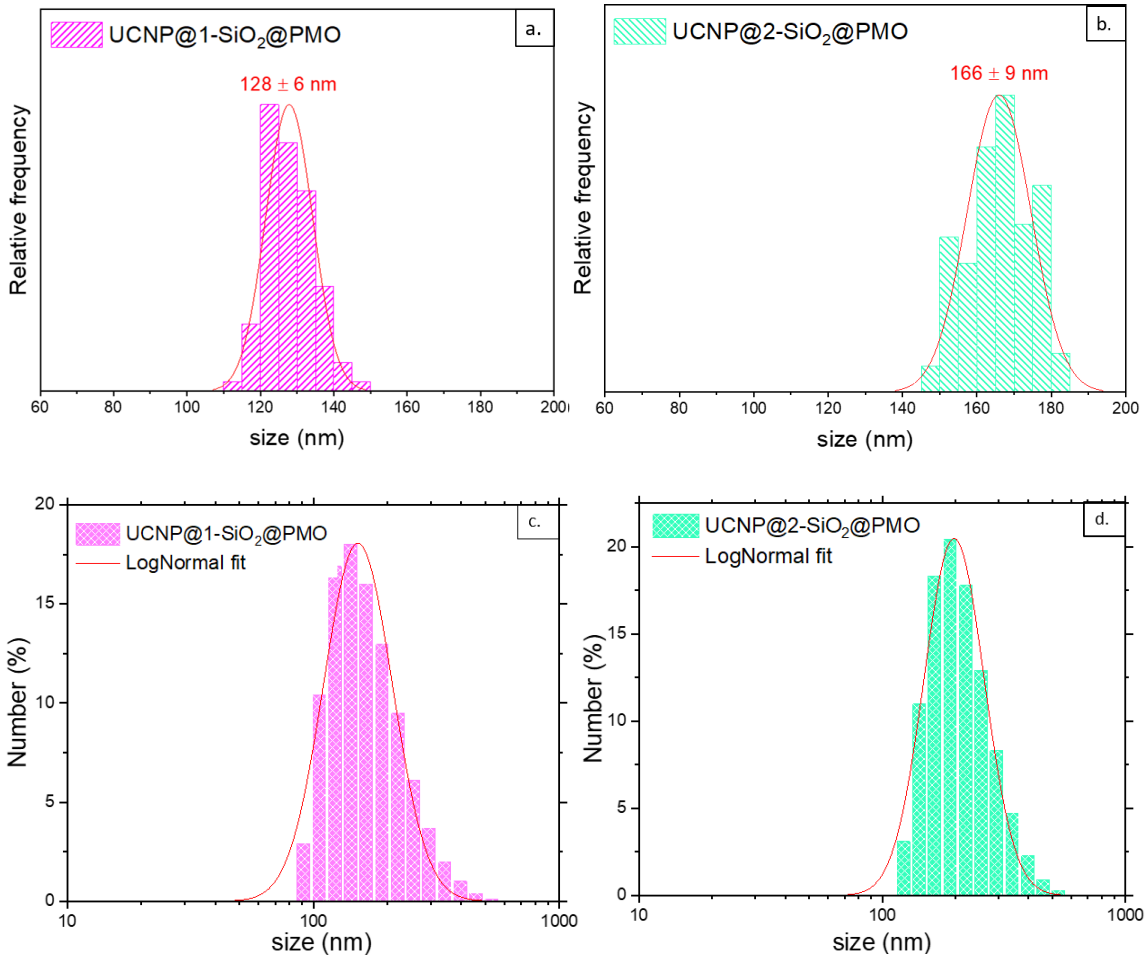

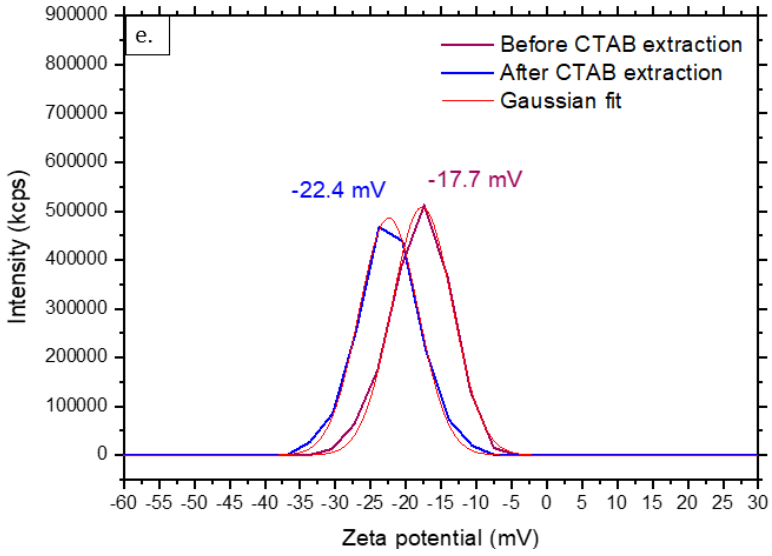

Figure III.26 a,b: *NPs size distributions measured from TEM image using Digimizer software.* ***c, d****: NPs size distribution using DLS analysis.* ***e.*** *Zeta potential analysis of UCNP@2-SiO$_2$@PMO suspension in deionized water before and after removal of surfactant (CTAB) from mesopores with curves fitted using a Gaussian function.*

3.4.2.4 Discussion

Following the conclusions for the sample series A, some modifications in the synthetic procedure were implemented and clearly led to the improvement of the quality of the NPs. The total amount of ethanol used was slightly increased in the step before adding BTEB (0.3 mL instead of 0.2 mL). Ethanol was added to the mixture after 7 mins from the beginning of the reaction to enhance the dissolution of remaining CTAB molecules, and after 3 mins from that the BTEB/ethanol mixture was added. By doing so, the alkaline solution does not have enough time to etch the silica layer, and the CTAB/BTEB co-assembly starts right away to form a PMO layer on the surface of negatively charged silica (hard template).

Zeta potential value shifting from -17.7 mV to -22.4 mV after CTAB removal shown in **Fig III.26** can be explained by the fact that when the cationic surfactant (CTAB) is still co-assembled with the hybrid silica framework through ionic bonds between the cationic head and $Si\text{-}O^-$, there is less free negative charges on NPs surface than when CTAB is removed and more negative charges appear. Hence, resulting in a larger charge repulsion and a good dispersion and stability in deionized water, which a crucial prerequisite to conduct spectroscopic experiment used for nanothermometry in an efficient an accurate way (**Chapter. IV**).

3.5 Conclusion

This part of the thesis was dedicated to the encapsulation of $NaYF_4$: Er, Yb nanocrystals acting as luminescent upconverting nanothermometers (UCNP) in a first shell made of amorphous silica, then a second periodic mesoporous organosilica (PMO) shell serving for a prospective functionalization.

This chapter started with a bibliographic review on the various synthesis routes used to prepare hexagonal $NaYF_4$: Er, Yb phosphors, and encapsulation strategies targeting the construction of multifunctional nanoplatforms. Then, the synthesis step for the preparation of uniform and pure hexagonal phase $NaYF_4$: Er, Yb nanocrystals (UCNP) following the methanol-assisted thermal decomposition was presented in detail, followed by their encapsulation in a silica shell using the reverse micro-emulsion strategy. The last step consisted on the encapsulation of the silica-coated UCNP in a layer of PMO, with the silica serving as an intermediate sacrificial hard template.

The PMO shell deposition was achieved by a sol-gel reaction involving the co-assembly of a bridged organosilane precursor (BTEB) with a cationic surfactant (CTAB) acting as a structure directing agent (SDA). This strategy was inspired from the work presented in **Chapter.II** dedicated to HPMO. However, this synthesis revealed some challenges, mainly the spontaneous nucleation of core-free small PMO NPs that disturbed the uniformity of the samples. Several attempts to overcome this issue were presented and their analysis served to qualitatively reveal the mechanism behind the formation of undesired NPs. Based on the suggested mechanism, a new protocol was developed targeting the improvement of the homogeneity of samples. The idea consisted on varying the water to ethanol ratio, and the time separating the addition of ammonia and the bridged organosilane precursors. The objective was to take control over the unwanted spontaneous nucleation of core-free PMO NPs. The volume fraction of the particles to coat in the solution was also a key point as it was initially demonstrated in **Chapter. II**. The use of the silica-coated UCNP in a considerable quantity was therefore crucial.

Two silica-coated UCNP samples provided in considerable amounts from Xiaogang Liu's group (the department of Chemistry of National University of Singapore), were utilized to try the new improved PMO coating protocol. Both having a 52 nm UCNP core nanocrystal coated

in one sample with a 13 nm and 27 nm for the other. PMO-coated UCNP-SiO_2 were obtained with a mean total size of 128 ± 6 nm and 166 ± 9 nm respectively.

Then, the same multistep approach leading the formation of hollow structures in **Chapter.II** were followed to obtain yolk/shell UCNP@PMO nanoplatforms, including the hard template silica etching and the removal of surfactant. Except that the acid treatment was conducted using NH_4NO_3 solution instead of HCl solution because the latter turned out to be UCNP destructive.

Samples from all the synthesis stage (**Fig III.27**) will be studied individually in the next chapter for the optical properties.

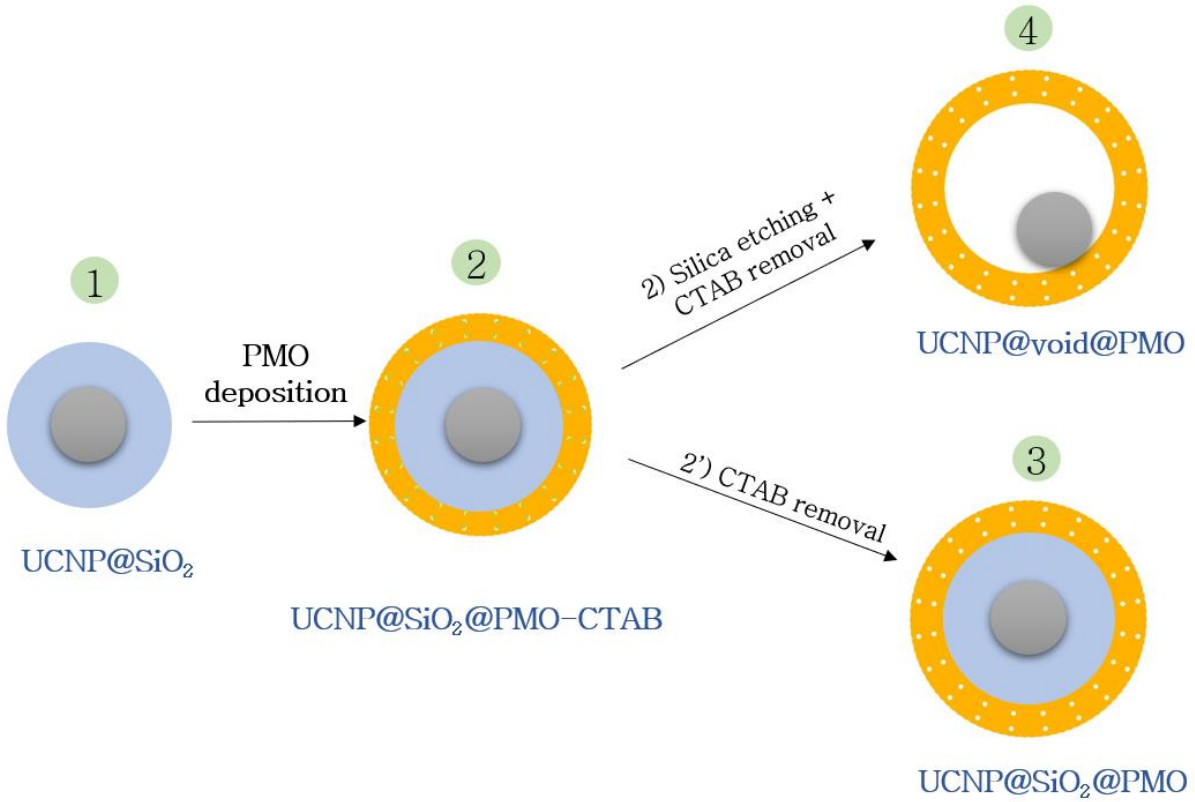

Figure III.27 *A treeview of the sampling process through the multi-step procedure leading to the yolk/shell PMO-encapsulated UCNP as the last product.* ***(1)*** *Silica-coated UCNP.* ***(2)*** *Silica-coated UCNP after the deposition of PMO-CTAB.* ***(3)*** *Nanoplatform after mesopores emptying by CTAB removal.* ***(4)*** *Removal of both CTAB and intermediate amorphous silica.*

Chapter IV.

The nanothermometric performance of PMO-encapsulated $NaYF_4$: Er, Yb upconverting nanophosphors

4.1 Introduction

Er,Yb co-doped $NaYF_4$ is widely considered as the most efficient upconverting phosphor [206, 279, 280] and is extensively used in many applications targeting the biomedical field like bioimaging and biosensing [23, 238, 261], because they own a combination of multiple attractive characteristics mentioned previously in the **Chapter.I**. Most of all, the upconversion efficiency of the Er,Yb sensitizer-activator pair enables the use of a low energy NIR excitation light converted to high energy emitted light, including two strong green emission at 524 nm and 540 nm emerging from two thermally coupled levels characteristic of Er^{3+} and which find widespread use in LIR nanothermometry method mentioned in **Chapter.I**. $NaYF_4$: Er,Yb phosphors also offer the advantage of being usable in a colloidal form by the synthesis of nanoparticles with tunable size and shape, broadly mastered in numerous reported works detailed in **Chapter.III**, as well as the possibility of surface functionalization with a large choice of strategies to adapt the nanocrystal to diverse targeted applications [279].

In fact, surface modification becomes a crucial step before employing the upconverting nanomaterials in a biological context for two reasons: the first one is to separate the cytotoxic upconverting nanomaterial from the external environment by performing a coating, and ensure their biocompatibility. The second is to convert the hydrophobic oleate-capped $NaYF_4$: Er, Yb into hydrophilic NPs ready to be dispersible in an aqueous environment such as cells.

With the purpose of assessing the nanothermometric performance under confinement effect, where the encapsulating layers are initially intended to meet the biological application, it becomes also fundamental to study the composite nanoplatform in a medium that closely replicate a cell-like environment, water for instance. Therefore, the targeted application prerequisites, the choice of the coating layer, and the suspension medium used for the optical properties' characterization, become all interdependent and must follow the same direction. For example, it would not make sense to study the performance of bare $NaYF_4$: Er, Yb NPs in a water suspension, first because the latter would rapidly agglomerate as they are hydrophobic, in this case, the optimal experimental conditions of these nanomaterials would be poorly maintained for accurate characterization, as the colloidal stability is not established. Second because their optical behavior would be totally different after their surface modification using coatings.

Despite their excellent properties of $NaYF_4$: Er, Yb as an upconverting material. Many researches have been focused on how some structural and morphological aspects can modify this performance. We mentioned previously in **Chapter.I** how the optical performance of the hexagonal phase of $NaYF_4$: Er, Yb far exceeds those of the cubic phase. Recent studies also demonstrate how $NaYF_4$: Er,Yb material luminescence emission intensity drops drastically from the bulk material to the nanosized particles, and from bigger nanoparticles to smaller ones [233, 280, 281]. The surface to volume ratio of small nanoparticles is high compared to relatively bigger nanoparticles, and even higher compared to a bulk material where a significant portion of Ln^{3+} is not exposed to the surface of the material and is therefore not prone to surface quenching effect caused by surrounding solvent molecules or ligands. As a matter of fact, -CH and -OH groups found in organic ligands and solvents like water respectively, are characterized with high vibrational frequencies that coincide with the same energy gaps of the emitting centers and favor the occurrence of non-radiative multi-phonon relaxation processes of the excited states [37, 261, 282]. Consequently, the optical performance of the upconverting material becomes not only dependent on the crystalline structure of the host lattice, its dimensions, or the encapsulating structure but on the local environment as well.

Surface passivation by the deposition of undoped $NaYF_4$ layer on the top $NaYF_4$: Er,Yb NPs surfaces by epitaxial growth to form a core/shell structure is by far the most efficient way to protect the nanoparticles from surface quenching, and results in the enhancement of the emission intensity as reported by several studies [52, 280, 283, 284]. However, an additional biocompatible coating would be necessary when targeting a biomedical application.

All of these points unambiguously suggest that the optical properties of $NaYF_4$: Er, Yb NPs or any other upconverting nanomaterial cannot be assessed in an absolute way and can only be determined within a well-defined context, when the latter rather targets applications such as nanothermometry in intracellular environments, the performance of the nanothermometers should be studied in an aqueous solvent to approximate the normal physiological conditions. Therefore, the encapsulating structure should not only be biocompatible but hydrophilic as well to ensure a good dispersion int the experimental medium.

These requirements lead to four conclusions. First, all the reported data on the optical properties in the bulk [280] and powder form [285] or the bare oleate-capped $NaYF_4$: Er, Yb nanocrystals dispersed in organic solvent like hexane and cyclohexane [52, 283, 286] are no longer reliable

to truly assess the optical behavior of such materials in the scope of a biomedical application. Second, coatings serving to protect nanocrystals surface and create a distance between the emitting center and the quencher is a critical step to reduce as much as possible the quenching effect caused by -OH vibrations of water, even though the damage caused by water molecules would still be inevitable, knowing that it absorbs the 980 nm light used to populate the Yb^{3+} excited state. Indeed, the transmission of light in 1 cm of optical path length in water is 61.6 %, for an absorptivity of 0.485 cm^{-1} at 980 nm [287] which essentially results in incident light losses and consequently affects the upconversion emission intensity of Er^{3+}. Third, surface passivation can only be performed using a biocompatible and a hydrophilic dense material such as silica. For this work, as we are interested in creating a multifunctional nanoplatform through the encapsulation of the nanothermometer in a PMO shell, the silica coating also serves as a pillar to the deposition of the PMO layer. Fourth, in order to distinctively analyze the effect of encapsulation on the nanothermometers performance, all the other parameters such as the nanocrystal phase (preferably the hexagonal one), the size and morphology, and the Ln^{3+} doping percentage should be fixed to avoid their contribution.

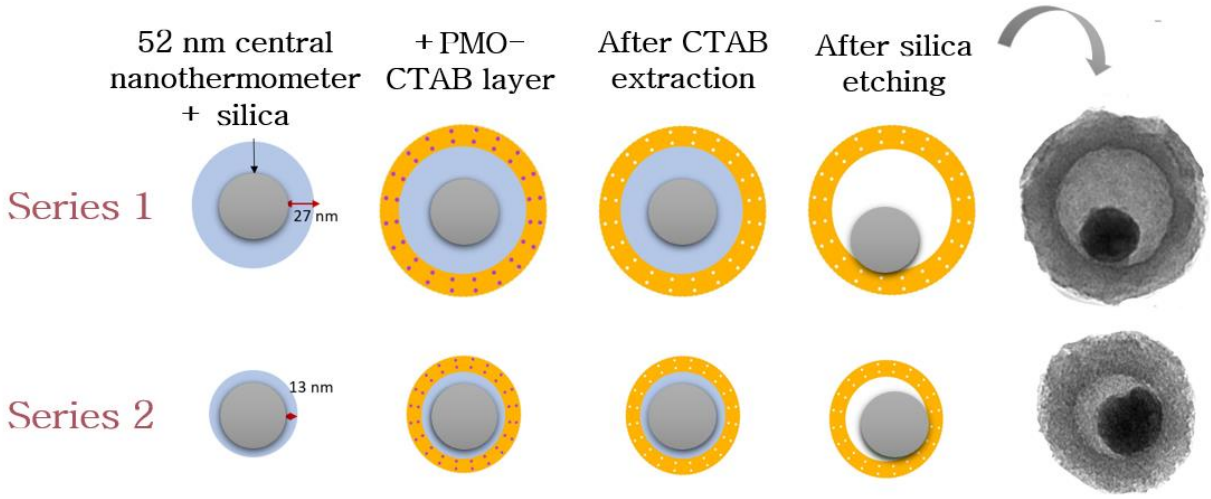

Figure IV.1 *Schematic representation of the two series of different core/shell structures analyzed and characterized in this chapter. Both series of samples hold the same size and composition, and almost the same thickness of the last deposited PMO layer as well (27.9 ± 1.9 nm and 27.8 ± 1.7 nm for S1 and S2 respectively). The only difference lies in the thickness of the amorphous silica shell, subsequently etched and giving place to voids with two different volumes.*

Samples	UCNP ($NaYF_4$:Er^{3+}, Yb^{3+}) + silica shell	UCNP + silica shell + PMO shell (with CTAB still in the mesopores)	UCNP + silica shell + PMO shell (CTAB removed, empty mesopores)	Yolk/shell structures
Series 1 **5**2 nm $NaYF_4$:40% Lu^{3+}, 18% Yb^{3+}, 2% Er^{3+}, + **13 nm** silica shell	UCNP@1-SiO_2	UCNP@1-SiO_2@PMO-CTAB	UCNP@1-SiO_2@PMO	UCNP@1-void@PMO
Series 2 **5**2 nm $NaYF_4$:40% Lu^{3+}, 18% Yb^{3+}, 2% Er^{3+}, + **27 nm** silica shell	UCNP@2-SiO_2	UCNP@2-SiO_2@PMO-CTAB	UCNP@2-SiO_2@PMO	UCNP@2-void@PMO

Table IV.1 *Summary of samples and their names.*

*In this chapter, we aim to conduct a comprehensive analysis of the luminescent properties and the nanothermometric performance of UCNPs in different encapsulation configurations (**Fig IV.1**). Samples are collected from each synthesis step for a comparative study and are divided into two series of samples described in **Table IV.1**.*

4.2 Luminescence properties of encapsulated $NaYF_4$: Er, Yb: Overview

Only few studies addressed the impact of upconverting nanoparticles surface silanization on their luminescence properties. For the core/shell multifunctional nanoplatforms including a central upconverting nanosensor, fewer studies report the impact of such complex structure on the nanothermometric performance involving the optical properties of the functional core and are summarized below.

4.2.1 Silica coating effect on the luminescence properties of $NaYF_4$: Er, Yb nanophosphor

Given the impact of water molecules on quenching the luminescence intensity of lanthanide ions, and the need to protect the upconverting nanocrystal's surface from the aqueous solvent by surface silanization, certain studies have examined the phosphor's optical properties both before and after the coating process. Y. Zhang *et al.* [238] compared the emission intensity of $NaYF_4$: Er,Yb before and after a 8 nm silica coating and observed a decrease in the emission

intensity. However, the spectroscopic experiments were performed on nanoparticles placed in two different solvents, as $NaYF_4$: Er, Yb are well dispersible in hexane whereas silica coated $NaYF_4$: Er, Yb are rather dispersible in water.

F. van Veggel *et al.* [242] first applied a ligand exchange on the oleate-capped $NaYF_4$: Er, Yb employing PVP as a hydrophilic ligand, which enabled the conversion of the nanocrystals into water soluble. On this basis, the emission intensities of PVP-stabilized and silica coated $NaYF_4$: Er, Yb both dispersed in a water solution were compared, showing that silica layer does act as a barrier, preventing to a certain extent the nanophosphor from surface quenching caused by water. R. Arppe *et al.* [287] conducted a detailed investigation to further elucidate water contribution in quenching the upconversion luminescence of nanophosphors. For that, oleate-capped $NaYF_4$: Er, Yb nanocrystals were first thoroughly washed with acid to protonate oleic acid responsible of the hydrophobicity of UCNPs, in a way to remove it from their surface. Once the nanocrystals were no longer hydrophobic, they were redispersed in ultrapure water (H_2O) and ultrapure heavy water (D_2O). Next, emission spectra and lifetime decays of $NaYF_4$: Er, Yb in H_2O and in D_2O, in addition to silica-coated $NaYF_4$: Er, Yb in H_2O and D_2O were compared. The findings show that silica-coated UCNPs in D_2O display the most intense emission, whereas the lowest emission is observed for bare UCNPs in H_2O. The emission spectra of silica-coated UCNP in H_2O exhibit only a slight variance compared to the uncoated UCNP in H_2O, and they remain below the emission of bare UCNP in D_2O. This suggests that surface silanization does not offer an optimal protection against water quenching. R. Arppe *et al.* [287] justify this by pointing out that silica might contain pores that provide access to water molecules until reaching the surface of UCNPs. In the same perspective, and for a different upconverting material, Q. Lü *et al.* [288] show that the emission spectra of Y_2O_3: Tm, Yb nanophosphor is improved when increasing the silica shell thickness, until reaching a critical thickness where the emission intensity start decreasing again. Q. Lü *et al.* [288] suggest that it is due to the decrease in the transmitted incident light with the increase of silica thickness.

The first work to be reported on the core/shell $NaYF_4$: Er, Yb employed in luminescence nanothermometry was by R.G. Geitenbeek *et al.* [289], who used a 10 nm silica coating to prevent 22 nm UCNPs from coalescence at temperatures above 600 K. The optical properties of $NaYF_4$: Er, Yb nanocrystals were monitored with both steady state and time resolved spectroscopy before and after silica coating. The nature of the solvent did not seem to be an essential detail to consider and was not mentioned. The results of bare $NaYF_4$: Er, Yb

suspension in cyclohexane were compared with the silica coated $NaYF_4$: Er, Yb ones in ethanol, and indicate a negligible difference of emission spectra before and after coating, and a decrease in luminescence lifetime of the $^4S_{3/2}$ and $^2H_{11/2}$ excited states after coating, which R.G. Geitenbeek *et al.* [289] explain by the presence of hydroxyl groups within the silica coating framework due to incomplete condensation of silanol groups (Si-OH) with high energy phonons (~3500 cm^{-1}) overlapping with the same energy gaps of Er^{3+}, that could cause quenching as well.

In summary, silanization seems to provide a relative protection against -OH groups vibrations when using water as medium for $NaYF_4$: Er, Yb nanocrystals. However, reports cited above also demonstrate that this protection is not sufficient and does not significantly help to enhance the emission intensity. Moreover, the mechanism and the factors inducing intensity losses remain undefined and unclear.

4.2.2 Multifunctional nanoplatforms for remote nanothermometry

The interest around designing multifunctional core/shell nanoplatforms dedicated to theranostic applications is only recent and is evolving at a slow pace. On the one hand because of the challenging task to elaborate such complex hierarchical structures, and on the other hand because of the difficulty of managing the combined functionalities altogether within the same nanoplatform, in a way that they do not negatively interfere with each other. This is why, when coupling temperature sensing and drug delivery for instance with the nanothermometer being the core and the drug carrier being the encapsulating layer, beside holding the functionality of a biocompatible protecting shell, it becomes crucial to first possess a fundamental knowledge on how the confinement created by the overall structure affects the physical properties of the functional core, and that, before and after the pore loading.

Limited number of papers were published on multifunctional nanoplatforms consisting of a central upconverting nanomaterial encapsulated in a single or double layer of functional mesoporous silica/hybrid silica with a drug loading/delivery potential targeting application in a biological environment. Some of these studies used the core/shell and rattle-structured nanoplatforms to couple functionalities like bioimaging, photodynamic therapy or drug delivery without necessary targeting nanothermometry, like X. Chen *et al.* [275] who reported the encapsulation of β-$NaLuF_4$: Gd,Yb,Er in a porous organosilica shell loaded with a

photosensitizer for energy transfer. The emission intensities and lifetimes of nanoplatforms in its different stages were studied from the core/shell to the rattle-structure and after loading the pores with photosensitizer molecules. X. Zhu *et al.* [290] built an upconverting multifunctional nanocomposite for cancer therapy with a rattle-structure combining drug delivery for chemotherapy and photothermal therapy. The upconverting nanocrystal $NaLuF_4$: Er, Yb was first encapsulated in a layer of undoped $NaLuF_4$: Er, Yb to enhance its optical properties, then encapsulated in porous silica. The void between the core/shell nanocrystal and the porous silica is filled with a photothermal agent and the pores are loaded with a chemodrug and a thermal responsive drug release to control the drug delivery. The study reports a mild decrease in Er^{3+} green emission intensities before and after loading the nanoplatform with the different molecules, because the latter absorb light at the same emission wavelengths.

Only two recently published works conducted a detailed study on the optical properties of upconverting nanomaterials, particularly used for remote nanothermometry and incorporated within a multifunctional nanoplatform. A. M. Kaczmarek *et al.* [199] studied the nanothermometric performance of rattle structure of $NaGdF_4$: Er,Yb inside a PMO shell. The study shows that luminescence intensity increased after etching the intermediate silica linking the nanothermometer to the PMO shell ($NaGdF_4$: Er, Yb@SiO_2@PMO), noting that the emission map was recorded in water and in the physiological temperature regime (293.15–333.15 K). Indeed, the emission profiles of Er^{3+} two green upconversion emissions $^2H_{11/2} \rightarrow {}^4I_{15/2}$ and $^4S_{3/2} \rightarrow {}^4I_{15/2}$ after silica etching are 3 times more intense than before etching, which is justified by the fact that the upconverting nanomaterial is no longer in direct contact with the silica containing -OSi and Si-OH groups inducing quenching. The second work was published by K. Kniec *et al.* [291], where the upconverting nanothermometer is other than a fluorid-based crystal doped with Er,Yb, but the interest in the study was also directed toward analyzing the silica and mesoporous silica effect on the spectroscopic properties of YAG: V,Nd nanocrystals. The research indicates that nanoparticles coated with mesoporous silica have longer life time than the one coated with dense silica, justified by the CTAB removal realized through a thermal treatment to decompose organic compounds to obtain the mesoporous structure, thus also delivering, to some extent, from the adsorbed -OH groups remaining in the surface of the samples, after being prepared in a wet-chemical route composed of water and ethanol.

Table IV.2 summarizes some of the reported core/shell, yolk/shell nanoplatforms involving an upconverting core destined for a nanothermometery application.

System	UCNP	Size	Coating layer	Thickness	ΔE (cm^{-1})	Max S_r % /K	Ref
Core/shell	β-NaYF4: Er,Yb	20 nm	Silica	10 nm	716	1.02 % at 300K	[289]
Core/shell	Bi_2SiO_5: Er,Yb	-	Silica	40 nm	747	1.1 % at 300 K	[292]
Core/shell	β-$NaYF_4$: Er,Yb	-	Silica	-	640	1.09 % at 293 K	[293]
Core/shell	β-$NaYF_4$: Er,Yb	Nanorods (94 x 315 nm)	Silica	25 nm	750	1.31 % at 299 K	[279]
Yolk/shell	β-$NaGdF_4$: Er,Yb	5 nm	Hybrid silica	-	782	1.31 % at 293.15 K	[199]

Table IV.2 *Core /shell, yolk/shell nanoplatforms for nanothermometry in literature.*

In this chapter, the optical properties enabling the evaluation of the nanothermometric performance of the distinct nanoplatforms described in ***Fig IV.1*** *will be studied in detail. Some of the hypotheses made in the reported studies cited above will be verified and discussed as well.*

4.3 Assessing the nanothermometric performance of the encapsulated $NaYF_4$: Er, Yb nanocrystals

With the aim to conduct a detailed study elucidating how multifunctionalization affects the upconverting nanothermometers performance, two series of samples as illustrated in **Fig IV.1**, each one of them is composed of four samples as summarized in the **Table IV.1**, are analyzed using the following methodology.

4.3.1 Methodology: Spectroscopy measurements

All samples have a good dispersibility in water (**Fig IV.2.b**) that can be maintained all along the experimental time and beyond. It arises from the negative charges on the NPs surface demonstrated previously by a Zeta potential measurement (**Chapter. III**). The NPs might precipitate in the bottom of the container after a long time, in the case, a 5 min sonication is enough to homogenously re-disperse them. To compare the spectroscopic properties of the distinct samples in terms of emission intensity, the concentration of the NPs in water was fixed to ~ 0.1 mg/ml. The nanothermometric performance of each sample are evaluated through a

steady-state regime by recording the power- and temperature-dependence of the upconversion emission spectra where the ratio of the two thermally coupled emissions of Er^{3+} will be used as the thermometric parameter following the LIR method. In addition, a time-resolved experiment based on luminescence decay measurement is performed as a complementary method to examine the different factors participating in mechanisms such luminescence quenching. Unlike emission intensities, LIR and decay values are independent from the concentration of NPs in the medium.

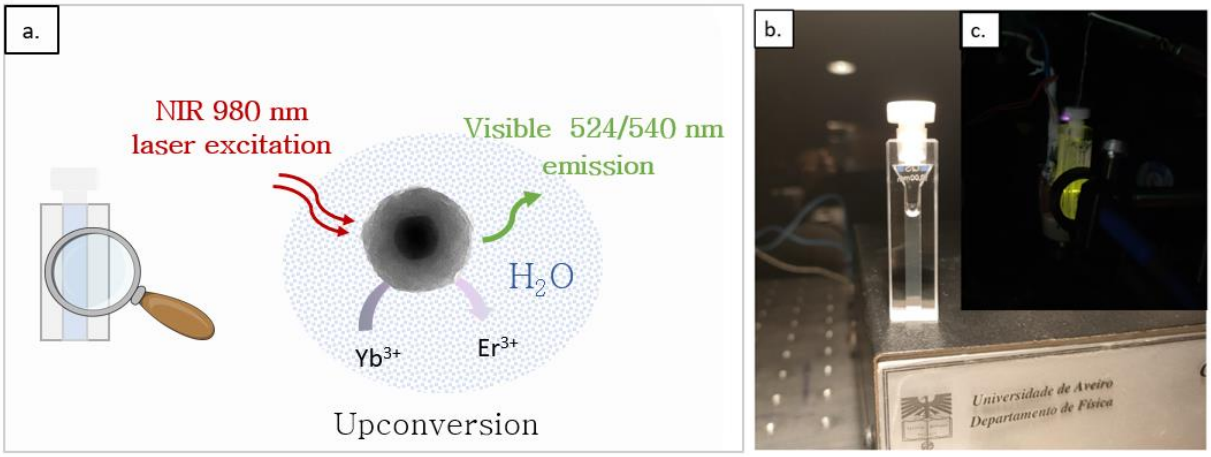

Figure IV.2 a. *Schematic representation of the multifunctional nanoparticles dispersed in water.* ***b.*** *The sample suspension in the quartz cuvette without excitation.* ***c.*** *The sample suspension displaying an upconversion green emission when excited with a 980 nm laser.*

4.3.1.1 Luminescence spectroscopy

Upconversion power- and temperature-dependent emission spectra are recorded following the set-up schematized in **Fig IV.3**. The excitation source is a 980 nm continuous wave (CW) laser (BrixX 980−1000 HD, Omicron Laser) placed at a focal distance of 7.5 cm from an optical lens to focus the laser beam and irradiate the sample. The aqueous suspension of NPs (**Fig IV.2.a**) in a Quartz cuvette (104F−10−40, Hellma Analytics) is placed in contact with a homemade Peltier system monitored with a heat controller to increase the samples temperature, and record the corresponding spectra accordingly. A thermocouple with a 0.1 K accuracy is immersed inside the suspension in proximity to the laser spot, where the increment in temperature induced by the laser beam is rapidly expressed more than on the surface of the suspension. The upconversion emission is detected in right-angle experimental configuration by a USB-portable spectrometer (Maya 2000 Pro, Ocean Optics) via an optical fiber (QP450-1-XSR, Ocean

Optics), placed after an edge pass filter (FESH0750, Thorlabs) to cut off the excitation wavelength.

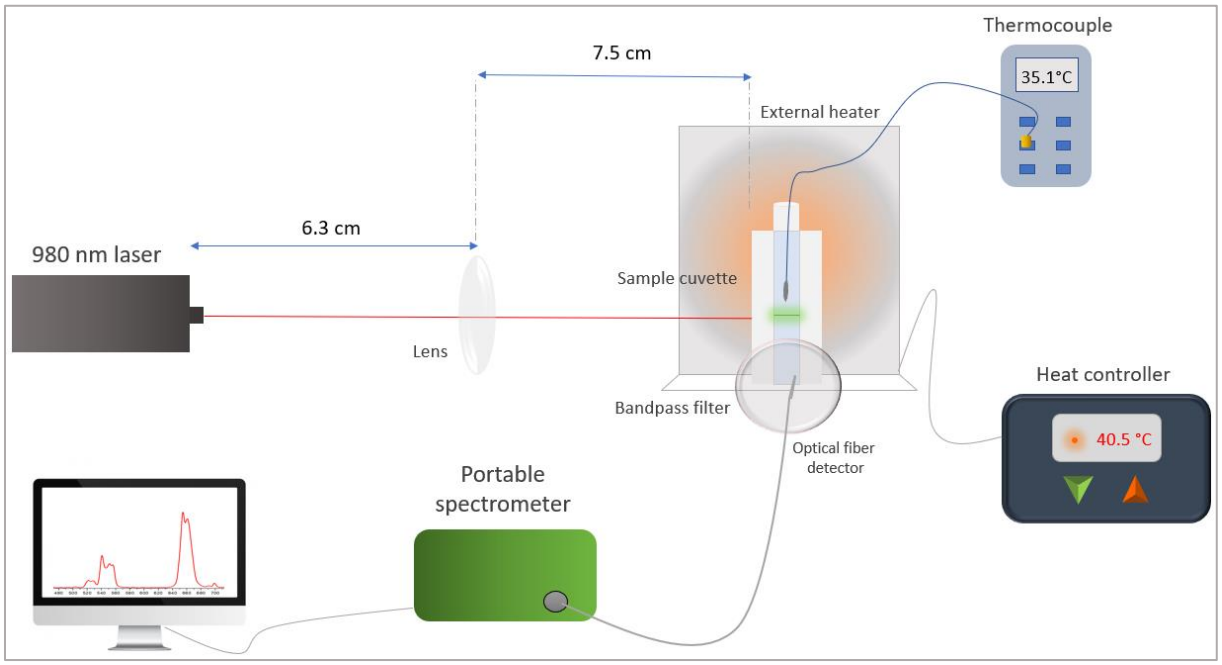

Figure IV.3 *Schematic representation of the experimental set-up to record the luminescence spectra of the emitting sample as a function of temperature.*

Emission spectra are recorded using different laser power densities (P_D) ranging from 12.6 to a maximum of 74.3 W/cm^2, with an adjustment based on the signal-to-noise ratio (SNR) of distinct samples. The temperature of the sample at room temperature and without the laser excitation denoted T_0 is first registered from the thermocouple reading. The mild temperature increment caused by the increase of the P_D, are registered as well. Next, the temperature-induced variation of the relative emission intensities is recorded by fixing the P_D with the minimum temperature increment contribution and the maximum SNR. The first set of spectra is recorded at the temperature of the fixed P_D when the heat controller is still off, then the temperature is increased using the heat controller, and within a physiological range (297-323 K). For each P_D and temperature values, the thermalization of the sample is left to stabilize for few minutes (5 mins), then spectra are recorded with an acquisition window fixed at 60 s for 60 recorded spectra and an integration time of 1 s. The same process is repeated for all the samples listed in the **Table IV.1**.

4.3.1.2 Luminescence decay

Emission decay profiles are obtained using a FluoTime 300 spectrofluorometer (FT300, PicoQuant) with an additive emission monochromator (fitted with 1200 grooves mm^{-1} grating blazed at 500 nm with a reciprocal linear density of 2.7 nm mm^{-1}) using the right-angle acquisition mode and a 980 nm pulsed laser (P-C-980MB, PicoQuant) as the excitation source, with a repetition rate of 40 MHz (pulse width = 25 ns). The emission decay profile was measured using the burst mode, exciting the sample with 8000 pulses per burst, resulting in a burst length of 200 microseconds. The temporal resolution of the time channels was 1.3 microseconds. The decay curves were registered by monitoring Er^{3+} emission arising from the excited states ($^2H_{11/2}$ = 524 nm, $^4S_{3/2}$ = 540 nm, and $^4F_{9/2}$ = 656 nm) to the ground state ($^4I_{15/2}$) upon 980 nm excitation. The obtained emission decay curves were normalized and adjusted to an exponential decay model using the EasyTau 2 software (PicoQuant). These measurements were performed by Dr. Fernando Maturi and Dr. Miguel Rodriguez.

4.3.2 Methodology: Nanothermometric parameters determination

4.3.2.1 $NaYF_4$: Er, Yb as a primary nanothermometer

Er^{3+}-doped nanomaterials represents one of the excellent choices for upconversion luminescence-based nanothermometers, considering the small energy gap (~ 600-700 cm^{-1}) separating the $^2H_{11/2}$ and $^4S_{3/2}$ electronic states of Er^{3+} with two thermally coupled transitions in $^2H_{11/2} \rightarrow {}^4I_{15/2}$ and $^4S_{3/2} \rightarrow {}^4I_{15/2}$ following Boltzmann statistics, yielding two strong green emission in 524/540 nm which is ideal for the ratiometric nanothermometry method. Er,Yb couple particularly remain one of the most investigated in Ln-based luminescence nanothermometry, where Yb^{3+} acts a sensitizer [294].

As a matter of fact, Er^{3+}-doped nanomaterials are also classified as primary thermometers, since the definition stated by S. Balabhadra et *al.* [74] in 2017 that considers that any upconverting thermometer with thermally coupled level are intrinsically primary thermometers ruled by an equation of state (**IV.1**), meaning that they can be employed for a straightforward prediction of the absolute temperature without needing a prior calibration. This was verified using SrF_2: Er, Yb nanothermometer in the same reported work and was followed by many others [294 - 297]. In order to use the equation of state (**IV.1**) to calculate the absolute temperature *T*, four

additional components remain to be determined: the thermometric parameter Δ (**IV.3**) which is the ratio of the integrated emission intensities $\boldsymbol{I_H}$ for the $^2\boldsymbol{H}_{11/2} \rightarrow {}^4I_{15/2}$ transition and $\boldsymbol{I_S}$ for the $^4\boldsymbol{S}_{3/2} \rightarrow {}^4I_{15/2}$ transition. Δ $(\boldsymbol{I_H} / \boldsymbol{I_S})$ typically increases linearly with the excitation laser power pump increase. This is explained by the thermally-induced population of the electronic state $^2\boldsymbol{H}_{11/2}$ according to Boltzmann distribution law, with the heat being generated by the optical excitation [74].

$$\frac{1}{T} = \frac{1}{T_0} - \frac{k_B}{\Delta E} \ln\left(\frac{\Delta}{\Delta_0}\right) \qquad \text{(IV.1)}$$

The uncertainty in calculated temperature is obtained using the following error propagation equation:

$$\Delta T = T^2 \sqrt{\left(\frac{\delta T_0}{T_0^2}\right)^2 + \left(\frac{k_B}{\Delta E}\right)^2 \left[\left(\frac{\delta \Delta E}{\Delta E} \ln\left(\frac{\Delta}{\Delta_0}\right)\right)^2 + \left(\frac{\delta \Delta_0}{\Delta_0}\right)^2 + \left(\frac{\delta \Delta}{\Delta}\right)^2\right]} \qquad \text{(IV.2)}$$

Δ_0 is the ratio of integrated intensities at the zero-excitation laser power pump, with the corresponding temperature denoted T_0 referring to the room temperature (**IV.4**), before the laser excitation would induce any temperature increment. Δ_0 is deduced by extrapolating the linear curve of Δ as a function of T, and ΔE is obtained by fitting the envelope of I_H and I_S transitions. One of the advantages of employing the equation (**IV.1**) is that the pre-exponential constant B based on the $^2H_{11/2}$, $^4S_{3/2}$ degeneracies (g) and spontaneous emission rates (A) and the transitions frequencies (υ), is no longer needed [74].

$$\Delta = B\, exp\left(\frac{-\Delta E}{k_B T}\right) = \frac{I_H}{I_S} \qquad \text{(IV.3)}$$

$$\Delta_0 = B\, exp\left(\frac{-\Delta E}{k_B T_0}\right) \qquad \text{(IV.4)}$$

The uncertainty in the measured Δ (I_H/I_S) is calculated using the following error propagation equation:

$$\delta\Delta = \Delta \sqrt{\left(\frac{\delta I_H}{I_H}\right)^2 + \left(\frac{\delta I_S}{I_S}\right)^2} \qquad \text{(IV.5)}$$

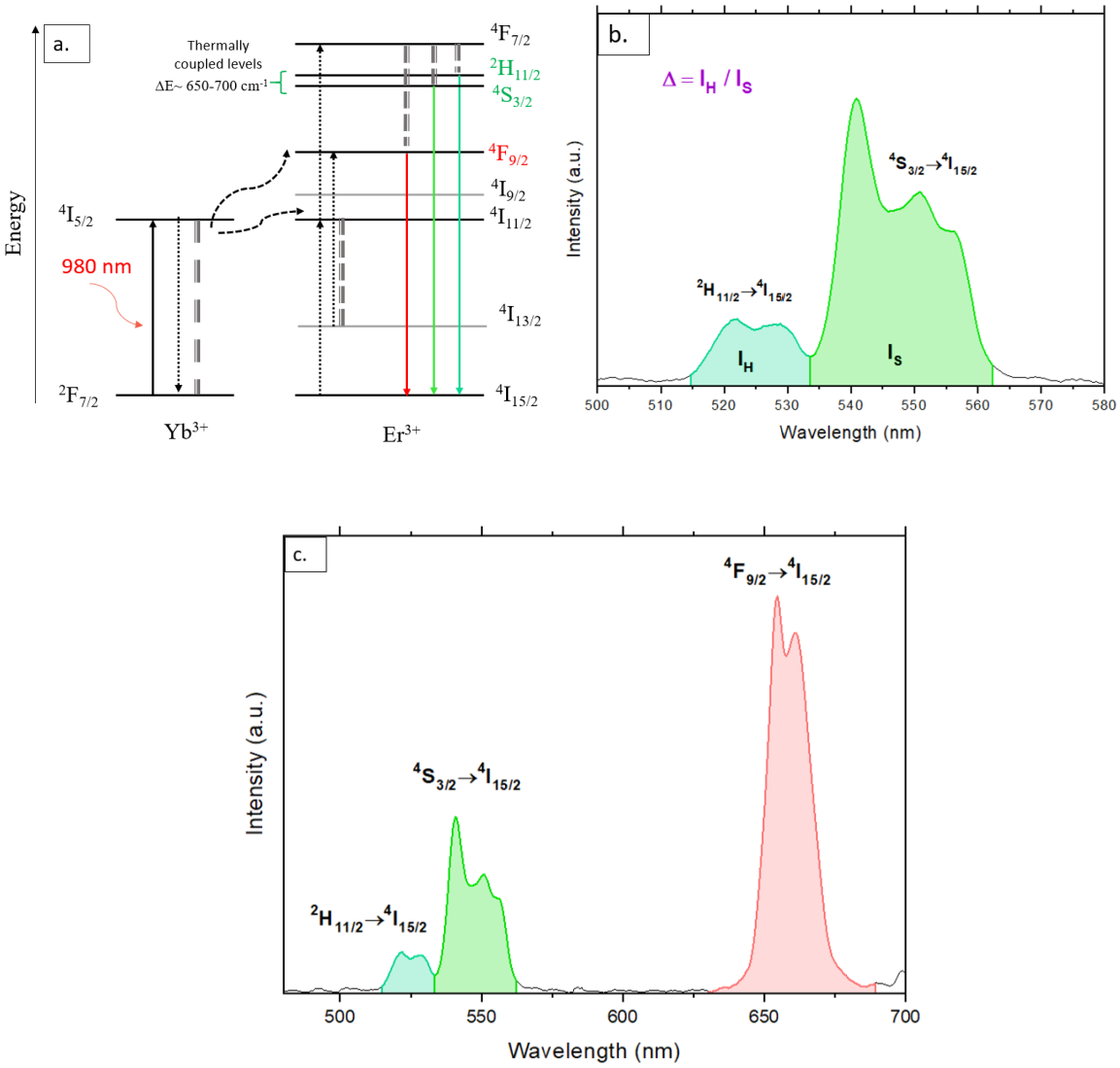

Figure IV.4 a. *Energy diagram describing the ground state excitation of Yb^{3+} and the upvonversion energy transfer to Er^{3+} exciting $^4F_{7/2}$ through a successive two-photon absorption process (dashed black arrows) from the ground state $^4I_{15/2}$ and the intermediate state $^4I_{11/2}$ of Er^{3+}. Subsequently, photons in $^4F_{7/2}$ non-radiatively relaxes following a Boltzmann distribution to the levels $^2H_{11/2}$ and $^4S_{3/2}$, and they transition radiatively from the latter states back to the ground state $^4I_{15/2}$ resulting in the two-green emission centered in 524 and 540 nm (green arrows). The photon in $^4F_{7/2}$ can also relax non-radiatively to $^4F_{9/2}$ then radiatively to the ground state $^4I_{15/2}$ resulting in the red emission centered in 660 nm. The non-radiative relaxation is represented with grey dashed doubled-lines.* ***b.*** *Emission spectrum of $NaYF_4$: Er, Yb (UCNP@1-SiO_2) in the 500-580 nm region with the two thermally coupled green emission I_H and I_S, with the thermometric parameter used in the LIR method being the ratio I_H/I_S.* ***c.*** *The emission spectrum in the 500-700 nm region showing, in addition, the red emission at 660 nm.*

4.3.2.2 Er^{3+} overlapping emissions correction for a reliable LIR nanothermometry readout

The upconversion emission spectra dependence on the excitation laser power pump, using Er,Yb co-doped materials, garnered much interest among researchers in the nanothermometry

community [280, 293, 298]. In 2021, A. Meijerink *et al.* [299] drew attention to the upconversion emission band around 555 nm (**Fig IV.5.b**) growing when increasing the laser power density, addressed by previous studies [49, 300]. This band is overlapping with the green emission of the $^4S_{3/2} \rightarrow {}^4I_{15/2}$ transition. It is originated from the radiative relaxation from $^2H_{9/2}$ to the first excited state $^4I_{13/2}$ of Er^{3+} and requires a three-photon upconversion process in order for it to take place. This explains its evolution when increasing the excitation intensity, knowing that the output intensity is proportional to the power *n* of the NIR excitation $I \propto P_D{}^n$ with *n* the number of photons involved in the upconversion process [301]. In this case, it becomes necessary to cut the intruding emission band $^2H_{9/2} \rightarrow {}^4I_{13/2}$ considered as an artefact and overlapping with green emission band I_S before integration, otherwise, the integrated area would be overestimated, thus leading to significant error in temperature readout using the LIR method and at high excitation power densities. P. Rühl *et al.* [302] indicate that this overlapping band can appear even at the lowest laser excitation down to 23 W/cm^2. Many recent reported works using $NaYF_4$: Er,Yb for the LIR temperature sensing still have not considered this point when estimating the thermometric parameter Δ [199, 289, 293].

In the same year, J.C. Martins *et al.* [303, 304] used the primary thermometer principle [74] to identify the interfering band arising from the $^2H_{9/2} \rightarrow {}^4I_{13/2}$ emission to subsequently correct the value of the thermometric parameter Δ (I_H / I_S) by decoupling the contribution of this overlapping band in the I_S integrated area, in a way to achieve an improved and reliable LIR temperature readout. Indeed, based on the assumption that $NaYF_4$: Er, Yb is a primary thermometer, and if the correction is done well, the calculated temperatures using the equation of state (**IV.1**) with Δ values derived from the corrected emission band I_S, should align with the experimental values of *T* obtained from the local temperature measurement using the thermocouple.

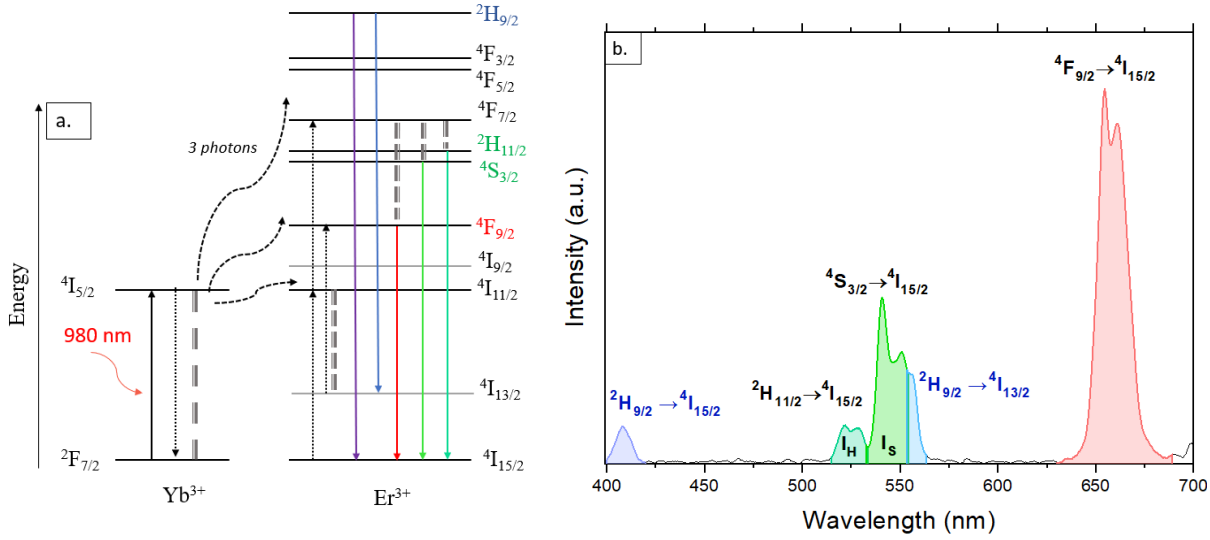

Figure IV.5 a. *Upconversion emission involving a three-photon energy transfer process and generating additional transitions* $^2H_{9/2} \rightarrow {}^4I_{15/2}$ *and* $^2H_{9/2} \rightarrow {}^4I_{13/2}$. ***b.*** *The two blue emissions resulting from the radiative relaxation of* $^2H_{9/2}$ *excited state centered at 410 nm and 555 nm* [49]. *The emission band of the transition* $^2H_{9/2} \rightarrow {}^4I_{13/2}$ *is overlapping with the transition* $^4S_{3/2} \rightarrow {}^4I_{15/2}$, *whereas the transition* $^2H_{11/2} \rightarrow {}^4I_{15/2}$ *is intact, and should therefore be subtracted from the total integrated area* I_S *for a proper* Δ (I_H/I_S) *calculation.*

4.3.2.3 $NaYF_4$: Yb, Er emission integrated areas calculation

LIR nanothermometry is based on calculating the variation of the thermometric parameter Δ, corresponding to the ratio of the integrated intensities of the transitions $^4S_{3/2} \rightarrow {}^4I_{15/2}$ and $^2H_{11/2} \rightarrow {}^4I_{15/2}$, as a function of temperature. The calculations described in the following steps are all computed using a MATLAB routine.

- The overall number of spectra for each measurement, recorded either by varying the P_D or temperature (60 spectra each), using the set-up described in **Fig IV.3**, is collected and averaged, and a baseline subtraction is applied.

- Averaged emission spectra expressed in wavelength (nm) units are converted to energy unit E (cm^{-1}) (**IV.6 (1)**), and the Jacobian transformation is employed to rescale the intensity I values as a function of energy units (**IV.6 (2)**) [305].

$$(1) \quad E = \frac{hc}{\lambda\, 10^{-7}} \qquad \text{(IV.6)}$$

$$(2)\quad I(E) = I(\lambda)\frac{d\lambda}{dE} = I(\lambda)\frac{d}{dE}\left(\frac{hc}{E}\right) = -\frac{I(\lambda)}{E^2 10^{-7}}$$

- A deconvolution is performed by fitting the emission areas in the 17500-19500 cm^{-1} region with Gaussian functions (**Fig IV.6**). The integrated intensities of I_H and I_S are calculated by summing the Gaussian fits, without counting the intruder band of the $^2H_{9/2} \rightarrow {}^4I_{13/2}$ transition. The thermometric parameter Δ is thus determined by calculating the ratio of the integrated areas I_H/I_S.

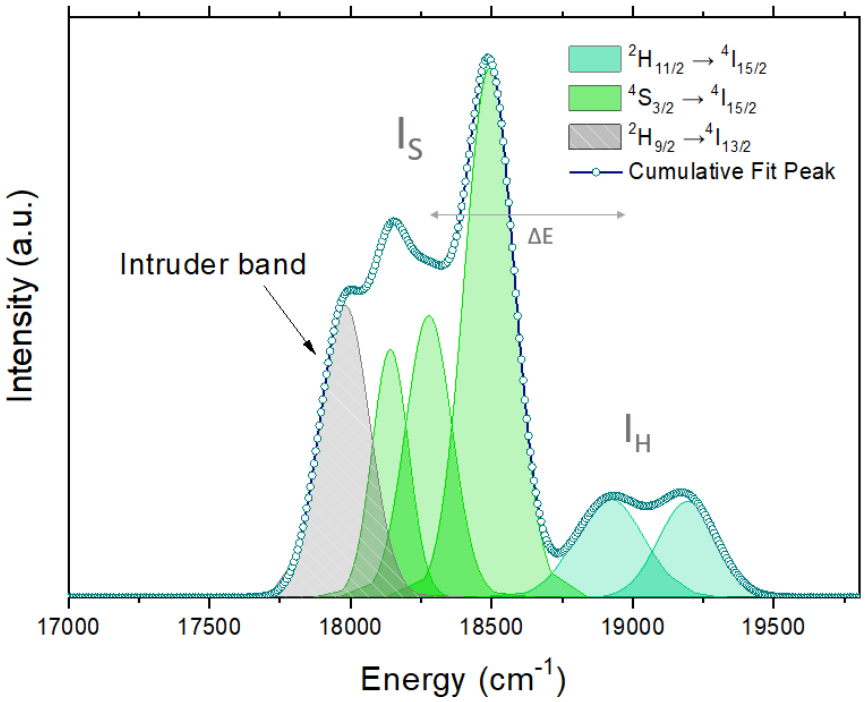

Figure IV.6 *The emission spectrum of $NaYF_4$: Er, Yb in an energy scale after applying the Jacobian transformation on the original spectrum in wavelength scale. (Here UCNP@1-SiO_2 spectrum is used as an example). The integration of areas is realized using Gaussian function fits, one in the 17750-18000 cm^{-1} corresponding to the intruding $^2H_{9/2} \rightarrow {}^4I_{13/2}$ emission, three functions in the 18000-18750 cm^{-1} region corresponding to the $^4S_{3/2} \rightarrow {}^4I_{15/2}$ transition, and two function in the 18750-19500 cm^{-1} region corresponding to $^2H_{11/2} \rightarrow {}^4I_{15/2}$.*

- The energy gap Δ*E* defined as the energy difference between barycenters of the two Stark levels $^4S_{3/2}$ and $^2H_{11/2}$, can be also determined from the emission spectrum expressed in energy units (**Fig IV.6**) using the Gaussian functions fit for each emission I_S and I_H. The energy *E* is calculated from the arithmetic mean using the energy peak E_i and the fitted area *Ai* of each Gaussian function (**IV.7**). It is important to highlight that Δ*E* is an intrinsic property and considered as a fingerprint of the emitting center as explained in

Chapter.I, and its value is therefore independent from the variation of temperature. However, since the value of Δ*E* is obtained from a fit, the mean value is calculated from the temperature-dependent spectra for the 60 recorded spectra at each temperature, which makes it 300 spectra. The uncertainty of Δ*E* *(δΔE)* in this case is the standard deviation from the mean value of Δ*E*.

$$\Delta E = E_2 - E_1 \quad \text{with} \quad E = \frac{\sum A_i \times E_i}{\sum A_i} \tag{IV.7}$$

4.3.2.4 Thermometric performance

For this work, two parameters used to evaluate the thermometric performance of nanothermometers are estimated with the following equations [18]:

The relative thermal sensitivity S_r:

$$S_r = \frac{1}{\Delta}\frac{\delta\Delta}{\Delta T} \tag{IV.8}$$

and the corresponding uncertainty expression:

$$\delta S_r = S_r \frac{\delta\Delta}{\Delta}\sqrt{2} \tag{IV.9}$$

Temperature uncertainty δT:

$$\delta T = \frac{1}{S_r}\frac{\delta\Delta}{\Delta} \tag{IV.10}$$

The uncertainty of δT is considered:

$$\frac{\delta S_r}{S_r} \approx \frac{\delta\delta T}{\delta T} \tag{IV.11}$$

4.3.2.5 Luminescence lifetime

The luminescence decay measurement provides the information about the emission lifetime of an excited state and serves to analyze the dynamics occurring within a luminescent material, such as upconversion and relaxation processes including radiative and non-radiative pathways.

The decay of the luminescence intensity follows an exponential pattern that can be modeled with the following equation [34]:

$$I(t) = I_0 \,.\, e^{-\frac{t}{\tau}} \qquad \text{(IV.12)}$$

Where, *I(t)* is the luminescence intensity at time *t*, I_0 is the intensity at t=0, τ is the decay time constant representing the average time it takes for the intensity to decrease to *1/e* (**IV.12**).

Luminescence decays of all samples in **Table IV.1** are collected for $^4S_{3/2} \rightarrow {}^4I_{15/2}$ (540 nm) and $^2H_{11/2} \rightarrow {}^4I_{15/2}$ (524 nm) transitions 0.2 ms after the 980 nm pulsed laser is turned and off, and 0.4 ms for the $^4F_{9/2} \rightarrow {}^4I_{15/2}$ (656 nm) transitions. Based on the decay profile shown in **Fig IV.7** of a selected sample taken as an example (UCNP@2-SiO_2, 540 nm emission lifetime), we can observe that the intensity of the emission keeps increasing after the pulsed laser excitation was turned off. The part of the profile where the curve exhibits an ascending section before decaying is referred to as "rise time", and indicates that the energy transfer feeding source is decaying [306]. In the Er,Yb upconverting system, Yb^{3+} serves as the feeding source, leading to the population of the Er^{3+} $^4F_{7/2}$ energy level while it is decaying (**Fig IV.5.a**) [307]. Which mean that the rise time actually corresponds to the Yb^{3+} decay time. This was demonstrated by H. Song *et al.* [308] who showed that the rising process does not occur in a single doped Er^{3+} $NaYF_4$ and only appears when the material is co-doped with the Er,Yb couple, and thus this rising time is definitely attributable to the upconversion process.

In this case, the decay profiles can be fitted using the following double exponential decay equation (**IV.13**) to obtain the lifetime values, where *N* and N_0 are the numbers of electron population at time t and t=0 respectively, and N_1 is number of electrons at t=0 in an upper feeding level [306], $\boldsymbol{\tau}_{rs}$ and $\boldsymbol{\tau}_{D0}$ correspond to the rise time and the decay time that will be denoted $\boldsymbol{\tau}_2$ and $\boldsymbol{\tau}_1$ respectively.

$$N = \left[N_0 + N_1 \left(1 - \exp\left(\frac{-t}{\tau_{rs}}\right)\right)\right] exp^{\left(\frac{-t}{\tau_{D0}}\right)} \qquad \text{(IV.13)}$$

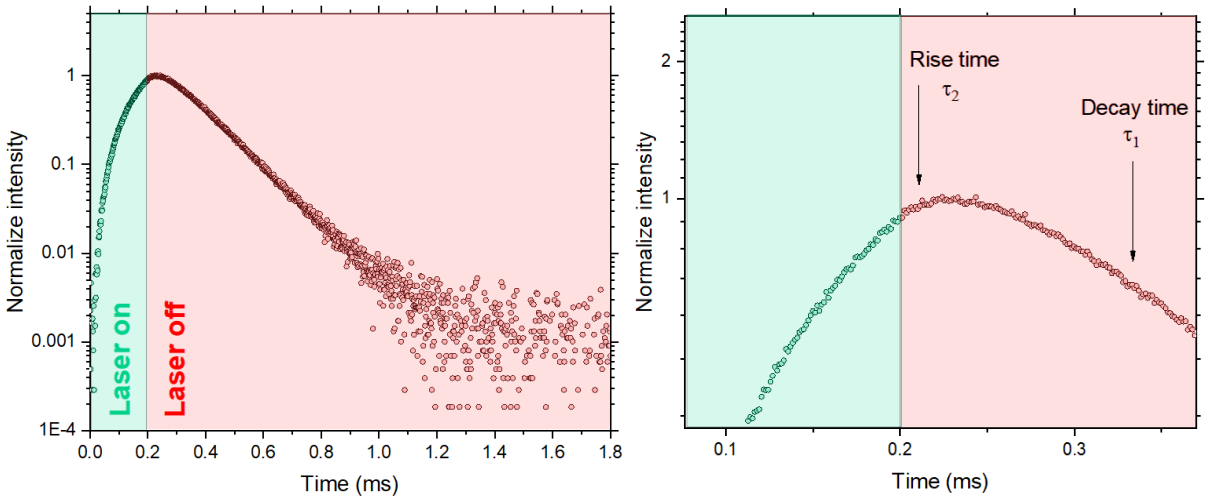

Figure IV.7 *Luminescence decay profile showing the intensity increase upon pulsed laser excitation in the green zone until 0.2 ms, then the luminescence exponential decay of the $^4S_{3/2}$ emitting level in the red zone occurs when laser is turned off. The figure on the right provides a close-up of the small rise time after 0.2 ms.*

*In the next section, the luminescence properties and the nanothermometric performance of distinct nanostructures from every elaboration step (**Fig IV.1)** and from both series of samples are compared, in order to analyze how these properties are affected with the addition of different layers. The effect of the first silica shell thickness which makes the only difference between series 1 and series 2 is also studied, and the principle of the primary thermometer used to validate the accuracy of spectroscopic data processing is verified.*

4.4 Results

4.4.1 Upconversion emission intensity

Emission spectra displayed in **Fig IV.8** of the series of samples 1 and 2 with fixed concentrations and P_D, provide some first indications about the effect of the multilayer structure on the luminescence properties of the UCNP. In both series, the overall emission intensity drops drastically in the presence of the PMO layer and after the removal of the sacrificial intermediate silica layer. The sample with the weakest emission intensity is UCNP@2-void@PMO from series 2, having the largest void between the UCNP and the PMO layer, which also displays the noisiest spectrum among the others. Interestingly, UCNP@1-void@PMO rather have an intermediate emission intensity between UCNP@1-SiO_2@PMO and UCNP@1-SiO_2@PMO-CTAB.

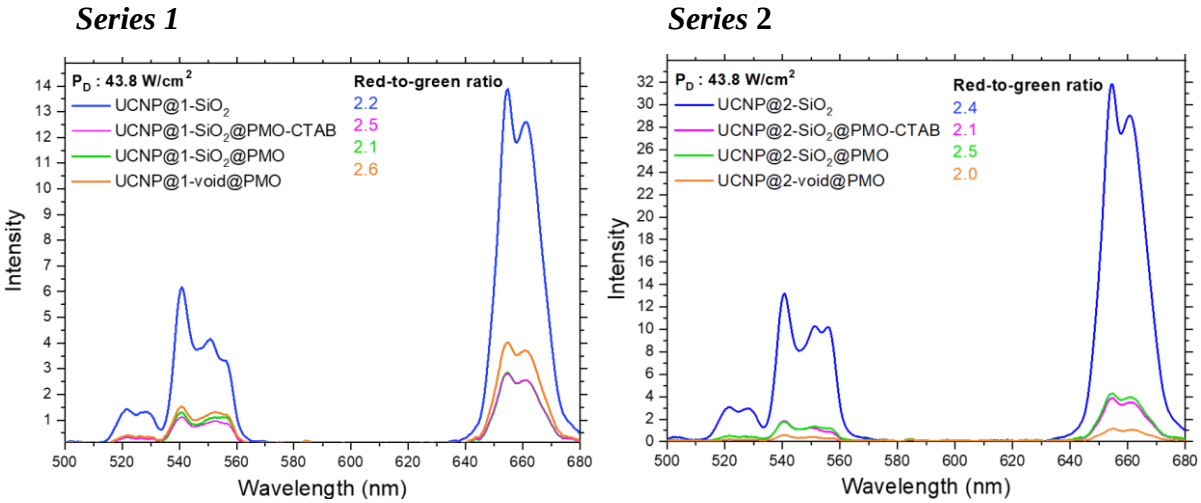

Figure IV.8 *Luminescence emission spectra of series 1 and 2 of samples from* ***Table IV.1****, all with concentrations fixed at ~ 0.1 mg/ml, and recorded at the same laser power density (P_D). Intensity ratio variations of red emission at 656 nm to the green emission at 540 nm are calculated and mentioned on the graphs.*

The variation of red-to-green ratio between the distinct samples from the two series has a different trend. For the series 1, the UCNP@1-SiO_2 and UCNP@1-SiO_2@PMO have the lowest red-to-green ratio, 2.2 and 2.1 respectively against 2.5 and 2.6 for UCNP@1-SiO_2@PMO-CTAB and UCNP@1-void@PMO respectively. Whereas for the series 2, this trend is inversed, UCNP@2-SiO_2@PMO-CTAB and UCNP@2-void@PMO exhibit the lowest red-to-green ratio, 2.1 and 2 respectively, against 2.4 and 2.5 for UCNP@2-SiO_2 and UCNP@2-void@PMO respectively.

In order to monitor the changes occurring at the level of the two green emission bands, spectra are normalized relatively to the red emission band at 656 nm. The complete spectra are shown in **Fig B.1.** (appendix B). **Fig IV.9** focuses on the two green emissions I_H and I_S. Some subtle differences can be observed between the band shape of each spectrum, mainly ruled by a variation of the ratio between the green band at 540 nm and the intruder blue band at 555 nm. For the series 1, this ratio is high in the silica coated material (UCNP@1-SiO_2) and decreases in the presence of the PMO layer in the three following structures, which means that the bleu emission intensity becomes more intense and get closer to the green one. The inverse is true for the series 2. The blue emission centered around 410 nm follows the same variation trend as the intruder band at 555 nm.

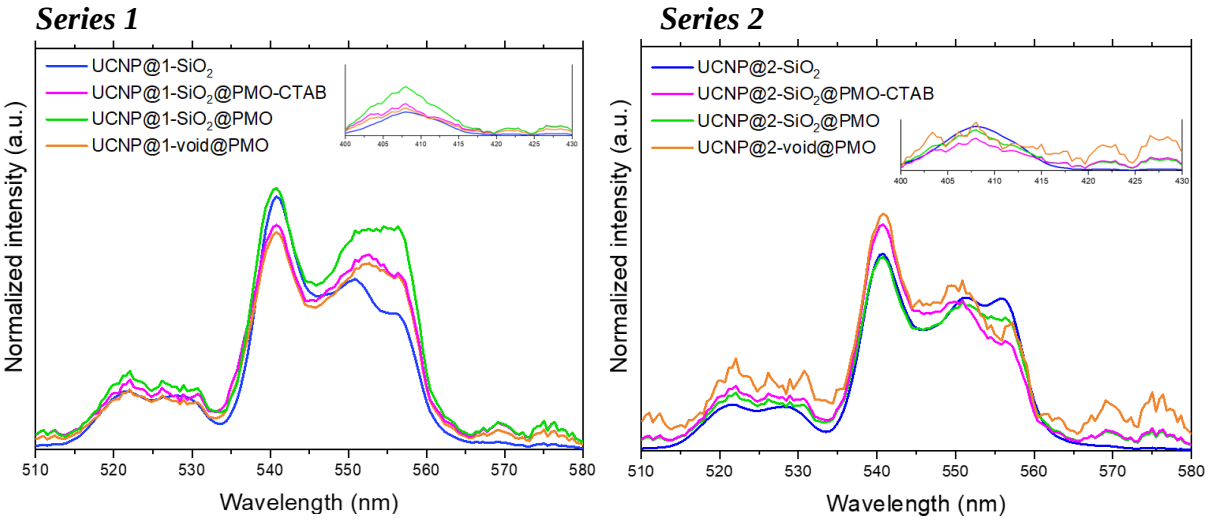

Figure IV.9 *Luminescence emission spectra with a main focus on the green spectral region, and the 400-420 nm region added on the top of the graphs. Intensities are normalized relatively to the red emission peak in 656 nm. Complete spectra are displayed in appendix B (figure.B.1).*

The variation of the intruder band intensity centered at 555 nm relatively to the green emission centered at 540 nm is even more evident when comparing structures of the same elaboration step from the two series of samples (**Fig IV.10**).

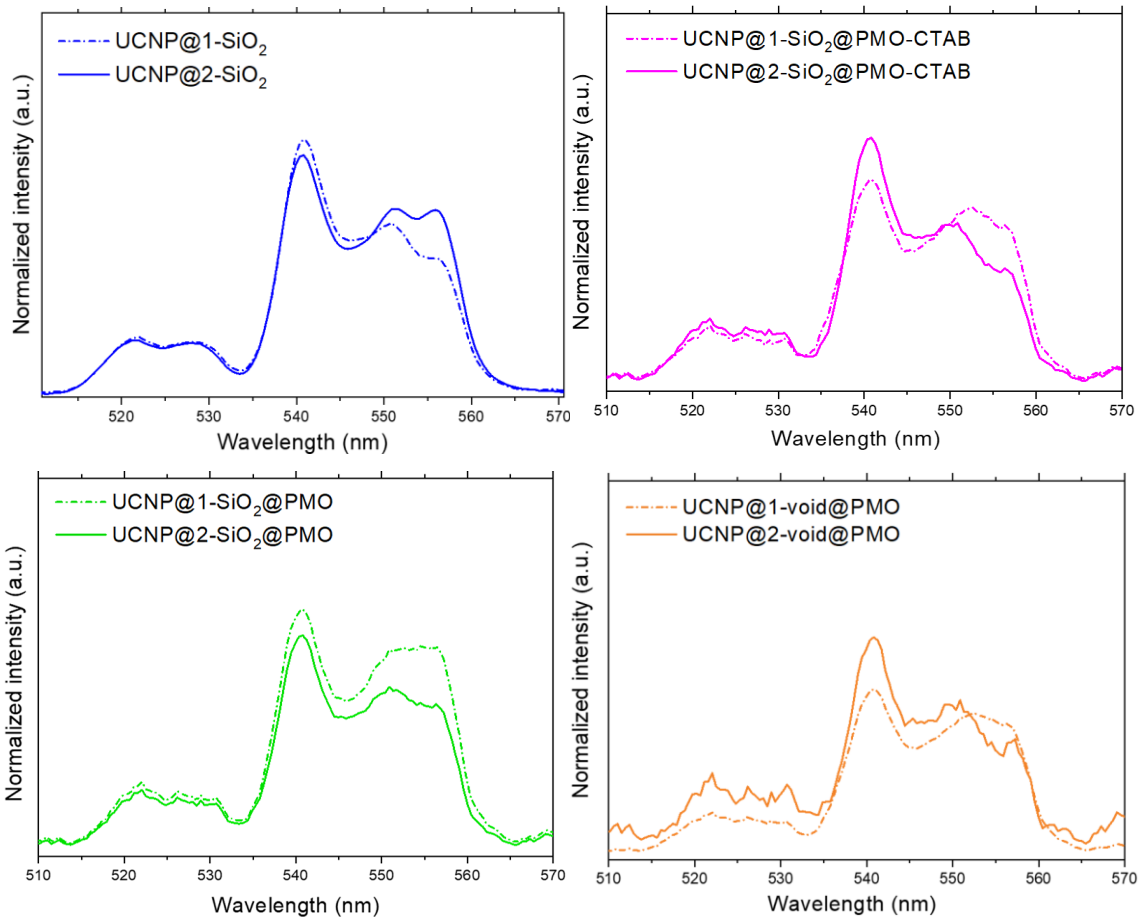

Figure IV.10 *Comparative plots of normalized intensity spectra of samples with similar structure from different series in the green spectral region. Dashed lines represent spectra from the series 1 and solid lines represent spectra from the series 2.*

4.4.2 Luminescence lifetime

Table IV.3 displays rise times and decay times values of the transition $^2H_{11/2} \rightarrow {}^4I_{15/2}$ (524 nm), $^4S_{3/2} \rightarrow {}^4I_{15/2}$ (540 nm), and $^4F_{9/2} \rightarrow {}^4I_{15/2}$ (656 nm) for all the samples.

Series 1	524 nm		540 nm		656 nm	
	τ_1 (ms)	τ_2 (ms)	τ_1 (ms)	τ_2 (ms)	τ_1 (ms)	τ_2 (ms)
UCNP@1-SiO_2	0.136 ± 0.001	0.047 ± 0.001	0.135 ± 0.001	0.047 ± 0.001	0.391 ± 0.002	0.099 ± 0.002
UCNP@1-SiO_2@PMO-CTAB	0.121 ± 0.012	0.053 ± 0.012	0.127 ± 0.001	0.045 ± 0.001	0.397 ± 0.007	0.089 ± 0.006
UCNP@1-SiO_2@PMO	0.120 ± 0.001	0.045 ± 0.002	0.124 ± 0.001	0.042 ± 0.001	0.376 ± 0.001	0.095 ± 0.003
UCNP@1-void@PMO	0.115 ± 0.002	0.036 ± 0.003	0.116 ± 0.001	0.036 ± 0.001	0.367 ± 0.005	0.080 ± 0.005
Series 2	524 nm		540 nm		656 nm	
	τ_1 (ms)	τ_2 (ms)	τ_1 (ms)	τ_2 (ms)	τ_1 (ms)	τ_2 (ms)
UCNP@2-SiO_2	0.134 ± 0.001	0.047 ± 0.001	0.134 ± 0.001	0.048 ± 0.001	0.390 ± 0.001	0.097 ± 0.002
UCNP@2-SiO_2@PMO-CTAB	0.126 ± 0.015	0.058 ± 0.015	0.131 ± 0.002	0.042 ± 0.003	0.405 ± 0.014	0.071 ± 0.012
UCNP@2-SiO_2@PMO	0.131 ± 0.002	0.052 ± 0.002	0.132 ± 0.001	0.050 ± 0.001	0.377 ± 0.003	0.102 ± 0.003
UCNP@2-void@PMO	0.116 ± 0.001	0.035 ± 0.002	0.114 ± 0.001	0.032 ± 0.001	0.351 ± 0.003	0.068 ± 0.004

Table IV.3 *All rise time τ_2 and decay time τ_1 values o of emitting levels $^2H_{11/2}$, $^4S_{3/2}$ and $^4F_{9/2}$.*

Rise time and decay times values obtained from the double exponential fit (decay profiles displayed in **Fig B.5 (appendix B)** are close to some reported values. Lifetimes between samples undergo only a slight change. Almost the same lifetime evolution trend is observed in both series from the first nanoplatform of the synthesis consisting of UCNP encapsulated in a single amorphous silica shell (UCNP@SiO_2) to the last yolk/shell nanoplatform consisting in a mobile UCNP inside a PMO shell (UCNP@void@PMO), in consideration to the uncertainty values.

The weakest lifetime values are observed in the yolk/shell systems and for all the emission wavelengths. The green emission in 524 nm and 540 nm decay time decreased in the same way by an average value of 15 % from UCNP@SiO_2 samples to UCNP@void@PMO samples. The shortening of the red emission lifetime at 656 nm is less important, reaching a maximum of 10 % for UCNP@2-void@PMO and a minimum of 6 % for UCNP@1-void@PMO.

Rise times are also subject to modification through the different structures in the three-emission wavelengths, with values decreasing to a maximum of 32 % at 524 nm and 540 nm from UCNP@SiO_2 samples to UCNP@void@PMO samples. Whereas for the red emission at 656 nm, the reduction of the risetime value was more significant for UCNP@1-void@PMO than for UCNP@2-void@PMO, 31 % and 17.5 % respectively.

Other small lifetime variations can be observed between UCNP@1-SiO_2 and UCNP@1-SiO_2@PMO, with the latter exhibiting a shorter green emission lifetime by 11 % and 8 % in 524 nm and 540 nm respectively, and by 4 % in 656 nm. Whereas for the series 2, lifetimes values of green emission remained the same when moving from UCNP@2-SiO_2 to UCNP@1-SiO_2@PMO, and only the red emission lifetime was shortened by 4 %.

4.4.3 Thermometric parameters and performance

4.4.3.1 Power-dependent upconversion emission intensities

Emission spectra of all samples were recorded upon a 980 nm laser excitation in different laser power densities (**Fig IV.11**). Intensities are clearly increasing as a function of P_D, which is in accordance with $I \propto P_D^n$. The variation of the band shape between samples of each series is quite visible when increasing P_D, notably the three-photon blue intruding emission at 555 nm relatively to the green emission in 540-550 nm. The normalized intensities of two selections of samples (UCNP@1-SiO_2@PMO and UCNP@2-SiO_2@PMO) are displayed in **Fig B.2**. (appendix B), showing that evolution of the intruder band and the red emission follow the same trend as a function of P_D, which was also observed in the study reported by J.C. Martins *et al* [303].

Samples displaying very weak intensities were recorded at a maximum P_D of 74.4 W/cm^2 to increase the signal-to-noise ratio. The pace of the emission intensities variation as a function of P_D is also quite different from one structure to another.

Spectra in **Fig IV.11** are employed to plot the ratio of integrated intensities Δ as a function of the different P_D and by extrapolating the linear fit to extract the Δ_0 (**Fig IV.12**), which is one of the components required to calculate the absolute temperature directly from the equation of state (**IV.1**), along with T_0, Δ and ΔE. Δ_0 values determined from each plot are summarized in **Table IV.6**.

Series 1

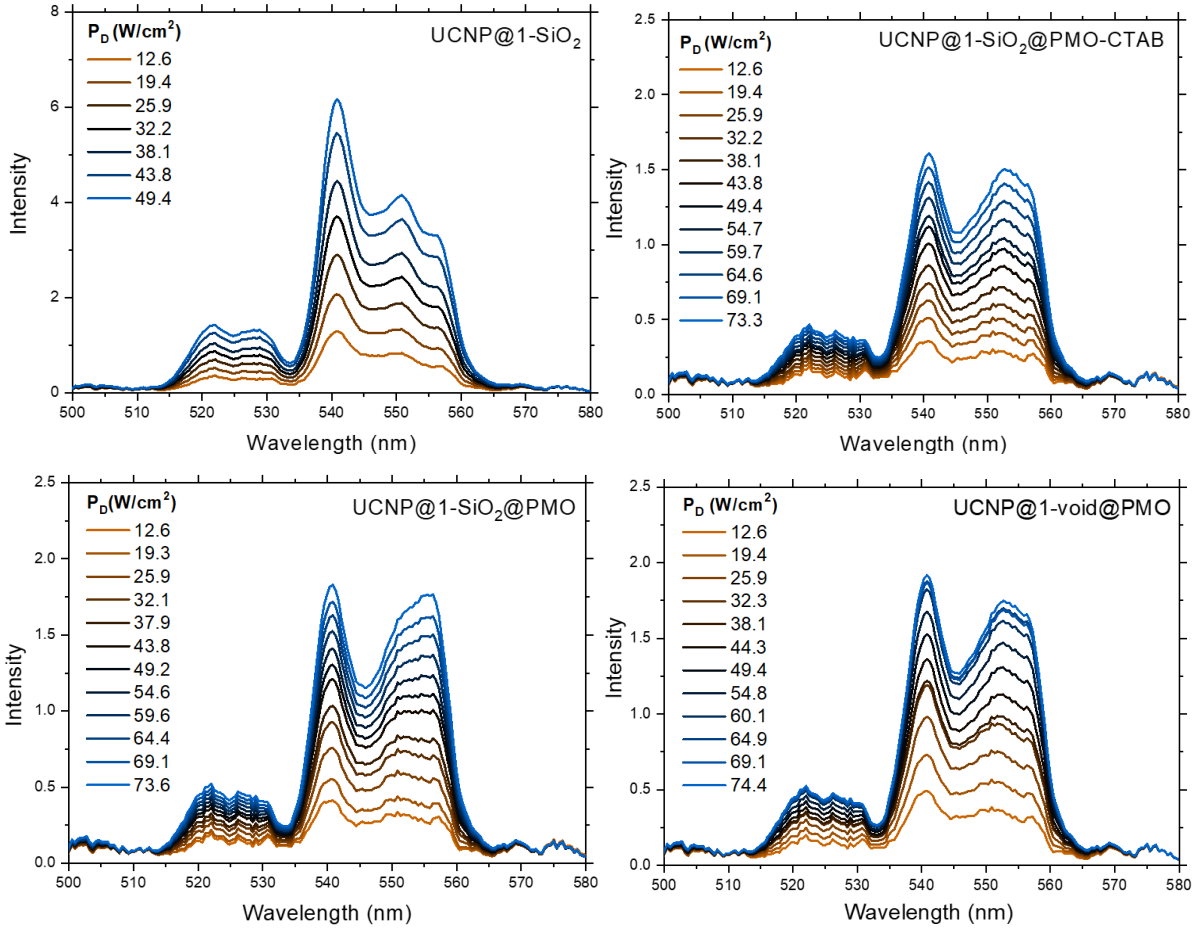

Series 2

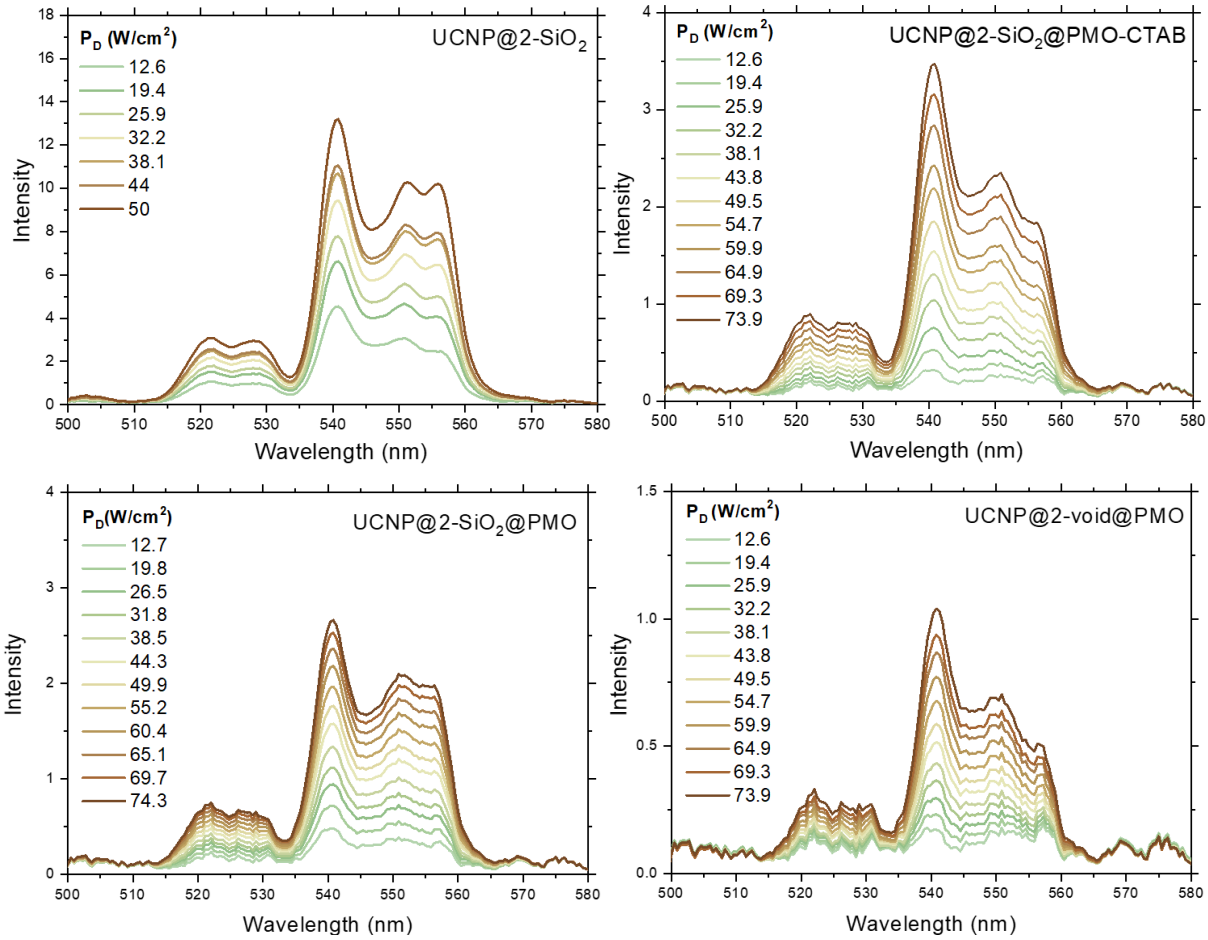

Figure IV.11 *Power-dependent upconversion emission intensities in the green spectral region. Spectra of series 1 have the blue palette and the spectra of series 2 have the green one.*

Data points of Δ plotted as a function of P_D are displayed in **Fig IV.12**, they are fitted by a linear fit (red curve). One noteworthy observation that can be drawn from these results is that in both series of samples, the UCNP coated with amorphous silica only (UCNP-SiO_2 type) exhibits a rising pattern as a function of $P_{D,}$ whereas for all the rest of the samples, characterized with the presence of a PMO shell, there is almost no variation of data points values when increasing the P_D, the fitting linear curve is horizontal and the Δ_0 can be obtained from the mean values of all these data points. Some spectra are recorded at high P_D to obtain the best signal-to-noise ratio (SNR).

Series 1

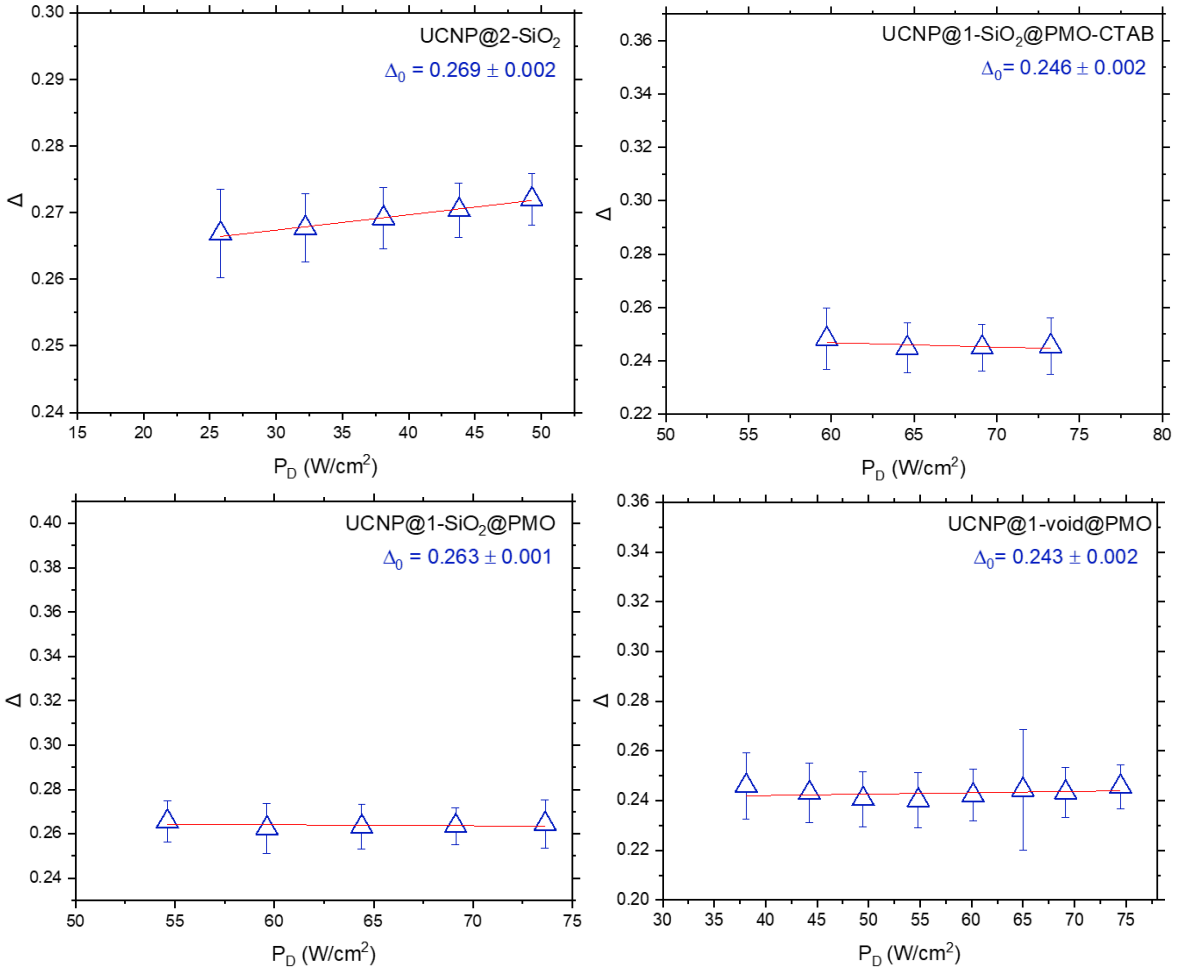

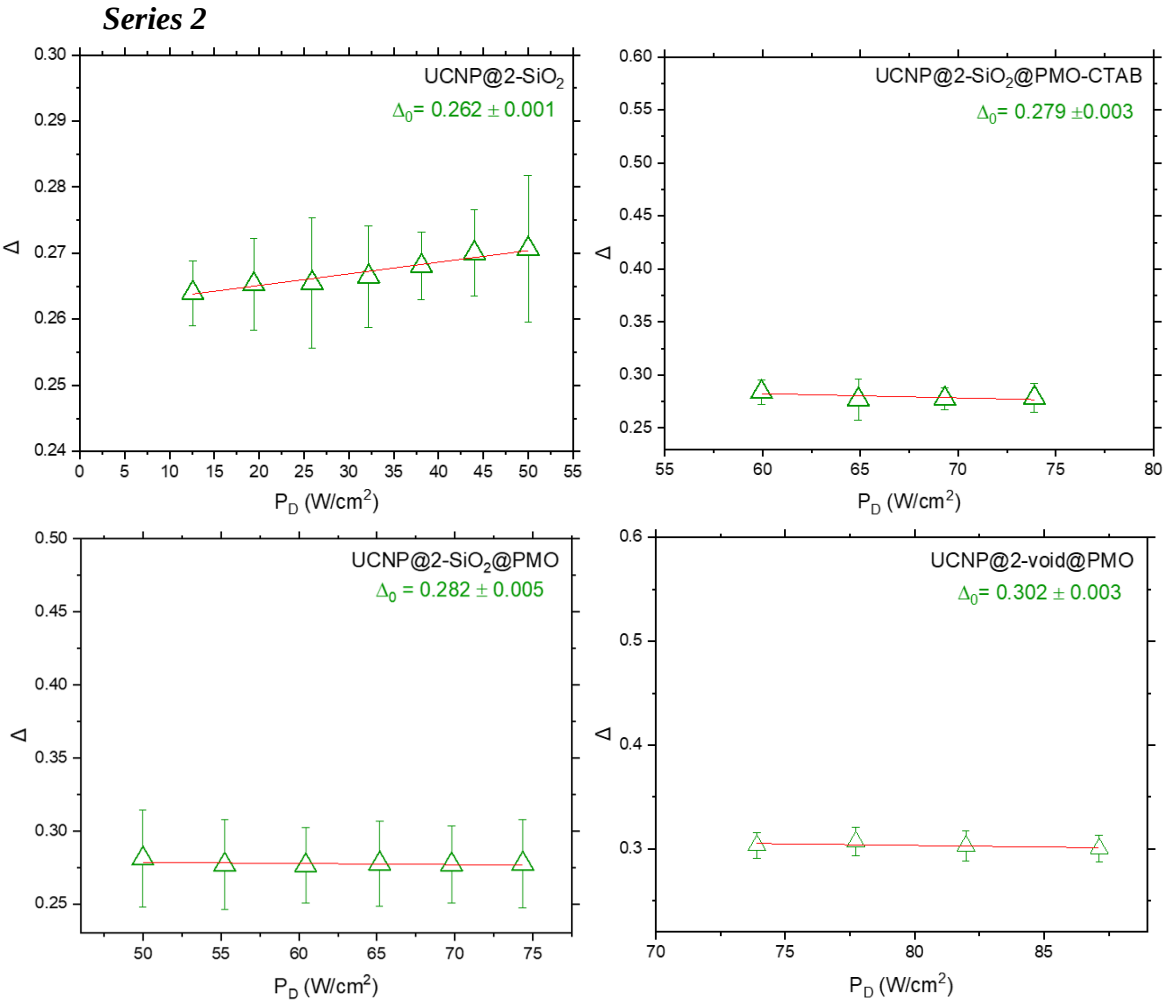

Figure IV.12 *Plots of the thermometric parameter Δ variation as function of P_D.*

4.4.3.2 Temperature-dependent upconversion emission intensities

Fig IV.13 displays the evolution of upconversion emission spectra as a function of temperature increment for nanothermometers with the eight distinct structures. Given the different characteristic SNR of each system, these temperature-dependent spectra are recorded using the minimum P_D providing the best SNR. As expected, the population equilibrium of the two thermally coupled levels $^2H_{11/2}$ and $^4S_{3/2}$ ruled by the Boltzmann distribution law, is modified when increasing the temperature [74, 309]. All the temperature-dependent upconversion spectra exhibit a decrease in the intensity of the $^4S_{3/2} \rightarrow {}^4I_{15/2}$ transition when increasing the temperature in the 297-323 K range, whereas the intensity of the $^2H_{11/2} \rightarrow {}^4I_{15/2}$ transition remains almost constant. It is noteworthy that the variation rate of the emission spectra as a function of temperature is also slightly different from one system to another, and all follow a regular downward trend except for UCNP@2-SiO_2 and UCNP@1-void@PMO that exhibit a

non-regular variation of I_S with the temperature increment, and a small variation of I_H as well. The band shape is conserved at all the recorded temperatures and for all samples.

Spectra in **Fig IV.13** are employed to obtain the values of the thermometric parameter Δ and the energy gap Δ*E* between $^2H_{11/2}$ and $^4S_{3/2}$ levels using the method described in *4.3.2* (All the computed values of ΔE are summarized in in **Table. IV.6**). These values can be employed directly to predict the absolute temperature using the equation **IV.1**. Otherwise, data points of each delta are plotted as a function of temperature (Δ *vs. T*), whom the evolution usually follows a linear trend, and are therefore fitted with a linear curve that serves as calibration curve. As a matter of fact, as the temperature-dependent distribution of population between thermally coupled levels ruled by Boltzmann statistic is expressed in an Arrhenius-type equation (**IV.3**), the variation of the thermometric parameter Δ as a function of temperature follows an exponential trend. To obtain a linear calibration curve, data points of *ln (Δ)* are plotted as a function of *1/T*, and the Δ*E* value is extracted from the linear fit. This approach is the one frequently used for LIR-based nanothermometer and found in several reported works [23, 284, 289, 310]. The evolution of the thermometric parameter Δ in a small temperature range such as the physiological range is still within the linear regime, which is why Δ (LIR) can be directly plotted as a function of temperature in this work.

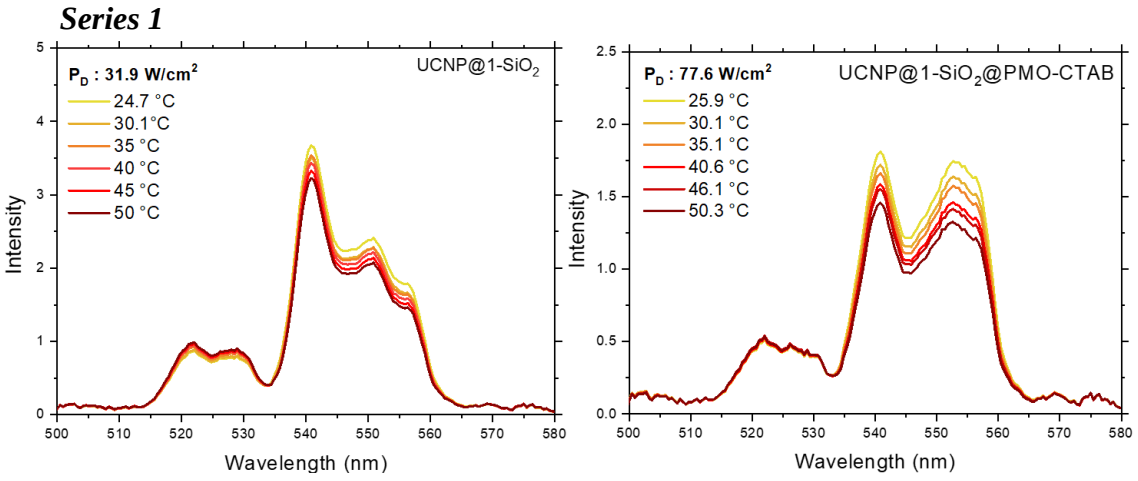

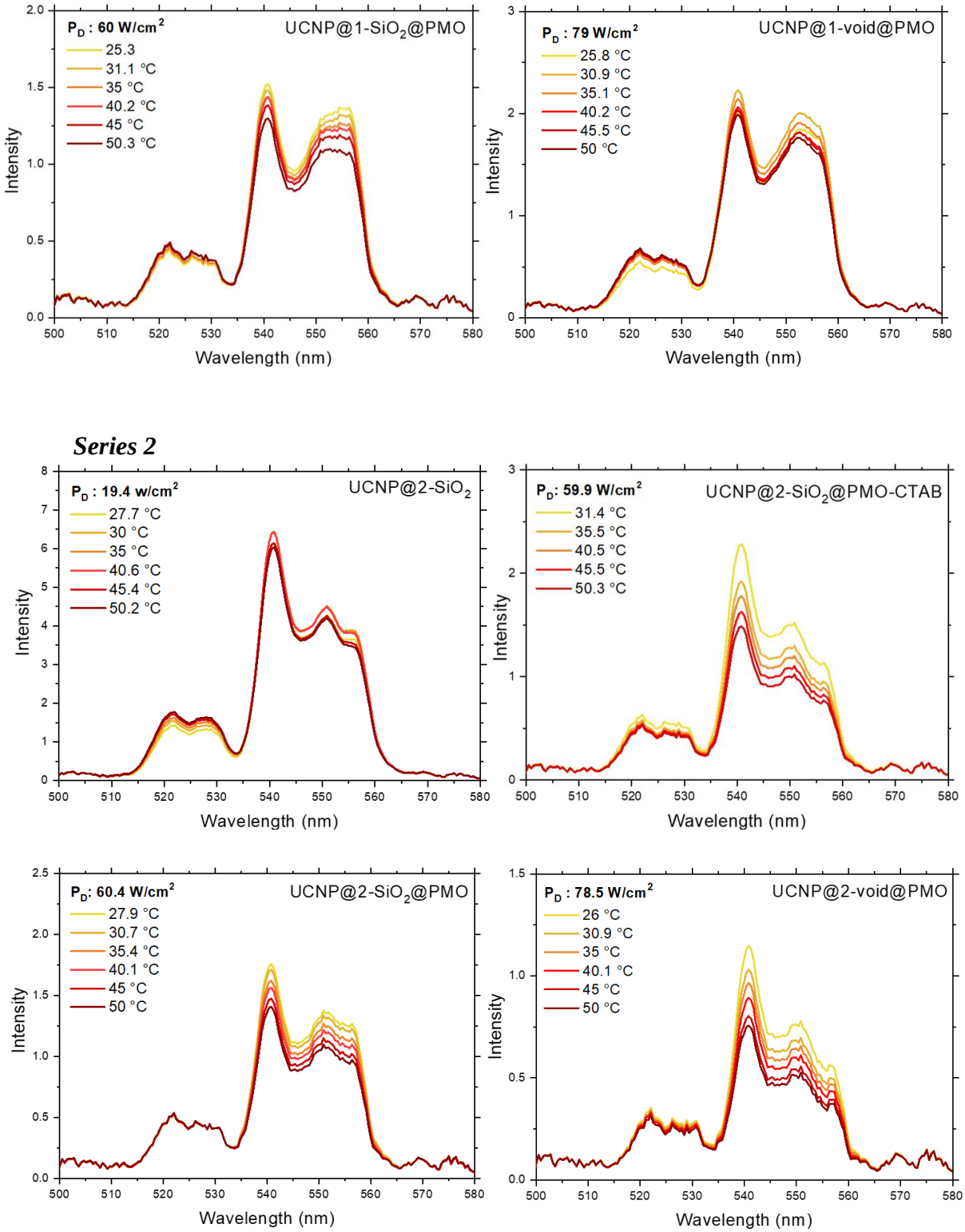

Figure IV.13 *Temperature-dependent upconversion emission spectra in the green spectral region. The P_D used for each experiment is mentioned in the top of each graph.*

4.4.3.3 Nanothermometers calibration curves (LIR vs. T)

Fig IV.14 displays calibration curves of all nanothermometers with distinct structure from the series 1 and 2. Data points of the thermometric parameter as a function of temperature show a good linear trendline with high R-squared values. The difference between calibration curves of the studied nanostructures lies in the variation of both the slope **a** and the intercept **b** of the linear curve with the equation $\Delta = \mathbf{aT+b}$. The values are listed in **Table IV.4**.

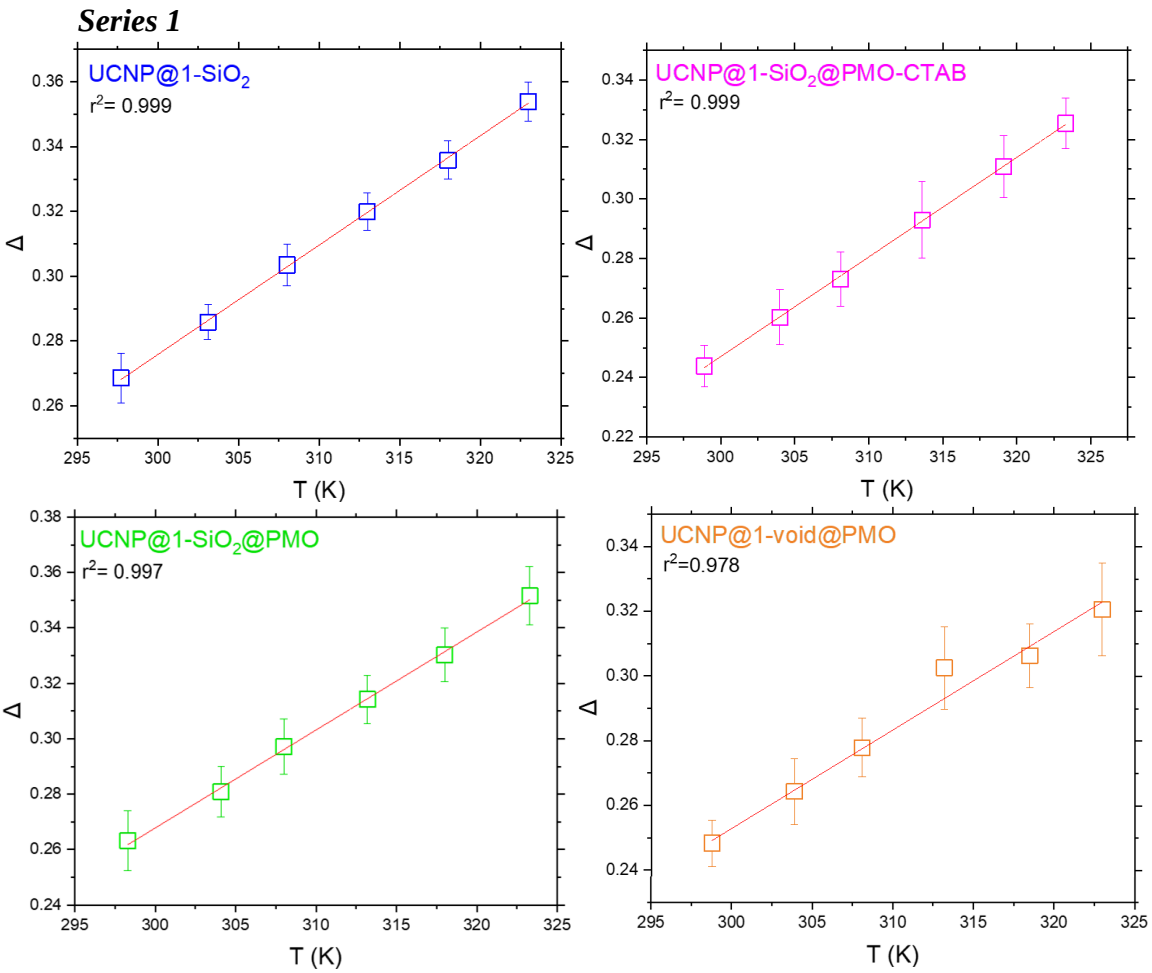

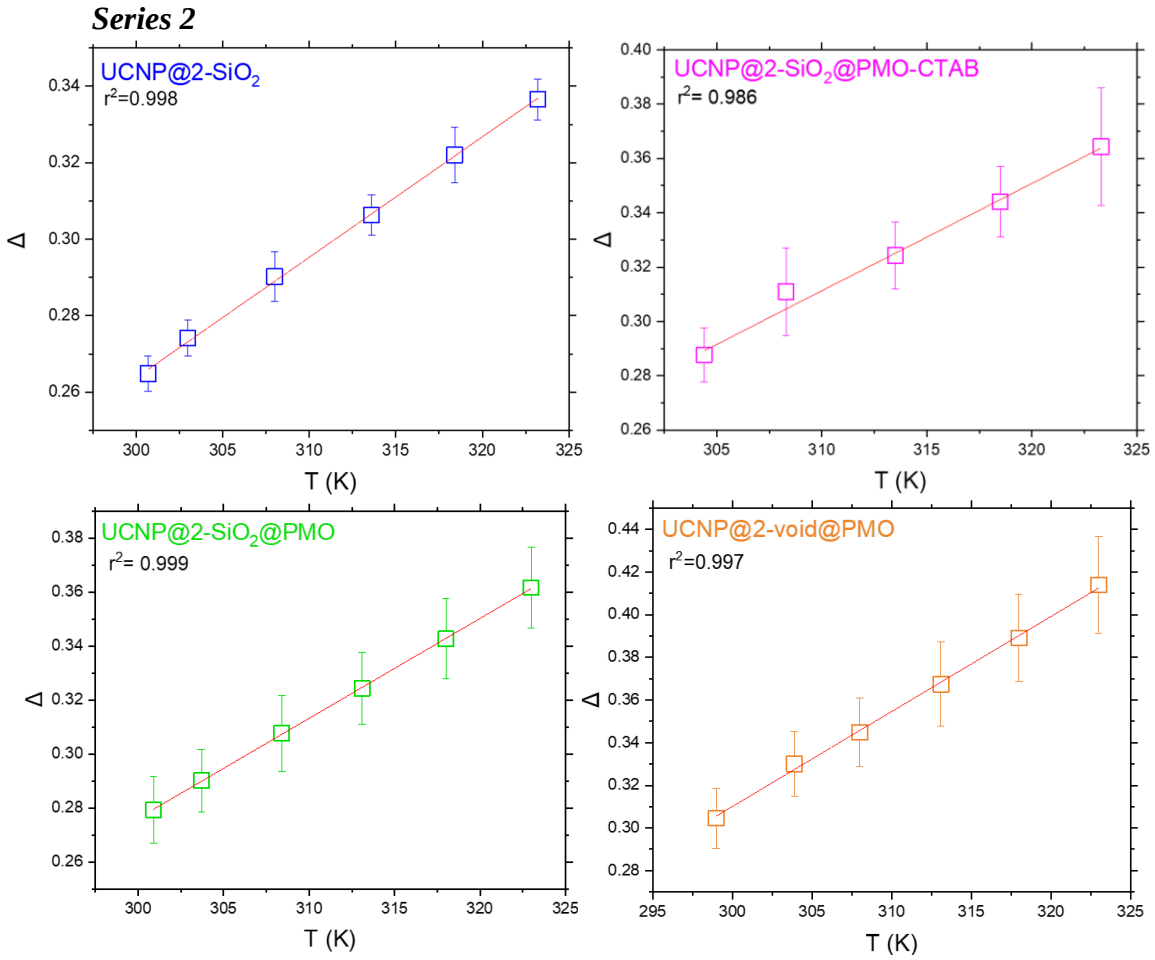

Figure IV.14 *Plot of the thermometric parameter Δ as a function of temperature. The red curve represents the least square fit (r^2>0.98) used as the nanothermometer calibration curve. The slope and the intercept of the linear fit are used the calculate the relative sensitivity S_r.*

Sample	*Slope a*	*Intercept b*
UCNP@1-SiO_2	$3.37x10^{-3} \pm 3.19x10^{-5}$	-0.736 ± 0.009
UCNP@1-SiO_2@PMO-CTAB	$3.35x10^{-3} \pm 2.93x10^{-5}$	-0.757 ± 0.009
UCNP@1-SiO_2@PMO	$3.35x10^{-3} \pm 7.38x10^{-5}$	-0.792 ± 0.022
UCNP@1-void@PMO	$3.04x10^{-3} \pm 2.01x10^{-4}$	-0.658 ± 0.061
UCNP@2-SiO_2	$3.15x10^{-3} \pm 5.05x10^{-5}$	-0.681 ± 0.015
UCNP@2-SiO_2@PMO-CTAB	$3.95x10^{-3} \pm 2.31x10^{-4}$	-0.913 ± 0.072
UCNP@2-SiO_2@PMO	$3.70x10^{-3} \pm 1.88x10^{-5}$	-0.834 ± 0.005
UCNP@2-void@PMO	$4.45x10^{-3} \pm 1.01x10^{-4}$	-1.026 ± 0.031

Table IV.4 *Values of the slopes and the intercepts of the linear equation fitting the plotted data points in* ***Fig IV.14****.*

4.4.3.4 Nanothermometers performance

a) Relative sensitivity S_r

Thermal sensitivity reflects the capacity of a nanothermometer to respond to the variation of the surrounding temperature, and is thus estimated using the equation (**IV.8**), from the derivative of the thermometric parameter Δ with respect to temperature variation, and relatively to a reference Δ. S_r of each distinct nanothermometer is therefore calculated based on the slope *a* and the intercept *b* specific to each calibration curve in **Fig IV.14**, presented in the **Table. IV.4**. The uncertainty of each calculated S_r is obtained using the equation (**IV.9**).

From a first glance to the data gathered in **Fig IV.15**, all S_r decrease when increasing the temperature and they do not vary significantly for nanothermometers of series 1 compared to the ones of series 2. Besides, S_r values from the first nanoplatform UCNP@SiO_2 type, to the UCNP@SiO_2@PMO type, passing through the UCNP@SiO_2@PMO-CTAB, seem to follow the same evolution trend, despite the difference in the gap between them. Whereas for the UCNP@void@PMO type, the evolution of S_r follows different directions, where UCNP@1-void@PMO drops back to the lowest S_r among samples of series 1, and UCNP@2-void@PMO go up again to the same sensitivity level as UCNP@2-SiO_2@PMO-CTAB.

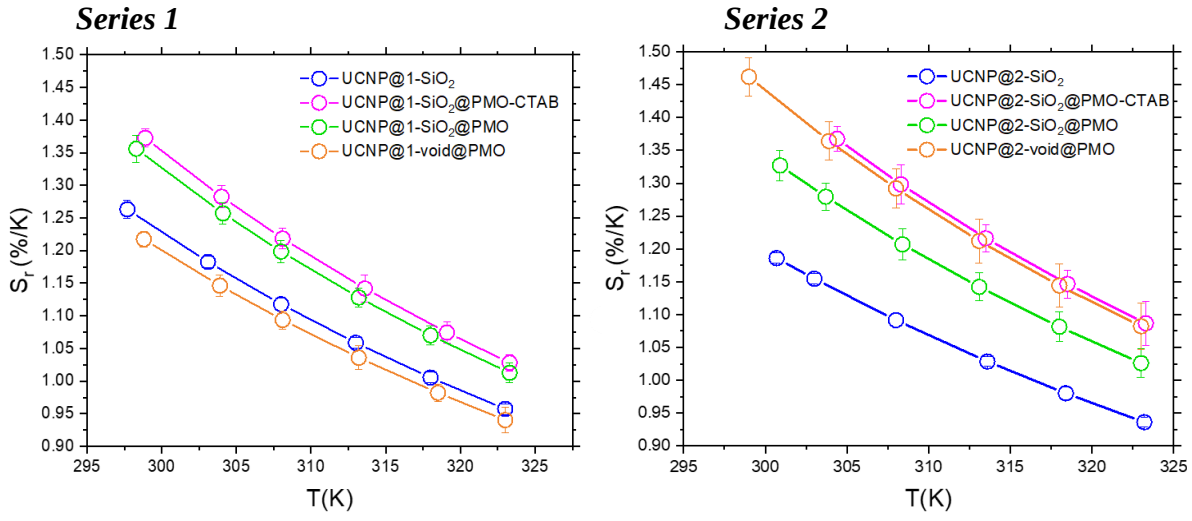

Figure IV.15 *Evolution of the relative sensitivity S_r as a function of temperature. S_r data points of nanothermometers from the same set of samples are gathered in the same graph for comparison. The same color code in previous figures is used.*

b) Temperature uncertainty δT

Temperature uncertainties displayed in **Fig IV.16** are calculated using the equation in **IV.10**, They depend on the previous S_r values and on the relative uncertainty of the thermometric parameter Δ *(δΔ/Δ)* calculated from **IV.5**. Hence, nanothermometers with high δΔ/Δ also have high temperature uncertainty readout.

For the two series of nanothermometers, uncertainty values seem to evolve in the same way for nanothermometer of the same type. Again, the gap between the uncertainties is more pronounced between samples of the series 2 than between samples of the series 1. The highest *δT* recorded is 2.1/K at 323 K, observed in the case UCNP@2-void@PMO corresponding to the yolk/shell nanoplatform with the largest void between the UCNP and the PMO shell. Whereas for the nanoplatform having the smallest void denoted UCNP@1-void@PMO, the uncertainty reaches only 1.51/K at 323 K. The lowest recorded *δT* values are observed in the case of silica coated UCNP from both series, and they have both almost the same value: 0.80/K at 323 K for UCNP@1-SiO_2 and 0.77/K at 323.2 K for UCNP@2-SiO_2.

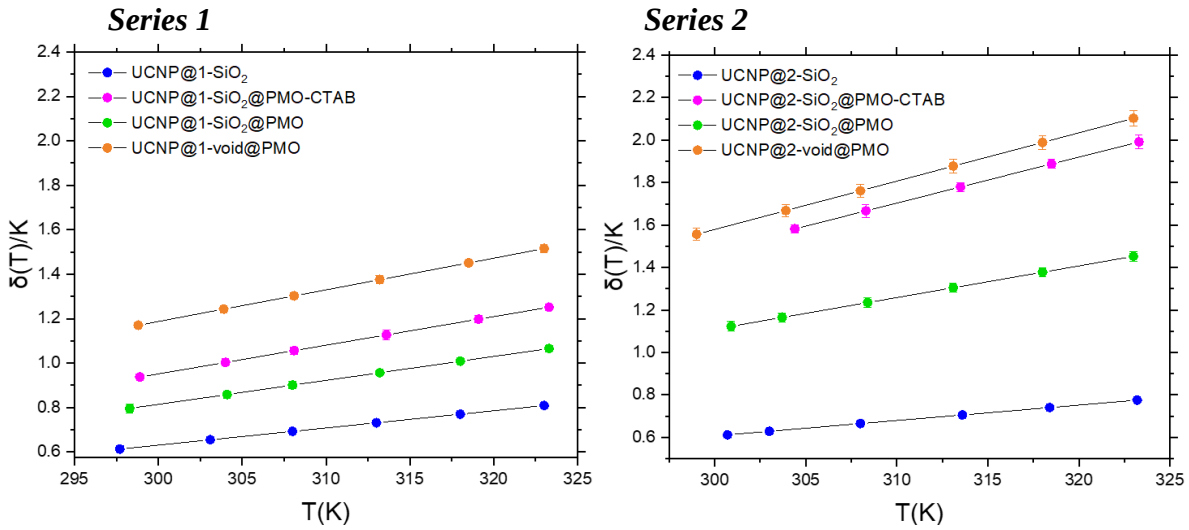

Figure IV.16 *Evolution of the temperature uncertainty δT as a function of temperature.*

Values of S_r and δT are summarized in the following table.

Samples	*Relative sensitivity S_r Max*	*Temperature uncertainty δT*
UCNP@1-SiO_2	1.26 %/K at 297.7 K	0.80 /K at 323 K
UCNP@1-SiO_2@PMO-CTAB	1.37 %/K at 298.9 K	1.25 /K at 323.3 K
UCNP@1-SiO_2@PMO	1.35 %/K at 298.3 K	1.06 /K at 323.3 K
UCNP@1-void@PMO	1.21 %/K at 298.8 K	1.51 /K at 323 K
UCNP@2-SiO_2	1.18 %/K at 300.7 K	0.77 /K at 323.2 K
UCNP@2-SiO_2@PMO-CTAB	1.37 %/K at 304.4 K	1.99 /K at 323.3 K
UCNP@2-SiO_2@PMO	1.32 %/K at 300.9 K	1.45 /K at 323 K
UCNP@2-void@PMO	1.46 %/K at 299 K	2.10 /K at 323 K

Table IV.5 *Summary of S_r and δT of all nanothermometers.*

4.4.3.5 Primary thermometer validation

a) Determination of Δ_0, T_0 *and* ΔE

Mean values and uncertainties of ΔE are calculated from the temperature-dependent upconversion emission spectra in **Fig IV.13**, using the method described in *4.3.2.* The values in **Table IV.6** are close to previous reported values [289, 293].

T_0 represents the local temperature surrounding nanothermometers when no laser excitation is applied. This temperature is measured using a thermocouple with an uncertainty of 0.1 K. Knowing that the increase of P_D results in heat generation [18], T_0 values are verified by fitting data points of measured temperature as a function of the corresponding P_D as depicted in **Fig B.6 (**appendix B).

ΔE (cm^{-1})	*UCNP@SiO_2*	*UCNP@SiO_2@PMO-CTAB*	*UCNP@SiO_2@PMO*	*UCNP@void@PMO*
Series 1	670 ± 1	693 ± 2	684 ± 3	692 ± 4
Series 2	679 ± 5	669 ± 1	677 ± 2	664 ± 2

Δ_0	*UCNP@SiO_2*	*UCNP@SiO_2@PMO-CTAB*	*UCNP@SiO_2@PMO*	*UCNP@void@PMO*
Series 1	0.269 ± 0.002	0.246 ± 0.002	0.263 ± 0.001	0.243 ± 0.002
Series 2	0.262 ± 0.001	0.279 ± 0.003	0.282 ± 0.005	0.302 ± 0.002

T_0 (K)	*UCNP@SiO₂*	*UCNP@SiO₂@PMO-CTAB*	*UCNP@SiO₂@PMO*	*UCNP@void@PMO*
Series 1	296.8 ± 0.1	296.9 ± 0.1	296.8 ± 0.1	295.8 ± 0.1
Series 2	299.4 ± 0.1	299.4 ± 0.1	299.6 ± 0.1	296.6 ± 0.1

Table IV.6 *Summary of* ΔE, Δ_0 *and* T_0 *values.*

b) Calculated vs. experimental temperature

The values of ΔE, Δ_0 and T_0 summarized in **Table IV.6** are employed to calculate the absolute temperature using the equation of state (**IV.1**), and using the Δ values calculated from the integrated intensities of spectra displayed in **Fig IV.13**. Calculated data points of the absolute temperature are then compared with the experimental ones measured using the thermocouple. Assuming that $NaYF_4$: Er,Yb is a primary thermometer, calculated values of the absolute temperature should be the same as experimental ones. This is verified by plotting the calculated values in the y-coordinate as a function of experimental values in the x-coordinate. The resulting data points should fit with the red linear curve corresponding to x=y.

The comparison between calculated temperatures and experimental ones is shown in the **Fig IV.17**. The y-error bars correspond to the error in the calculation of T denoted δT and is obtained using the error propagation expression in **IV.2**, while the x-error bars correspond to the error in the measurement using the thermocouple (0.1 K).

Data points are generally fitting well with the x=y line. Very good fits are observed for some types of nanothermometers in both series of samples like UCNP@SiO_2 and UCNP@SiO_2@PMO types, and others are less satisfying like UCNP@SiO_2@PMO-CTAB and UCNP@void@PMO.

Series 1

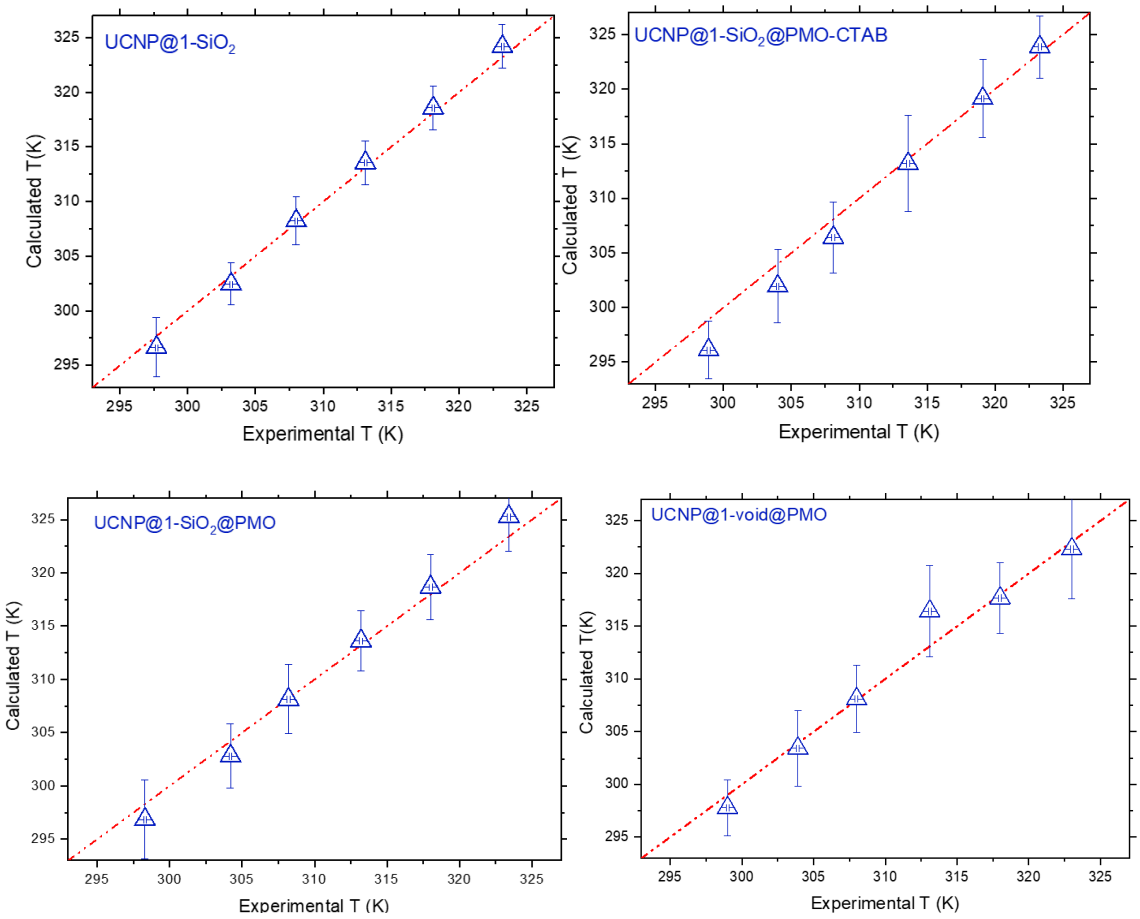
UCNP@1-SiO2
UCNP@1-SiO2@PMO-CTAB
UCNP@1-SiO2@PMO
UCNP@1-void@PMO
Calculated T(K)
Experimental T (K)
295
300
305
310
315
320
325

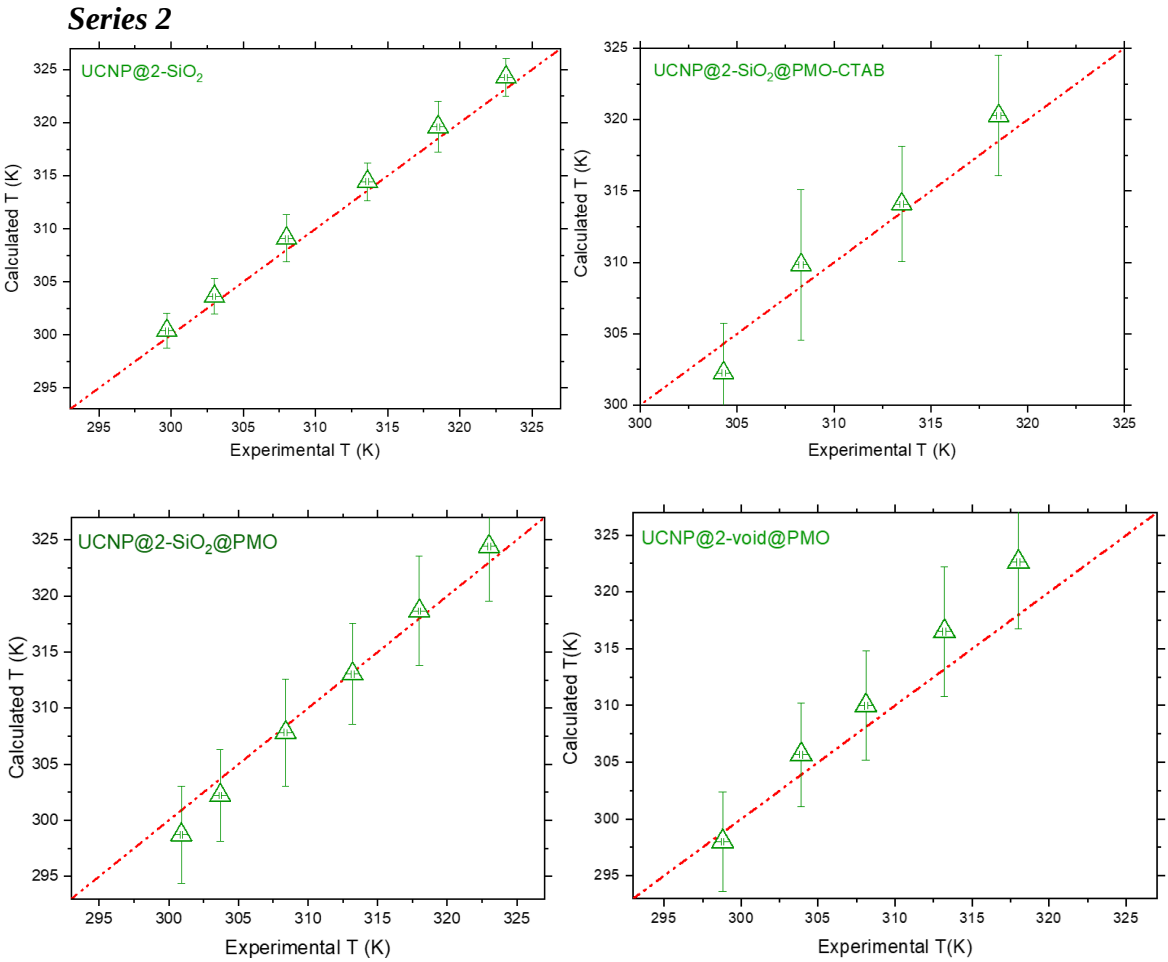

Figure IV.17 *Calculated temperature vs. Experimental temperature. The calculated temperatures are obtained from the equation (**IV.1**) using the parameters values in **Table IV.6**.*

4.5 Discussion

4.5.1 Upconversion emission intensity: red-to-green ratio analysis

At a first look of the upconversion emission of each set of nanothermometers with different structures as described in the beginning of this chapter (**Fig IV.1**), a vast difference between the emission intensity can be noticed between silica coated UCNP (UCNP@SiO_2-type in blue) and the rest of nanoplatforms, and this, for both series of samples. Emission intensities cannot be compared directly because they might be influenced by the experimental conditions, despite using the same laser P_D and the same nanoparticles concentration in the studied suspension. However, the possibility of the presence of another factor linked to the structure of the nanothermometer responsible of lowering the emission intensity should not be excluded, because such a dramatic decrease in intensity from the material with the silica material only to the one with a PMO layer (with and after removal of surfactant from the mesopores) is obvious in both series of samples (**Fig IV.8**).

The calculated red-to-green ratio values (656/540nm) are different between spectra of each series of nanoplatforms. The difference is not important but enough to build an analysis. A first idea that comes to mind when observing an increase in the red-to-green ratio is occurrence of surface quenching that can be caused by water's -OH vibrations for instance, leading to multi-phonons relaxation pathway of the $^4S_{3/2} \rightarrow {}^4I_{15/2}$ and $^2H_{11/2} \rightarrow {}^4I_{15/2}$ transitions, which is known to favor the population of the $^4F_{9/2}$ state and results in an increase of the red emission relatively to the green emission [287, 311]. However, from the UCNP@SiO_2-type (blue spectra) to UCNP@SiO_2@PMO-CTAB-type (pink spectra) in **Fig IV.8**, the only difference lies in the deposition of a second layer of PMO on the silica layer, which means that the UCNP surface is still protected by the initial silica layer and surface quenching have not way to take place. When removing the surfactant (CTAB) from mesopores (UCNP@SiO_2@PMO-type, green spectra), the red-to-green ratio is modified again. Interestingly, the ratio evolution trend is inversed between the series 1 and series 2. For the last nanoplatform UCNP@void@PMO type (orange spectra) consisting on a yolk shell structure, the UCNP surface is no longer protected by the silica coating following its etching. Quenching by water molecules is expected in this case if the mesoporous structure of the PMO outer shell is permeable. Surface quenching of UCNP NPs from both series should impact the luminescence properties in the same way independently from the PMO shell, since the same sized UCNP NPs become submerged in a "nanopool" of

water with two different volumes. The red-to-green ratio changed in this case as well, however, the values are still different between the yolk/shell structures from the series 1 and the series 2.

In **Fig IV.9**, spectra of each series of samples were normalized with the respect of the red emission centered at 656 nm. On the basis of this normalization, band shapes in the green spectral region can be analyzed. Difference in intensities is not tremendous between each spectrum of the same set of samples, but modifications of the band shape in the 535-560 nm zone is observed and arises from slight variation of the band at 540 nm and 550 nm corresponding to the $^4S_{3/2} \rightarrow {}^4I_{15/2}$ transition, and the intruder band centered at 555 nm of the $^2H_{9/2} \rightarrow {}^4I_{13/2}$ transition, following the same trend of the blue emission at 410 nm of the $^2H_{9/2} \rightarrow {}^4I_{15/2}$ transition.

When comparing the band shape of the same type of nanoplatform from each series in the green spectral region (**Fig IV.10**), the blue, pink, and orange pair of spectra seem to follow the same pattern of intensity variation between the dashed and the solid line spectra. One can notice that the peak at 540 nm increases in some spectra at the expense of the intruder peak at 555 nm, and inversely, in a way to form a sort of equilibrium between these two bands. This means that the intensity of the green band at 540 nm cannot be compared to the red band at 656 nm without considering the blue intruder band at 555 nm. The green pair of spectra appears to have a dissimilar behavior and should be analyzed differently.

Recent studies addressed the P_D dependence of the complex and competitive dynamics conditioning the population distribution between the green and the red emitting levels [298, 312]. These dynamics either favor the population of the $^4F_{9/2}$ emitting level through a bi-photonic process upon low P_D ($^4I_{13/2} \rightarrow {}^4F_{9/2,}\ {}^2H_{11/2}$ / $^4S_{3/2} \rightarrow {}^4F_{9/2}$) or through a three-photonic process at high P_D with a population provided from higher energy levels of Er^{3+} ($^4G_{11/2} \rightarrow {}^4F_{9/2}$). The population of $^4F_{9/2}$ energy level can also be promoted at high P_D due to the saturation of the $^4S_{3/2}$ and $^2H_{11/2}$ energy levels, in addition to the enhanced non-radiative processes caused by the excitation-induced heating [313]. Martins *et al.* [304] showed that the evolution of the red emission as a function of the P_D exhibits a similar pattern to that of the intruder band at 555 nm, knowing that the latter requires a three-photon process, unlike green emissions that require only a two-photon process. The same trend was also observed for the samples studied in the current work (**Fig B.2,** appendix B) when studying the evolution of emission spectra as a function of P_D.

Now when normalizing the distinct spectra from the two series of nanothermometers, recorded at the same P_D, relatively to the 540 nm band (**Fig B.3**, appendix B), spectra of types UCNP@SiO_2 and UCNP@SiO_2@PMO-CTAB, also exhibit the same evolution trend at the level of the intruder band at 555 nm and the red band at 656 nm. This leads to the conclusion that the increase of the red-to-green ratio observed initially in some samples is originated from the saturation of the $^4S_{3/2}$ and $^2H_{11/2,}$ and the population of $^4F_{9/2}$ energy level via the three-photon process the same as the $^2H_{9/2}$ energy level, and/or through the non-radiative relaxation of $^4S_{3/2}$ and $^2H_{11/2}$. This is specific to some nanoplatforms over others within the same series, where the only difference lies in the UCNP surrounding structure, which suggest that saturation of energy level and the promotion of three-photon processes is ruled by the structural properties of the encapsulating layers. This suggestion is not directly valid for UCNP@void@PMO types (orange spectra) even if they follow the same trend, because the bare surface of the UCNP is exposed to water quenching, which can be also involved in modifying the red-to-green ratio values.

4.5.2 Effect of the amorphous silica layer: UCNP@SiO_2 nanoplatforms

The effect of the silica shell on the luminescence properties of UCNPs is assessed by comparing the emission spectra of UCNPs confined in two thicknesses of silica ~ 13 nm (UCNP@1-SiO_2) and ~ 27 nm (UCNP@2-SiO_2) in **Fig B.4**. (blue pair of spectra, appendix C). Using the normalization at 540 nm band, we can observe that indeed the blue intruder band at 555 nm of each spectrum, follows the same evolution as the red band at 656 nm. The intensity of these two bands is more pronounced in UCNP@2-SiO_2 having the thicker silica shell. This suggest that the thickness of the silica layer plays a role in the Er^{3+} high energy levels population through the three-photon process, thus producing a similar outcome to that of increasing P_D.

4.5.3 Effect of the PMO-CTAB layer: UCNP@SiO_2@PMO-CTAB

The deposition of a PMO layer containing CTAB in the pores on the previous silica-coated UCNPs seems to maintain the same evolution of the intruder band and the red band. However, it also seems to have inversed luminescence properties compared to the UCNP@SiO_2 nanoplatforms from each series, considered as a benchmark. In fact, UCNP@1-SiO_2 have more intense intruder and red band after the deposition of the PMO-CTAB layer (UCNP@1-SiO_2@PMO-CTAB), unlike UCNP@2-SiO_2 where these two intensities drop after the

deposition of the PMO-CTAB layer (UCNP@2-SiO_2@PMO-CTAB). Here again, it seems that these alterations stem from structural factors.

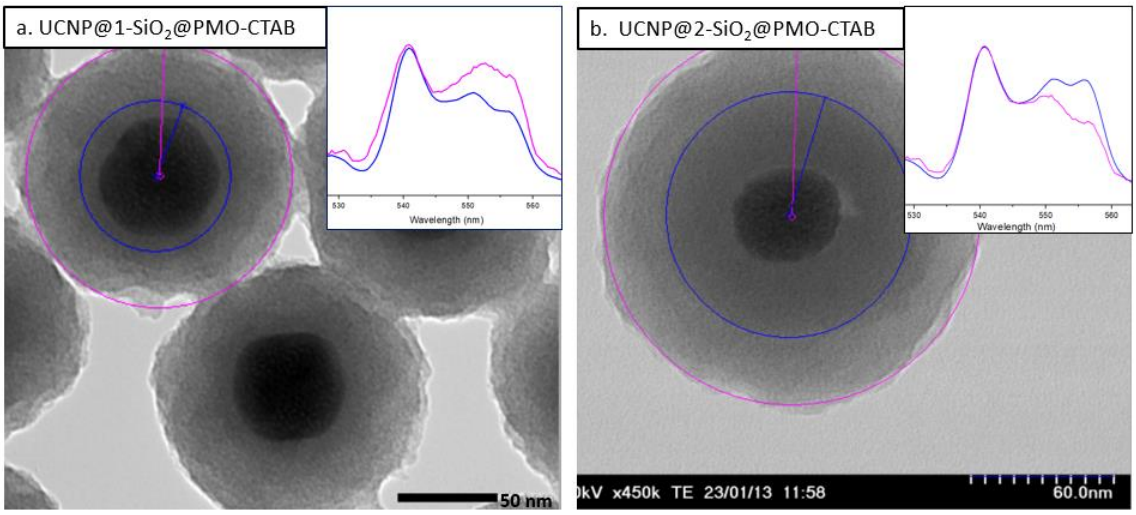

Figure IV.18 *Association between structural and spectral properties of UCNP@ SiO_2@PMO-CTAB nanoplatforms from series* ***(a)*** *and series 2* ***(b)****. The blue circle corresponds to the limit of silica coating in each nanoplatform (UCNP@SiO_2 samples), the corresponding spectra is presented with the same color. The pink circle corresponds to the total nanoplatform with both layers (silica+ PMO). Here the PMO is still filled with CTAB molecules.*

Two hypotheses can be made to explain the inversed properties described above:

-The PMO layer structure in the nanoplatform in **Fig IV.18.a** is different from the one in the **Fig IV.18.b**, considering their different hard template thicknesses (in analogy to the structural differences observed in HPMO NPs when size tuning the hard template).

-The overall shell thickness of each nanoplatform is responsible of altering the luminescence properties. The total nanoplatform in **(a)** is almost of the same size of the single-silica shell nanoplatform in **(b)**, circled with blue.

Concerning the luminescence lifetime analysis of the UCNP@SiO_2 and UCNP@SiO_2@PMO-CTAB types from both series, values presented in the **Table IV.3** show similar rise times and decay times in the three recorded wavelengths, with consideration to their uncertainties. This means that the deposition of the PMO shell loaded with a surfactant does not affect the upconversion emission lifetime.

4.5.4 Effect of CTAB removal from mesopores: UCNP@SiO_2@PMO

As mentioned before and as observed in the green pair of spectra in **Fig B.4**. (appendix B), the increase of the intruder emission is not followed by the increase of the red emission for this type of nanoplatform. The red-to-green ratio of UCNP@2-SiO_2@PMO is higher than UCNP@1-SiO_2@PMO one, while the intruded intensity is not affected and still higher in the latter. This implies the presence of an additional factor involved in decreasing the emission of the red intensity and possibly even the green emission, leading to a variation of the overall red-to-green ratio.

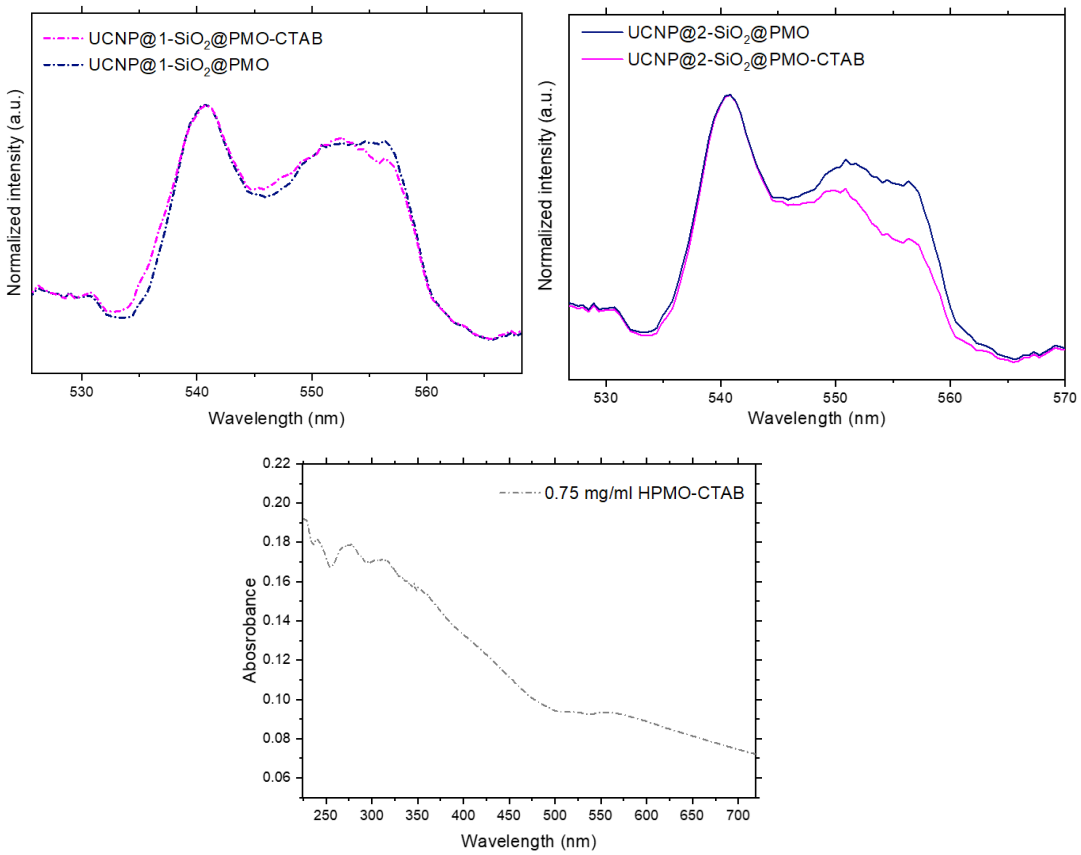

Figure IV.19 ***Top:*** *Emission spectra in the green spectral region showing the difference of the nanoplatforms of series 1 (dashes lines) and 2 (solid lines) before and after CTAB extraction.* ***Bottom:*** *Extinction spectrum of HPMO NPs filled with CTAB.*

In both series of samples, a slight increase of the intruder band after CTAB removal, with the difference being more pronounced between spectra of the series 2 (**Fig IV.19 top**). This indicates that CTAB absorbs the UCNPs emission in this region, which can be supported by the extinction spectrum of HPMO NPs with mesopores containing CTAB (**Fig IV.19 bottom)** considered as a reference for the PMO-CTAB deposited on the silica-coated UCNPs. The

spectrum exhibits some absorption peaks mainly in the blue wavelength region and around 550-555 nm.

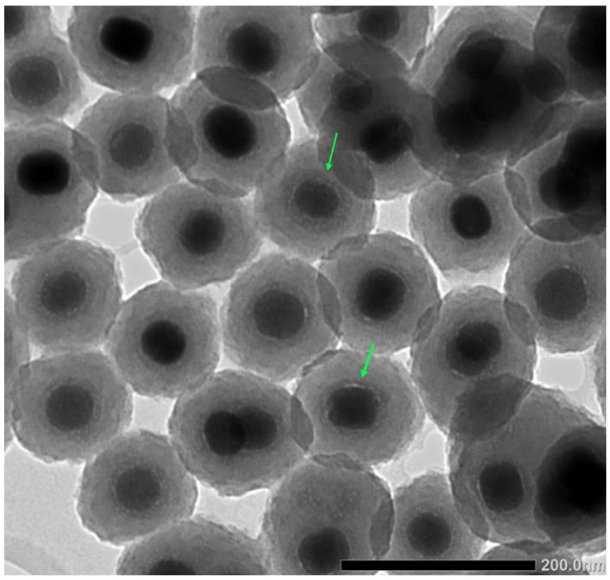

Figure IV.20 *TEM micrograph of UCNP@1-SiO_2@PMO, the green arrows show an initiated etching process in the inner part of the silica coating.*

The red emission lifetime decreased to a small extent for UCNP@SiO_2@PMO both series, whereas the lifetime of the two green emissions decreased only for UCNP@1-SiO_2@PMO-CTAB. This can be explained by the fact that during the PMO layer deposition on the 13 nm silica shell, a minor portion of silica is subject to etching or creation of porosity (**Fig IV.20**). This mechanism is known as the PMO-induced etching (mentioned in **Chapter. III**). Obviously, a 13 nm silica shell can be more impacted than a 27 nm one. It is possible that when CTAB was removed, the mesoporous shell became permeable to the surrounding water, which could infiltrate through the partially impacted silica layer until reaching the UCNP surface. A mild water quenching could explain the lifetime shortening in the three wavelengths and might also be responsible of the observed red-to-green ratio variation. While the shortening of the red emission in both samples can be explained by the absorption and the scattering losses caused by the PMO structure after the removal of the surfactant [314]. In fact, CTAB is a cationic surfactant known to co-assemble with polycondensed bridged organosilane molecules through an ionic bond with $Si\text{-}O^-$. The removal of CTAB not only gives place to a mesoporous structure that could be responsible of light scattering, but also release the $Si\text{-}O^-$ subsequently turning to Si-OH bonds whom the vibration might be associated to light absorption [314].

4.5.5 Effect of the void: UCNP@void@PMO

The orange pair of spectra displayed in **Fig B.4** (appendix B), show a low red-to-green ratio in UCNP@2-void@PMO compared to UCNP@1-void@PMO. In both nanoplatforms, empty mesopores and the presence of a void between the UCNP and the PMO layer, provide a pathway for water infiltration, thus easily exposing the luminescence of the UCNP to quenching effect. After the etching of the silica layer separating UCNP from the PMO layer, the UCNP nanoparticle falls on the inner surface of the PMO shell under gravity effect. The different thicknesses of the sacrificial silica shell give place to different void volumes, and the curvature of the PMO shell is different accordingly, as seen in **Fig IV.21**. The portion of UCNP surface in contact with the PMO layer is greater in **(a)** than in (**b)**. This contact with the PMO can have the same surface passivation effect as the removed silica shell, and can partially protect the UCNP from the infiltrated water. The extent to which the UCNP is protected depend on how much surface is in contact with the PMO. This could justify why UCNP@2-void@PMO exhibits the weakest emission intensity. The low red-to-green ratio can be explained by the fact that the red emission is affected by water to the same extent as green emissions, unlike UCNP@1-void@PMO.

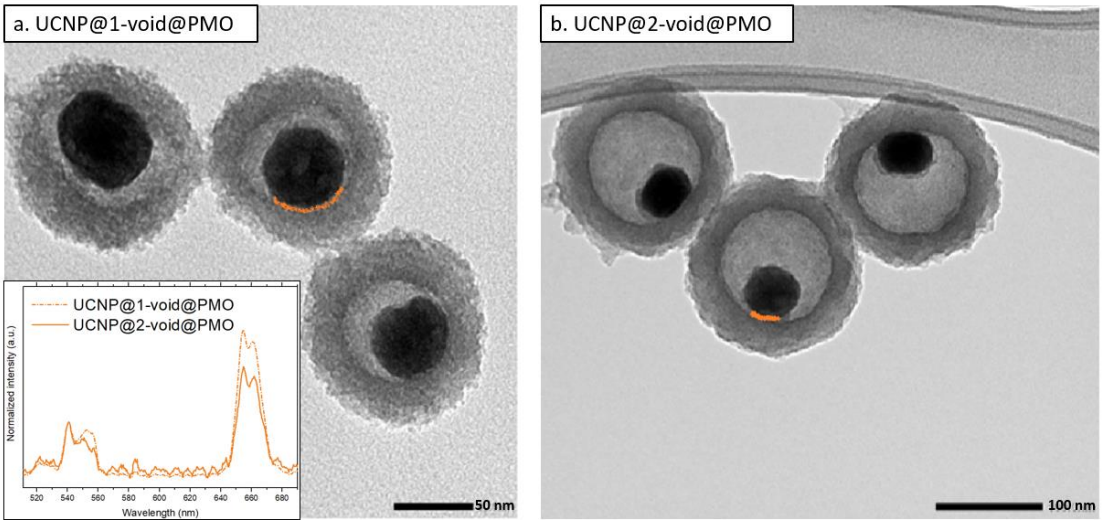

Figure IV.21 *TEM images highlighting in orange the difference in the surface fraction of UCNPs touching the inner surface of the PMO layer in the yolk/shell nanoplatforms and a possible correlation with the difference in the emission intensity observed in the spectra below the image* ***(a)***.

Measured lifetimes of yolk/shell nanoplatforms in both series listed in **Table IV.3** show a decrease in green emission decays time by 15 % and in the same way for both series of samples. The red emission is less impacted by water quenching but it still more important for UCNP@2-

void@PMO (10 %) than for UCNP@1-void@PMO (6 %). This could explain the difference of the red-to-green ratio between the two samples, even if the emission lifetimes and emission intensities are not always correlated. Indeed, the emission intensity can be caused by the decrease of the intermediate energy level deactivation via -OH vibrations leading population reduction of the emissive energy levels, without necessarily affecting the lifetime of the output emission [287]. On the other hand, non-radiative multi-phonon relaxation can affect both emission intensity and lifetime. The fact that such complex nanoplatforms are not only exposed to non-radiative processes and energy levels deactivation caused by water but also to the absorption (filter effect) caused by the complex surrounding structure, makes it challenging to precisely attribute each process to its effect on luminescence intensity and lifetime, mainly for the emission intensity, where the red-to-green ratio can be affected through multiple processes involvement. The differences in lifetime between the reference nanoplatforms protected with silica coating, and the yolk/shell nanoplatform are not tremendous, but can serve to prove the permeability of PMO shell to water molecules.

In the analogous work reported by. M. Kaczmarek *et al.* [199], the study shows that luminescence intensity increased after etching the intermediate silica between the nanothermometer and the PMO shell. This raises a question mark on the PMO structure presented in the study and supports the comments made in **Chapter. III** on the synthesis route that was followed without the use of a structure directing agent co-assembling with the bridged organosilane precursor. As a matter of fact, if the PMO shell was accessible to water through mesopores, the water would be in direct contact with the upconverting nanoparticles as well, which is expected to cause even more quenching than silica, but this was not the case in the study.

4.5.6 Nanothermometers performance

4.5.6.1 P_D dependent Δ

The variation of the thermometric parameter Δ as a function of P_D shown in **Fig IV.12** for both series of samples indicates that the silica-coated samples in both series are impacted by the laser power pump induced heating. This is observed ever since low P_D values because of the increasing pattern of data points between 10 and 50 W/cm^2. In contrast, for all the structures having a PMO layer (with or without CTAB, before and after silica etching), data points are

constant even at higher P_D. Actually, given the low signal to noise ratio of these samples, the spectra had to be recorded at a maximum P_D of 74.4 W/cm^2, and though, they still have not shown any increasing trend.

As a matter of fact, power induced heating remains one of the undesired effects in nanothermometry because of potential induced errors in temperature readout. P_D induced self-heating were demonstrated for β-$NaYF_4$: Er,Yb phosphors in the powder form [315], where 50 W/cm^2 was reported as a critical P_D limit after which the upconversion emission intensity of UCNP starts decreasing [316]. Generally, to address this issue, the minimum P_D at the limit of which no heat is generated should be determined, and it varies from one UCNP to another [317]. This also implies that the UCNP should be bright enough to provide a satisfying signal-to-noise ratio at that critical limit of P_D. Which means that a compromise should be made by selecting the right UCNP.

When it comes to aqueous suspensions of UCNPs, the heat generation under 980 nm laser excitation could be caused by both UCNPs and water because both absorb at this wavelength and convert the radiation into heat, with the amount of generated heat being proportional to the absorption cross-section of each one of them. In this case, the heat transfer can occur in both directions, from the UCNP to water or/and from water to UCNP under specific values of P_D. In this context, A. R. N. Bastos *et al.* [318] studied more closely the aspects of heat generation and heat transfer between water and UCNP ($LiYF_4$: Er,Yb). In order to evaluate the contribution in heat generation of each one of them, the evolution of the temperature (ΔT), measured with a thermocouple, as a function of P_D, was compared between uncapped UCNP in D_2O (weak absorption at 980 nm) and H_2O with no UCNP in it. The results show that temperature increment is more important in H_2O than in the suspension of UCNP D_2O (ΔT (H_2O) = 3 K against ΔT (uncapped UCNP) =1 K at 75 W/cm^2).

In the case of a suspension of UCNP in H_2O and at a limit of 75 W/cm^2, the heat generated by H_2O should be felt by the UCNP, and the temperature increment should induce an increase of the thermometric parameter Δ. In the current study, the UCNP@SiO_2 systems do exhibit an increase of Δ as a function of P_D, but all the rest of the samples endowed with a PMO shell do not manifest such a phenomenon (**Fig IV.12**). This is an interesting point because it could deliver to some extent from temperature measurement errors due to heat generated at high P_D. However, it remains intriguing since the nanoplatforms with and without the PMO layer display

two distinct thermal behaviors, which raises fundamental questions on how the nature of the encapsulating layer is involved in such behavior, through heat dissipation or light absorption for instance.

4.5.6.2 Relative sensitivity S_r and temperature uncertainty δT

The same S_r variation pattern is observed in the same type of nanoplatforms from each series of samples as shown in **Fig IV.15**, except for the yolk/shell nanoplatforms, where S_r appears to have a distinct behavior between the two series, which can be explained by the different disposition of the UCNP toward the PMO shell as shown in **Fig IV.21**. This variation, though it may be minor, strongly indicated that the composition and the structure of the encapsulating layers have a different impact on the relative sensitivity of the nanothermometer. Indeed, S_r value increases after the addition of the PMO layer, and is even higher when the surfactant (CTAB) is still occupying mesopores. S_r values vary between 1.18 %/K and 1.46 %/K, these values are consistent with reported values of Er^{3+} based nanothermometers [293]. The highest S_r values to be yielded is 1.46 %/K at 299 K and is slightly higher than the recent reported value of encapsulated UCNPs [199].

Temperature uncertainties increase in the same way for the same nanoplatforms of both series of nanothermometers. The lowest values are registered for the UCNP coated with silica (UCNP@SiO_2 type) which also have the lowest S_r. Silica thickness does not seem to impact the performance of the UCNP because similar values are yielded for both thicknesses. δT values begin to escalate after the deposition of the PMO layer, and increase further following the etching of the intermediate silica layer. The pace of evolution seems to be a bit higher for nanoplatforms with the thickest silica layer (series 2). Nanoplatforms yielding the highest S_r among all nanothermometers also have the highest temperature uncertainties, notably nanoplatforms containing CTAB in the mesopores and the yolk/shell ones. Except for UCNP@1-void@PMO that exhibits a low S_r comparable to UCNP@1-SiO_2 one, but the uncertainty is still the highest among nanothermometers of its series. These results also suggest that the composition and the structure of the UCNP surrounding layers impact its temperature uncertainty.

4.6 Conclusion

In this chapter, the optical properties and the thermometric performance of four pairs of nanoplatforms are studied using both the steady-state and time-resolved regimes with the aim to analyze the nanoconfinement effect. The confined nanothermometers were divided on purpose into two series of samples composed of hierarchical systems from the same four steps of elaboration, and having as the only difference the thickness of the sacrificial silica layer separating the luminescent UpConverting NanoParticle (UCNP) from the Periodic Mesoporous Organosilca layer (PMO). The assessment of their thermometric performance was achieved following the Luminescence Intensity Ratio method (LIR) in the physiological temperature range (20-50 °C), using aqueous NPs dispersions.

The first positive point that can be drawn from the experiments is that similar trends are observed in both series of nanothermometers with very subtle distinctions that we discussed. Moreover, the different behavior of the UCNPs shown under distinct confinement configurations (core/shell, yolk/shell) collected from the four steps of elaboration (i) silica coating (ii) addition of PMO-CTAB layer (iii) CTAB removal from mesopores (iiii) silica etching; validates the success of the multistep approach addressed in the **Chapter. III**.

Emission intensity was significantly reduced by the addition of PMO layer, probably because of absorption and scattering effects caused by the hybrid structure. The CTAB absorption in the green and blue region, contributing in emission intensity decrease, was also demonstrated. The luminescence quenching was observed in yolk/shell structures based on both emission intensity and the luminescence lifetime. This led to the conclusion that the mesoporous structure is accessible to water molecules that infiltrate through mesopores and get close to the UCNP.

The evaluation of the thermometric performance based on the relative sensitivity S_r and the temperatures uncertainty δT showed that these parameters are highly conditioned by the thickness (13 vs 27 nm intermediate silica) and the different encapsulating layers. The highest temperature uncertainties were registered for the series of samples having the thicker intermediate silica layer 2.1/K and 1.9/K at 323 K. The best performance at both δT (1.06 /K at 323.2 K) and S_r (1.35 %/K at 298.3 K) was registered for the UCNP@1-SiO_2@PMO, where the 13 nm silica was kept and the mesopores were emptied from CTAB. Moreover, we

demonstrated that the PMO shell somehow prevents from the 980 nm laser excitation-induced additional heating.

General conclusion and perspectives

This manuscript was focused on the encapsulation of a luminescent upconverting nanomaterial functioning as a nanothermometer in core/shell and yolk/shell configurations, aiming to build a multifunctional nanoplatform. The purpose was then to assess the nanothermometers optical properties and performance under the confinement effect. The encapsulating shell consists of a Periodic Mesoporous Organosilica (PMO) that holds many potential functionalization routes.

We were first interested in studying the structural properties of the PMO shell independently from the functional core. For this matter, Hollow Periodic Mesoporous Organosilica Nanoparticles (HPMO NPs) served as a reference nanomaterial and was synthesized following the hard template strategy, where the core material is made of a sacrificial amorphous silica on which a PMO layer is deposited. The evolution of the mesoporous network structuring is investigated. Two principal parameters were varied: the size of the hard template employed to tailor the size of the final HPMO NPs, and the chemical composition of the shell by using different bridged organosilane precursors. The structural analysis based on IR spectroscopy, X-ray diffraction and nitrogen physisorption suggests that the variation of both the size and the chemical composition of HPMO NPs strongly modifies the pore size distribution and structuring, thus affecting the specific surface area of the shell. The interplay between these aspects and the π-π stacking of the phenylene-bridged system was suggested.

The HPMO nanoplatform synthesis served as an inspiration to form the multifunctional nanoplatforms. Indeed, the same sacrificial silica core is used to coat the nanothermometer before the deposition of the PMO layer. It is subsequently etched to obtain a void separating the core from the PMO shell, and the resulting structure is known as "yolk/shell". The challenge of achieving uniform samples was progressively overcome. The mechanism ruling the quality of the PMO deposition without the formation of undesired core-free PMO NPs was suggested in the **Chapter. III**. The multistep elaboration strategy enables the collection of nanoplatforms from all the steps of the synthesis, with the intention of studying their optical properties distinctively, for comparison.

Two sets of nanoplatforms were prepared, consisting of β-$NaYF_4$: Er, Yb nanocrystals serving as upconverting nanothermometers, encapsulated within a PMO shell to form core/shell and yolk/shell systems. They have a total size of 128 ± 6 nm and 166 ± 9 nm. The variation in the overall size is attributed to the difference of the intermediate silica shell thickness, 13 nm and

27 nm respectively. We could demonstrate that the selective etching of these sacrificial silica layers gives place to void spaces that conserve the volume of the etched silica.

Next, the as-prepared nanoplatforms are studied using both steady-state and time-resolved spectroscopies to evaluate their spectroscopic properties and thermometric performance under different configurations: (i) silica coating, (ii) added PMO layer with CTAB still filling the mesopores (core/shell), (iii) the NPs after CTAB removal from mesopores, (iiii) the NPs after etching of the sacrificial silica (yolk/shell). The results presented and compared in the **Chapter. IV** suggest that the variation of the red-to-green emission ratio and the blue intruding band at 555 nm is structure-dependent. The decrease of lifetimes of the two green emissions at 524 nm and 540 nm and the red emission at 656 nm for the yolk/shell system indicates the presence of water quenching. This quenching suggests that the PMO shell is permeable and that water molecules infiltrate through mesopores.

Additionally, the thermometric parameter Δ remains constant as the laser power density (P_D) increases, and that, only for the systems equipped with a PMO shell. Although the dissipation of the additional heat generated by water is a positive point because it delivers from induced errors in temperature readout, its mechanism remains not well understood in the current study and requires further fundamental investigations specific to the elaborated nanoplatforms.

The differences in nanothermometric performances are subtle. The comparison is based on the variation trends observed between the calculated relative sensitivities (S_r) and temperature uncertainties (δT). These parameters seem to be affected by both the nanothermometers surrounding layers and the silica thickness/void distance separating the nanothermometer from the PMO shell. The highest S_r 1.46 %/K at 299 K is recorded for the yolk/shell (UCNP@2-void@PMO) and core/shell containing CTAB (UCNP@2-SiO_2@PMO-CTAB) structures from the series 2. Those are also the samples having the highest δT 2.1/K and 1.9/K at 323 K. The sample that provided the best performance at both levels is the core/shell sample from series 1 with the 13 nm shell thickness and no CTAB in the mesopores (UCNP@1-SiO_2@PMO) with S_r being equal to 1.35 %/K at 299 K and δT equal 1.06 /K at 323 K.

The accuracy of the thermometric performance is affirmed by satisfactory alignment of calculated and experimental data, thus validating the primary thermometer principle as outlined in the methodology part in **Chapter. IV**.

Perspectives

In perspective we are interested in several questions:

- The optimization of synthesis protocols to obtain better monodisperse HPMO NPs, while mastering the control of the shell thickness and the total elimination of impurities.

- A deeper investigation on the evolution of π-π stacking as a function of the diameter of the HPMO NPs in the case of phenylene-bridged organosilane used as a precursor.

- The findings outlined in the preceding chapter emphasized the crucial influence of the interfacial layer that separates the UCNP core from the PMO shell in modifying the thermometric performances. In perspective, an in-depth study can provide a deeper understanding of the dependency between the structural properties and thermometric performance.

- The successful encapsulation of nanothermometers in the PMO shell, opens up an opportunity for temperature sensing in biological media. It would be interesting to evaluate the cell uptake by endocytosis and EPR effect, as well as the evaluation of the biocompatibility.

Appendix A

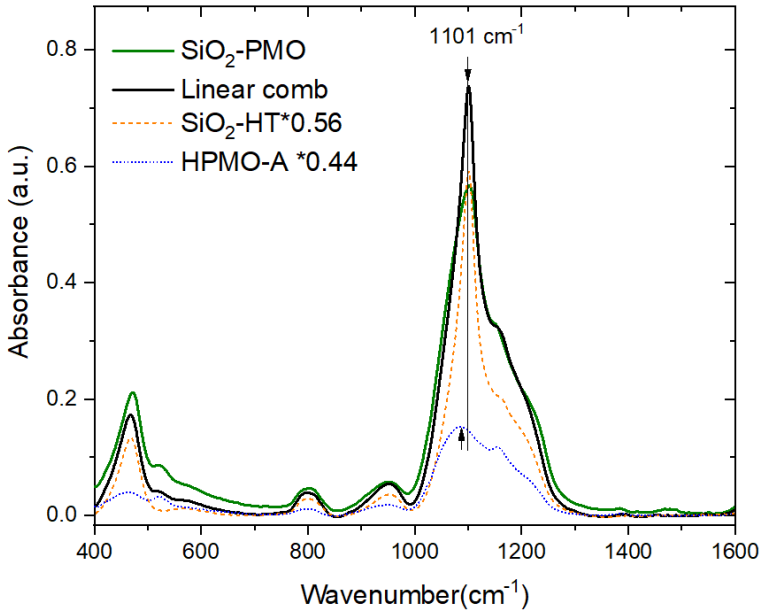

Figure A.1 *Linear combination of the spectra of the samples SiO_2-HT (56 %) and HPMO-A (44 %) compared with the experimental spectrum of SiO_2-PMO.*

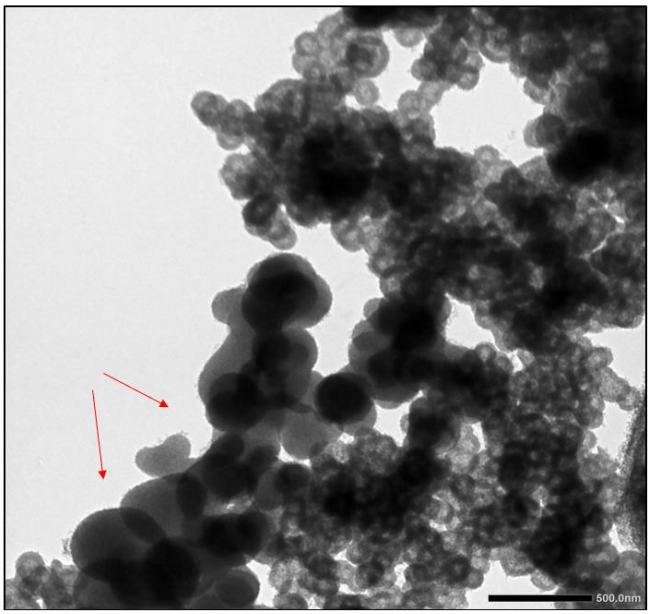

Figure A.2 *TEM image highlighting the presence of large PMO NPs formed independently from the hollow structures.*

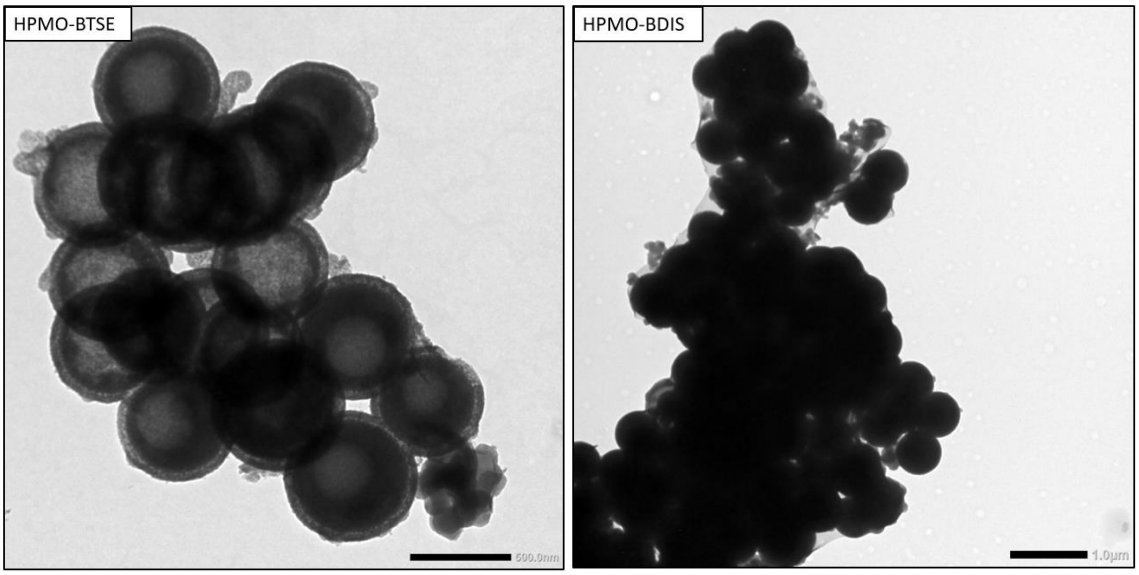

Figure A.3 *Additional TEM micrographs of BTSE and BDIS HPMO NPs.*

Frequency (cm^{-1})	*Assignments*
901	Bending C-H (CH_3)
929	Bending C-H (CH_3) + wagging C-H (CH_2)
942	Bending CH (CH_3) + bending CH (ring)
1005	Rocking C-H (ring)
1053	Anti-symmetric stretching O-C-C
1060	Bending O-Si-O
1071	Twisting C-H (CH_3)
1082	In plane deformation (ring) Twisting C-H (CH_3)
1090	Twisting O-C-H (CH_2)
1117, 1132	Rocking C-H (CH_2, CH_3)
1251, 1260	Twisting C-H (CH_2)
1324 1356	Wagging C-H (CH_2, CH_3)
2929	Symmetric stretching C-H (CH_2)
2943,2972, 3004	Anti-symmetric stretching C-H (CH_2)
3063	symmetric stretching C-H (CH_3)

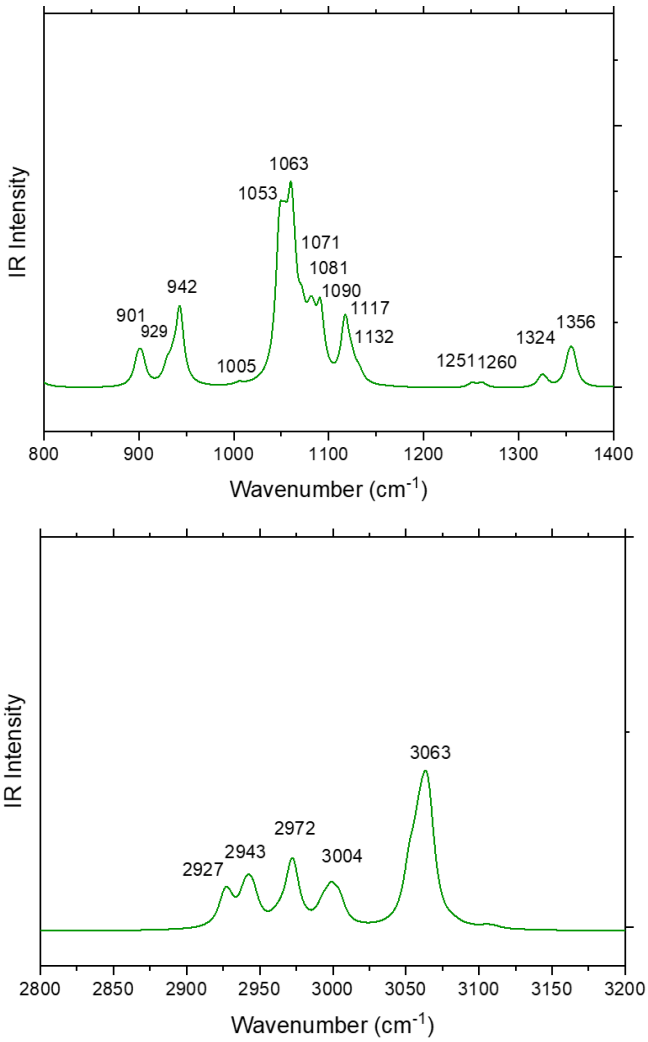

Tables A.1 *One BTEB molecule vibrational modes based on a DFT calculated spectrum.*

Appendix B

Normalized emission intensities

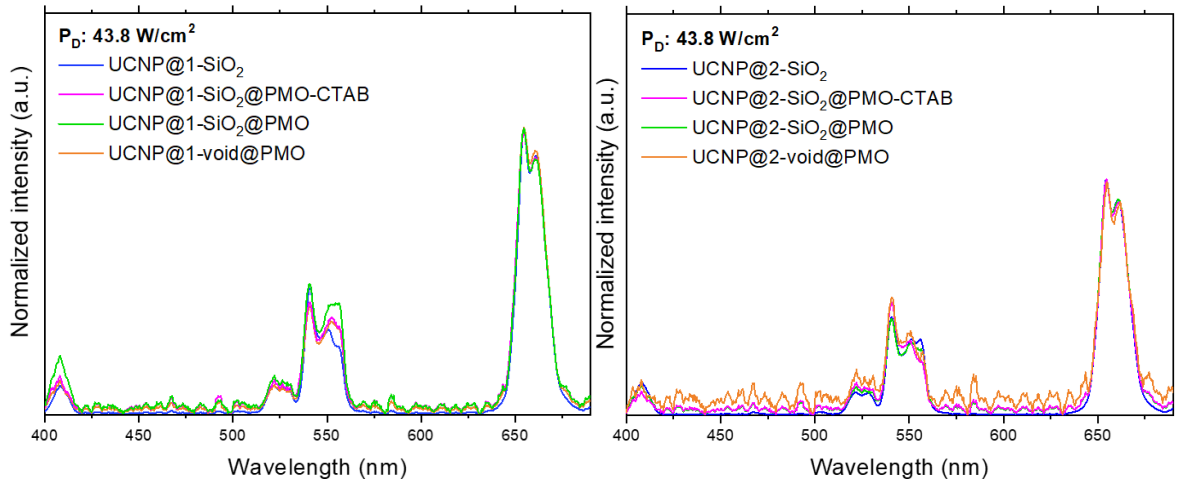

Figure B.1 *Upconversion emissions spectra of distinct nanoplatforms from each series of samples at fixed P_D, with normalized intensity relatively to the most intense pic which is the red emission at 656 nm.*

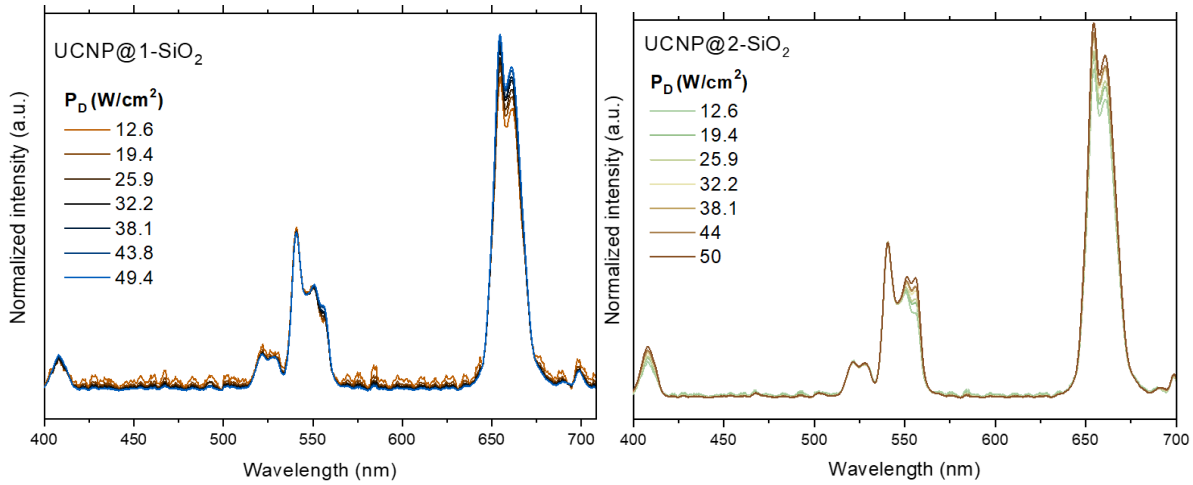

Figure B.2 *Power-dependent upconversion emission normalized relatively to green emission at 540 nm to highlight the evolution of the red emission at 656 nm and the bleu intruder emission at 555 nm as a function of P_D.*

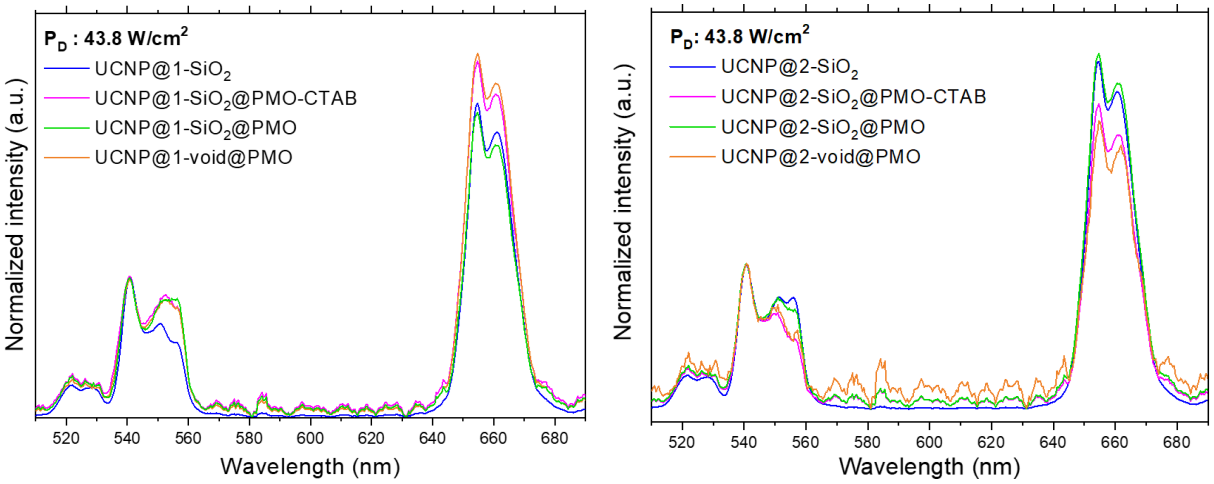

Figure B.3 *Upconversion emissions spectra of distinct nanoplatforms from each series of samples at fixed P_D, with normalized intensity relatively to green emission at 540 nm.*

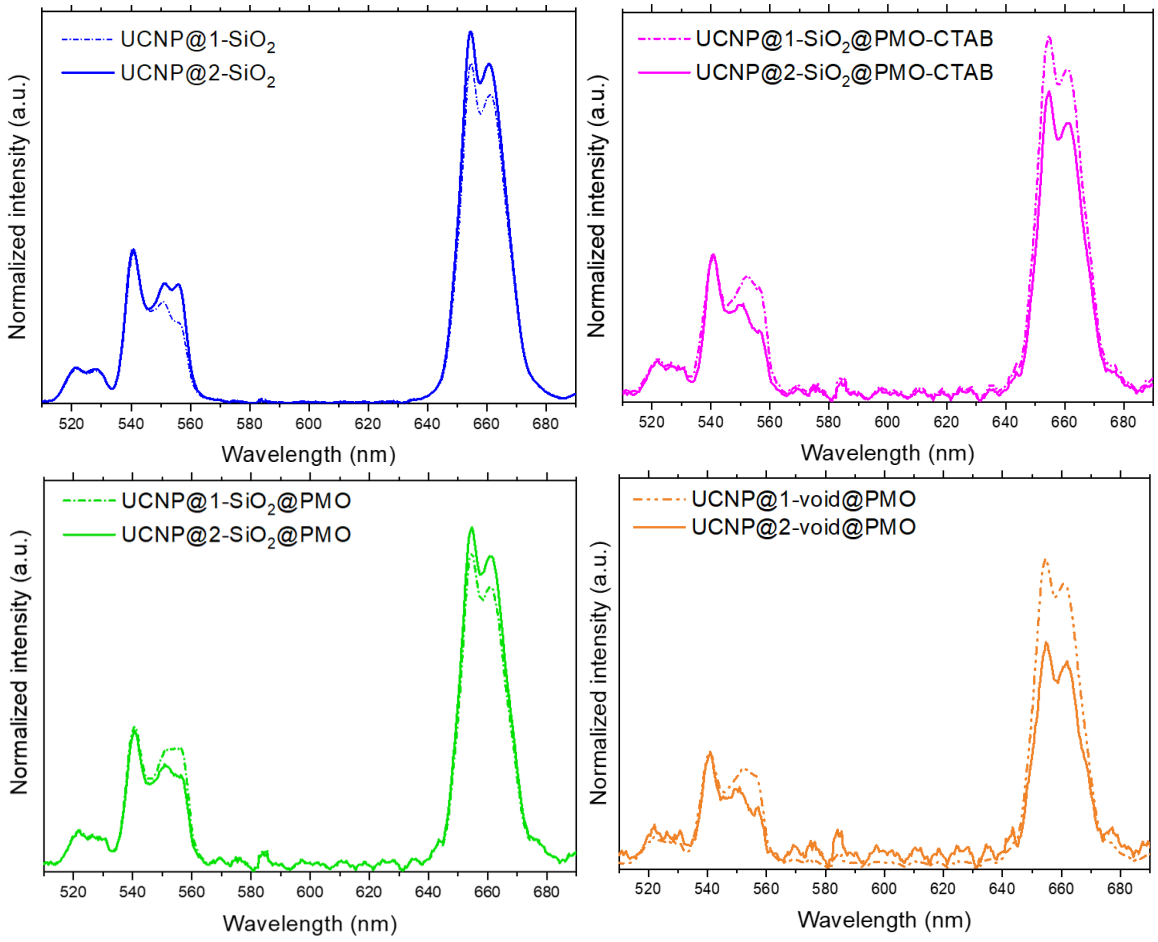

Figure B.4 *Comparison of upconversion emission spectra with normalized intensities of nanoplatforms from series 1 (dashed lined) and their counterparts from series 2 (solid lines).*

Decay profiles

Series 1

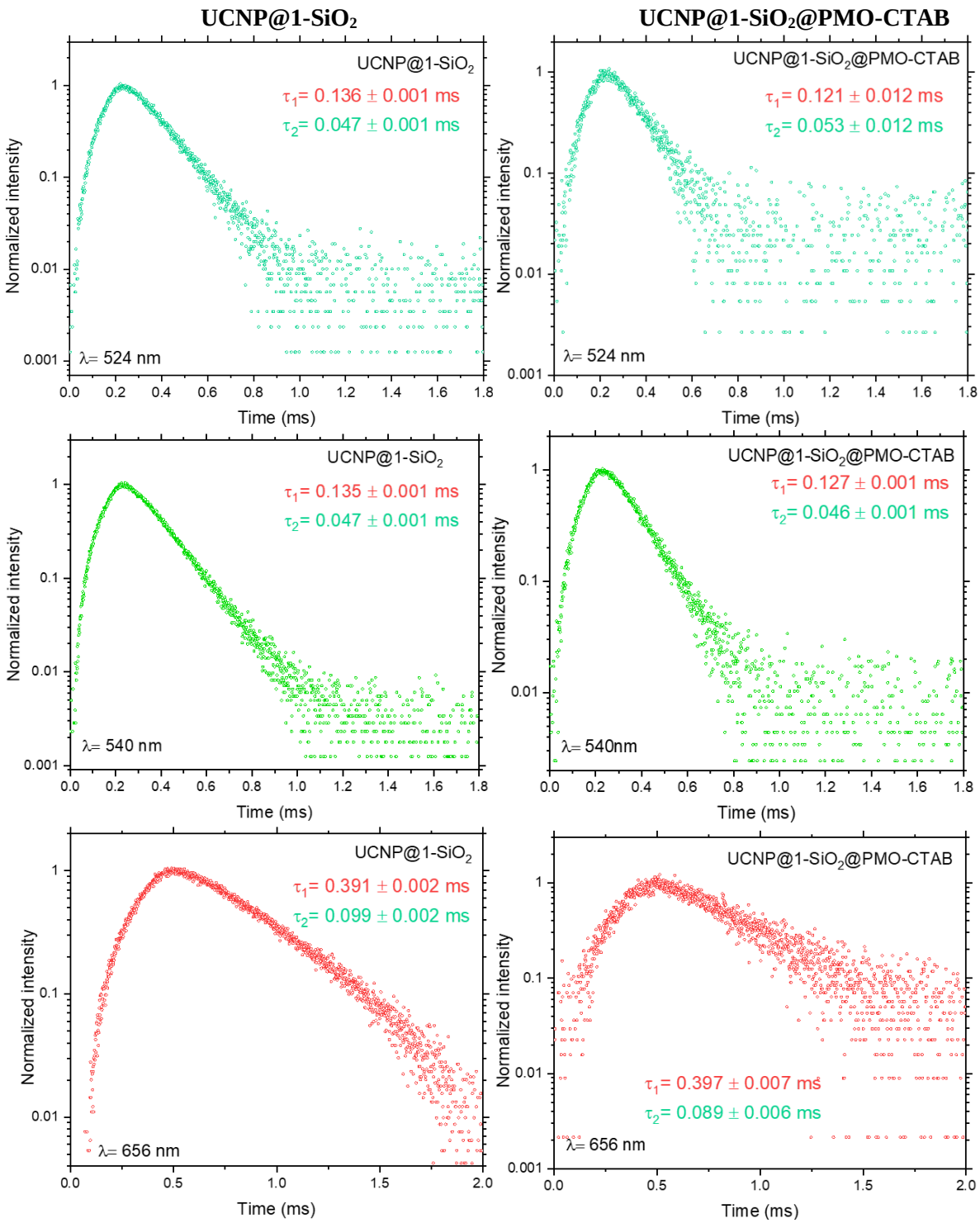

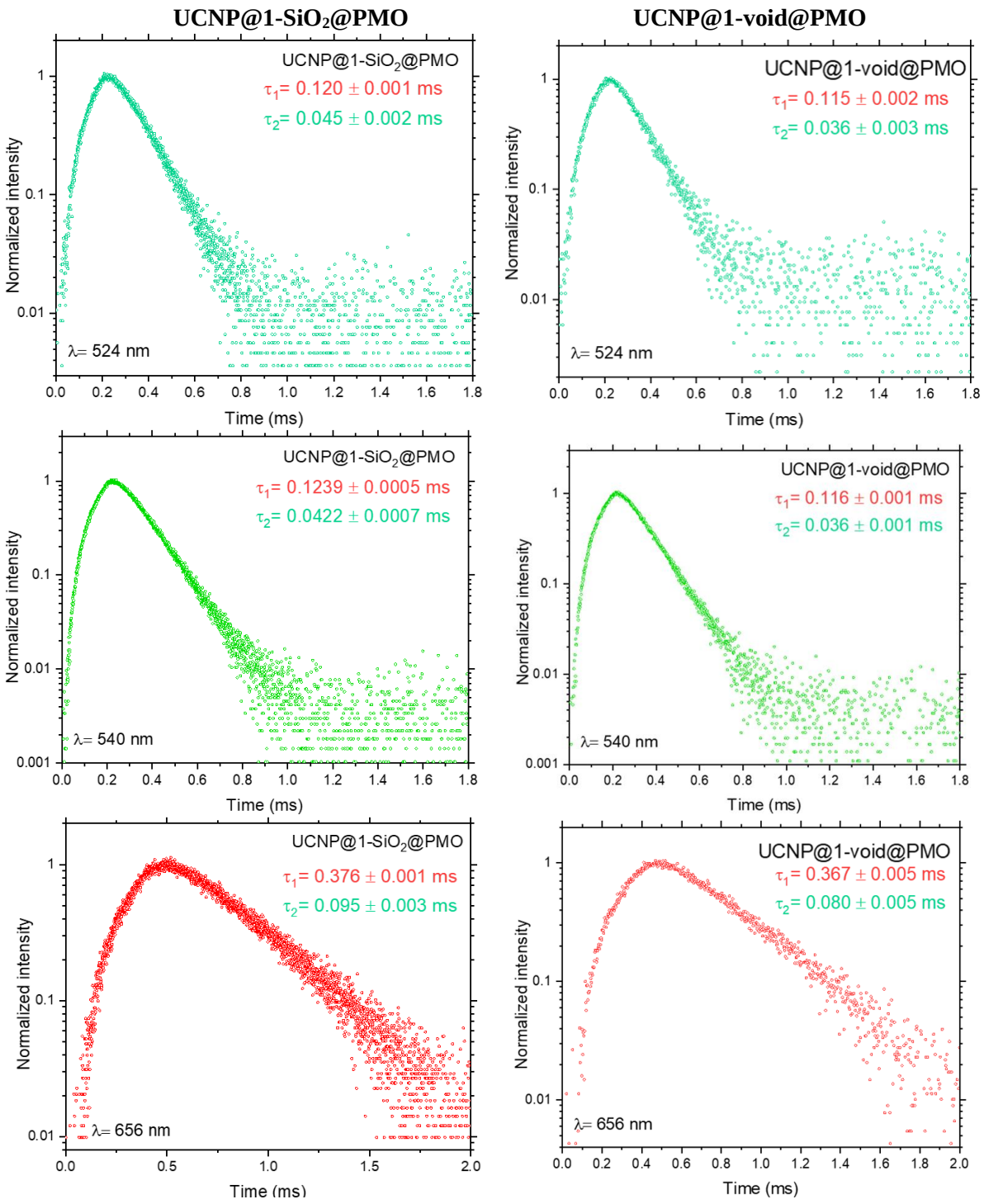
UCNP@1-SiO2@PMO
UCNP@1-void@PMO
UCNP@1-SiO2@PMO
τ1= 0.120 ± 0.001 ms
τ2= 0.045 ± 0.002 ms
λ= 524 nm
UCNP@1-void@PMO
τ1= 0.115 ± 0.002 ms
τ2= 0.036 ± 0.003 ms
λ= 524 nm
UCNP@1-SiO2@PMO
τ1= 0.1239 ± 0.0005 ms
τ2= 0.0422 ± 0.0007 ms
λ= 540 nm
UCNP@1-void@PMO
τ1= 0.116 ± 0.001 ms
τ2= 0.036 ± 0.001 ms
λ= 540 nm
UCNP@1-SiO2@PMO
τ1= 0.376 ± 0.001 ms
τ2= 0.095 ± 0.003 ms
λ= 656 nm
UCNP@1-void@PMO
τ1= 0.367 ± 0.005 ms
τ2= 0.080 ± 0.005 ms
λ= 656 nm
Normalized intensity
Time (ms)

Series 2

UCNP@2-SiO$_2$

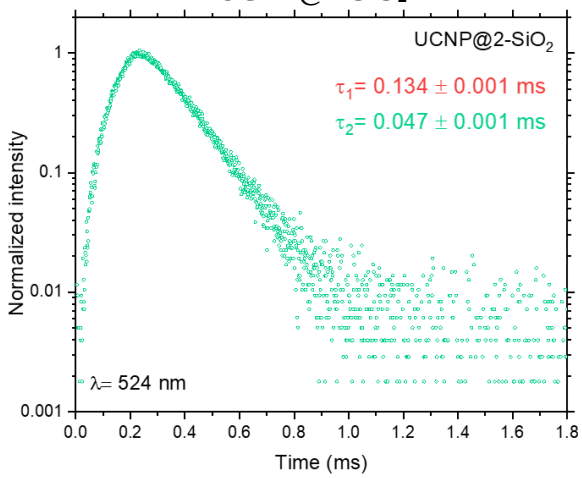

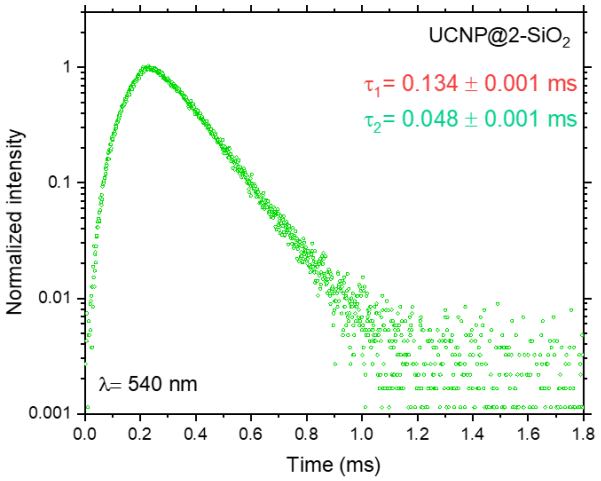

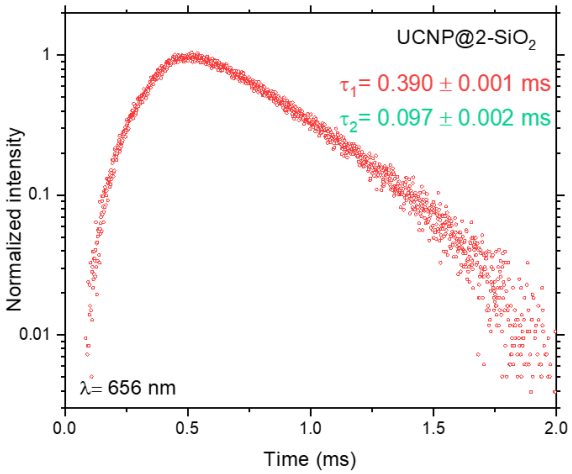

UCNP@2-SiO$_2$@PMO-CTAB

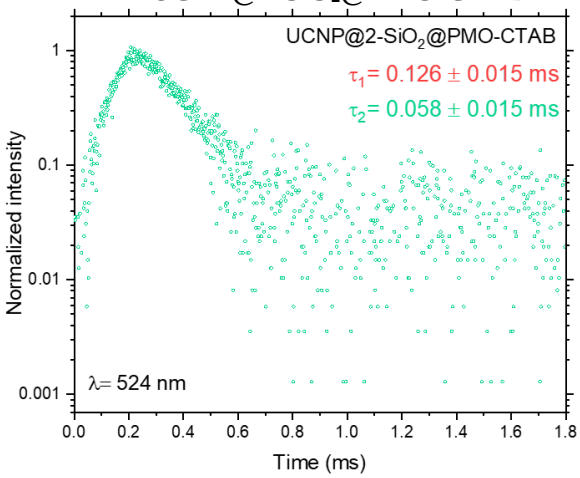

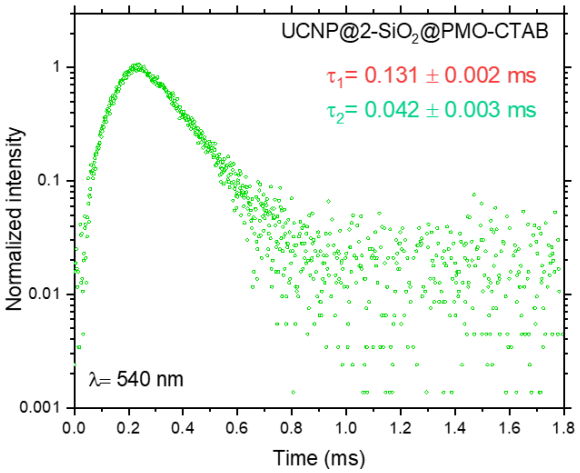

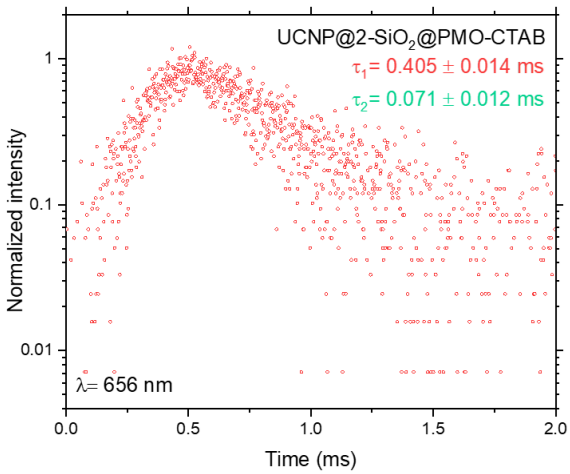

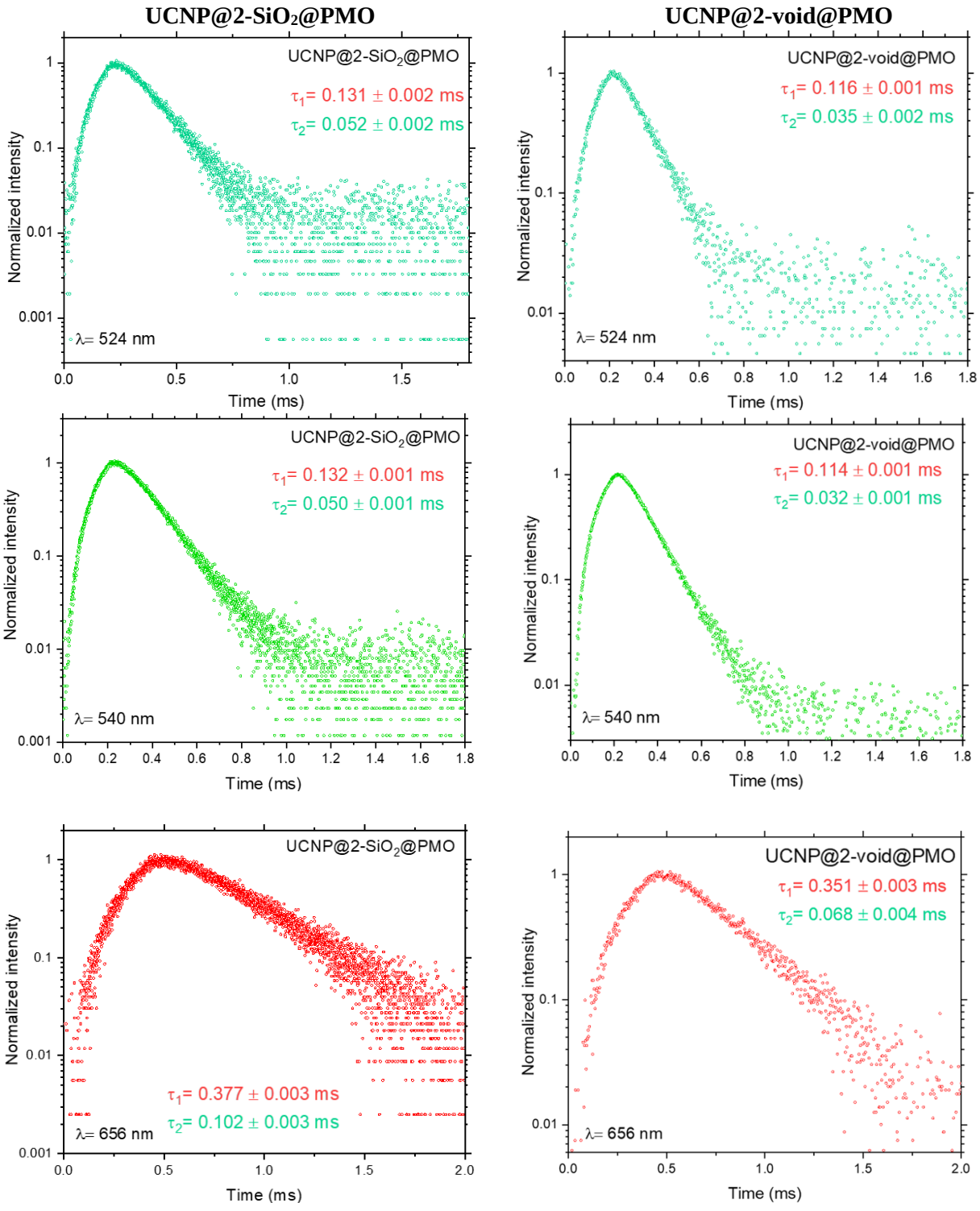

Figure B.5 *Decay profiles of all nanothermometer recorded at 524nm, 540 and 656 nm. The rise time and decay time are summarized in the* ***Table IV.3****.*

Determination of T_0

Series 1

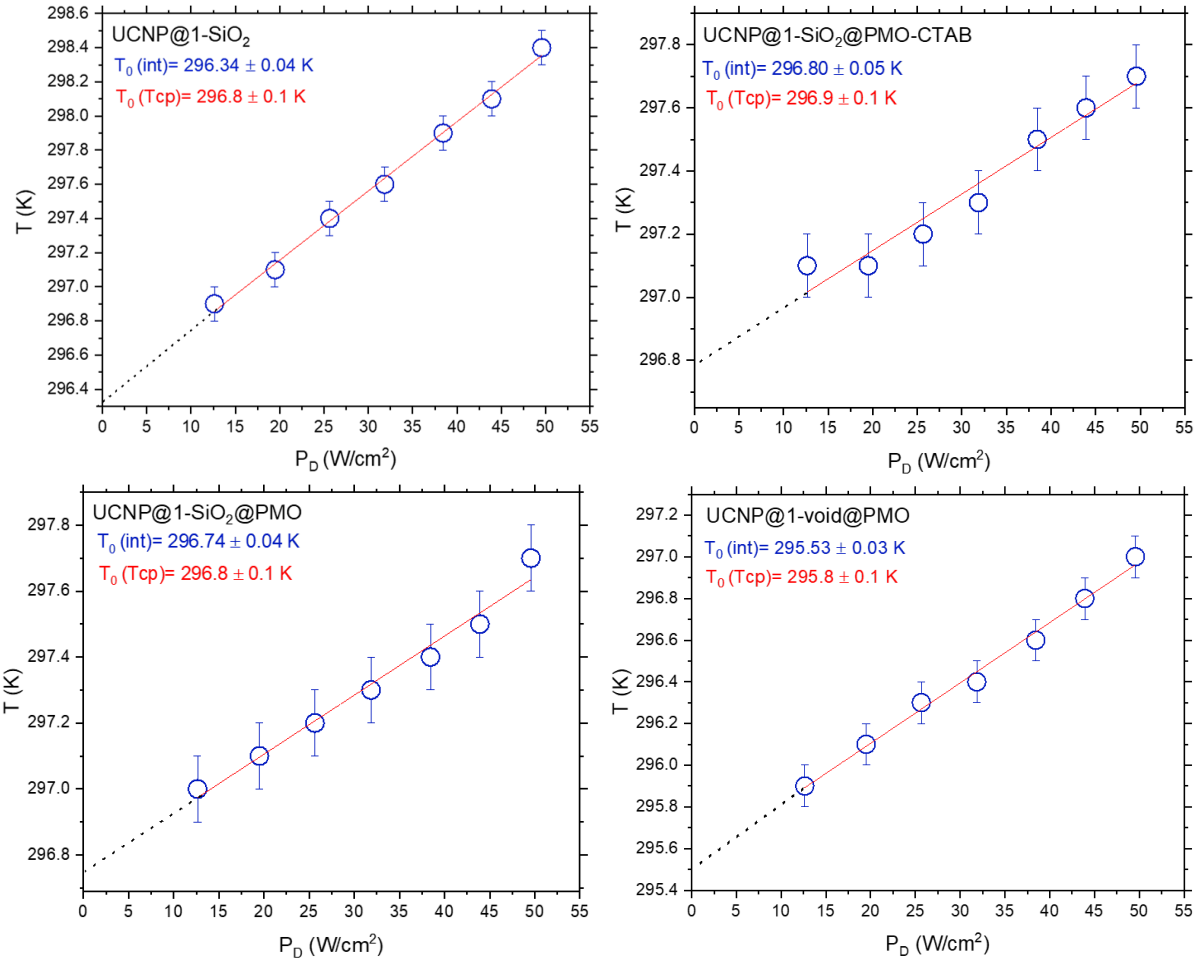

Series 2

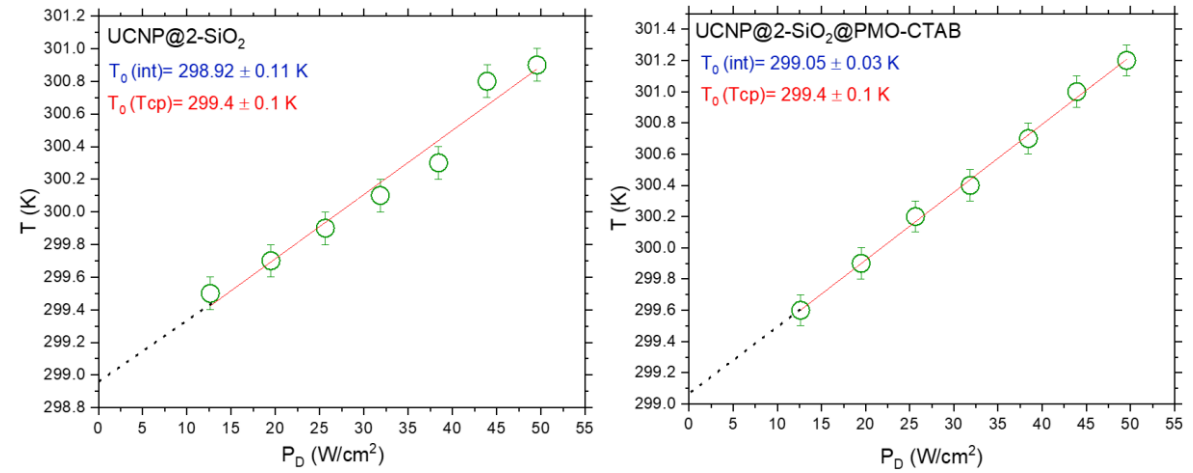

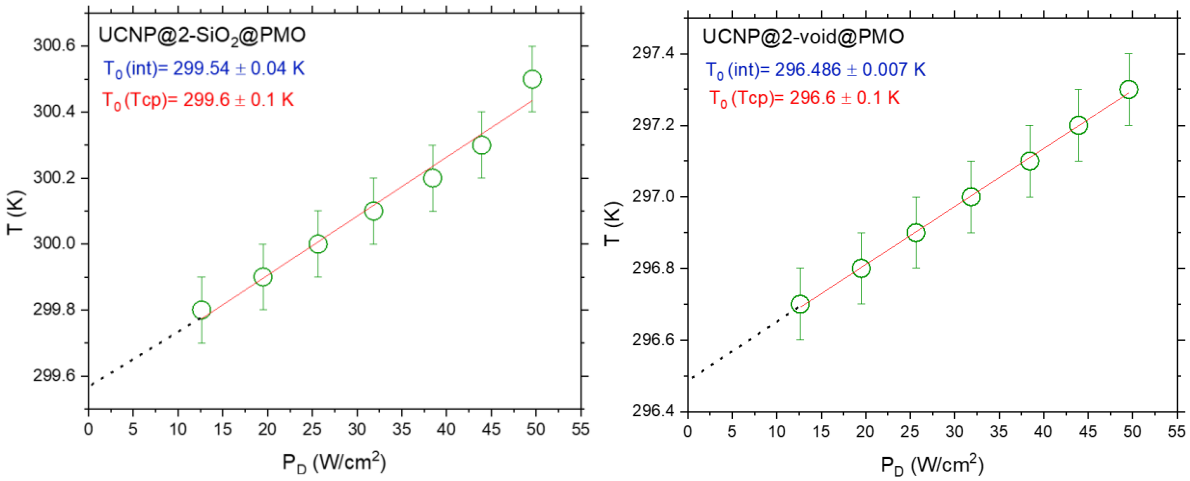

Figure B.6 *Plots of the induced temperature measured using the thermocouple T_0(Tcp) as a function of the corresponding P_D, the linear fit of the data points (blue for series 1 and green for series 2). T_0 (int) correspond to the calculated T_0 values obtained by extrapolation of the linear fit, and should be close to measured values T_0(Tcp).*

Analytical techniques

Microscopy

The Scanning Electron Microscopy (SEM) (**Chapter. II**) images were performed by **Said Tahir** in high vacuum and samples are observed at live mode with fast scanning time (1 to 3 s) using a FEI Inspect S50 tungsten filament SEM.

The Transmission Electron Microscopy (TEM) (**Chapter. II**, **III**) images were collected on a JEOL 1200 EX II operating at 120 kV prepared by deposition on a copper grid coated with carbon film. Images were recorded under the supervision of **Franck Godiard** (Université de Montpellier).

The High-Resolution Transmission Electron Microscopy (HRTEM) images (**Chapter. II**) were obtained using the TEM 2200 FS operated at 200 kV. The samples must be thin enough for the electron beam to pass through. The type of preparation depends on the nature of the samples, but in all cases the size of the sample is limited in thickness (20-100 nm) and surface area (max 500 µm x 500 µm). Large samples must be cut into ultrathin sections to be observed. For this, they are included in a resin (epoxy) to be able to be sectioned by the Leica EM UC7 ultramicrotome which allows semi-thin and ultrathin sections (70 nm) of samples to be prepared for TEM. HRTEM images were recorded by **Erwan Oliviero** (Université de Montpellier).

TEM images in **Figure III.24 (e,f,g,h)** were obtained using a Scanning Transmission Electron Microscope (STEM) Hitachi HD-2700, operating at 200 kV. The resolution of the crystal lattice reaches 0.144 nm under ideal conditions. Its illumination-lens system supports ultra-high-resolution image observation, high-resolution image observation combined with elemental analysis, as well as standard image observation and elemental mapping. The images in **Figure III.24 (g,h)** were obtained using the projector-lens modes that facilitate dark-field Z contrast. TEM images were recorded by **Ana Violeta Girão** (Universisade de Aveiro).

Small and wide-angle X-ray scattering (SAXS/WAXS)

The SAXS experiments (**Chapter. II**) were conducted by **Guillaume Toquer** (CEA, Marcoule) using a Guinier-Mering set-up coupled to a 2D image plate detector. The X-ray source was a molybdenum anode, delivering a high energy monochromatic beam (λ = 0.71 Å, E = 17.4 keV) and providing structural information over scattering vectors *q* ranging from 0.02 to 2.5 $Å^{-1}$. The region between the sample and the image plate was purged with flowing helium, to avoid air absorption. The data acquisition time was 3600 s and the glass capillaries used to hold the samples (Higenberg) had a thickness of 2 mm. The image azimuthal average was determined using FIT2D software from ESRF (France), and data corrections and radial averaging were performed via standard procedures.

The WAXS experiments (wide angle X-ray scattering) (**Chapter. III**) were performed by **Philippe Dieudonné** with an in-house setup of the Laboratoire Charles Coulomb, Université de Montpellier, France. A high brightness low power X-ray tube, coupled with aspheric multilayer optic (GeniX3D from Xenocs) is employed. It delivers an ultralow divergent beam (0.5 mrad, λ=0.15418 nm). Scatterless slits are used to give a clean 0.7 mm beam diameter with a flux of 35 Mphotons/s at the sample. The transmission configuration is used and scattered intensity are measured by a 2D "Pilatus" 300K pixel detector by Dectris (490*600 pixels) with pixel size of 172×172 $μm^2$, at a distance of 0.2 m from the sample for WAXS configuration. The image azimuthal average is determined using FIT2D software from ESRF (France). All Intensities I(*q*)=f(*q*) were corrected by transmission and the empty cell contribution was substracted.

Nitrogen sorption

Nitrogen sorption experiments (**Chapter. II**) were performed by **Philippe Trens** (Ecole Nationale Supérieure de Chimie de Montpellier). The adsorption isotherms of nitrogen are determined at 77.35 K by using a Micromeritics Tristar II surface area analyzer. All materials analyzed are treated thermally at 80 °C for 12 h under secondary vacuum (< 10^{-5} torr) before measurements were taken. The BET model is applied in the relative pressure range 0.05-0.30 to determine the equivalent specific surface areas of the different materials. The cross-sectional area of the nitrogen molecule is taken as 0.162 nm^2.

DFT calculations

DFT calculations (**Chapter. II**) were performed by **Patrick Hermet** (Institut Charles Gerhardt Montpellier). Calculation of the vibrational spectra are performed from density functional theory using SIESTA package. Perdew, Burke and Ernzerhof functional (belonging to the generalized gradient approximation) is used for the parameterization of the exchange-correlation term. Core electrons are replaced by non-local norm-conserving pseudopotentials (Troullier-Martins scheme). The valence electrons are described by a double-zeta singly polarized basis set. The localization of the basis is controlled by an energy shift of 50 ~ meV. Real space integration is performed on a regular grid corresponding to a plane-wave cutoff of 350 Ry. The dynamical matrix has been calculated at the harmonic level using finite difference (0.03 A) via the knowledge of Hellmann-Feynman forces. Born effective charges have been computed using the Berry phase technique.

Raman spectroscopy

Raman spectra in **Chapter. III** were obtained using The RENISHAW Invia Raman Spectrometer with a spectral range spanning from 100 to 4500 cm^{-1}. Its versatile modes include a confocal microscope for high-resolution imaging, enabling both transmission and backscattering optical microscopy. It is equipped with laser sources emitting at 532 nm, 633 nm, and 785 nm.

Zeta Potential

Zeta Potential experiments in **Chapter. III** was performed using Zetasizer Nano and folded capillary cells (DTS1070). DLS analysis was performed using the Zetasizer on NPs suspensions in ethanol. Data are processed in Malvern Zetasizer software.

UV-visible

Extinction spectra in **Chapter. IV** were obtained using The Cary 5000 UV-Visible absorption.

References

[1] M. L. Begasse, M. Leaver, F. Vazquez, S. W. Grill and A. A. Hyman, « Temperature dependence of cell division timing accounts for a shift in the thermal limits of C. elegans and C. briggsae », *Cell Reports*, vol. 10, n° 5, p. 647-653, **2015**, doi: 10.1016/j.celrep.2015.01.006.

[2] R. M. Daniel, M. J. Danson, R. Eisenthal, C. K. Lee and M. E. Peterson, « The effect of temperature on enzyme activity: new insights and their implications », *Extremophiles*, vol. 12, n° 1, p. 51-59, **2008**, doi: 10.1007/s00792-007-0089-7.

[3] R. Tanimoto, T Hiraiwa, Y Nakai, Y Shindo, K Oka, N Hiroi and A Funahash., « Detection of temperature difference in neuronal cells », *Sci Rep*, vol. 6, n° 1, p. 22071, **2016**, doi: 10.1038/srep22071.

[4] T. D. Vreugdenburg, C. D. Willis, L. Mundy and J. E. Hiller, « A systematic review of elastography, electrical impedance scanning, and digital infrared thermography for breast cancer screening and diagnosis », *Breast Cancer Res Treat*, vol. 137, n° 3, p. 665-676, **2013**, doi: 10.1007/s10549-012-2393-x.

[5] M. Monti, L. Brandt, J. Ikomi-Kumm and H. Olsson, « Microcalorimetric investigation of cell metabolism in tumour cells from patients with non-Hodgkin lymphoma (NHL) », *Scandinavian Journal of Haematology*, vol. 36, n° 4, p. 353-357, **2009**, doi: 10.1111/j.1600-0609. 1986.tb01749.x.

[6] C. D. S. Brites, PP Lima, NJO Silva, A Millán, VS Amaral, F Palacio and LD Carlos « Thermometry at the nanoscale », *Nanoscale*, vol. 4, n° 16, p. 4799, **2012**, doi: 10.1039/c2nr30663h.

[7] M. K. Barnett, « The development of thermometry and the temperature concept », *Osiris*, vol. 1, p. 269-341, **1956**, doi: 10.1086/368601

[8] F. S. Taylor, « The origin of the thermometer », *Annals of Science*, vol. 5, n° 2, p. 129-156, **1942**, doi: 10.1080/00033794200201401.

[9] W. F. Wright, « Early evolution of the thermometer and application to clinical medicine », *Journal of Thermal Biology*, vol. 56, p. 18-30, **2016**, doi: 10.1016/j.jtherbio.2015.12.003.

[10] E. Grodzinsky and M. Sund Levander, « History of the thermometer », in *Understanding Fever and Body Temperature*, **2020**, p. 23-35. doi: 10.1007/978-3-030-21886-7_3.

[11] P. S. Dobson, J. M. R. Weaver and G. Mills, « New methods for calibrated scanning thermal microscopy (SThM) », in *2007 IEEE Sensors*, **2007**, p. 708-711. doi: 10.1109/ICSENS.2007.4388498.

[12] K. Kim, W. Jeong, W. Lee and P. Reddy, « Ultra-high vacuum scanning thermal microscopy for nanometer resolution quantitative thermometry », *ACS Nano*, vol. 6, n° 5, p. 4248-4257, **2012**, doi: 10.1021/nn300774n.

[13] M. S. Watanabe, N. Kakuta, K. Mabuchi and Y. Yamada, « Micro-thermocouple probe for measurement of cellular thermal responses », in *2005 IEEE Engineering in Medicine and Biology 27th Annual Conference*, **2005**, p. 4858-4861. doi: 10.1109/IEMBS.2005.1615560.

[14] Y. Gao, Y. Bando, Z. Liu, D. Golberg and H. Nakanishi, « Temperature measurement using a gallium-filled carbon nanotube nanothermometer », *Appl. Phys. Lett.*, vol. 83, nº 14, p. 2913-2915, **2003**, doi: 10.1063/1.1616201.

[15] Y. Gao, Y. Bando, « Carbon nanothermometer containing gallium », *Nature*, vol. 415, nº 6872, p. 599-599, **2002**, doi: 10.1038/415599a.

[16] Y. B. Li, Y. Bando, D. Golberg and Z. W. Liu, « Ga-filled single-crystalline MgO nanotube: Wide-temperature range nanothermometer », *Appl. Phys. Lett.*, vol. 83, nº 5, p. 999-1001, **2003**, doi: 10.1063/1.1597422.

[17] M. Quintanilla and L. M. Liz-Marzán, « Guiding rules for selecting a nanothermometer », *NanoToday*, vol.19, p.126-145, **2018**, doi: 10.1016/j.nantod.2018.02.012.

[18] C. D. S. Brites, A. Millán and L. D. Carlos, « Lanthanides in luminescent thermometry », in *Handbook on the Physics and Chemistry of Rare Earths*, vol. 49, Elsevier, p. 339-427, **2016**, doi: 10.1016/bs.hpcre.2016.03.005.

[19] D. Jaque and F. Vetrone, « Luminescence nanothermometry », *Nanoscale*, vol. 4, nº 15, p. 4301, **2012**, doi: 10.1039/c2nr30764b.

[20] S. Sandell, E. Chávez-Ángel, A. El Sachat, J. He, C. M. Sotomayor Torres and J. Maire, « Thermoreflectance techniques and Raman thermometry for thermal property characterization of nanostructures », *Journal of Applied Physics*, vol. 128, nº 13, p. 131101, **2020**, doi: 10.1063/5.0020239.

[21] Kenneth E. Goodson and Mehdi Ashegh, « Near-field optical thermometry », *Microscale Thermophysical Engineering*, vol. 1, nº 3, p. 225-235, **1997**, doi: 10.1080/108939597200241.

[22] M. M. Ogle, A. D. Smith McWilliams, M. J. Ware, S. A. Curley, S. J. Corr and A. A. Martí, « Sensing Temperature in Vitro and in Cells Using a BODIPY Molecular Probe », *J. Phys. Chem. B*, vol. 123, nº 34, p. 7282-7289, **2019,** doi: 10.1021/acs.jpcb.9b04384.

[23] F. Vetrone, R Naccache, A Zamarrón, « Temperature sensing using fluorescent nanothermometers », *ACS Nano*, vol. 4, nº 6, p. 3254-3258, **2010**, doi: 10.1021/nn100244a.

[24] Z. Wang, X. He, T. Yong, Y. Miao, C. Zhang and B. Zhong Tang, « Multicolor tunable polymeric nanoparticle from the tetraphenylethylene cage for temperature sensing in living cells », *J. Am. Chem. Soc.*, vol. 142, nº 1, p. 512-519, **2020**, doi: 10.1021/jacs.9b11544.

[25] R. N. Lawson and M. S. Chughtai, « Breast Cancer and Body Temperature », *Canadian medical association journal*, **1963**.

[26] E. A. Repasky, S. S. Evans and M. W. Dewhirst, « Temperature matters! and why tt should matter to tumor immunologists », *Cancer Immunology Research*, vol. 1, n° 4, p. 210-216, **2013**, doi: 10.1158/2326-6066.CIR-13-0118.

[27] B. del Rosal, E. Ximendes, U. Rocha and D. Jaque, « In vivo luminescence nanothermometry: from materials to applications », *Advanced Optical Materials*, vol. 5, n° 1, p. 1600508, **2017**, doi: 10.1002/adom.201600508.

[28] A. A. Skaptsov, V. V. Goftman, V. V. Galushka, A. V. Markin, V. I. Kochubey and I. Y. Goryacheva, « Thermosensitivity of nanothermometer: CdSe/ZnS vs. $CuInS_2$/ZnS », présenté à Saratov Fall Meeting 2015, E. A. Genina, V. V. Tuchin, V. L. Derbov, D. E. Postnov, I. V. Meglinski, K. V. Larin, et A. B. Pravdin, Éd., Saratov, Russian Federation, **2016**, p. 991712. doi: 10.1117/12.2229842.

[29] C.-Y. Chen and C.-T. Chen, « A PNIPAM-based fluorescent nanothermometer with ratiometric readout », *Chem. Commun.*, vol. 47, n° 3, p. 994-996, **2011**, doi: 10.1039/C0CC04450D.

[30] C. Mi, J. Zhou, F. Wang, G. Lin and D. Jin, « Ultrasensitive Ratiometric Nanothermometer with Large Dynamic Range and Photostability », *Chem. Mater.*, vol. 31, n° 22, p. 9480-9487, **2019**, doi: 10.1021/acs.chemmater.9b03466.

[31] S. Parola, B. Julián-López, L. D. Carlos and C. Sanchez, « Optical properties of hybrid organic-inorganic materials and their applications », *Adv. Funct. Mater.*, vol. 26, n° 36, p. 6506-6544, **2016**, doi: 10.1002/adfm.201602730.

[32] X. Zhu, Q. Su, W. Feng and F. Li, « Anti-Stokes shift luminescent materials for bio-applications », *Chem. Soc. Rev.*, vol. 46, n° 4, p. 1025-1039, **2017**, doi: 10.1039/C6CS00415F.

[33] K.-L. Wong, J.-C. G. Bünzli and P. A. Tanner, « Quantum yield and brightness », *Journal of Luminescence*, vol.224, p.117256, **2020**, doi: 10.1016/j.jlumin.2020.117256.

[34] T. Jiang, H. Wang, M. Xing, Y. Fu, Y. Peng and X. Luo, « Luminescence decay evaluation of long-afterglow phosphors », *Physica B: Condensed Matter*, vol. 450, p. 94-98, 2**014**, doi: 10.1016/j.physb.2014.04.080.

[35] X. Fu, Shuai Fu, Qi Lu, Jing Zhang, Pingping Wan, Jinliang Liu, Yong Zhang, Chia-Hung Chen, Wei Li, Huadong Wang and Qingsong Mei, « Excitation energy mediated cross-relaxation for tunable upconversion luminescence from a single lanthanide ion », *Nat Commun*, vol. 13, n° 1, p. 4741, **2022**, doi: 10.1038/s41467-022-32498-4.

[36] J. Zhou, Q. Liu, W. Feng, Y. Sun and F. Li, « Upconversion luminescent materials: advances and applications », *Chem. Rev.*, vol. 115, n° 1, p. 395-465, **2015**, doi: 10.1021/cr400478f.

[37] F. T. Rabouw, P. T. Prins, P. Villanueva-Delgado, M. Castelijns, R. G. Geitenbeek and A. Meijerink, « Quenching pathways in $NaYF_4$: Er^{3+}, Yb^{3+} upconversion nanocrystals », *ACS Nano*, vol. 12, n° 5, p. 4812-4823, **2018**, doi: 10.1021/acsnano.8b01545.

[38] J. Liu, H. Zhang, G. S. Selopal, S. Sun, H. Zhao and F. Rosei, « Visible and near-infrared, multiparametric, ultrasensitive nanothermometer based on dual-emission colloidal quantum dots », *ACS Photonics*, vol. 6, nº 10, p. 2479-2486, **2019**, doi: 10.1021/acsphotonics.9b00763.

[39] A. Ćirić and M. D. Dramićanin, « LumTHools - Software for fitting the temperature dependence of luminescence emission intensity, lifetime, bandshift, and bandwidth and luminescence thermometry and review of the theoretical models », *Journal of Luminescence*, vol. 252, p. 119413, **2022**, doi: 10.1016/j.jlumin.2022.119413.

[40] A. Kawski, « Fluorescence anisotropy: Theory and applications of rotational depolarization », *Critical Reviews in Analytical Chemistry*, Pages 459-529, **2006**, doi: 10.1080/10408349308051654.

[41] B. M. Walsh, « Judd-Ofelt theory: Principles and practices », in *Advances in Spectroscopy for Lasers and Sensing*, p. 403-433, **2006**, doi: 10.1007/1-4020-4789-4_21.

[42] P. S. Peijzel, A. Meijerink, R. T. Wegh, M. F. Reid and G. W. Burdick, « A complete energy level diagram for all trivalent lanthanide ions », *Journal of Solid-State Chemistry*, vol. 178, nº 2, p. 448-453, **2005**, doi: 10.1016/j.jssc.2004.07.046.

[43] Q. Tian, W. Yao, W. Wu and C. Jiang, « NIR light-activated upconversion semiconductor photocatalysts », *Nanoscale Horiz.*, vol. 4, nº 1, p. 10-25, **2019**, doi: 10.1039/C8NH00154E.

[44] S. V. Eliseeva and J.-C. G. Bünzli, « Lanthanide luminescence for functional materials and bio-sciences », *Chem. Soc. Rev.*, vol. 39, nº 1, p. 189-227, **2010**, doi: 10.1039/B905604C.

[45] A. Nadort, J. Zhao and E. M. Goldys, « Lanthanide upconversion luminescence at the nanoscale: fundamentals and optical properties », *Nanoscale*, vol. 8, nº 27, p. 13099-13130, **2016**, doi: 10.1039/C5NR08477F.

[46] L. Labrador-Páez, M. Pedroni, A. Speghini, J. García-Solé, P. Haro-González and D. Jaque, « Reliability of rare-earth-doped infrared luminescent nanothermometers », *Nanoscale*, vol. 10, nº 47, p. 22319-22328, **2018**, doi: 10.1039/C8NR07566B.

[47] C. D. S. Brites, S. Balabhadra and L. D. Carlos, « Lanthanide-based thermometers: At the cutting-edge of luminescence thermometry », *Advanced Optical Materials*, vol. 7, nº 5, p. 1801239, **2019**, doi: 10.1002/adom.201801239.

[48] F. Wang and X. Liu, « Recent advances in the chemistry of lanthanide-doped upconversion nanocrystals », *Chem. Soc. Rev.*, vol. 38, nº 4, p. 976, **2009**, doi: 10.1039/b809132n.

[49] C. Renero-Lecuna, R. Martín-Rodríguez, R. Valiente, J. González, F. Rodríguez, K. W. Krämer and H. U. Güdel., « Origin of the high upconversion green luminescence efficiency in β-$NaYF_4$:2%Er^{3+} ,20%Yb^{3+} », *Chem. Mater.*, vol. 23, nº 15, p. 3442-3448, **2011**, doi: 10.1021/cm2004227.

[50] J. F. Suyver, J. Grimm, M. K. Van Veen, D. Biner, K. W. Krämer and H. U. Güdel, « Upconversion spectroscopy and properties of $NaYF_4$ doped with Er^{3+}, Tm^{3+} and/or Yb^{3+} », *Journal of Luminescence*, vol. 117, nº 1, p. 1-12, **2006**, doi: 10.1016/j.jlumin.2005.03.011.

[51] J. F. Suyver, J. Grimm, K. W. Krämer and H. U. Güdel, « Highly efficient near-infrared to visible up-conversion process in $NaYF_4$: Er^{3+}, Yb^{3+} », *Journal of Luminescence*, vol. 114, nº 1, p. 53-59, **2005**, doi: 10.1016/j.jlumin.2004.11.012.

[52] H.-X. Mai, Y.-W. Zhang, L.-D. Sun and C.-H. Yan, « Highly efficient multicolor up-conversion emissions and their mechanisms of monodisperse $NaYF_4$: Yb, Er core and core/shell-structured nanocrystals », *J. Phys. Chem. C*, vol. 111, nº 37, p. 13721-13729, **2007**, doi: 10.1021/jp073920d.

[53] E. Harju, I. Hyppänen, J. Hölsä, J. Kankare, M. Lahtinen, M. Lastusaari, L. Pihlgren and T. Soukka « Polymorphism of $NaYF_4$: Yb^{3+}, Er^{3+} up-conversion luminescence materials », in *European Powder Diffraction Conference*, p. 381-388, **2010**, doi: 10.1524/9783486991321-063.

[54] Q. Dou and Y. Zhang, « Tuning of the structure and emission spectra of upconversion nanocrystals by alkali ion doping », *Langmuir*, vol. 27, nº 21, p. 13236-13241, **2011**, doi: 10.1021/la201910t.

[55] D. Tu, Y. Liu, H. Zhu, R. Li, L. Liu and X. Chen, « Breakdown of crystallographic site symmetry in lanthanide-doped $NaYF_4$ crystals », *Angew. Chem.*, vol. 125, nº 4, p. 1166-1171, **2013**, doi: 10.1002/ange.201208218.

[56] K. W. Krämer, D. Biner, G. Frei, H. U. Güdel, M. P. Hehlen and S. R. Lüthi, « Hexagonal sodium yttrium fluoride based green and blue emitting upconversion phosphors », *Chem. Mater.*, vol. 16, nº 7, p. 1244-1251, **2004**, doi: 10.1021/cm031124o.

[57] B. Szefczyk, R. Roszak and S. Roszak, « Structure of the hexagonal NaYF4 phase from first-principles molecular dynamics », *RSC Adv.*, vol. 4, nº 43, p. 22526, **2014**, doi: 10.1039/c4ra00211c.

[58] F. Wang, Y Han, C.S Lim, Y. Lu, J. Wang, J. Xu, H. Chen, C. Zhang, M. Hong and X. Liu, « Simultaneous phase and size control of upconversion nanocrystals through lanthanide doping », *Nature*, vol. 463, nº 7284, p. 1061-1065, **2010**, doi: 10.1038/nature08777.

[59] F. Wang and X. Liu, « Multicolor tuning of lanthanide-doped nanoparticles by single wavelength excitation », *Acc. Chem. Res.*, vol. 47, nº 4, p. 1378-1385, **2014**, doi: 10.1021/ar5000067.

[60] F. Wang, J. Wang and X. Liu, « Direct evidence of a surface quenching effect on size-dependent luminescence of upconversion nanoparticles », *Angewandte Chemie*, vol. 122, nº 41, p. 7618-7622, **2010**, doi: 10.1002/ange.201003959.

[61] M. D. Wisser, M. Chea, Y. Lin, Di M. Wu, W. L. Mao, A. Salleo, and J. A. Dionne, « Strain-induced modification of optical selection rules in lanthanide-based upconverting nanoparticles », *Nano Lett.*, vol. 15, nº 3, p. 1891-1897, **2015**, doi: 10.1021/nl504738k.

[62] J. Hao, Y. Zhang and X. Wei, « Electric-induced enhancement and modulation of upconversion photoluminescence in epitaxial $BaTiO_3$: Yb/Er thin films », *Angew. Chem. Int. Ed.*, vol. 50, nº 30, p. 6876-6880, **2011**, doi: 10.1002/anie.201101374.

[63] D. T. Klier and M. U. Kumke, « Analysing the effect of the crystal structure on upconversion luminescence in Yb^{3+}, Er^{3+} -co-doped $NaYF_4$ nanomaterials », *J. Mater. Chem. C*, vol. 3, nº 42, p. 11228-11238, **2015**, doi: 10.1039/C5TC02218E.

[64] M. Eichelbaum and K. Rademann, « Plasmonic enhancement or energy transfer? On the luminescence of gold-, silver-, and lanthanide-doped silicate glasses and its potential for light-emitting devices », *Adv. Funct. Mater.*, vol. 19, nº 13, p. 2045-2052, **2009**, doi: 10.1002/adfm.200801892.

[65] M. Runowski, S. Goderski, J. Paczesny, M. Księżopolska-Gocalska, A. Ekner-Grzyb, T. Grzyb, J. D. Rybka, M. Giersig, and S. Lis, « Preparation of biocompatible, luminescent-plasmonic core/shell nanomaterials based on lanthanide and gold nanoparticles exhibiting SERS effects », *J. Phys. Chem. C*, vol. 120, nº 41, p. 23788-23798, **2016**, doi: 10.1021/acs.jpcc.6b06644.

[66] M. Saboktakin, X. Ye, U. K. Chettiar, N. Engheta, C. B. Murray and C. R. Kagan, « Plasmonic enhancement of nanophosphor upconversion luminescence in Au nanohole arrays », *ACS Nano*, vol. 7, nº 8, p. 7186-7192, **2013**, doi: 10.1021/nn402598e.

[67] W. Zhang, F. Ding and S. Y. Chou, « Large enhancement of upconversion luminescence of $NaYF_4$:Yb^{3+}/Er^{3+} nanocrystal by 3D plasmonic nano-antennas », *Adv. Mater.*, vol. 24, nº 35, p. OP236-OP241, **2012**, doi: 10.1002/adma.201200220.

[68] M. Quintanilla, M. Henriksen-Lacey, C. Renero-Lecuna and L. M. Liz-Marzán, « Challenges for optical nanothermometry in biological environments », *Chem. Soc. Rev.*, vol. 51, nº 11, p. 4223-4242, **2022**, doi: 10.1039/D2CS00069E.

[69] A. Nexha, J. J. Carvajal, M. C. Pujol, F. Díaz and M. Aguiló, « Lanthanide doped luminescence nanothermometers in the biological windows: strategies and applications », *Nanoscale*, vol. 13, nº 17, p. 7913-7987, **2021**, doi: 10.1039/D0NR09150B.

[70] L.-D. Sun, Y.-F. Wang and C.-H. Yan, « Paradigms and challenges for bioapplication of rare earth upconversion luminescent nanoparticles: small size and tunable emission/excitation spectra », *Acc. Chem. Res.*, vol. 47, nº 4, p. 1001-1009, **2014**, doi: 10.1021/ar400218t.

[71] A. Skripka, A. Benayas, R. Marin, P. Canton, E. Hemmer and F. Vetrone, « Double rare-earth nanothermometer in aqueous media: opening the third optical transparency window to temperature sensing », *Nanoscale*, vol. 9, nº 9, p. 3079-3085, **2017**, doi: 10.1039/C6NR08472A.

[72] A. Bednarkiewicz, L. Marciniak, L. D. Carlos and D. Jaque, « Standardizing luminescence nanothermometry for biomedical applications », *Nanoscale*, vol. 12, nº 27, p. 14405-14421, **2020**, doi: 10.1039/D0NR03568H.

[73] D. Pominova, V. Proydakova, I. Romanishkin, A. Ryabova, S. Kuznetsov, O. Uvarov, P. Fedorov and V. Loschenov, « Temperature sensing in the short-wave infrared spectral region using core-shell $NaGdF_4$: Yb^{3+}, Ho^{3+}, Er^{3+}@$NaYF_4$ nanothermometers », *Nanomaterials*, vol. 10, nº 10, p. 1992, **2020**, doi: 10.3390/nano10101992.

[74] S. Balabhadra, M. L. Debasu, C. D. S. Brites, R. A. S. Ferreira and L. D. Carlos, « Upconverting nanoparticles working as primary thermometers in different media », *J. Phys. Chem. C*, vol. 121, nº 25, p. 13962-13968, 2**017**, doi: 10.1021/acs.jpcc.7b04827.

[75] T. Asefa and Z. Tao, « Biocompatibility of mesoporous silica nanoparticles », *Chem. Res. Toxicol.*, vol. 25, nº 11, p. 2265-2284, **2012**, doi: 10.1021/tx300166u.

[76] S. Zhang, H. Gao and G. Bao, « Physical principles of nanoparticle cellular endocytosis », *ACS Nano*, vol. 9, nº 9, p. 8655-8671, **2015**, doi: 10.1021/acsnano.5b03184.

[77] A. M. E. Abdalla, L. Xiao, M. W. Ullah, M. Yu, C. Ouyang and G. Yang, « Current challenges of cancer anti-angiogenic therapy and the promise of nanotherapeutics », *Theranostics*, vol. 8, nº 2, p. 533-548, 2**018**, doi: 10.7150/thno.21674.

[78] Y. Gu, R. Piñol, R. Piñol, R. Moreno-Loshuertos, C. D. S. Brites, J. Zeler, A. Martínez, G. Maurin-Pasturel, P. Fernández-Silva, J. Marco-Brualla, P. Téllez, R. Cases, R. Navarro Belsué, D. Bonvin, L. D. Carlos and A. Millán, « Local temperature increments and induced cell death in intracellular magnetic hyperthermia », *ACS Nano*, vol. 17, nº 7, p. 6822-6832, **2023**, doi: 10.1021/acsnano.3c00388.

[79] X. Ma, J. Zhang, M. Dang, J. Wang, Z. Tu, L. Yuwen, G. Chen, X. Su and Z. Teng, « Hollow periodic mesoporous organosilica nanospheres by a facile emulsion approach », *Journal of Colloid and Interface Science*, vol. 475, p. 66-71, **2016**, doi: 10.1016/j.jcis.2016.04.026.

[80] J. Liu, S. B. Hartono, Y. G. Jin, Z. Li, G. Q. (Max) Lu and S. Z. Qiao, « A facile vesicle template route to multi-shelled mesoporous silica hollow nanospheres », *J. Mater. Chem.*, vol. 20, nº 22, p. 4595, **2010**, doi: 10.1039/b925201k.

[81] S. Z. Qiao, C. X. Lin, Y. Jin, Z Li, Z. Yan, Z. Hao, Y. Huang, and G. Q. (Max) Lu, « Surface-functionalized periodic mesoporous organosilica hollow spheres », *J. Phys. Chem. C*, vol. 113, nº 20, p. 8673-8682, **2009**, doi: 10.1021/jp810844p.

[82] H. Blas, M. Save, P. Pasetto, C. Boissière, C. Sanchez and B. Charleux, « Elaboration of monodisperse spherical hollow particles with ordered mesoporous silica shells via dual latex/surfactant templating: radial orientation of mesopore channels », *Langmuir*, vol. 24, nº 22, p. 13132-13137, **2008**, doi: 10.1021/la801897k.

[83] O. W. Flörke, H. A. Graetsch and F. Brunk, « Silica », in *Ullmann's Encyclopedia of Industrial Chemistry*, **2008,** doi: 10.1002/14356007.a23_583.pub3.

[84] M. Hildebrand, « Diatoms, biomineralization processes, and genomics », *Chem. Rev.*, vol. 108, n° 11, p. 4855-4874, **2008**, doi: 10.1021/cr078253z.

[85] N. Nassif and J. Livage, « From diatoms to silica-based biohybrids », *Chem. Soc. Rev.*, vol. 40, n° 2, p. 849-859, **2011**, doi: 10.1039/C0CS00122H.

[86] M. Faustini, L. Nicole, E. Ruiz-Hitzky and C. Sanchez, « History of organic-inorganic hybrid materials: prehistory, art, science, and advanced applications », *Adv. Funct. Mater.*, vol. 28, n° 27, p. 1704158, **2018**, doi: 10.1002/adfm.201704158.

[87] R. Ciriminna, A. Fidalgo, V. Pandarus, F. Béland, L. M. Ilharco and M. Pagliaro, « The sol–gel route to advanced silica-based materials and recent applications », *Chem. Rev.*, vol. 113, n° 8, p. 6592-6620, **2013**, doi: 10.1021/cr300399c.

[88] T. Graham, « XXXV. —On the properties of silicic acid and other analogous colloidal substances », *J. Chem. Soc.*, vol. 17, n° 0, p. 318-327, **1864**, doi: 10.1039/JS8641700318.

[89] H. Dislich and P. Hinz, « History and principles of the sol-gel process, and some new multicomponent oxide coatings », *Journal of Non-Crystalline Solids*, vol. 48, n° 1, p. 11-16, **1982**, doi: 10.1016/0022-3093(82)90242-3.

[90] C. Jeffrey Brinker and George W. Scherer, *The Physics and Chemistry of Sol–Gel Processing*, **1990**, doi: 10.1016/C2009-0-22386-5.

[91] C. J. Brinker, « Hydrolysis and condensation of silicates: Effects on structure », *Journal of Non-Crystalline Solids*, vol. 100, n° 1-3, p. 31-50, **1988**, doi: 10.1016/0022-3093(88)90005-1.

[92] R. J. P. Corriu and D. Leclercq, « Recent developments of molecular chemistry for sol–gel processes », *Angew. Chem. Int. Ed. Engl.*, vol. 35, n° 13-14, p. 1420-1436, **1996**, doi: 10.1002/anie.199614201.

[93] W. Stöber, A. Fink and E. Bohn, « Controlled growth of monodisperse silica spheres in the micron size range », *Journal of Colloid and Interface Science*, vol. 26, n° 1, p. 62-69, **1968**, doi: 10.1016/0021-9797(68)90272-5.

[94] G. H. Bogush, M. A. Tracy and C. F. Zukoski, « Preparation of monodisperse silica particles: Control of size and mass fraction », *Journal of Non-Crystalline Solids*, vol. 104, n° 1, p. 95-106, **1988**, doi: 10.1016/0022-3093(88)90187-1.

[95] G. H. Bogush and C. F. Zukoski, « Studies of the kinetics of the precipitation of uniform silica particles through the hydrolysis and condensation of silicon alkoxides », *Journal of Colloid and Interface Science*, vol. 142, n° 1, p. 1-18, **1991**, doi: 10.1016/0021-9797(91)90029-8.

[96] G. H. Bogush and C. F. Zukoski, « Uniform silica particle precipitation: An aggregative growth model », *Journal of Colloid and Interface Science*, vol. 142, n° 1, p. 19-34, **1991**, doi: 10.1016/0021-9797(91)90030-C.

[97] S.-L. Chen, P. Dong, G.-H. Yang and J.-J. Yang, « Kinetics of formation of monodisperse colloidal silica particles through the hydrolysis and condensation of tetraethylorthosilicate », *Ind. Eng. Chem. Res.*, vol. 35, n° 12, p. 4487-4493, **1996**, doi: 10.1021/ie9602217.

[98] D. J. Tobler, S. Shaw and L. G. Benning, « Quantification of initial steps of nucleation and growth of silica nanoparticles: An in-situ SAXS and DLS study », *Geochimica et Cosmochimica Acta*, vol. 73, n° 18, p. 5377-5393, **2009**, doi: 10.1016/j.gca.2009.06.002.

[99] T. Matsoukas and E. Gulari, « Dynamics of growth of silica particles from ammonia-catalyzed hydrolysis of tetra-ethyl-orthosilicate », *Journal of Colloid and Interface Science*, vol. 124, n° 1, p. 252-261, **1988**, doi: 10.1016/0021-9797(88)90346-3.

[100] T. Matsoukas and E. Gulari, « Monomer-addition growth with a slow initiation step: A growth model for silica particles from alkoxides », *Journal of Colloid and Interface Science*, vol. 132, n° 1, p. 13-21, **1989**, doi: 10.1016/0021-9797(89)90210-5.

[101] V. K. LaMer and R. H. Dinegar, « Theory, production and mechanism of formation of monodispersed hydrosols », *J. Am. Chem. Soc.*, vol. 72, n° 11, p. 4847-4854, **1950**, doi: 10.1021/ja01167a001.

[102] I. A. M. Ibrahim, A. A. F. Zikry and M. A. Sharaf, « Preparation of spherical silica nanoparticles: Stober silica », *J. Am. Sci*, p. 5, **2010**.

[103] K. S. Rao, K. El-Hami, T. Kodaki, K. Matsushige and K. Makino, « A novel method for synthesis of silica nanoparticles », *Journal of Colloid and Interface Science*, vol. 289, n° 1, p. 125-131, **2005**, doi: 10.1016/j.jcis.2005.02.019.

[104] S. K. Park, K. D. Kim and H. T. Kim, « Preparation of silica nanoparticles: determination of the optimal synthesis conditions for small and uniform particles », *Colloids and Surfaces A: Physicochemical and Engineering Aspects*, vol. 197, n° 1-3, p. 7-17, **2002**, doi: 10.1016/S0927-7757(01)00683-5.

[105] H. Schmidt, « New type of non-crystalline solids between inorganic and organic materials », *Journal of Non-Crystalline Solids*, vol. 73, n° 1-3, p. 681-691, **1985**, doi: 10.1016/0022-3093(85)90388-6.

[106] T. Miyanaga and N. Naga, « Synthesis and properties of organic-inorganic hybrid porous polymers obtained with click addition reactions of thiol-functionalized random type silsesquioxane by a diacrylate or diisocyanate compounds », *OJPChem*, vol. 10, n° 01, p. 1-20, **2020**, doi: 10.4236/ojpchem.2020.101001.

[107] J. G. Croissant, X. Cattoën, J.-O. Durand, M. Wong Chi Man and N. M. Khashab, « Organosilica hybrid nanomaterials with a high organic content: syntheses and applications of silsesquioxanes », *Nanoscale*, vol. 8, n° 48, p. 19945-19972, **2016**, doi: 10.1039/C6NR06862F.

[108] D. A. Loy and K. J. Shea, « Arylsilsesquioxane gels and related materials. New hybrids of organic and inorganic networks », *J.Am. Chem. Soc.* **1992** 114, 6700-6710.

[109] R. J. P. Corriu, J. J. E. Moreau, P. Thepot and M. Wong Chi Man, « New mixed organic-inorganic polymers: hydrolysis and polycondensation of bis(trimethoxysilyl)organometallic precursors », *Chem. Mater.*, vol. 4, n° 6, p. 1217-1224, **1992**, doi: 10.1021/cm00024a020.

[110] D. A. Loy and K. J. Shea, « Bridged polysilsesquioxanes. Highly porous hybrid organic-inorganic materials », *Chem. Rev.*, vol. 95, n° 5, p. 1431-1442, **1995**, doi: 10.1021/cr00037a013.

[111] S. Shylesh, R. K. Jha and A. P. Singh, « Assembly of hydrothermally stable ethane-bridged periodic mesoporous organosilicas with spherical and wormlike structures », *Microporous and Mesoporous Materials*, vol. 94, n° 1-3, p. 364-370, **2006**, doi: 10.1016/j.micromeso.2006.04.012.

[112] K. J. Shea, D. A. Loy and O. W. Webster, « Aryl-bridged polysilsesquioxanes--new microporous materials ». *Chemistry of Materials*, Vol. 1, No. 6, **1989**.

[113] T. Yanagisawa, T. Shimizu, K. Kuroda, C. Kato, « The preparation of alkyltrimethylammonium–kanemite complexes and their conversion to microporous materials », *Bulletin of the Chemical Society of Japan*, vol. 63, Issue 4, Pages 988–992, **1990**, https://doi.org/10.1246/bcsj.63.988

[114] J. S. Beck, J.C. Vartuli, W.J. Roth, M.E. Leonowicz, C.T. Kresge, K.D. Schmitt, C. T-W. Chu, D.H. Olson, E.W. Sheppard, S. B. McCullen, J. B. Higgins, and J. L. Schlenker, « A new family of mesoporous molecular sieves prepared with liquid crystal templates », *J. Am. Chem. Soc.*, vol. 114, n° 27, p. 10834-10843, **1992**, doi: 10.1021/ja00053a020.

[115] F. Di Renzo, H. Cambon and R. Dutartre, « A 28-year-old synthesis of micelle-templated mesoporous silica », *Microporous Materials*, vol. 10, n° 4-6, p. 283-286, **1997**, doi: 10.1016/S0927-6513(97)00028-X.

[116] A. Monnier, F. Schüth, Q. Huo, D. Kumar, D. Margolese, R. S. Maxwell, G. D. Stucky, M. Krishnamurty, P. Petroff, A. Firouzi, M. Janicke, and B. F. Chmelka, « Cooperative formation of inorganic-organic interfaces in the synthesis of silicate mesostructures », *Science*, vol. 261, n° 5126, p. 1299-1303, **1993**, doi: 10.1126/science.261.5126.1299.

[117] F. Michaux, N. Baccile, M. Impéror-Clerc, L. Malfatti, N. Folliet, C. Gervais, S. Manet, F. Meneau, J. S. Pedersen and F. Babonneau, « In situ time-resolved SAXS study of the formation of sesostructured organically modified silica through modeling of micelles evolution during surfactant-semplated self-assembly », *Langmuir*, vol. 28, n° 50, p. 17477-17493, **2012**, doi: 10.1021/la3038318.

[118] J. Patarin, B. Lebeau and R. Zana, « Recent advances in the formation mechanisms of organized mesoporous materials », *Current Opinion in Colloid & Interface Science*, vol. 7, n° 1-2, p. 107-115, **2002**, doi: 10.1016/S1359-0294(02)00012-2.

[119] J. C. Vartuli, D. Schmitt, C. T. Kresge, W. J. Roth, M. E. Leonowicz, S. B. McCullen, S. D. Hellring, J. S. Beck, J. L. Schlenker, D. H. Olson and E. W. Sheppard, « Effect of surfactant/silica molar ratios on the formation of mesoporous molecular sieves: inorganic

mimicry of surfactant liquid-crystal phases and mechanistic implications », *Chem. Mater.*, vol. 6, nº 12, p. 2317-2326, **1994**, doi: 10.1021/cm00048a018.

[120] R. Alvarado Meza, T. Santori and X. Cattoën, « A kinetic approach to the mechanism of formation of mesoporous silica nanoparticles », *J Sol-Gel Sci Technol*, **2023**, doi: 10.1007/s10971-023-06130-w.

[121] C. T. Kresge and W. J. Roth, « The discovery of mesoporous molecular sieves from the twenty year perspective », *Chem. Soc. Rev.*, vol. 42, nº 9, p. 3663, **2013**, doi: 10.1039/c3cs60016e.

[122] Q. Huo, D. I. Margolese, U. Ciesla, P. Feng, T. E. Gier, P. Sieger, R. Leon, P. M. Petroff, F. Schüth and G. D. Stucky, « Generalized synthesis of periodic surfactant/inorganic composite materials », *Nature*, vol. 368, nº 6469, p. 317-321, **1994**, doi: 10.1038/368317a0.

[123] F. Hoffmann, M. Cornelius, J. Morell and M. Fröba, « Silica-Based Mesoporous Organic–Inorganic Hybrid Materials », *Angew. Chem. Int. Ed.*, vol. 45, nº 20, p. 3216-3251, **2006**, doi: 10.1002/anie.200503075.

[124] D. Zhao, J. Sun, Q. Li and G. D. Stucky, « Morphological control of highly ordered mesoporous silica SBA-15 », *Chem. Mater.*, vol. 12, nº 2, p. 275-279, **2000**, doi: 10.1021/cm9911363.

[125] S. Inagaki, S. Guan, Y. Fukushima, T. Ohsuna and O. Terasaki, « Novel mesoporous materials with a uniform distribution of organic groups and inorganic oxide in their frameworks », *J. Am. Chem. Soc.*, vol. 121, nº 41, p. 9611-9614, **1999**, doi: 10.1021/ja9916658.

[126] T. Asefa, M. J. MacLachlan, N. Coombs and G. A. Ozin, « Periodic mesoporous organosilicas with organic groups inside the channel walls », *Nature*, vol. 402, nº 6764, p. 867-871, **1999**, doi: 10.1038/47229.

[127] B. J. Melde, B. T. Holland, C. F. Blanford and A. Stein, « Mesoporous sieves with unified hybrid inorganic/organic frameworks », *Chem. Mater.*, vol. 11, nº 11, p. 3302-3308, **1999**, doi: 10.1021/cm9903935.

[128] S. Inagaki, S. Guan, T. Ohsuna and O. Terasaki, « An ordered mesoporous organosilica hybrid material with a crystal-like wall structure », *Nature*, vol. 416, nº 6878, p. 304-307, **2002**, doi: 10.1038/416304a.

[129] B. Feneuil, O. Pitois and N. Roussel, « Effect of surfactants on the yield stress of cement paste », *Cement and Concrete Research*, vol. 100, p. 32-39, **2017**, doi: 10.1016/j.cemconres.2017.04.015.

[130] J. N. Israelachvili, « Intermolecular and Surface Forces ».

[131] A. Noureddine and C. J. Brinker, « Pendant/bridged/mesoporous silsesquioxane nanoparticles: Versatile and biocompatible platforms for smart delivery of therapeutics », *Chemical Engineering Journal*, vol. 340, p. 125-147, **2018**, doi: 10.1016/j.cej.2018.01.086.

[132] P. N. Durfee, Y. Lin, D. R. Dunphy, A. J. Muñiz, K. S. Butler, K. R. Humphrey, A. J. Lokke, J.O. Agola, S. S. Chou, I-M. Chen, W. Wharton, J. L. Townson, C. L. Willman and C. J. Brinker, « Mesoporous silica nanoparticle-supported lipid bilayers (protocells) for active targeting and delivery to individual leukemia cells », *ACS Nano*, vol. 10, n° 9, p. 8325-8345, **2016**, doi: 10.1021/acsnano.6b02819.

[133] Y. Shi, M. L. Miller and A. J. Di Pasqua, « Biocompatibility of mesoporous silica nanoparticles? », *Comments on Inorganic Chemistry*, vol. 36, n° 2, p. 61-80, **2016**, doi: 10.1080/02603594.2015.1088439.

[134] H. Yang, N. Coombs and G. A. Ozin, « Morphogenesis of shapes and surface patterns in mesoporous silica », *Nature*, vol. 386, n° 6626, p. 692-695, **1997**, doi: 10.1038/386692a0.

[135] M. Grün, I. Lauer and K. K. Unger, « The synthesis of micrometer- and submicrometer-size spheres of ordered mesoporous oxide MCM-41 », *Adv. Mater.*, vol. 9, n° 3, p. 254-257, **1997**, doi: 10.1002/adma.19970090317.

[136] C. E. Fowler, D. Khushalani, B. Lebeau and S. Mann, « Nanoscale materials with mesostructured interiors », *Adv. Mater.*, vol. 13, n° 9, p. 649-652, **2001**, doi: 10.1002/1521-4095(200105)13:9<649::AID-ADMA649>3.0.CO;2-G.

[137] R. I. Nooney, D. Thirunavukkarasu, Y. Chen, R. Josephs and A. E. Ostafin, « Synthesis of nanoscale mesoporous silica spheres with controlled particle size », *Chem. Mater.*, vol. 14, n° 11, p. 4721-4728, **2002**, doi: 10.1021/cm0204371.

[138] Y.-T. Shi, H.-Y. Cheng, Y. Geng, H.-M. Nan, W. Chen, Q. Cai, B.-H. Chen, X-D. Sun, Y.-W. Yao, H.-D. Li, « The size-controllable synthesis of nanometer-sized mesoporous silica in extremely dilute surfactant solution », *Materials Chemistry and Physics*, vol. 120, n° 1, p. 193-198, **2010**, doi: 10.1016/j.matchemphys.2009.10.045.

[139] J. G. Croissant, X. Cattoën, M. Wong Chi Man, J.-O. Durand and N. M. Khashab, « Syntheses and applications of periodic mesoporous organosilica nanoparticles », *Nanoscale*, vol. 7, n° 48, p. 20318-20334, **2015**, doi: 10.1039/C5NR05649G.

[140] Y. Fatieiev, J. G. Croissant, K. Alamoudi and N. M. Khashab, « Cellular internalization and biocompatibility of periodic mesoporous organosilica nanoparticles with tunable morphologies: From nanospheres to nanowires », *ChemPlusChem*, vol. 82, n° 4, p. 631-637, **2017**, doi: 10.1002/cplu.201600560.

[141] J. Croissant, X. Cattoën, M. W. C. Man, A. Gallud, L. Raehm, P. Trens, M. Maynadier and J.-O. Durand, « Biodegradable ethylene-bis(propyl)disulfide-based periodic mesoporous organosilica nanorods and nanospheres for efficient in-vitro drug delivery », *Adv. Mater.*, vol. 26, n° 35, p. 6174-6180, **2014**, doi: 10.1002/adma.201401931.

[142] J. G. Croissant, Y. Fatieiev, K. Julfakyan, J. Lu, A.-H. Emwas, D. H. Anjum, H. Omar, F. Tamanoi, J. I. Zink, N. M. Khashab « Biodegradable oxamide-phenylene-based mesoporous organosilica nanoparticles with unrecedented drug payloads for delivery in cells », *Chem. Eur. J.*, vol. 22, n° 42, p. 14806-14811, **2016**, doi: 10.1002/chem.201601714.

[143] J. Li, Y. Wei, Y. Deng, D. Gu, X. Yang, L. Zhang, B. Tu, D. Zhao, « An unusual example of morphology controlled periodic mesoporous organosilica single crystals », *J. Mater. Chem.*, vol. 20, n° 31, p. 6460, **2010**, doi: 10.1039/c0jm00663g.

[144] F. Lu, S. Wu, Y. Hung and C. Mou, « Size effect on cell uptake in well-suspended, uniform mesoporous silica nanoparticles », *Small*, vol. 5, n° 12, p. 1408-1413, **2009**, doi: 10.1002/smll.200900005.

[145] N. Hoshyar, S. Gray, H. Han and G. Bao, « The effect of nanoparticle size on *in vivo* pharmacokinetics and cellular interaction », *Nanomedicine*, vol. 11, n° 6, p. 673-692, **2016**, doi: 10.2217/nnm.16.5.

[146] S.-W. Kim, M. Kim, W. Y. Lee and T. Hyeon, « Fabrication of hollow palladium spheres and their successful application to the recyclable heterogeneous catalyst for suzuki coupling reactions », *Am. Chem. Soc.* **2002**, 124, 26, 7642–7643, doi: 10.1021/ja026032z.

[147] J. Fu, Q. Xu, J. Chen, Z. Chen, X. Huang and X. Tang, « Controlled fabrication of uniform hollow core porous shell carbon spheres by the pyrolysis of core/shell polystyrene/cross-linked polyphosphazene composites », *Chem. Commun.*, vol. 46, n° 35, p. 6563, **2010**, doi: 10.1039/c0cc01185a.

[148] P. M. Arnal, C. Weidenthaler and F. Schüth, « Highly monodisperse zirconia-coated silica spheres and zirconia/silica hollow spheres with remarkable textural properties », *Chem. Mater.*, vol. 18, n° 11, p. 2733-2739, **2006**, doi: 10.1021/cm052580a.

[149] A. Chenan, S. Ramya, R. P. George and U. Kamachi Mudali, « Hollow mesoporous zirconia nanocontainers for storing and controlled releasing of corrosion inhibitors », *Ceramics International*, vol. 40, n° 7, p. 10457-10463, **2014**, doi: 10.1016/j.ceramint.2014.03.016.

[150] S. Haffer, M. Tiemann and M. Fröba, « Periodic Mesoporous Organosilica (PMO) materials with uniform spherical core-shell structure », *Chem. Eur. J.*, vol. 16, n° 34, p. 10447-10452, **2010**, doi: 10.1002/chem.201000643.

[151] Y. Che, P. Xu, H. Chen, Y. Li, W. Bu, Z. Shu, Y. Li, J. Zhang, L. Zhang, L. Pan, X. Cui, Z. Hua., « Colloidal HPMO nanoparticles: silica-etching chemistry tailoring, topological transformation, and nano-biomedical applications », *Adv. Mater.*, vol. 25, n° 22, p. 3100-3105, **2013**, doi: 10.1002/adma.201204685.

[152] Y. Chen, Q. Meng, M. Wu, S. Wang, P. Xu, H. Chen, Y. Li, L Zhang, L Wang and J. Shi, « Hollow Mesoporous Organosilica Nanoparticles: A generic intelligent framework-hybridization approach for biomedicine », *J. Am. Chem. Soc.*, vol. 136, n° 46, p. 16326-16334, **2014**, doi: 10.1021/ja508721y.

[153] Y. Chen, H. Chen, L. Guo, Q. He, F. Chen, J. Zhou, J. Feng and J. Shi « Hollow/Rattle-type mesoporous nanostructures by a structural difference-based selective etching strategy », *ACS Nano*, vol. 4, n° 1, p. 529-539, **2010**, doi: 10.1021/nn901398j.

[154] X. Fang, C. Chen, Z. Liu, P. Liu and N. Zheng, « A cationic surfactant assisted selective etching strategy to hollow mesoporous silica spheres », *Nanoscale*, vol. 3, n° 4, p. 1632, **2011**, doi: 10.1039/c0nr00893a.

[155] N. Koike, W. Chaikittisilp, A. Shimojima and T. Okubo, « Surfactant-free synthesis of hollow mesoporous organosilica nanoparticles with controllable particle sizes and diversified organic moieties », *RSC Adv.*, vol. 6, n° 93, p. 90435-90445, **2016**, doi: 10.1039/C6RA22926C.

[156] W. Fan, N. Lu, Z. Shen, W. Tang, B. Shen, Z. Cui, « Generic synthesis of small-sized hollow mesoporous organosilica nanoparticles for oxygen-independent X-ray-activated synergistic therapy », *Nat Commun*, vol. 10, n° 1, p. 1241, **2019**, doi: 10.1038/s41467-019-09158-1.

[157] L. P. Singh, S. K. Agarwal, S. K. Bhattacharyya, U. Sharma and S. Ahalawat, « Preparation of silica nanoparticles and its beneficial role in cementitious materials », *Nanomaterials and Nanotechnology*, vol. 1, p. 9, **2011**, doi: 10.5772/50950.

[158] E. C. de O. Nassor, L. R. Ávila, P. F. dos S. Pereira, K. J. Ciuffi, P. S. Calefi and E. J. Nassar, « Influence of the hydrolysis and condensation time on the preparation of hybrid materials », *Mat. Res.*, vol. 14, n° 1, p. 1-6, 2**011**, doi: 10.1590/S1516-14392011005000003.

[159] N. Primeau, C. Vautey and M. Langlet, « The effect of thermal annealing on aerosol-gel deposited SiO2 films: a FTIR deconvolution study », *Thin Solid Films*, vol. 310, n° 1-2, p. 47-56, **1997**, doi: 10.1016/S0040-6090(97)00340-4.

[160] F. Rubio, J. Rubio and J. L. Oteo, « A FT-IR Study of the hydrolysis of tetraethylorthosilicate (TEOS). », *Spectroscopy Letters*, vol. 31, n° 1, p. 199-219, **1998**, doi: 10.1080/00387019808006772.

[161] J.K. Kim, D.F. Lawler, « Characteristics of Zeta Potential Distribution in Silica Particles », *Bulletin of the Korean Chemical Society*, vol. 26, n° 7, p. 1083-1089, **2005**, doi: 10.5012/BKCS.2005.26.7.1083.

[162] S. Fujita and S. Inagaki, « Self-organization of organosilica solids with molecular-scale and mesoscale periodicities », *Chem. Mater.*, vol. 20, n° 3, p. 891-908, **2008**, doi: 10.1021/cm702271v.

[163] F. Hoffmann, M. Güngerich, P. J. Klar and M. Fröba, « Vibrational spectroscopy of periodic mesoporous organosilicas (PMOs) and their precursors: A closer look », *J. Phys. Chem. C*, vol. 111, n° 15, p. 5648-5660, **2007**, doi: 10.1021/jp0668596.

[164] Z.-A. Qiao, L. Zhang, M. Guo, Y. Liu and Q. Huo, « Synthesis of Mesoporous Silica Nanoparticles via controlled hydrolysis and condensation of silicon alkoxide », *Chem. Mater.*, vol. 21, n° 16, p. 3823-3829, **2009**, doi: 10.1021/cm901335k.

[165] S.-J. Park, Y.-J. Kim and S.-J. Park, « Size-dependent shape evolution of silica nanoparticles into hollow structures », *Langmuir*, vol. 24, n° 21, p. 12134-12137, **2008**, doi: 10.1021/la8028885.

[166] G. C. Carvalho, G. D. Marena, J. C. F. Karnopp, J. Jorge, « Cetyltrimethylammonium bromide in the synthesis of mesoporous silica nanoparticles: General aspects and in vitro toxicity », *Advances in Colloid and Interface Science*, vol. 307, p. 102746, **2022**, doi: 10.1016/j.cis.2022.102746.

[167] J. Feng, Z. Wang, B. Shen, L. Zhang, X. Yang and N. He, « Effects of template removal on both morphology of mesoporous silica-coated gold nanorod and its biomedical application », *RSC Adv.*, vol. 4, n° 54, p. 28683-28690, **2014**, doi: 10.1039/C4RA03122A.

[168] R. J. Soto, L. Yang and M. H. Schoenfisch, « Functionalized mesoporous silica via an aminosilane surfactant ion exchange reaction: Controlled scaffold design and nitric oxide release », *ACS Appl. Mater. Interfaces*, vol. 8, n° 3, p. 2220-2231, **2016**, doi: 10.1021/acsami.5b10942.

[169] J.-L. Bantignies, L. Vellutini, D. Maurin, P. Hermet, P. Dieudonné, M. Wong Chi Man, J. R. Bartlett, C. Bied, J.-L. Sauvajol and J. J. E. Moreau, « Insights into the self-directed structuring of hybrid organic−inorganic silicas through infrared Studies », *J. Phys. Chem. B*, vol. 110, n° 32, p. 15797-15802, **2006**, doi: 10.1021/jp060975r.

[170] M. Laird, C. Carcel, E. Oliviero, G. Toquer, P. Trens, J.R. Bartlett, M. W. C. Man, « Single-template periodic mesoporous organosilica with organized bimodal mesoporosity », *Microporous and Mesoporous Materials*, vol. 297, p. 110042, **2020**, doi: 10.1016/j.micromeso.2020.110042.

[171] T. R. Prisk, M. S. Bryan and P. E. Sokol, « Electronic supplementary information: diffusive and rotational dynamics of condensed n-H2 confined in MCM-41 », *Phys. Chem. Chem. Phys*., **2014**, 16, 17960-17974, doi: 10.1039/C4CP02281E.

[172] T. J. Mays, « A new classification of pore sizes », in *Studies in Surface Science and Catalysis*, vol. 160, Elsevier, **2007**, p. 57-62. doi: 10.1016/S0167-2991(07)80009-7.

[173] M. D. Donohue and G. L. Aranovich, « Classification of Gibbs adsorption isotherms », *Advances in Colloid and Interface Science*, vol. 76-77, p. 137-152, **1998**, doi: 10.1016/S0001-8686(98)00044-X.

[174] K. S. W. Sing and R. T. Williams, « Physisorption hysteresis loops and the characterization of nanoporous materials », *Adsorption Science & Technology*, vol. 22, n° 10, p. 773-782, **2004**, doi: 10.1260/0263617053499032.

[175] M. Thommes, « Physical adsorption characterization of nanoporous materials », *Chemie Ingenieur Technik*, vol. 82, n° 7, p. 1059-1073, **2010**, doi: 10.1002/cite.201000064.

[176] M. Thommes, K. Kaneko, A. V. Neimark, J. P. Olivier, F. Rodriguez-Reinoso, J. Rouquerol and K. S.W. Sing, « Physisorption of gases, with special reference to the evaluation of surface area and pore size distribution (IUPAC Technical Report) », *Pure and Applied Chemistry*, vol. 87, n° 9-10, p. 1051-1069, **2015**, doi: 10.1515/pac-2014-1117.

[177] S. Pan, M. Zha, C. Gao, J. Qu and X. Ding, « Pore structure and fractal characteristics of organic-rich lacustrine shales of the kongdian formation, Cangdong Sag, Bohai Bay basin », *Front. Earth Sci.*, vol. 9, p. 760583, **2021**, doi: 10.3389/feart.2021.760583.

[178] K. A. Cychosz and M. Thommes, « Progress in the physisorption characterization of nanoporous gas storage materials », *Engineering*, vol. 4, n° 4, p. 559-566, **2018**, doi: 10.1016/j.eng.2018.06.001.

[179] V. Patel, N. Dharaiya, D. Ray, V. K. Aswal and P. Bahadur, « pH-controlled size/shape in CTAB micelles with solubilized polar additives: A viscometry, scattering and spectral evaluation », *Colloids and Surfaces A: Physicochemical and Engineering Aspects*, vol. 455, p. 67-75, **2014**, doi: 10.1016/j.colsurfa.2014.04.025.

[180] J. Hu, F. Gao, Y. Shang, C. Peng, H. Liu and Y. Hu, « One-step synthesis of micro/mesoporous material templated by CTAB and imidazole ionic liquid in aqueous solution », *Microporous and Mesoporous Materials*, vol. 142, n° 1, p. 268-275, **2011**, doi: 10.1016/j.micromeso.2010.12.011.

[181] S. Liu, P. Cool, O. Collart, P. Van Der Voort, E. F. Vansant, O. I. Lebedev, G. Van Tendeloo and Minhua Jiang, « The Influence of the alcohol concentration on the structural ordering of mesoporous silica: Cosurfactant versus cosolvent », *J. Phys. Chem. B*, vol. 107, n° 38, p. 10405-10411, **2003**, doi: 10.1021/jp034410w.

[182] B. Tan and S. E. Rankin, « Interfacial alignment mechanism of forming spherical silica with radially oriented nanopores », *J. Phys. Chem. B*, vol. 108, n° 52, p. 20122-20129, **2004**, doi: 10.1021/jp046425f.

[183] F. Lin, X. Meng, M. Mertens, P. Cool and S. Van Doorslaer, « Probing framework–guest interactions in phenylene-bridged periodic mesoporous organosilica using spin-probe EPR », *Phys. Chem. Chem. Phys.*, vol. 16, n° 41, p. 22623-22631, **2014**, doi: 10.1039/C4CP03778B.

[184] A. Birault, E. Molina, P. Trens, D. Cot, G. Toquer, N. Marcotte, C. Carcel, J. R. Bartlett, C. Gérardin, M. Wong Chi Man « Periodic Mesoporous Organosilicas from polyion complex micelles – Effect of organic bridge on nanostructure », *Eur J Inorg Chem*, vol. 2019, n° 27, p. 3157-3164, **2019**, doi: 10.1002/ejic.201900487.

[185] J. Croissant, X. Cattoën, M. Wong Chi Man, P. Dieudonné, C. Charnay, L. Raehm, J.-O. Durand, « One-Pot construction of multipodal hybrid periodic mesoporous organosilica nanoparticles with crystal-like architectures », *Adv. Mater.*, vol. 27, n° 1, p. 145-149, **2015**, doi: 10.1002/adma.2l404226.

[186] M. Wahab, Kim, C.-S. Ha, « Hybrid periodic mesoporous organosilica materials prepared from 1,2-bis(triethoxysilyl)ethane and (3-cyanopropyl) triethoxysilane », *Microporous and Mesoporous Materials*, vol. 69, n° 1-2, p. 19-27, **2004**, doi: 10.1016/j.micromeso.2004.01.001.

[187] L. Tan, T. Liu, L. Li, H. Liu, X. Wu, F. Gao, X. He, X. Meng, D. Chen and F. Tang « Uniform double-shelled silica hollow spheres: acid/base selective-etching synthesis and their drug delivery application », *RSC Adv.*, vol. 3, n° 16, p. 5649, **2013**, doi: 10.1039/c3ra40733k.

[188] M. Priebe and K. M. Fromm, « Nanorattles or yolk-shell nanoparticles-what are they, how are they made, and what are they good for? », *Chem. Eur. J.*, vol. 21, n° 10, p. 3854-3874, **2015**, doi: 10.1002/chem.201405285.

[189] M. Wang, Y. Boyjoo, J. Pan, S. Wang and J. Liu, « Advanced yolk-shell nanoparticles as nanoreactors for energy conversion », *Chinese Journal of Catalysis*, vol. 38, n° 6, p. 970-990, **2017**, doi: 10.1016/S1872-2067(17)62818-3.

[190] J.-N. Liu, W.-B. Bu and J.-L. Shi, « Silica coated upconversion nanoparticles: A versatile platform for the development of efficient theranostics », *Acc. Chem. Res.*, vol. 48, n° 7, p. 1797-1805, **2015**, doi: 10.1021/acs.accounts.5b00078.

[191] S. T. Selvan, T. T. Tan and J. Y. Ying, « Robust, non-cytotoxic, silica-coated CdSe quantum dots with efficient photoluminescence », *Adv. Mater.*, vol. 17, n° 13, p. 1620-1625, **2005**, doi: 10.1002/adma.200401960.

[192] Y. Han, J. Jiang, S. S. Lee and J. Y. Ying, « Reverse microemulsion-mediated synthesis of silica-coated gold and silver nanoparticles », *Langmuir*, vol. 24, n° 11, p. 5842-5848, **2008**, doi: 10.1021/la703440p.

[193] H. L. Ding, Y. X. Zhang, S. Wang, J. M. Xu, S. C. Xu and G. H. Li, « Fe_3O_4 @SiO_2 core/shell nanoparticles: The silica coating regulations with a single core for different core sizes and shell thicknesses », *Chem. Mater.*, vol. 24, n° 23, p. 4572-4580, **2012**, doi: 10.1021/cm302828d.

[194] M. K. Gnanasammandhan, N. M. Idris, A. Bansal, K. Huang and Y. Zhang, « Near-IR photoactivation using mesoporous silica–coated $NaYF_4$: Yb, Er/Tm upconversion nanoparticles », *Nat Protoc*, vol. 11, n° 4, p. 688-713, **2016**, doi: 10.1038/nprot.2016.035.

[195] W. Fan, B. Shen, W. Bu, F. Chen, Q. He, K. Zhao, S. Zhang, L. Zhou, W. Peng, Q. Xiao, D. Ni, J. Liu, J. Shi, « A smart upconversion-based mesoporous silica nanotheranostic system for synergetic chemo-/radio-/photodynamic therapy and simultaneous MR/UCL imaging », *Biomaterials*, vol. 35, n° 32, p. 8992-9002, **2014**, doi: 10.1016/j.biomaterials.2014.07.024.

[196] Y. Yang, J. Liu, X. Li, X. Liu and Q. Yang, « Organosilane-assisted transformation from core–shell to yolk–shell Nanocomposites », *Chem. Mater.*, vol. 23, n° 16, p. 3676-3684, **2011**, doi: 10.1021/cm201182d.

[197] Y. Wei, X. Li, A.A. Elzatahry, R. Zhang, W. Wang, X. Tang, J. Yangac, J. Wanga, D. Al-Dahyane and D. Zhao « A versatile in situ etching-growth strategy for synthesis of yolk–shell structured periodic mesoporous organosilica nanocomposites », *RSC Adv.*, vol. 6, n° 56, p. 51470-51479, **2016**, doi: 10.1039/C6RA08541E.

[198] X. Wang, Y. He, C. Liu, Y. Liu, Z.-A. Qiao and Q. Huo, « A controllable asymmetrical/symmetrical coating strategy for architectural mesoporous organosilica nanostructures », *Nanoscale*, vol. 8, n° 28, p. 13581-13588, **2016**, doi: 10.1039/C6NR03229J.

[199] A. M. Kaczmarek, M. Suta, H. Rijckaert, A. Abalymov, I. Van Driessche, A. G. Skirtach, A. Meijerink, P. Van Der Voort, « Visible and NIR upconverting Er^{3+} –Yb^{3+} luminescent nanorattles and other hybrid PMO-inorganic structures for in Vivo nanothermometry », *Adv. Funct. Mater.*, vol. 30, n° 32, p. 2003101, **2020**, doi: 10.1002/adfm.202003101.

[200] S. Lu, D. Tu, X. Li, R. Li and X. Chen, « A facile "ship-in-a-bottle" approach to construct nanorattles based on upconverting lanthanide-doped fluorides », *Nano Res.*, vol. 9, n° 1, p. 187-197, **2016**, doi: 10.1007/s12274-015-0979-4.

[201] T. Zhao, L. Chen, R. Lin, P. Zhang, K. Lan., W. Zhang, X. Li and D. Zhao « Interfacial assembly directed unique mesoporous architectures: from symmetric to asymmetric », *Acc. Mater. Res.*, vol. 1, n° 1, p. 100-114, **2020**, doi: 10.1021/accountsmr.0c00028.

[202] L. Yu, P. Pan, Y. Zhang, Y. Zhang, L. Wan, X. Cheng, Y. Deng, « Nonsacrificial self-template synthesis of colloidal magnetic yolk–shell mesoporous organosilicas for efficient oil/water interface catalysis », *Small*, vol. 15, n° 14, p. 1805465, **2019**, doi: 10.1002/smll.201805465.

[203] J. G. Croissant, Y. Fatieiev, A. Almalik and N. M. Khashab, « Mesoporous silica and organosilica nanoparticles: physical chemistry, biosafety, delivery strategies, and biomedical Applications », *Adv. Healthcare Mater.*, vol. 7, n° 4, p. 1700831, **2018**, doi: 10.1002/adhm.201700831.

[204] X. Du, X. Li, L. Xiong, X. Zhang, F. Kleitz and S. Z. Qiao, « Mesoporous silica nanoparticles with organo-bridged silsesquioxane framework as innovative platforms for bioimaging and therapeutic agent delivery », *Biomaterials*, vol. 91, p. 90-127, **2016**, doi: 10.1016/j.biomaterials.2016.03.019.

[205] J. Liu, S. Z. Qiao, J. S. Chen, X. W. (David) Lou, X. Xing and G. Q. (Max) Lu, « Yolk/shell nanoparticles: new platforms for nanoreactors, drug delivery and lithium-ion batteries », *Chem. Commun.*, vol. 47, n° 47, p. 12578, **2011**, doi: 10.1039/c1cc13658e.

[206] N. Menyuk, K. Dwight and J. W. Pierce, « $NaYF_4$: Yb, Er—an efficient upconversion phosphor », *Appl. Phys. Lett.*, vol. 21, n° 4, p. 159-161, **1972**, doi: 10.1063/1.1654325.

[207] N. Martin, P. Boutinaud, R. Mahiou, J.-C. Cousseins and M. Bouderbala, « Preparation of fluorides at 80 °C in the NaF-(Y, Yb, Pr) F_3 system », *J. Mater. Chem.*, vol. 9, n° 1, p. 125-128, **1999**, doi: 10.1039/a804472d.

[208] L. Liang, H. Wu, H. Hu, M. Wu and Q. Su, « Enhanced blue and green upconversion in hydrothermally synthesized hexagonal NaY1−xYbxF4:Ln3+ (Ln3+ = Er3+ or Tm3+) », *Journal of Alloys and Compounds*, vol. 368, n° 1-2, p. 94-100, **2004**, doi: 10.1016/j.jallcom.2003.07.010.

[209] G. Yi, H. Lu, S. Zhao, Y. Ge, W. Yang, D. Chen, L.H. Guo, « Synthesis, characterization, and biological application of size-controlled nanocrystalline $NaYF_4$: Yb, Er infrared-to-visible up-conversion phosphors », *Nano Lett.*, vol. 4, n° 11, p. 2191-2196, **2004**, doi: 10.1021/nl048680h.

[210] J.-H. Zeng, J. Su, Z.-H. Li, R.-X. Yan and Y.-D. Li, « Synthesis and upconversion luminescence of hexagonal-phase $NaYF_4$: Yb, Er phosphors of controlled size and morphology », *Adv. Mater.*, vol. 17, n° 17, p. 2119-2123, **2005**, doi: 10.1002/adma.200402046.

[211] D. Kumar, K. Verma, S. Verma, B. Chaudhary, S. Som, V. Sharma, V. Kumar and H. C. Swart, « Recent advances in enhanced luminescence upconversion of lanthanide-doped NaYF 4 phosphors », *Physica B: Condensed Matter*, vol. 535, p. 278-286, **2018**, doi: 10.1016/j.physb.2017.08.003.

[212] Y. Wei, F. Lu, X. Zhang and D. Chen, « Polyol-mediated synthesis and luminescence of lanthanide-doped $NaYF_4$ nanocrystal upconversion phosphors », *Journal of Alloys and Compounds*, vol. 455, n° 1-2, p. 376-384, **2008**, doi: 10.1016/j.jallcom.2007.01.107.

[213] S. Gai, C. Li, P. Yang and J. Lin, « Recent progress in rare earth micro/nanocrystals: soft chemical synthesis, luminescent properties, and biomedical applications », *Chem. Rev.*, vol. 114, n° 4, p. 2343-2389, **2014**, doi: 10.1021/cr4001594.

[214] G. S. Yi and G. M. Chow, « Synthesis of hexagonal-phase $NaYF_4$: Yb, Er and $NaYF_4$: Yb, Tm nanocrystals with efficient up-Conversion fluorescence », *Adv. Funct. Mater.*, vol. 16, n° 18, p. 2324-2329, **2006**, doi: 10.1002/adfm.200600053.

[215] J. E. Roberts, « Lanthanum and neodymium salts of trifluoroacetic Acid », *J. Am. Chem. Soc.*, vol. 83, n° 5, p. 1087-1088, **1961**, doi: 10.1021/ja01466a020.

[216] Y.-W. Zhang, X. Sun, R. Si, L.-P. You and C.-H. Yan, « Single-crystalline and monodisperse LaF_3 triangular nanoplates from a single-source precursor », *J. Am. Chem. Soc.*, vol. 127, n° 10, p. 3260-3261, **2005**, doi: 10.1021/ja042801y.

[217] Z. Li and Y. Zhan, « An efficient and user-friendly method for the synthesis of hexagonal-phase $NaYF_4$: Yb, Er/Tm nanocrystals with controllable shape and upconversion fluorescence », *Nanotechnology*, vol.1, n° 34, **2008**, doi: 10.1088/0957-4484/19/34/345606.

[218] N. Kang, C.-C. Ai, Y.-M. Zhou, Z. Wang and L. Ren, « Facile synthesis of upconversion nanoparticles with high purity using lanthanide oleate compounds », *Nanotechnology*, vol. 29, n° 7, p. 075601, **2018**, doi: 10.1088/1361-6528/aa96ee.

[219] Y. Wei, F. Lu, X. Zhang and D. Chen, « Synthesis of oil-dispersible hexagonal-phase and hexagonal-shaped $NaYF_4$: Yb, Er nanoplates », *Chem. Mater.*, vol. 18, n° 24, p. 5733-5737, **2006**, doi: 10.1021/cm0606171.

[220] J. Park, K. An, Y. Hwang, J.G. Park, H. J. Noh, J.Y. Kim, J.-H. Park, N.-M. Hwang and T. Hyeon, « Ultra-large-scale syntheses of monodisperse nanocrystals », *Nature Mater*, vol. 3, n° 12, p. 891-895, **2004**, doi: 10.1038/nmat1251.

[221] P. Ghosh andA. Patra, « Tuning of crystal phase and luminescence properties of Eu^{3+} doped sodium yttrium fluoride nanocrystals », *J. Phys. Chem. C*, vol. 112, n° 9, p. 3223-3231, **2008**, doi: 10.1021/jp7099114.

[222] J. Liu, X. Liu, X. Kong and H. Zhang, « Controlled synthesis, formation mechanism and upconversion luminescence of $NaYF_4$: Yb, Er nano-/submicrocrystals via ionothermal approach », *Journal of Solid-State Chemistry*, vol. 190, p. 98-103, **2012**, doi: 10.1016/j.jssc.2012.01.058.

[223] C. Li znd J. Lin, « Rare earth fluoride nano-/microcrystals: synthesis, surface modification and application », *J. Mater. Chem.*, vol. 20, n° 33, p. 6831, **2010**, doi: 10.1039/c0jm00031k.

[224] X. Liang, X. Wang, J. Zhuang, Q. Peng andY. Li, « Synthesis of $NaYF_4$ Nanocrystals with predictable phase and shape », *Adv. Funct. Mater.*, vol. 17, n° 15, p. 2757-2765, **2007**, doi: 10.1002/adfm.200600807.

[225] H. Li, X. Liu and X. Li, « Solvothermal synthesis and modification of $NaYF_4$: Yb/Er@$NaLuF_4$: Yb for enhanced up-conversion luminescence for bioimaging », *RSC Adv.*, vol. 9, n° 72, p. 42163-42171, **2019**, doi: 10.1039/C9RA08921G.

[226] F. Wang, D. K. Chatterjee, Z. Li, Y. Zhang, X. Fan and M. Wang, « Synthesis of polyethylenimine/$NaYF_4$ nanoparticles with upconversion fluorescence », *Nanotechnology*, vol. 17, n° 23, p. 5786-5791, **2006**, doi: 10.1088/0957-4484/17/23/013.

[227] C. Li, Z. Quan, P. Yang, S. Huang, H. Lian and J. Lin, « Shape-controllable synthesis and upconversion properties of lutetium fluoride (doped with Yb^{3+} /Er^{3+}) microcrystals by hydrothermal process », *J. Phys. Chem. C*, vol. 112, n° 35, p. 13395-13404, **2008**, doi: 10.1021/jp802826k.

[228] F. Wang and X. Liu, « Upconversion multicolor fine-tuning: sisible to near-infrared emission from lanthanide-doped $NaYF_4$ nanoparticles », *J. Am. Chem. Soc.*, vol. 130, n° 17, p. 5642-5643, **2008**, doi: 10.1021/ja800868a.

[229] Z. Wang, F. Tao, W. Cai, L. Yao and X. Li, « Controlled-synthesis and up-conversion luminescence of NaY F_4: Yb, Er phosphors », *Solid State Communications*, vol. 144, n° 5-6, p. 255-258, **2007**, doi: 10.1016/j.ssc.2007.08.021.

[230] Q. Zhang, K. Song, J. Zhao, X. Kong, Y. Sun, X. Liu, Y. Zhang, Q. Zeng, H. Zhang « Hexanedioic acid mediated surface–ligand-exchange process for transferring $NaYF_4$: Yb/Er (or Yb/Tm) up-converting nanoparticles from hydrophobic to hydrophilic », *Journal of Colloid and Interface Science*, vol. 336, n° 1, p. 171-175, **2009**, doi: 10.1016/j.jcis.2009.04.024.

[231] J.-C. Boyer, L. A. Cuccia and J. A. Capobianco, « Synthesis of Colloidal Upconverting $NaYF_4$: Er^{3+} /Yb^{3+} and Tm^{3+} /Yb^{3+} Monodisperse Nanocrystals », *Nano Lett.*, vol. 7, n° 3, p. 847-852, **2007**, doi: 10.1021/nl070235+.

[232] H.-X. Mai, Y.-W. Zhang, L.-D. Sun and C.-H. Yan, « Size- and phase-controlled synthesis of monodisperse $NaYF_4$: Yb, Er nanocrystals from a unique delayed nucleation pathway monitored with upconversion spectroscopy », *J. Phys. Chem. C*, vol. 111, n° 37, p. 13730-13739, **2007**, doi: 10.1021/jp073919e.

[233] D. Yuan, M. C. Tan, R. E. Riman and G. M. Chow, « Comprehensive study on the size effects of the optical properties of $NaYF_4$: Yb, Er nanocrystals », *J. Phys. Chem. C*, vol. 117, n° 25, p. 13297-13304, **2013**, doi: 10.1021/jp403061h.

[234] C. Liu, H. Wang, X. Zhang and D. Chen, « Morphology- and phase-controlled synthesis of monodisperse lanthanide-doped $NaGdF_4$ nanocrystals with multicolor photoluminescence », *J. Mater. Chem.*, vol. 19, n° 4, p. 489-496, **2009**, doi: 10.1039/B815682D.

[235] H. Li, X. Shi, X. Li and L. Zong, « Size-tunable β-$NaYF_4$: Yb/Er up-converting nanoparticles with a strong green emission synthesized by thermal decomposition », *Optical Materials*, vol. 108, p. 110144, **2020**, doi: 10.1016/j.optmat.2020.110144.

[236] C. Liu, H. Wang, X. Li and D. Chen, « Monodisperse, size-tunable and highly efficient β-$NaYF_4$: Yb, Er (Tm) up-conversion luminescent nanospheres: controllable synthesis and their surface modifications », *J. Mater. Chem.*, vol. 19, n° 21, p. 3546, **2009**, doi: 10.1039/b820254k.

[237] Y. Ye, Z. Jiang, W. Qizheng, Z. Zhu, X. Wang, Z. Sui, R. Dai, Z. Wang, Z. Zhang, Z. Ding, « Upconversion luminescence of $NaYF_4$: Yb, Er nanocrystals with high uniformity », *Journal of Rare Earths*, vol. 32, n° 9, p. 802-805, **2014**, doi: 10.1016/S1002-0721(14)60144-7.

[238] Z. Li, Y. Zhang and S. Jiang, « Multicolor core/shell-structured upconversion fluorescent nanoparticles », *Adv. Mater.*, vol. 20, n° 24, p. 4765-4769, **2008**, doi: 10.1002/adma.200801056.

[239] K. Huang, M. K. G. Jayakumar and Y. Zhang, « Lutetium doping for making big core and core–shell upconversion nanoparticles », *J. Mater. Chem. C*, vol. 3, n° 39, p. 10267-10272, **2015**, doi: 10.1039/C5TC00817D.

[240] S. Gai, G. Yang, X. Li, C. Li, Y. Dai, F. Hea and P. Yan, « Facile synthesis and up-conversion properties of monodisperse rare earth fluoride nanocrystals », *Dalton Trans*., 41, 11716-11724, **2012**, doi: 10.1039/C2DT30954H

[241] F. Wang, J. Wang, J. Xu, X. Xue, H. Chen and X. Liu, « Tunable upconversion emissions from lanthanide-doped monodisperse β-$NaYF_4$ nanoparticles », *Spectroscopy Letters*, vol. 43, n° 5, p. 400-405, **2010**, doi: 10.1080/00387010.2010.487018.

[242] N. J. J. Johnson, N. M. Sangeetha, J.-C. Boyer and F. C. J. M. van Veggel, « Facile ligand-exchange with polyvinylpyrrolidone and subsequent silica coating of hydrophobic upconverting β-$NaYF_4$: Yb^{3+}/Er^{3+} nanoparticles », *Nanoscale*, **2010**, doi: 10.1039/B9NR00379G.

[243] M. Quintanilla, E. Hemmer, J. Marques-Hueso, S. Rohani, G. Lucchini, M. Wang, R.R. Zamani, V. Roddatis, A. Speghini, B. S. Richards and F. Vetrone, « Cubic *versus* hexagonal – phase, size and morphology effects on the photoluminescence quantum yield of $NaGdF_4$: Er^{3+} /Yb^{3+} upconverting nanoparticles », *Nanoscale*, vol. 14, n° 4, p. 1492-1504, **2022**, doi: 10.1039/D1NR06319G.

[244] X. Wang, X. Zhang, Y. Wang, H. Li, J. Xie, T. Wei, Q. Huang, X. Xie, L. Huang, W. Huang, « Comprehensive studies of the Li^+ effect on $NaYF_4$: Yb/Er nanocrystals: morphology, structure, and upconversion luminescence », *Dalton Trans.*, vol. 46, n° 28, p. 8968-8974, 2017, doi: 10.1039/C7DT01820G.

[245] T. Rinkel, J. Nordmann, A. N. Raj and M. Haase, « Ostwald-ripening and particle size focussing of sub-10 nm $NaYF_4$ upconversion nanocrystals », *Nanoscale*, vol. 6, n° 23, p. 14523-14530, **2014**, doi: 10.1039/C4NR03833A.

[246] D. Yang, D. Chen, H. He, Q. Pan, Q. Xiao, J. Qiu, G. Dong, « Controllable phase transformation and mid-infrared emission from Er^{3+}-doped hexagonal-/cubic-$NaYF_4$ nanocrystals », *Sci Rep*, vol. 6, n° 1, p. 29871, **2016**, doi: 10.1038/srep29871.

[247] H. Assaaoudi, G.-B. Shan, N. Dyck and G. P. Demopoulos, « Annealing-induced ultra-efficient NIR-to-VIS upconversion of nano-/micro-scale α and β NaYF4:Er^{3+}, Yb^{3+} crystals », *CrystEngComm*, vol. 15, n° 23, p. 4739, **2013**, doi: 10.1039/c3ce40362a.

[248] H. Schäfer, P. Ptacek, H. Eickmeier and M. Haase, « Synthesis of Hexagonal Yb^{3+}, Er^{3+} -Doped $NaYF_4$ Nanocrystals at Low Temperature », *Adv. Funct. Mater.*, vol. 19, n° 19, p. 3091-3097, **2009**, doi: 10.1002/adfm.200900642.

[249] J. Lumeau, K. Chamma, L. Glebova and L. B. Glebov, « X-ray diffraction study of NaF nano-crystals in photo-thermo-refractive glass », *Journal of Non-Crystalline Solids*, vol. 405, p. 188-195, **2014**, doi: 10.1016/j.jnoncrysol.2014.09.019.

[250] H.-X. Mai, Y.-W. Zhang, R. Si, Z.-G. Yan, L.-d. Sun, L.-P. You and C.-H. Yan, « High-quality sodium rare-earth fluoride nanocrystals: controlled synthesis and optical properties », *J. Am. Chem. Soc.*, vol. 128, n°19, p. 6426–6436, **2006**, doi: 10.1021/ja060212h.

[251] J. Shan, M. Uddi, N. Yao and Y. Ju, « Anomalous Raman scattering of colloidal Yb^{3+}, Er^{3+} codoped $NaYF_4$ nanophosphors and dynamic probing of the upconversion luminescence », *Adv. Funct. Mater.*, vol. 20, n°20, p. 3530-3537, **2010**, doi: 10.1002/adfm.201000933.

[252] L. U. Khan, Z. U. Khan, R. V. Rodrigues, L. S. Da Costa, M. Gidlund and H. F. Brito, « Synthesis and characterization of tunable color upconversion luminescence β-$NaGdF_4$:Yb^{3+}, Er^{3+} nanoparticles », *J Mater Sci: Mater Electron*, vol. 30, n° 18, p. 16856-16863, **2019**, doi: 10.1007/s10854-019-01462-2.

[253] R. A. Janjua, C. Gao, R. Dai and Z. Sui, « Na^+ -Driven Nucleation of $NaYF_4$: Yb, Er Nanocrystals and effect of temperature on their structural transformations and luminescent properties », *J. Phys. Chem. C*, vol. 122, n° 40, p. 23242-23250, **2018**, doi: 10.1021/acs.jpcc.8b09327.

[254] W.-B. Pei, B. Chen, L. Wang, J. Wu, X. Teng, R. Lau, L. Huang, W. Huang, « NaF-mediated controlled-synthesis of multicolor Na_xScF_{3+x}: Yb/Er upconversion nanocrystals », *Nanoscale*, vol. 7, n° 9, p. 4048-4054, **2015**, doi: 10.1039/C4NR06637E.

[255] T. Zhang, J. Ge, Y. Hu and Y. Yin, « A general approach for transferring hydrophobic nanocrystals into water », *Nano Lett.*, vol. 7, n° 10, p. 3203-3207, **2007**, doi: 10.1021/nl071928t.

[256] C. Sun, G. Pratx, C. M. Carpenter, H. Liu, Z. Cheng, S. S. Gambhir, L. Xing, « Synthesis and Radioluminescence of PEGylated Eu^{3+}-doped Nanophosphors as Bioimaging Probes », *Adv. Mater.*, vol. 23, n° 24, p. H195-H199, **2011**, doi: 10.1002/adma.201100919.

[257] M. S. Nikolic, M. Krack, V. Aleksandrovic, A. Kornowski, S. Förster and H. Weller, « Tailor-Made ligands for biocompatible nanoparticles », *Angewandte Chemie International Edition*, **2006**, doi: 10.1002/anie.200602209.

[258] W. Kong, T. Sun, B. Chen, X. Chen, F. Ai, X. Zhu, M. Li, W. Zhang, G. Zhu and F. Wang, « A General Strategy for Ligand Exchange on Upconversion Nanoparticles », *Inorg. Chem.*, **2017**, doi: 10.1021/acs.inorgchem.6b02479

[259] Z. Chen, H. Chen, H. Hu, M. Yu, F. Li, Q. Zhang, Z. Zhou, T. Yi and C. Huang, « Versatile Synthesis Strategy for Carboxylic Acid−functionalized Upconverting Nanophosphors as Biological Labels », *J. Am. Chem. Soc.*, vol. 130, n° 10, p. 3023-3029, **2008**, doi: 10.1021/ja076151k.

[260] Y. Wu, D. Li, F. Zhou, H. Liang, Y. Liu, W. Hou, Q. Yuan, X. Zhang, W. Tan, « Versatile *in situ* synthesis of MnO_2 nanolayers on upconversion nanoparticles and their application in activatable fluorescence and MRI imaging », *Chem. Sci.*, vol. 9, n° 24, p. 5427-5434, 2**018**, doi: 10.1039/C8SC00490K.

[261] G.-S. Yi and G.-M. Chow, « Water-Soluble $NaYF_4$: Yb, Er (Tm)/$NaYF_4$/polymer core/shell/shell nanoparticles with significant enhancement of upconversion fluorescence », *Chem. Mater.*, vol. 19, n° 3, p. 341-343, **2007**, doi: 10.1021/cm062447y.

[262] L. Wang, R. Yan, Z. Huo, L. Wang, J. Zeng, J. Bao, X. Wang, Q. Peng, Y. Li., « Fluorescence resonant energy transfer biosensor based on upconversion-luminescent Nanoparticles », *Angew. Chem. Int. Ed.*, vol. 44, n° 37, p. 6054-6057, **2005**, doi: 10.1002/anie.200501907.

[263] K. Chatterjee, S. Sarkar, K. Jagajjanani Rao and S. Paria, « Core/shell nanoparticles in biomedical applications », *Advances in Colloid and Interface Science*, vol. 209, p. 8-39, **2014**, doi: 10.1016/j.cis.2013.12.008.

[264] J. Lu, M. Liong, Z. Li, J. I. Zink and F. Tamanoi, « Biocompatibility, biodistribution, and drug-delivery efficiency of mesoporous silica nanoparticles for cancer therapy in animals », *Small*, **2010**, doi: 10.1002/smll.201000538.

[265] R. Abdul Jalil and Y. Zhang, « Biocompatibility of silica coated NaYF4 upconversion fluorescent nanocrystals », *Biomaterials*, vol. 29, n° 30, p. 4122-4128, **2008**, doi: 10.1016/j.biomaterials.2008.07.012.

[266] V. V. Goftman, T. Aubert, D.V. Ginste, R. Van Deun, N. V. Beloglazova, Z. Hens, S. De Saeger, I. Y. Goryacheva, « Synthesis, modification, bioconjugation of silica coated

fluorescent quantum dots and their application for mycotoxin detection », *Biosensors and Bioelectronics*, vol. 79, p. 476-481, **2016**, doi: 10.1016/j.bios.2015.12.079.

[267] Y. Zhang, J. Shen, R. Hu, X. Shi, X. Hu, B. He, A. Qin, B.Z. Tang, « Fast surface immobilization of native proteins through catalyst-free amino-yne click bioconjugation », *Chem. Sci.*, vol. 11, nº 15, p. 3931-3935, **2020**, doi: 10.1039/D0SC00062K.

[268] C. Li, Z. Hou, Y. Dai, D. Yang, Z. Cheng, J. Lin., « A facile fabrication of upconversion luminescent and mesoporous core–shell structured β-$NaYF_4$: Yb^{3+}, Er^{3+}@mSiO_2 nanocomposite spheres for anti-cancer drug delivery and cell imaging », *Biomater. Sci.*, vol. 1, nº 2, p. 213-223, **2013**, doi: 10.1039/C2BM00087C.

[269] J. Liu, W. Bu, S. Zhang, F. Chen, H. Xing, L. Pan, L. Zhou, W. Peng, J. Shi, « Controlled synthesis of uniform and monodisperse upconversion core/mesoporous silica shell nanocomposites for bimodal imaging », *Chem. Eur. J.*, vol. 18, nº 8, p. 2335-2341, **2012**, doi: 10.1002/chem.201102599.

[270] M. Zhang, B. L. Cushing and C. J. O'Connor, « Synthesis and characterization of monodisperse ultra-thin silica-coated magnetic nanoparticles », *Nanotechnology*, vol. 19, nº 8, p. 085601, **2008**, doi: 10.1088/0957-4484/19/8/085601.

[271] J. Dai, H. Zou, R. Wang, Y. Wang, Z. Shi and S. Qiu, « Yolk–shell Fe_3O_4@SiO_2 @PMO: amphiphilic magnetic nanocomposites as an adsorbent and a catalyst with high efficiency and recyclability », *Green Chem.*, vol. 19, nº 5, p. 1336-1344, **2017**, doi: 10.1039/C6GC02926D.

[272] Q. Zhang, T. Zhang, J. Ge and Y. Yin, « Permeable silica shell through surface-protected etching », *Nano Lett.*, vol. 8, nº 9, p. 2867-2871, **2008**, doi: 10.1021/nl8016187.

[273] Y. Hu, Q. Zhang, J. Goebl, T. Zhang and Y. Yin, « Control over the permeation of silica nanoshells by surface-protected etching with water », *Phys. Chem. Chem. Phys.*, vol. 12, nº 38, p. 11836, **2010**, doi: 10.1039/c0cp00031k.

[274] Q. Zhang, J. Ge, J. Goebl, Y. Hu, Z. Lu and Y. Yin, « Rattle-type silica colloidal particles prepared by a surface-protected etching process », *Nano Res.*, vol. 2, nº 7, p. 583-591, **2009**, doi: 10.1007/s12274-009-9060-5.

[275] S. Lu, D. Tu, P. Hu, J. Xu, R. Li, M. Wang, Z. Chen, M. Huang, X. Chen, « Multifunctional nano-bioprobes based on rattle-structured upconverting luminescent nanoparticles », *Angew. Chem.*, vol. 127, nº 27, p. 8026-8030, **2015**, doi: 10.1002/ange.201501468.

[276] M. Eftekhari, K. Schwarzenberger, A. Javadi and K. Eckert, « The influence of negatively charged silica nanoparticles on the surface properties of anionic surfactants: electrostatic repulsion or the effect of ionic strength? », *Phys. Chem. Chem. Phys.*, vol. 22, nº 4, p. 2238-2248, **2020**, doi: 10.1039/C9CP05475H.

[277] S. Rahmani, C. M. Jimenez, D. Aggad, D. González-Mancebo, M. Ocaña, L. M. A. Ali, C. Nguyen, A. I. B. Nieto, N. Francolon, E. Oliveiro, D. Boyer, M. Gary-Bobo, J.-O. Durand, R. Mahiou and C. Charnay « Encapsulation of upconversion nanoparticles in

periodic mesoporous organosilicas », *Molecules*, vol. 24, n° 22, p. 4054, **2019**, doi: 10.3390/molecules24224054.

[278] G. Tsagkaropoulou, F. J. Allen, S. M. Clarke and P. J. Camp, « Self-assembly and adsorption of cetyltrimethylammonium bromide and didodecyldimethylammonium bromide surfactants at the mica–water interface », *Soft Matter*, vol. 15, n° 41, p. 8402-8411, **2019**, doi: 10.1039/C9SM01464K.

[279] M. Runowski, N. Stopikowska, D. Szeremeta, S. Goderski, M. Skwierczyńska and S. Lis, « Upconverting lanthanide fluoride core@shell nanorods for luminescent thermometry in the first and second biological windows: β-$NaYF_4$: Yb^{3+} – Er^{3+} @SiO_2 Temperature Sensor », *ACS Appl. Mater. Interfaces*, vol. 11, n° 14, p. 13389-13396, **2019**, doi: 10.1021/acsami.9b00445.

[280] Y. Wang, L. Tu, J. Zhao, Y. Sun, X. Kong and H. Zhang, « Upconversion luminescence of β-$NaYF_4$: Yb^{3+}, Er^{3+} @β-$NaYF_4$ core/shell nanoparticles: excitation power density and surface dependence », *J. Phys. Chem. C*, vol. 113, n° 17, p. 7164-7169, **2009**, doi: 10.1021/jp9003399.

[281] Z. Feng, L. Lin, Z. Wang and Z. Zheng, « Highly efficient and wide range low temperature sensing of upconversion luminescence of $NaYF_4$: Er^{3+} nanoparticles: Effects of concentration of active or sensitive ions, excitation power and particle size on temperature sensing sensitivity », *Optics Communications*, vol. 491, p. 126942, **2021**, doi: 10.1016/j.optcom.2021.126942.

[282] C. Homann, L. Krukewitt, F. Frenzel, B. Grauel, C. Würth, U. Resch-Genger, M. Haase, « $NaYF_4$: Yb, Er/$NaYF_4$ core/shell nanocrystals with high upconversion luminescence quantum yield », *Angew. Chem. Int. Ed.*, vol. 57, n° 28, p. 8765-8769, **2018**, doi: 10.1002/anie.201803083.

[283] J. Ding, H. Liao, L. Pang, D. Wang and S. Ye, « Improved up-conversion behaviors and temperature sensitivity based on Stark sublevels of Er^{3+} in β-$NaYF_4$:Yb^{3+}, Er^{3+} and β-$NaYF_4$:Yb^{3+}, Er^{3+}@$NaGdF_4$ », *Optical Materials*, vol. 128, p. 112304, **2022**, doi: 10.1016/j.optmat.2022.112304.

[284] D. Li, Q. Shao, Y. Dong and J. Jiang, « Temperature sensitivity and stability of $NaYF_4$: Yb^{3+}, Er^{3+} core-only and core–shell upconversion nanoparticles », *Journal of Alloys and Compounds*, vol. 617, p. 1-6, **2014**, doi: 10.1016/j.jallcom.2014.07.197.

[285] L. Li, F. Qin, Y. Zhou, Y. Zheng, H. Zhao and Z. Zhang, « Study on the thermal sensitivity of β-$NaYF_4$: Yb^{3+}-Er^{3+} nano-thermometers based on luminescence ratiometric technology », *Current Applied Physics*, vol. 19, n° 4, p. 480-485, **2019**, doi: 10.1016/j.cap.2019.01.021.

[286] L. Liu, F. Qin, H. Zhao, T. Lv, Z. Zhang and W. Cao, « Shell thickness dependence of upconversion luminescence of β-$NaYF_4$: Yb, Er/β-$NaYF_4$ core-shell nanocrystals », *Opt. Lett.*, vol. 38, n° 12, p. 2101, **2013**, doi: 10.1364/OL.38.002101.

[287] R. Arppe, I. Hyppänen, N. Perälä, R. Peltomaa, M. Kaiser, C. Würth, S. Christ, U. Resch-Genger, M. Schäferling and T. Soukka, « Quenching of the upconversion

luminescence of $NaYF_4$: Yb^{3+}, Er^{3+} and $NaYF_4$: Yb^{3+}, Tm^{3+} nanophosphors by water: the role of the sensitizer Yb^{3+} in non-radiative relaxation », *Nanoscale*, vol. 7, n° 27, p. 11746-11757, **2015**, doi: 10.1039/C5NR02100F.

[288] Q. Lü, F. Guo, L. Sun, A. Li and L. Zhao, « Silica-/titania-coated Y_2O_3:Tm^{3+}, Yb^{3+} nanoparticles with improvement in upconversion luminescence induced by different thickness shells », *Journal of Applied Physics*, vol. 103, n° 12, p. 123533, **2008**, doi: 10.1063/1.2946730.

[289] R. G. Geitenbeek, P. T. Prins, W. Albrecht, A. Van Blaaderen, B. M. Weckhuysen and A. Meijerink, « $NaYF_4$: Er^{3+}, Yb^{3+}/SiO_2 Core/Shell upconverting nanocrystals for luminescence thermometry up to 900 K », *J. Phys. Chem. C*, vol. 121, n° 6, p. 3503-3510, **2017**, doi: 10.1021/acs.jpcc.6b10279.

[290] X. Zhu, J. Li, X. Qiu, Y. Liu, W. Feng and F. Li, « Upconversion nanocomposite for programming combination cancer therapy by precise control of microscopic temperature », *Nat Commun*, vol. 9, n° 1, p. 2176, **2018**, doi: 10.1038/s41467-018-04571-4.

[291] K. Kniec, K. A. Ledwa and L. Marciniak, « Role of SiO_2 coating on YAG: V^{3+}, Nd^{3+} nanoparticles in luminescence thermometry », *ACS Appl. Nano Mater.*, vol. 5, n° 6, p. 8271-8278, **2022**, doi: 10.1021/acsanm.2c01180.

[292] M. Back, E. Casagrande, C. A. Brondin, E. Ambrosi, D. Cristofori, J. Ueda, S. Tanabe, E. Trave and P. Riello « Lanthanide-doped Bi_2SiO_5 @SiO_2 core–shell upconverting nanoparticles for stable ratiometric pptical thermometry », *ACS Appl. Nano Mater.*, vol. 3, n° 3, p. 2594-2604, **2020**, doi: 10.1021/acsanm.0c00003.

[293] I. Hyppänen, N. Perälä, R. Arppe, M. Schäferling and T. Soukka, « Environmental and excitation power effects on the ratiometric upconversion luminescence-based temperature sensing ssing nanocrystalline $NaYF_4$: Yb^{3+}, Er^{3+} », *ChemPhysChem*, vol. 18, n° 6, p. 692-701, **2017**, doi: 10.1002/cphc.201601355.

[294] C. D. S. Brites, E. D. Martínez, R. R. Urbano, C. Rettori and L. D. Carlos, « Self-calibrated double luminescent thermometers through upconverting nanoparticles », *Front. Chem.*, vol. 7, p. 267, **2019**, doi: 10.3389/fchem.2019.00267.

[295] A. Nexha, M. C. Pujol, F. Díaz, M. Aguiló and J. J. Carvajal, « Luminescence nanothermometry using self-assembled Er^{3+}, Yb^{3+} doped Y_2O_3 nanodiscs: Might the upconversion mechanism condition their use as primary thermometers? », *Optical Materials*, vol. 134, p. 113216, **2022**, doi: 10.1016/j.optmat.2022.113216.

[296] N. M. Bhiri, M. Dammak, J. J. Carvajal, M. Aguiló, F. Díaz and M. C. Pujol, « Excitation power density dependence of a primary luminescent thermometer based on Er^{3+}, Yb^{3+}: $GdVO_4$ microcrystals operating in the visible », *Journal of Alloys and Compounds*, vol. 921, p. 166020, **2022**, doi: 10.1016/j.jallcom.2022.166020.

[297] E. D. Martínez, C. D. S. Brites, L. D. Carlos, A. F. García-Flores, R. R. Urbano and C. Rettori, « Electrochromic switch devices mixing small- and large-sized upconverting nanocrystals », *Adv Funct Materials*, vol. 29, n° 8, p. 1807758, **2019**, doi: 10.1002/adfm.201807758.

[298] M. Kraft, C. Würth, V. Muhr, T. Hirsch and U. Resch-Genger, « Particle-size-dependent upconversion luminescence of $NaYF_4$: Yb, Er nanoparticles in organic solvents and water at different excitation power densities », *Nano Res.*, vol. 11, nº 12, p. 6360-6374, **2018**, doi: 10.1007/s12274-018-2159-9.

[299] T. P. Van Swieten, T. van Omme, D. J. van den Heuvel, S. J.W. Vonk, R. G. Spruit, F. Meirer, H. H. Pérez Garza, B. M. Weckhuysen, A. Meijerink, F. T. Rabouw and R. G. Geitenbeek, « Mapping elevated temperatures with a micrometer resolution using the luminescence of chemically stable upconversion nanoparticles », *ACS Appl. Nano Mater.*, vol. 4, nº 4, p. 4208-4215, **2021**, doi: 10.1021/acsanm.1c00657.

[300] S. Zhou, K. Deng, X. Wei, G. Jiang, C. Duan, Y. Chen., M. Yin, « Upconversion luminescence of $NaYF_4$: Yb^{3+}, Er^{3+} for temperature sensing », *Optics Communications*, vol. 291, p. 138-142, **2013**, doi: 10.1016/j.optcom.2012.11.005.

[301] M. Pollnau, D. R. Gamelin, S. R. Lüthi, H. U. Güdel and M. P. Hehlen, « Power dependence of upconversion luminescence in lanthanide and transition-metal-ion systems », *Phys. Rev. B*, vol. 61, nº 5, p. 3337-3346, **2000**, doi: 10.1103/PhysRevB.61.3337.

[302] P. Rühl, D. Wang, F. Garwe, R. Müller, M. Haase, K. W. Krämer, W. Paa, R. Heintzmann, S. H. Heinemann and H. Stafast, « Notes on thermometric artefacts by Er^{3+} luminescence band interference », *Journal of Luminescence*, vol. 232, p. 117860, **2021**, doi: 10.1016/j.jlumin.2020.117860.

[303] J. C. Martins, A. R. N. Bastos, R. A. S. Ferreira, X. Wang, G. Chen and L. D. Carlos, « Primary luminescent nanothermometers for temperature measurements reliability assessment », *Adv Photo Res*, vol. 2, nº 5, p. 2000169, **2021**, doi: 10.1002/adpr.202000169.

[304] J. C. Martins, A. Skripka, C.D.S. Brites, A. Benayas, R.A.S Ferreira, F. Vetrone, L.D. Carlos, « Upconverting nanoparticles as primary thermometers and power sensors », *Front. Photon.*, vol. 3, p. 1037473, **2022**, doi: 10.3389/fphot.2022.1037473.

[305] J. Mooney and P. Kambhampati, « Get the basics right: Jacobian conversion of wavelength and energy scales for quantitative analysis of emission spectra », *J. Phys. Chem. Lett.*, vol. 4, nº 19, p. 3316-3318, **2013**, doi: 10.1021/jz401508t.

[306] M. L. Debasu, D. Ananias, A. G. Macedo, J. Rocha and L. D. Carlos, « Emission-decay curves, energy-transfer and effective-refractive index in Gd_2O_3: Eu^{3+} nanorods », *J. Phys. Chem. C*, vol. 115, nº 31, p. 15297-15303, **2011**, doi: 10.1021/jp205093x.

[307] B. Chen, B. Dong, J. Wang, S. Zhang, L. Xu, W. Yu, H. Song, « Amphiphilic silane modified $NaYF_4$: Yb, Er loaded with Eu (TTA)3(TPPO)2 nanoparticles and their multi-functions: dual mode temperature sensing and cell imaging », *Nanoscale*, vol. 5, nº 18, p. 8541, **2013**, doi: 10.1039/c3nr02670a.

[308] D. Li, B. Dong, X. Bai, Y. Wang and H. Song, « Influence of the TGA Modification on Upconversion Luminescence of Hexagonal-Phase $NaYF_4$: Yb^{3+}, Er^{3+} Nanoparticles », *J. Phys. Chem. C*, vol. 114, nº 18, p. 8219-8226, **2010**, doi: 10.1021/jp100893k.

[309] R. G. Geitenbeek, H. W. De Wijn and A. Meijerink, « Non-Boltzmann luminescence in $NaYF_4 : Eu^{3+}$: Implications for luminescence thermometry », *Phys. Rev. Applied*, vol. 10, n° 6, p. 064006, **2018**, doi : 10.1103/PhysRevApplied.10.064006.

[310] D. Vásquez Mazzotti, L. Alvarado, R. Puga and H. Loro, « Calibration of remote nanothermometers using nanoparticles of $NaYF_4$: Er^{3+}, Yb^{3+}, Nd^{3+} », *J. Phys.: Conf. Ser.*, vol. 1143, p. 012023, **2018**, doi: 10.1088/1742-6596/1143/1/012023.

[311] N. Bogdan, F. Vetrone, G. A. Ozin and J. A. Capobianco, « Synthesis of ligand-free colloidally stable water dispersible brightly luminescent lanthanide-doped upconverting nanoparticles », *Nano Lett.*, vol. 11, n° 2, p. 835-840, **2011**, doi: 10.1021/nl1041929.

[312] C. Würth, M. Kaiser, S. Wilhelm, B. Grauel, T. Hirsch and U. Resch-Genger, « Excitation power dependent population pathways and absolute quantum yields of upconversion nanoparticles in different solvents », *Nanoscale*, vol. 9, n° 12, p. 4283-4294, **2017**, doi: 10.1039/C7NR00092H.

[313] F. E. Maturi, C.D.S. Brites, R. R. Silva, K. Nigoghossian, D. Wilson, R.A.S. Ferreira, S.J.L. Ribeiro and L.D. Carlos, « Sustainable smart tags with two-step verification for anticounterfeiting triggered by the photothermal sesponse of upconverting nanoparticles », *Advanced Photonics Research*, vol. 3, n° 6, p. 2100227, **2022**, doi: 10.1002/adpr.202100227.

[314] J. K. West, G. LaTorre and L. L. Hench, « The UV-visible spectrum in porous type VI silica: application and theory », *Journal of Non-Crystalline Solids*, vol. 195, n° 1-2, p. 45-53, **1996**, doi: 10.1016/0022-3093(95)00529-3.

[315] A. D. Pickel, A. Teitelboim, E. M. Chan, N. J. Borys, P. J. Schuck and C. Dames, « Apparent self-heating of individual upconverting nanoparticle thermometers », *Nat Commun*, vol. 9, n° 1, p. 4907, **2018**, doi: 10.1038/s41467-018-07361-0.

[316] R. E. Joseph, D. Busko, D. Hudry, G. Gao, D. Biner, K. Krämer, A. Turshatov, B. S. Richards, I. A. Howard, « A method for correcting the excitation power density dependence of upconversion emission due to laser-induced heating », *Optical Materials*, vol. 82, p. 65-70, **2018**, doi: 10.1016/j.optmat.2018.05.025.

[317] G. B. Nair, S. Tamboli, S. J. Dhoble and H. C. Swart, « LaOF: Yb^{3+}, Er^{3+} upconversion nanophosphors operating at low laser powers for nanothermometry applications », *ACS Appl. Nano Mater.*, vol. 6, n° 16, p. 15255-15265, **2023**, doi: 10.1021/acsanm.3c03208.

[318] A. R. N. Bastos, C.D.S. Brites, P.A. Rojas-Gutierrez, C. DeWolf, R.A.S. Ferreira, J.A. Capobianco and L.D. Carlos « thermal properties of lipid bilayers determined using upconversion nanothermometry », *Adv Funct Materials*, vol. 29, n° 48, p. 1905474, **2019**, doi: 10.1002/adfm.201905474.

Résumé

Ce travail de thèse porte sur l'élaboration de nanoplatformes multifonctionnelles de type cœur/coquille incluant un cœur fonctionnel qui agit comme nanothermomètre encapsulé dans une couche de silice hybride mésoporeuse de type PMO (Periodic Mesoporous Organosilica). L'élaboration des systèmes a été effectuée dans un premier temps suivant la stratégie d'un dépôt de silice hybride mésoporeuse sur un cœur condensé à base de silice « hard template ». Une étude fondamentale de la structure, de la nature chimique et de la taille de la coquille de confinement est menée par une approche expérimentale multi-échelle. La modulation de la taille des nano-objets sur un ordre de grandeur entre 50 et 500 nm environ a été démontrée, ainsi que la modulation de la composition chimique basée sur l'utilisation de différents précurseurs organosilanes pontés. Les résultats ont révélé que l'organisation des mésopores de la couche est conditionnée par les interactions supramoléculaires entre sous structures organiques de la silice hybride. L'élaboration d'un cœur fonctionnel photoluminescent dopé de terres rares (β-$NaYF_4$: Yb^{3+}, Er^{3+}) a été ensuite effectuée, suivie du dépôt d'une couche hybride afin d'obtenir des systèmes multicoquilles. Ces systèmes ont été modifiés pour introduire un espace creux entre les deux phases. Les performances thermométriques des nanoparticules fonctionnelles en fonction du type de confinement ont été étudiées en détail sur la base de leur réponse en photoluminescence. L'évaluation des performances des nanothermomètres obtenues est encourageante pour des applications dans le domaine biologique.

Abstract

The thesis work focuses on the development of multifunctional core/shell nanoplatforms including a functional core acting as a nanothermometer encapsulated in a PMO-type mesoporous hybrid silica layer. The elaboration of the systems was initially carried out according to the strategy of a mesoporous hybrid silica deposition on a silica-based condensed core ("hard template" strategy). A fundamental study of the structure, chemical nature and size of the shell is conducted using a multi-scale experimental approach. The nano-object size modulation in a range between 50 and 500 nm approximately has been demonstrated, as well as the modulation of the chemical composition based on the use of different bridged organosilane precursors. The results revealed that the organization of the mesopores of the layer is conditioned by the supramolecular interactions between organic substructures of the hybrid silica. The elaboration of a photoluminescent functional core doped with rare earths (β-$NaYF_4$: Yb^{3+}, Er^{3+}) was then carried out, followed by the deposition of a hybrid layer in order to obtain multishell systems. These systems have been modified to introduce a hollow space between the two phases. The thermometric performance of the functional nanoparticles as a function of the confinement type were studied in detail on the basis of their photoluminescence response. The evaluation of the performance of the resulting nanothermometers is encouraging for applications in the biological field.